UNIVERSITÀ DEGLI STUDI DI MILANO

Scuola di Dottorato in Fisica, Astrofisica e Fisica Applicata
Dipartimento di Fisica

Corso di Dottorato in Fisica, Astrofisica e Fisica Applicata
Ciclo XXXVI

The impact of triple stellar systems on protostellar disc dynamics

Settore Scientifico Disciplinare FIS/05

Supervisore: Professor Giuseppe Lodato
Co-supervisore: Professor Nicolás Cuello

Coordinatore: Professoressa Roberta Vecchi

Tesi di Dottorato di:

Simone Ceppi

Anno Accademico 2022-2023

Commission of the final examination:

External Referees:
Kaitlin Kratter
François Ménard

External Members:
François Ménard
Cornelis P. Dullemond

Internal Member:
Giuseppe Lodato

Final examination:

Date 5th of February 2024

Università degli Studi di Milano, Dipartimento di Fisica, Milano, Italy

"Two is company, three is a crowd."

Conventional wisdom also suggests staying
away from more than two-body systems.

"Running, running on tracks
With feet on the ground
It will only slow me down
And which way the wind blows
I run like a man ready to go anywhere.

[...]

Sometimes I spin around for days
Skip and chase and say
Forget about tomorrow
Until I realize
This valid and logic motion
Is what keeps me from moving
Keeps you from leaving
And what keeps us from leaving
I don't know, I understand."

Melody of certain three, Blonde Redhead.

The first part is more about me,
the second part more about hierarchical systems.
But it could be the opposite.

MIUR subjects:

FIS/05

PACS:

97.82.Jw

Contents

Part I

Introduction & Fundamental Theory

CHAPTER 1

Motivation and outline

Motivation

The quest for understanding the origin of our planet is as old as humankind, as it is a milestone in understanding ourselves. The modern idea that planets form inside disc-like structures orbiting stars was born in the 17th and 18th centuries by Swedenborg, and then Kant (1755) and Laplace (1796). From that seminal idea, in the middle of the last century, astrophysicists started modelling accretion discs, the precursors of planetary systems, without having observations to compare with (Hoyle 1960). Indeed, the first observations of these structures were taken by the Hubble Space Telescope only in the Nineties (e.g. McCaughrean & O'Dell 1996, Fig. 1.1a). Starting in the sixties, astrophysicists modelled stellar and planet formation with the simplest possible model. Collapsing gas settling in a central protostar surrounded by a flat rotating disc-like structure formed due to angular momentum conservation (now condensed in the 'classical accretion disc theory', e.g. Frank et al. 2002, see Part I Chap. 4). This successful idea, rooted in philosophy and galactic models, soon highlighted a whole bunch of missing crucial details, starting the still ongoing hunt for a global and complete theory.

Only in the last 10 years, modern telescopes and facilities such as ALMA and SPHERE have given us the sharp and detailed observations we are nowadays used to (like the ones in Fig. 1.1b from Andrews et al. 2018). Also, we have now access to a vast amount of information about stellar system statistics. This data taught us that, among the many peculiarities of our own Solar System compared to other planetary systems, the most common condition for a star is to belong to a multiple stellar system, rather than to live in isolation (e.g. Duchêne & Kraus 2013; Offner et al. 2022, Part I Chap. 3).

Hints that systems with more than one star could be common in the universe were there well before the observational evidence. Seminal work by Larson (1972) suggested that most, if not all, stars formed inside a multiple stellar system. Thus, scientists soon started working on modelling the interaction between accretion discs and binary systems (e.g. Lin & Pringle 1976; Papaloizou & Pringle 1977, Part I Chap. 4.2). These crucial works greatly advanced the theory of disc evolution and allowed us to interpret features in observations.

Multiplicity, other than being useful, is unavoidable. First, we know from evolved stellar population surveys that multiple stellar systems are common, even if not the majority below the solar mass. However, even accounting only for field population statistics, most stars live in multiple stellar systems. But, we know that the number of multiple stellar systems tends to decrease with time, and we do observe a higher occurrence of multiple stellar systems in younger populations (Tobin et al. 2022). The younger the system, the harder it is to observe — due to the surrounding environment which becomes progressively thicker. On the other hand, numerical simulations of collapsing molecular

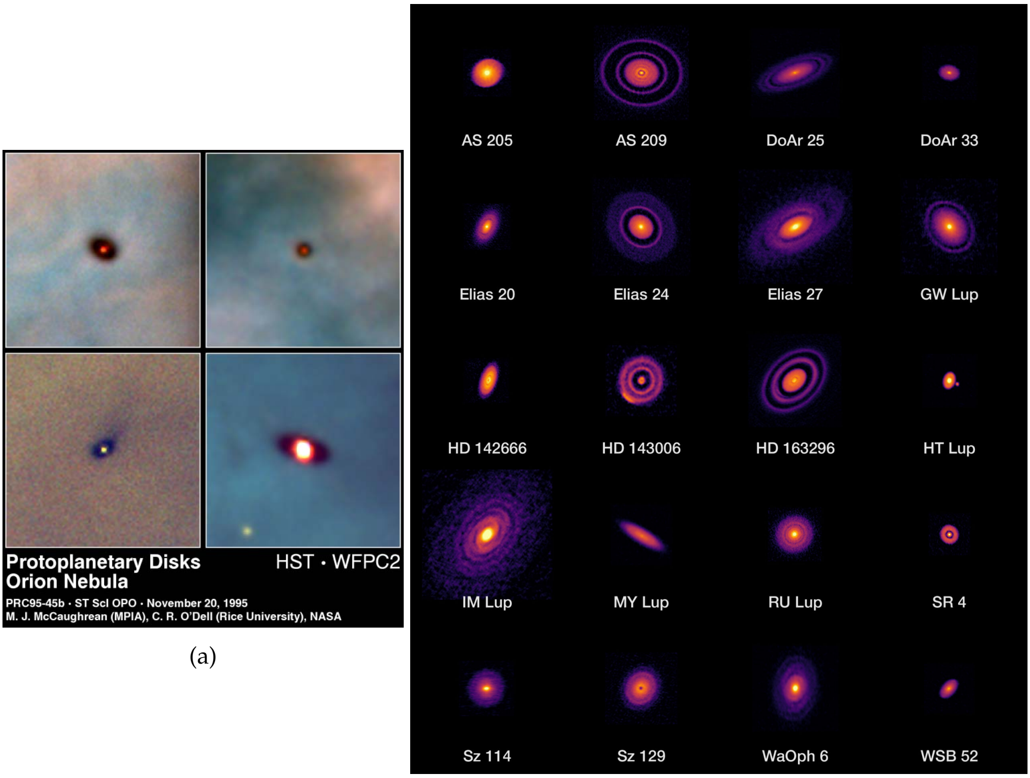

(a)

(b)

Figure 1.1: Left panel: HST Orion nebula image (McCaughrean & O'Dell 1996). Right panel: DSHARP survey of high-resolution dust images of 20 nearby protoplanetary disks observed with ALMA (Andrews et al. 2018).

clouds are extremely relevant and useful to track the early phases of evolution in the stellar formation process (Bate et al. 2002; Krumholz et al. 2012; Bate 2018, 2019; Mathew & Federrath 2021; Mathew et al. 2023; Lebreuilly et al. 2023). The current goal is to reduce the age of the populations for which we have reliable and complete surveys in order to consistently compare them with the most recent numerical predictions. Both numerical simulations and observations are converging towards the following facts: i) most of the stars are born in multiple stellar systems; ii) discs are born and get destroyed within these systems; and iii) planet formation processes (which are believed to act nearly at the same time as stellar formation processes) are deeply affected by stellar multiplicity. Taking its effects into account is not just a theoretical exercise or an effort to study atypical configurations, but rather the way in which we can really understand what is actually happening in realistic star-forming environments.

With the advent of modern instruments allowing the observation of snapshots of the ongoing planet and stellar formation process, scientists were forced to deal with these additional complexities found in nature. Remarkably, there is little trace of the (classical) smooth flat homogeneous axisymmetric disc-like structure orbiting a single protostar. Discs show substructures, they present asymmetric features, they are not smooth but full of gaps and bumps, they are not planar but often distorted and broken. And, finally, a lot of them are orbiting within or around multiple stellar systems. It is even possible that all of them were once part of a system made of several young stars.

To have a grasp of the diversity of the protoplanetary discs zoo, Figure 1.1b shows a survey of protoplanetary discs known as the Disk Substructures at High Angular Resolution Project (DSHARP Andrews et al. 2018). This set of ALMA observations collects high-resolution dust images of 20 nearby protoplanetary disks and showcases the variety of features they contain. A satisfactory and natural way to explain many of these features is the presence of more than one body in the system. Namely, it could be a planet carving gaps in the disc or a (often undetected) stellar companion inside or outside the disc, distorting and tilting it.

I am going to give some examples of observation of specific multiple stellar systems to showcase the early stages of stellar evolution in these configurations (a broader discussion about observations of discs within multiple stellar systems can be found in Zurlo et al. 2023). By focusing on single sources, the intricacies due to the presence of additional bodies are stunning. The young stellar system GG Tauri A stands as a crucial focal point in the investigation of stellar and planetary formation processes. This system is located within the Taurus-Auriga star-forming region, approximately 145 parsecs from Earth (Galli et al. 2019). GG Tauri A consists of a hierarchical triple system surrounded by a circumtriple accretion disc with unresolved material in the disc central cavity. Moreover, the system is orbited by a binary, GG Tauri B, which makes GG Tauri a quintuple hierarchical system (Köhler 2011a; Cazzoletti et al. 2017; Aly et al. 2018; Keppler et al. 2020). Having both gas and dust observations, the protoplanetary disk surrounding GG Tauri A presents an exceptional opportunity to delve into the mechanisms underlying planetesimal assembly and planetary system formation in multiple stellar systems. Figure 1.2 shows SPHERE and ALMA images of dust and gas components (Keppler et al. 2020; Phuong et al. 2020). From these observations, it is evident the presence of a central cavity carved by the triple stellar system, along with the material inside it supplied by the accretion streams launched from the edge of the cavity.

The young protostellar system GW Orionis (Kraus et al. 2020; Bi et al. 2020; Smallwood et al. 2021) emerges as another prime example of a forming multiple stellar system. Situated in the well-studied Orion Molecular Cloud complex, GW Orionis captivates researchers with its dynamic and complex configuration. This protostellar system

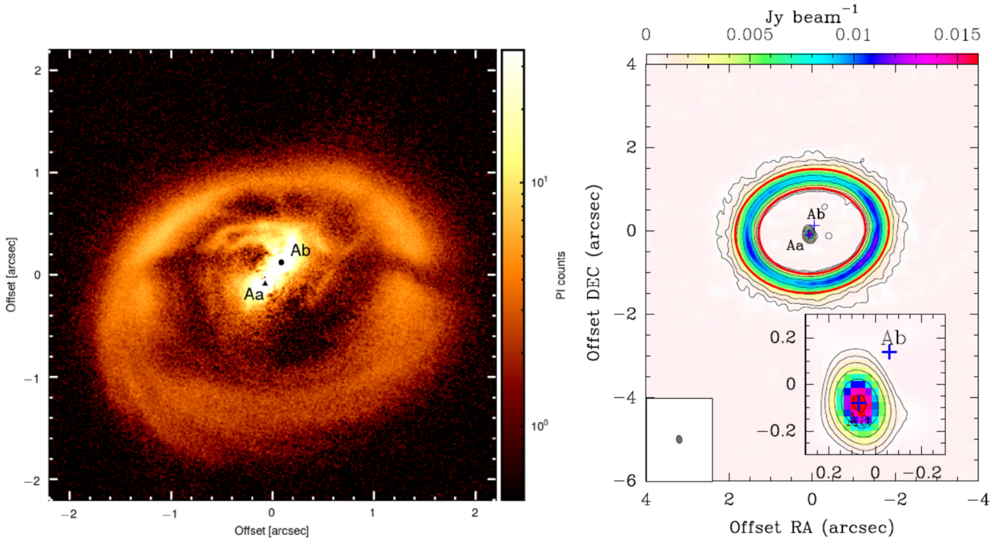

(a)

(b)

Figure 1.2: (a): SPHERE polarised intensity image of GG Tau A, from Keppler et al. (2020). (b): ALMA continuum image at 0.9 mm, from Phuong et al. (2020)

comprises three stars, with discs orbiting different hierarchical levels. Particularly, the circumtriple disc presents gaps and it is broken into three rings which are misaligned to each other. Figure 1.3 shows dust observation taken with ALMA along with a sketch of the system configuration with its three rings and the inner disc orbiting the stars of this triple system.

The last example I want to mention is the protostellar system HD 98800 (Kennedy et al. 2012; Zúñiga-Fernández et al. 2021). This system is a well-known hierarchical quadruple stellar system 44.9 parsecs from Earth, in the TW Hydrae Association. It consists of two pairs of binaries orbiting each other. The most peculiar characteristic of this system is that one of its two binaries hosts the first observed polar accretion disc, which is nearly perpendicular to the central binary orbit. Figure 1.4 shows dust observation from ALMA of the disc orbiting HD 98800B along with the orbits of the inner binary and the outer orbit traced by the centre of mass of HD 98800A binary.

Such systems offer a unique laboratory for studying the intricate interplay of gravitational forces and accretion phenomena that govern the formation of stars and planetary bodies. Investigating these stellar configurations not only contributes to our understanding of the specific evolutionary trajectory of these systems but also provides broader insights into the processes shaping stellar and planet populations during their early stages.

Ultimately, this vivid and complex display of order within chaos, showcasing a wide variety of forms, arises from the laws of physics. All these irregularities, imperfections, rough textures, and chaotic elements are not just unfortunate side effects; rather, they are an integral part of the process of star and planet formation. This aspect is a crucial component of the process and provides a valuable chance to gain a more profound understanding of how things have developed to reach their current state. According to

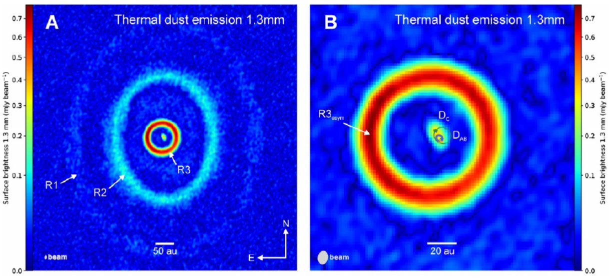

(a) GW Ori ALMA observation

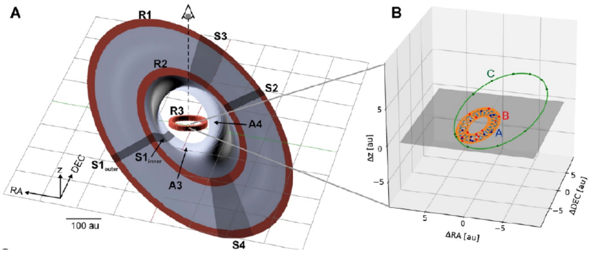

(b) GW Ori 3D model

Figure 1.3: Observations and model for the GW Ori system. On the top line: 1.3mm thermal dust continuum emission observed with ALMA. On the bottom line: illustration of the 3-dimensional orientation of the disk (left) and stellar (right) components. R1, R2 and R3 label the three dusty rings. Images from Kraus et al. (2020)

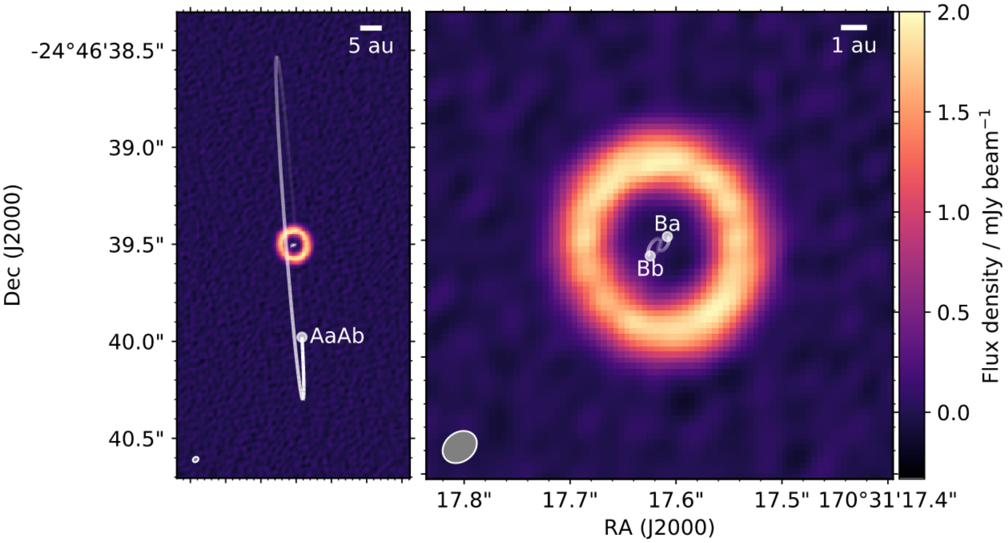

Figure 1.4: ALMA 1.3 millimetre continuum image of the HD 98800 dust disc. White lines show the inner binary's orbits and the outer binary's path. Image from Kennedy et al. (2012)

Occam's razor, these additional complexities could not be a strange avoidable ingredient for stepping from the initial conditions to the configurations we observe. Complexity has to be one key ingredient, otherwise, it would not be there. This is how the role of multiple stellar systems in stellar and planet formation theory is to be approached. Stellar multiplicity does not constitute an undesirable complexity in our theories, but rather allows us to look into the gears of astrophysical processes.

In the same way scientist initially simplified their models assuming discs orbiting single stars, nowadays we simplify the interaction between accretion discs and multiple stellar systems assuming them to behave like the simplest of them, a binary. An isolated binary orbit is well described by analytical solutions, it is predictable and immutable (e.g. Murray & Dermott 1999, Part I Sec. 2.1). We can more easily investigate how the binary impact disc evolution and vice-versa. However, reality is certainly more complex than this simplified view. A good portion of multiple stellar systems studied as binaries (like GG Tau and HD 98800, to name two already presented previously) are made of more than two stars. Therefore, modern astrophysicists are currently expanding this theoretical framework to include systems with more than two stars. While these systems resemble pure binary systems over shorter timescales, they exhibit distinct behaviours and uniquely impact their surrounding environment. Indeed, once we introduce an additional companion to a binary we have no analytical solutions for the system motion and we have to deal with the chaotic nature of N-body systems (e.g. Valtonen & Karttunen 2006, Part I Chap. 2). The presence of more than two stars implies the possibility of misalignment, orbits are not immutable anymore even if isolated, they can result in chaotic motion and more complex evolution. However, we are now aware that stellar multiplicity is a key ingredient to understand disc and planet evolution. This constitutes the main objective of my thesis.

Thesis outline

During my PhD, I generalised physical processes studied in the context of binary systems to systems with more than two stars. The aim of my research is, at the same time, to explain what we observe in stellar and planetary populations and to exploit the additional degrees of freedom of multiple stellar systems. This allowed me to put constraints on the properties of the environment in which stars form and also to study their expected evolution in detail. The thesis is organised as follows:

- **Part I** introduces the fundamental concepts on which my work is rooted. I present multiple stellar system dynamics both for binaries and for systems with more than two stars (mainly taking hierarchical triple systems as the reference). Binary systems help me introduce properties and definitions useful for multiple stellar systems in general. Then, I discuss what are the consequences of adding a third body to the system and how we can deal with the chaotic behaviour of such configurations. In this, I also discuss multiple stellar systems statistics, to underline what was already stated previously: multiple stellar systems are the common playground for young stars and planets. Finally, I present the hydrodynamics of accretion discs, starting from discs orbiting single stars and, then, generalising concepts to discs interacting with more than one star and introducing additional considerations about phenomena typical of multiple stellar systems with discs.

- With the foundations laid down, I step into presenting the works I carried out during my PhD. **Part II** presents my investigation on accretion rates in hierarchical triple systems with discs based on the paper Ceppi et al. (2022). In the hunt for extrasolar planets, astronomers look for tiny deviations in different kinds of stellar system emissions to spot formed massive bodies orbiting the stars. In the last 20 years, the observed planet population has risen up to more than 5000 observed exoplanets. This statistic acts both as a test and as a guide for planet formation theories. Indeed, on the one hand, theory must be able to justify the observed population in terms of mass, composition and configuration (both the planetary architecture and the configuration of the hosting system). On the other hand, once we correct surveys for detection biases we find clues on which planets are more likely to form and where. Given that multiple stellar systems are very common, particularly during the planet formation epoch, such surveys guide our understanding of which conditions are favourable to planet formation in complex stellar system configurations. Going backwards, a planet formed in a multiple stellar system has to form on a stable orbit[1]. Otherwise, it will be soon ejected from the system. Even before, regions in which we observe planets must have had enough material for them to form. In multiple stellar systems, this could be a limiting factor. Indeed, once the system and its discs have formed, inner discs in the system see their dust quickly drift away depleting them from material needed for planet formation. This means discs have to both be able to form and they need to be replenished of gas and dust from the surrounding environment. One interesting aspect of this problem is the so-called *differential accretion* dynamics in multiple stellar systems, that is how mass from an accretion disc distributes over the star of a multiple stellar system. In the context of binaries, material in the circum-binary disc accretes towards the binary and accretes on one of the two binary stars. The way material distributes over the stars depends on both the binary orbit and disc properties. Broadly speaking, the lightest star of the binary is generally favoured slowly leading binary systems towards mass equalisation. On top of modifying stellar masses, this process dictates also where material needed for building planets is more abundant and, thus, where planets are more likely to form. In Ceppi et al. (2022) I investigated this process, generalising it to systems with more than two stars, with an analytical approach tested against state-of-the-art numerical simulations. This work presents the deviations of hierarchical stellar system differential accretion processes from the binary configuration, which was the only one studied in the literature. In addition, it discusses the expected impact of this process on populations of hierarchical stellar systems.

- **Part III** presents the investigation I carried out on the process of polar alignment in hierarchical systems with more than two stars. As previously discussed, the study of multiple stellar systems constitutes a precious opportunity for developing a deeper understanding of stellar and planet formation. Indeed, compared to single stellar systems, they offer us a wider set of processes and parameters to investigate. Surveys of multiple stellar system parameters, like surveys of exoplanets, are valuable to gain insight into the physical processes shaping the population. One of these interesting parameter surveys is the distribution of the angle between a circum-multiple disc plane and the orbit of the system inside the disc cavity (so-called *mutual inclination*). Indeed, the mutual inclination distribution encodes information both on the formation history of the stellar and disc population (i.e. how

---

[1] Moreover, stable orbits in the presence of surrounding disc gas could be unstable once the disc disappears.

it was distributed at the onset of stellar formation) and on its evolution, which depends on crucial parameters in the disc physics such as the amount of viscosity driving disc evolution. The process of *polar alignment* in discs within multiple stellar systems, which drives a disc to become orthogonal with respect to the (inner) stellar orbital plane, is of particular interest. This process is invoked to explain the small population of perpendicular discs we observe, which otherwise should have no reason to form and remain stable. Usually, mutual inclination surveys are interpreted ignoring crucial differences between binaries and systems with more than two stars. However, in surveys of mutual angle, a predominant fraction of non-coplanar discs are orbiting in systems with more than two stars. In the paper Ceppi et al. (2023), I found that binary criteria for polar alignment are necessary but not sufficient when two stars are at play. In particular, the additional analytical criterion I introduced suggests a new interpretation of mutual inclination surveys which was not taken into account before.

- **Part IV** discusses the result I obtained in the paper Ceppi et al. (2024), where I developed a simple statistical model to retrieve the initial mutual angle and eccentricity distributions in a multiple stellar system population. This estimate is done from the mean properties of the observed polar disc population only. Surveys of mutual angles can inform us about the distribution of multiple stellar systems and disc properties at the onset of stellar formation and, possibly, about the molecular cloud properties in which stars are forming. Indeed, while most of the discs in multiple stellar systems slowly dissipate their mutual angle with time, the population of polar discs quickly settle into a polar configuration as long as the conditions for polar alignment are met. Thanks to the sharp and faster evolutionary track of polar discs we can link the statistical properties of the polar population in more evolved stages to the conditions of the population in which these configurations formed at the onset of stellar formation processes. Such distributions are hard to measure because newly formed systems are still embedded in their natal clouds. However, via the model I developed, it is possible to measure them. Once these primordial distributions are constrained, numerical simulations can retrieve their dependency on molecular cloud properties. Indeed, such distributions have to result from the condition in which stellar formation occurs in general (e.g. level of turbulence, strength of magnetic fields). Thus, a precise measure of such distribution along with numerical investigations of the physics producing them will allow us to put constraints on the condition in which stars and planets form, both in single and multiple stellar systems.

- In **Part V** I conclude this thesis by giving my perspective and discussing the significance of my results in the context of the dynamics of accretion discs in multiple stellar systems. Last, I suggest future developments in the field of astrophysics related to the research topics I covered in this thesis.

CHAPTER 2

Binary and triple systems celestial mechanics

I introduce the mechanics of the two-body gravitational problem, in order to obtain relations and concepts that will be useful in the rest of the thesis. In Section 2.1 I show that the two-body problem is integrable and I discuss the geometry of the orbit (detailed demonstration in Valtonen & Karttunen (2006), Chapter 3). In Section 2.2 hierarchical triple systems are discussed, along with the problem of chaos and orbital stability and the evolution of stable hierarchical configurations. Finally, in Section 2.3 I present the way in which I implemented the setup of generic hierarchical systems for hydrodynamical simulations of accretion discs orbiting systems with more than two stars in the code PHANTOM.

2.1 Binary celestial mechanics

The two-body gravitational problem pertains to the study of a system composed of two point-like massive bodies that interact through the force of gravity. In this context, we denote the two masses as m_1 (heavier body) and m_2 (lighter body), and their respective positions as $\mathbf{r}_1$ and $\mathbf{r}_2$. The vector $\mathbf{r}$ represents the relative position of m_2 with respect to m_1, and r is the magnitude of this vector. The gravitational interaction between these two bodies is described by the following force equations:

$$\mathbf{F}_1 = \mathcal{G}\frac{m_1 m_2}{r^3}\mathbf{r} \tag{2.1}$$

and

$$\mathbf{F}_2 = -\mathcal{G}\frac{m_1 m_2}{r^3}\mathbf{r}, \tag{2.2}$$

where, $\mathcal{G}$ represents the universal gravitational constant.

From Newton's second law, we can write the following equation of motion:

$$\ddot{\mathbf{r}} = \ddot{\mathbf{r}}_2 - \ddot{\mathbf{r}}_1 = -\mathcal{G}\frac{M}{r^3}\mathbf{r}, \tag{2.3}$$

where $M = m_1 + m_2$. Notably, this equation can be rewritten as:

$$\mu\ddot{\mathbf{r}} + \mathcal{G}\mu M\frac{\mathbf{r}}{r^3} = 0, \tag{2.4}$$

Here, $\mu = \frac{m_1 m_2}{M}$ is known as the "reduced mass." The vector $\mathbf{r}$ in Equation (2.4) characterises the motion of a point particle with mass μ in a gravitational force field generated by a mass M fixed at $\mathbf{r} = 0$. At any given time, the position and velocity of μ are represented by $\mathbf{r}$ and $\dot{\mathbf{r}}$, which correspond to the relative position and velocity of m_2 with respect to m_1. Thus, the relative position and velocity between the two stars evolve as the position and velocity of a star of mass μ orbiting a star of mass M, fixed in the origin.

Additionally, it is important to note that the total energy and angular momentum of the reduced system are the same as those of the original system, even if the reduced system is not inertial.

To solve the two-body problem equation of motion, we require 12 integration constants. The conservation of total energy and angular momentum is a consequence of the system's isolation, i.e., the absence of external forces and torques, as well as the conservative nature of gravitational forces. The conservation of angular momentum implies that the orbit of the system lies in a fixed plane, referred to as the orbital plane. This plane is perpendicular to the angular momentum and passes through the center of mass. Furthermore, it can be demonstrated that the center of mass of the system undergoes uniform rectilinear motion, allowing us to determine the first 6 integration constants, namely the position and velocity of the center of mass.

In the frame of reference of the heavier body m_1, we can express the total angular momentum per unit mass, $\mathbf{h}$, as:

$$\mathbf{h} = \mathbf{r} \times \dot{\mathbf{r}}. \tag{2.5}$$

Since this vector is constant, we obtain three additional integration constants.

Two more integration constants can be found by computing the time derivative of the vector product $\mathbf{h} \times \dot{\mathbf{r}}$. In fact:

$$\begin{aligned}
\frac{\mathrm{d}}{\mathrm{d}t}(\mathbf{h} \times \dot{\mathbf{r}}) &= \mathbf{h} \times \ddot{\mathbf{r}} = \\
&= -(\mathbf{r} \times \dot{\mathbf{r}}) \times \frac{\mathcal{G}M\mathbf{r}}{r^3} = \\
&= -\frac{\mathcal{G}M}{r^3}((\mathbf{r} \cdot \mathbf{r})\dot{\mathbf{r}} - (\mathbf{r} \cdot \dot{\mathbf{r}})\mathbf{r}) = \\
&= -\mathcal{G}M\left(\frac{\dot{\mathbf{r}}}{r} - \frac{\dot{r}\mathbf{r}}{r^2}\right) = \\
&= \frac{\mathrm{d}}{\mathrm{d}t}\left(-\frac{\mathcal{G}M\mathbf{r}}{r}\right),
\end{aligned} \tag{2.6}$$

and thus:

$$\frac{\mathrm{d}}{\mathrm{d}t}\left(\mathbf{h} \times \dot{\mathbf{r}} + \frac{\mathcal{G}M\mathbf{r}}{r}\right) = 0. \tag{2.7}$$

When integrated over time, this gives:

$$\mathbf{A} = -\left(\mathbf{h} \times \dot{\mathbf{r}} + \frac{\mathcal{G}M\mathbf{r}}{r}\right) = \mathcal{G}M\mathbf{e} \tag{2.8}$$

where $\mathbf{A}$ is a constant vector known as Lenz vector and $\mathbf{e}$, constant as well, is a vector called the "eccentricity vector", which interpretation is discussed later in the section.

Given that $\mathbf{h}$ and $\mathbf{e}$ are not mutually independent (it can be shown that $\mathbf{h} \cdot \mathbf{e} = 0$), the conservation of the eccentricity vector yields only two more independent integration constants. With 11 integration constants in hand, we can determine the orientation and shape of the orbit, but not the position of the stars at a given time.

To determine the position of m_2 at a specific time, we need one additional integration constant. For practical reasons, we define a time τ at which the secondary is at a reference position $\mathbf{r}_0$.

The total energy of the system per unit mass is given by:

$$\mathcal{E} = \frac{1}{2}\dot{\mathbf{r}}^2 - \mathcal{G}\frac{m_1 m_2}{r}. \tag{2.9}$$

While $\mathcal{E}$ is conserved, it can also be expressed in terms of **h** and **e**. Thus, it doesn't provide additional integration constants. Indeed, taking the scalar product of the definition of **e** in (2.8):

$$\mathcal{G}M\left(\frac{\mathbf{r}}{r} + \mathbf{e}\right) = \dot{\mathbf{r}} \times \mathbf{h}, \tag{2.10}$$

and using the fact that $\dot{\mathbf{r}}$ and **h** are mutually perpendicular, we obtain:

$$\mathcal{G}^2 M^2 \left(1 + 2\frac{\mathbf{r}\cdot\mathbf{e}}{r} + |\mathbf{e}|^2\right) = \dot{r}^2 h^2. \tag{2.11}$$

By rewriting $\mathbf{r}\cdot\mathbf{e}$ with the definition of **e** in (2.8):

$$\mathbf{r}\cdot\mathbf{e} = \frac{h^2}{\mathcal{G}M} - r, \tag{2.12}$$

and rewriting $\dot{r}^2$ with the definition of $\mathcal{E}$ in (2.9), we can deduce from (2.11):

$$\mathcal{E} = \frac{\mathcal{G}M}{2h^2}(|\mathbf{e}|^2 - 1). \tag{2.13}$$

The geometry of the orbit can be obtained from (2.12), writing $\mathbf{r}\cdot\mathbf{e} = r|\mathbf{e}|\cos\phi$, where the angle ϕ is called the "true anomaly," resulting in:

$$r = \frac{h^2/(\mathcal{G}M)}{1 + |\mathbf{e}|\cos\phi}. \tag{2.14}$$

Equation (2.14) can be expressed in the form:

$$r = \frac{p}{1 + e\cos(\phi)}. \tag{2.15}$$

This is the general equation of a conic in polar coordinates, where e is the "eccentricity", p is the "semilatus rectum", and ϕ is the angle between the direction of **r** and a reference fixed direction.

The comparison between (2.14) and (2.15) clarifies why we refer to **e** as the "eccentricity" vector. Its absolute value corresponds to the eccentricity of the orbit. Moreover, ϕ in (2.14) represents the angle between **r** and **e**. We observe that **r** is minimum when $\phi = 0$. Consequently, **e** points in the direction of the "pericenter", which is the point of the orbit where m_1 and m_2 reach their shortest relative distance.

Equation (2.13) demonstrates that in a bound orbit, where the total energy must be negative, the eccentricity must be strictly less than 1. Therefore, a bound two-body system follows an elliptical orbit, which is a specific conic curve. The semilatus rectum of an ellipse is defined as $p = a(1 - e^2)$, where a represents the semi-major axis of the ellipse. In addition, for a given orbital angular momentum, the orbit with the lowest energy is the circular one.

From the same comparison, we can derive that $p = h^2/(\mathcal{G}M)$, and consequently:

$$a(1 - e^2) = h^2/(\mathcal{G}M). \tag{2.16}$$

Substituting h^2 in the previous, using (2.13), gives us

$$a = -\frac{\mathcal{G}M}{2\mathcal{E}}. \tag{2.17}$$

The previous equation reveals that the total energy of the orbit is entirely defined by its semi-major axis, and vice versa.

Using (2.17) and (2.16), we can express the eccentricity as:

$$e^2 = 1 - \frac{h^2}{\mathcal{G}Ma}. \tag{2.18}$$

The previous equation highlights that for fixed energy (or a fixed semi-major axis), the total angular momentum of the orbit is entirely determined by its eccentricity, and vice versa.

In celestial mechanics, the information about the geometry of a binary system orbit is condensed into six parameters called *orbital elements* (also called Campbell elements) and sketched in Fig. 2.1:

- the *eccentricity* e;
- the *semimajor axis* a;
- the *inclination* I;
- the *longitude of the ascending node* Ω;
- the *argument of periapsis* ω;
- the *true anomaly* f;

We already encountered e and a. Together, they fix the shape and size of the elliptic orbit. Given a frame of reference (X, Y, Z), the inclination and longitude of the ascending node fix the orbital plane (x, y, z) onto which the orbit lies. I is the angle between the z and the Z axes. Ω is the angle between a reference direction and the *line of nodes* (i.e. the intersection between the orbital plane and a reference plane). Finally, ω is the angle between the pericenter direction and the line of nodes and sets the orientation of the ellipse on the plane of the orbit, while f defines the position of the two bodies at a given epoch. These elements, together with the two systems' masses, fully define the configuration of the system at each epoch.

2.2 Triple celestial mechanics

The general three-body problem is known for lacking a closed-form solution. Even if Sundman in 1912 published an analytical solution to the problem as a power series, the convergence is so slow it is less efficient than direct numerical integration. In general, contrary to the two-body problem, three-body motion is not periodic and the dynamic is chaotic (meaning that infinitesimally close initial conditions soon undergo drastically different evolution paths). In Section 2.2.1 we briefly present the problem of chaos and how to deal with it. However, in astrophysics, we are mostly interested in solutions to the problem that show long-lasting stability. Luckily, there are specific configurations which show periodic motion (see some examples in Fig. 2.2) and a class of them in particular is stable over small perturbations: the hierarchical configurations. We discuss hierarchical triple systems in Section 2.2.2 and how I implemented their setup in the hydrodynamical code PHANTOM in Section 2.3.

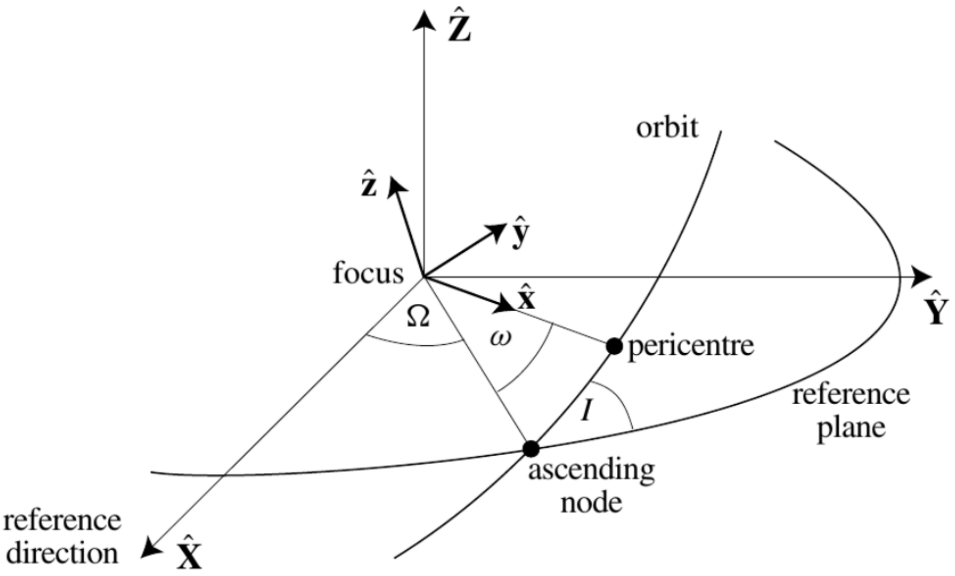

Figure 2.1: (x, y, z) orbital plane coordinate system and (X, Y, Z) reference plane coordinate system with the two-body elliptic orbit and the geometrical meaning of Eulerian angles. Figure from Murray & Dermott (1999)

2.2.1 Chaos and triple systems stability

Chaos is a well-studied feature within the 3-body problem. Each point in the system phase space can be mapped to a unique orbit, but the orbits in the neighbourhood of this point are in general very different from the original orbit, and there's no closed-form analytical solution for the general problem.

Given the lack of a useful analytical theory that can describe 3-body orbits, a statistical approach is useful in order to study the stability of a triple system given its initial condition.

The moment of inertia of a three-body system computed in its center of mass is

$$I = m_1 r_1^2 + m_2 r_2^2 + m_3 r_3^2, \tag{2.19}$$

where m_i are the three masses of the triple and $r_i = |\mathbf{r}_i|$ are their distances from the center of mass. Differentiating twice the moment of inertia with respect to time leads to the *Lagrange-Jacoby* identity

$$\frac{1}{2}\ddot{I} = 2T + V = 2E - V, \tag{2.20}$$

where T and V are the kinetic and potential energy, and $E = T + V$ is the total energy. The moment of inertia measures the compactness of the three-body system. When $\ddot{I} > 0$, the expansion is accelerating, and this leads to the escape of one body. However, when $\langle \ddot{I} \rangle \approx 0$ the system is bounded within a fixed volume. From numerical orbit calculations the potential energy V is known to fluctuate a lot, and since E is a constant, $\ddot{I}$ must fluctuate around zero as well.

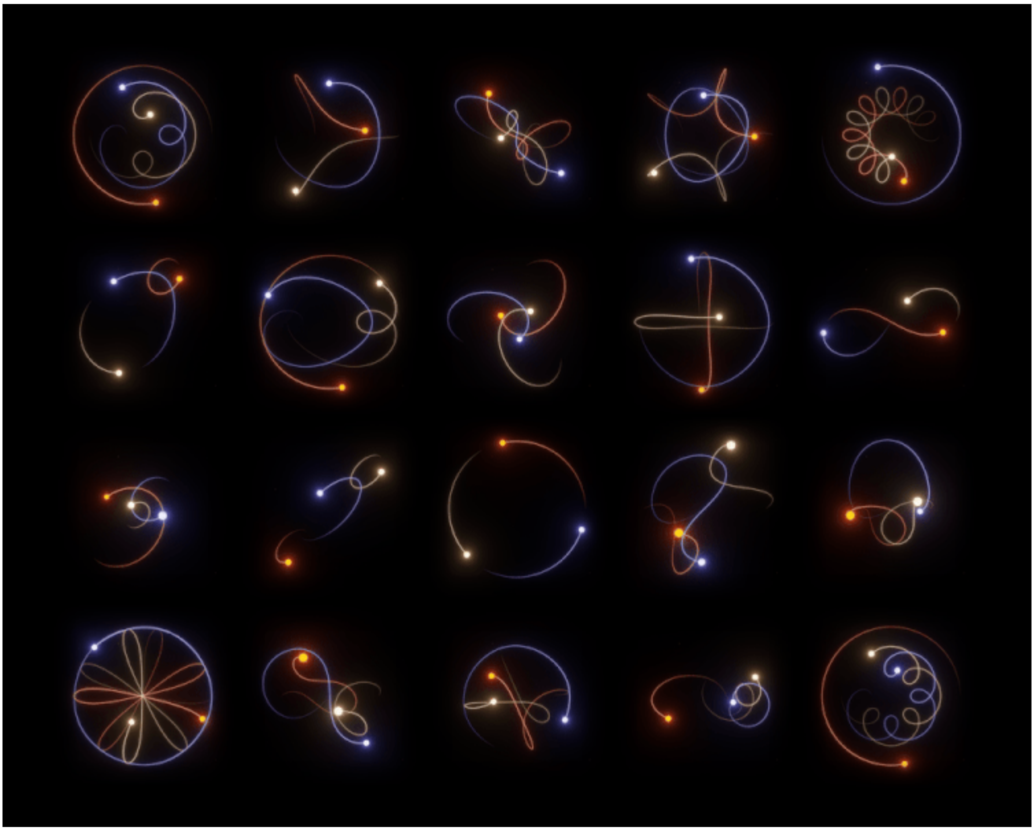

Figure 2.2: 20 different examples of periodic solutions to the three body problem. From Wikipedia, here is the animated version of this image.

Thus, equation (2.20) along with numerical orbit calculations show that the dynamic of the system consists in a repetition of compact configurations followed by ejections. This does not prove that escape unavoidably occurs, but when the possibility of escape is offered often enough, the ejection of one of the bodies in the system becomes likely (Valtonen & Karttunen 2006).

The study of the stability of a triple configuration consists of first determining the perturbation of the binary orbital parameters in the presence of a third body, setting a threshold to define the disruption of the system (based for example on a threshold in the energy exchange between the bodies). Secondly one has to exploit this relation over many orbits and define a stability limit to guarantee long-lasting stability (Valtonen et al. 2006). This stability threshold usually results in conditions for the minimum stable ratio between the semi-major axis of the binary and of the third body as a function of the other orbital elements and stellar masses.

Different studies resulted in different expressions for the semi-major axes ratio (e.g. Eggleton & Kiseleva 1995; Mardling & Aarseth 2001), with slightly different dependencies on masses and orbital elements. This is due to the different definitions of stability thresholds used. Moreover, as previously said, the phase space of a triple system is extremely complicated and it is possible to find examples that contradict each of these relations, and the definitive check for stability is the actual orbit integration, especially

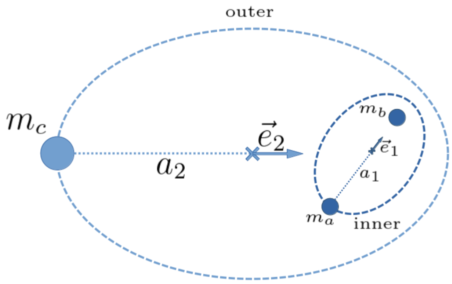

Figure 2.3: Hierarchical triple system sketch (not to scale). Light blue refers to the outer orbit, dark blue to the inner one. Dashed curves, crosses and arrows are the orbit, center of mass and eccentricity vector of the hierarchical level considered.

in the vicinity of the stability limit (Mikkola 2008).

Given the chaotic nature of multiple stellar system evolution, modern machine learning techniques are starting to be used in order to predict the stability of a system. Recently, Vynatheya et al. (2022) presented a machine learning application aiming at classifying hierarchical triple systems as stable or unstable based on their osculating elements. By training machine learning algorithms on simulated three-body system trajectories, the model is able to learn non-linear interactions and predict the long-term system evolution, outmatching criteria obtained with a perturbative approach.

As pointed out in Valtonen & Karttunen (2006) and in Mikkola (2008), the distribution of lifetime in the phase space is chaotic but not random. There are islands of stability where neighbour orbits have lifetimes similar to each other. These islands form structures, that in turn show in turn substructures, in a fractal behaviour.

These islands of weak chaos are found also at two extremes of the three-body behaviour: rapid encounters and hierarchical systems. The former are configurations with zero lifetime, in which a third body in a hyperbolic orbit approaches a binary perturbing it and leaves the system on a new hyperbolic orbit. The latter are the vast majority of the stable configuration for an N-body gravitational system and are also organised in a fractal structure. Indeed, in a hierarchical system, we have hierarchy levels that split in hierarchical systems themselves, as represented in figure 2.6 for the hierarchical quintuple stellar system GG Tauri.

2.2.2 Hierarchical configuration

The structures of observed triples tend to be hierarchical, as different configurations have a shorter life-time. A hierarchical triple (hereafter HT) system, shown in Fig. 2.3, consists of a binary (m_a and m_b) and a distant star (m_c) that orbits the center of mass of the inner binary.

If the third body is sufficiently distant, an analytical perturbative approach is possible in order to compute the evolution of the system. In that case, a first approximation of the inner and the outer orbit is the exact two-body orbit.

A system is considered hierarchical if there is no energy exchange between the two orbits and thus the inner and outer semi-major axes remain constant. However, angular momentum exchange between the inner and the outer orbit is allowed and leads to periodic oscillations in their eccentricities. In a non-coplanar configuration, Kozai-Lidov cycles are possible (Kozai 1962; Lidov 1962, see Naoz (2016) for a recent review), in which the conservation of the angular momentum makes the eccentricity and the mutual inclination of the orbits to oscillate on a period larger than the orbital periods.

At each instant, we can neglect the perturbations due to the triple nature of the system and compute the orbital elements of the elliptical orbits that the three bodies would follow. These elements are called *osculating* elements. The set regarding the inner binary describes the orbit that the inner bodies would follow if the third body would instantaneously disappear. The set referring to the third body describes the orbit that it would follow if the inner binary was reduced to a single body with the total mass of the binary and in its center of mass.

In the case of a hierarchical triple system, we can thus describe the instantaneous state of the system with 10 elements: the binary mass ratio $q = m_2/m_1$, the triple mass ratio $Q = m_3/(m_1 + m_2)$, the semi-major axes ratio, the two eccentricities, the two initial anomalies and the three Eulerian angles to orient the orbits in respect to each other.

When a clearly defined binary and a distant third body can be identified, as in the hierarchical triple case, it is useful to describe the system in the *Jacobi* system of coordinates. We call the position of the center of mass of the binary $\mathbf{r}_\mathrm{B}$. Calling $\mathbf{r}_1$ and $\mathbf{r}_2$ the position of the primary and of the secondary of the inner binary respectively, we define the relative position vector of the binary as $\mathbf{r} = \mathbf{r}_2 - \mathbf{r}_1$. Moreover we call $\mathbf{R}_3$ the position of the third body from the center of mass of the binary. m_1, m_2 and m_3 are the primary and secondary mass of the inner binary, and the third body mass, respectively. These quantities are represented in Fig. 2.4.

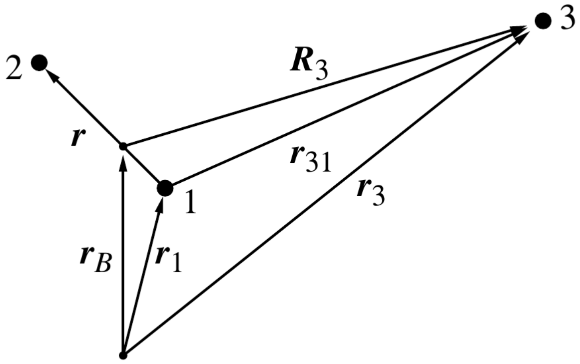

Figure 2.4: Jacobi coordinates: m_1 and m_2 form the inner binary and m_3 is the distant third body.

We can express $\mathbf{R}_3$ as

$$\begin{aligned}\mathbf{R}_3 &= \frac{m_1}{m_1+m_2}\mathbf{r}_{31} + \frac{m_2}{m_1+m_2}\mathbf{r}_{32} = \\ &= \left(\frac{m_1}{m_1+m_2} + \frac{m_2}{m_1+m_2}\right)\mathbf{R}_3 + \left(\frac{m_1 m_2}{(m_1+m_2)^2} - \frac{m_1 m_2}{(m_1+m_2)^2}\right)\mathbf{r},\end{aligned} \tag{2.21}$$

where $\mathbf{r}_{31}$ and $\mathbf{r}_{32}$ are the distances of the third body from the primary and the secondary respectively. Note that we can write

$$\mathbf{r}_{31} = \mathbf{R}_3 + \frac{m_2}{m_1+m_2}\mathbf{r}, \tag{2.22}$$

and

$$\mathbf{r}_{32} = \mathbf{R}_3 - \frac{m_1}{m_1 + m_2}\mathbf{r}. \tag{2.23}$$

From Newton's second law we can write

$$\ddot{\mathbf{r}}_1 = -\mathcal{G}\left(m_2\frac{\mathbf{r}_{12}}{\mathbf{r}_{12}^3} + m_3\frac{\mathbf{r}_{13}}{\mathbf{r}_{13}^3}\right) \tag{2.24}$$

and

$$\ddot{\mathbf{r}}_2 = -\mathcal{G}\left(m_3\frac{\mathbf{r}_{23}}{\mathbf{r}_{23}^3} + m_1\frac{\mathbf{r}_{21}}{\mathbf{r}_{21}^3}\right), \tag{2.25}$$

and subtracting the previous two equations we obtain

$$\ddot{\mathbf{r}} = -\mathcal{G}\left[(m_1 + m_2)\frac{\mathbf{r}}{\mathbf{r}^3} + m_3\left(\frac{\mathbf{r}_{31}}{\mathbf{r}_{31}^3} - \frac{\mathbf{r}_{32}}{\mathbf{r}_{32}^3}\right)\right]. \tag{2.26}$$

The same can be done in equation (2.21) for the third body:

$$\begin{aligned}\ddot{\mathbf{R}}_3 &= \frac{m_1}{m_1 + m_2}\ddot{\mathbf{r}}_{31} + \frac{m_2}{m_1 + m_2}\ddot{\mathbf{r}}_{32} = \\ &= -\mathcal{G}M\left(\frac{m_1}{m_1 + m_2}\frac{\mathbf{r}_{31}}{\mathbf{r}_{31}^3} + \frac{m_2}{m_1 + m_2}\frac{\mathbf{r}_{32}}{\mathbf{r}_{32}^3}\right).\end{aligned} \tag{2.27}$$

Note that if $r << R_3$, then $\mathbf{r}_{31} \approx \mathbf{r}_{32} \approx \mathbf{R}_3$. Then equations (2.26) and (2.27) reduce to, respectively,

$$\ddot{\mathbf{r}} = -\mathcal{G}(m_1 + m_2)\frac{\mathbf{r}}{r^3}, \tag{2.28}$$

and

$$\ddot{\mathbf{R}}_3 = -\mathcal{G}M\frac{\mathbf{R}_3}{R_3^3}, \tag{2.29}$$

that are two-body equations of motion, which solutions are Keplerian orbits. This approximation hides the perturbation that makes the osculating elements of the inner and outer orbits to vary over time, as discussed in section 2.2.3.

The approach described in section 2.2.1 in order to predict the stability of a triple system checks that its semi-major axes ratio respects a certain condition. In a hierarchical triple system the semi-major axes of the two orbits are constant and thus an initially stable system will always maintain long-lasting stability. The stability criterion adopted in this thesis is the criterion of Mardling & Aarseth (2001), as it requires that two orbits initially differing by a fixed amount in orbital elements should remain close to each other after 100 orbits. This condition can be expressed as follows:

$$\frac{P_\mathrm{o}}{P_\mathrm{i}} > 4.7(1 - e_\mathrm{o})^{-1.8}(1 + e_\mathrm{o})^{0.6}(1 + q_\mathrm{o})^{0.1}, \tag{2.30}$$

where P_o and P_i are the period of the outer and inner orbit respectively, and e_o and q_o are the eccentricity and the mass ratio of the outer orbit.

Note that this criterion is conservative because it is based on the concept of chaos, and chaotic behaviour does not automatically imply instability. Again, the ultimate way to check for stability is to integrate the orbit explicitly.

2.2.3 Secular evolution in coplanar triples

In the two-body problem the orbital elements a, e, i, ω, Ω, and τ are constant and are uniquely determined from the position and velocity of the two masses. In the presence of a perturbation, it remains possible to compute from the instantaneous positions and velocities the so-called osculating elements of the orbits, but these are not constant anymore.

Even if a complete analytical solution is not available for systems with more than two stars, we can study a hierarchical triple system as a perturbed two-body problem and see how its osculating elements evolve with time.

This section aims to show how to analytically compute the precession rate of a coplanar hierarchical triple. We want to calculate the variation over time of the argument of the pericenter of the inner and outer orbits.

The introduction of a perturbing function is the first step to study of the general nonintegrable problem of the motion of a third body under the gravitational effects of the two other bodies. This perturbing function modifies the two body potential and allows us to derive the evolution over time of the osculating elements of the two orbits within the triple system.

The potential energy of the system is

$$V = -\mathcal{G}\frac{m_1 m_2}{r} - \mathcal{G}\frac{m_1 m_3}{r_{13}} - \mathcal{G}\frac{m_2 m_3}{r_{23}}. \tag{2.31}$$

We can expand the r_{j3}^{-1} in the previous expression with Legendre polynomials. In general we have

$$\frac{1}{|\mathbf{r} - \mathbf{r}'|} = \frac{1}{r}\sum_{n=0}^{\infty}\left(\frac{r'}{r}\right)^n P_n(\cos\psi). \tag{2.32}$$

Where ψ is the angle between $\mathbf{r}$ and $\mathbf{r}'$. In order to expand r_{32}^{-1} or r_{31}^{-1} we use respectively

$$\mathbf{r} \to \mathbf{R}_3, \tag{2.33}$$

$$\mathbf{r}' \to \frac{m_1}{m_1 + m_2}\mathbf{r} \quad \text{or} \quad \mathbf{r}' \to -\frac{m_2}{m_1 + m_2}\mathbf{r}, \tag{2.34}$$

$$t \to \frac{m_1}{m_1 + m_2}\frac{r}{R_3} \quad \text{or} \quad t \to -\frac{m_2}{m_1 + m_2}\frac{r}{R_3}. \tag{2.35}$$

Note that for a hierarchical triple r/R_3 is typically a small factor.

We can expand to the second order, obtaining

$$\begin{aligned} V = -\mathcal{G}\frac{m_1 m_2}{r} &- \mathcal{G}\frac{m_1 m_3}{R_3}\sum_{n=0}^{2}\left(-\frac{m_2}{m_1 + m_2}\right)^n\left(\frac{r}{R_3}\right)^n P_n(\cos\psi) \\ &- \mathcal{G}\frac{m_2 m_3}{R_3}\sum_{n=0}^{2}\left(\frac{m_1}{m_1 + m_2}\right)^n\left(\frac{r}{R_3}\right)^n P_n(\cos\psi) = \end{aligned}$$

$$\begin{aligned} = -\mathcal{G}\frac{m_1 m_2}{r} - \mathcal{G}\frac{m_3}{R_3}\Bigg[(m_1 + m_2) + \left(-\frac{m_1 m_2}{m_1 + m_2} + \frac{m_1 m_2}{m_1 + m_2}\right)\frac{r}{R_3}\cos\psi \\ + \left(\frac{m_1 m_2^2}{(m_1 + m_2)^2} + \frac{m_1^2 m_2}{(m_1 + m_2)^2}\right)\left(\frac{r}{R_3}\right)^2 \frac{1}{2}\left(3\cos^2\psi - 1\right)\Bigg] = \end{aligned}$$

$$\begin{aligned}
&= -\,\mathcal{G}\frac{m_1 m_2}{r} - \mathcal{G}\frac{m_3(m_1+m_2)}{R_3} \\
&\quad - \frac{\mathcal{G}}{2}\frac{m_1 m_2 m_3}{(m_1+m_2)R_3}\left(\frac{r}{R_3}\right)^2\left(3\cos^2\psi - 1\right).
\end{aligned} \tag{2.36}$$

In the last equation the first two terms are the potential of two-body problem for the inner and the outer orbit. The last term, that is

$$R = -\frac{\mathcal{G}}{2}\frac{m_1 m_2 m_3}{(m_1+m_2)R_3}\left(\frac{r}{R_3}\right)^2\left(3\cos^2\psi - 1\right), \tag{2.37}$$

is the first order expression of the perturbing function of the system.

Let us now derive the evolution of the osculating elements of the triple produced by the perturbation R. It is way simpler to approach the problem with the Hamiltonian formalism. As we want to study the evolution of the orbital elements it would be useful to make use of the orbital elements a, e, i, ω, Ω, and τ. However, these do not constitute a conjugate set variables. Thanks to newly defined functions it is possible to obtain a conjugate set. Here, we will use the Delaunay's elements defined by

$$l = \bar{M}, \quad g = \omega, \quad h = \Omega \tag{2.38}$$

$$L = \mu\sqrt{\mathcal{G}Ma}, \quad G = \mu\sqrt{\mathcal{G}Ma\,(1-e^2)}, \tag{2.39}$$

and

$$H = \mu\sqrt{\mathcal{G}Ma\,(1-e^2)}\cos I \tag{2.40}$$

where $\bar{M}$ is the mean anomaly, M is the total mass of the binary and μ it the reduced mass. The two-body Hamiltonian with these coordinates is

$$\mathcal{H} = -\frac{\mathcal{G}^2 M^2 \mu^3}{2L^2}, \tag{2.41}$$

from which we can infer the constancy of five quantities: g, h, L, G and H as expected for a two body problem. Indeed, g and h equal the argumenta of pericenter and longitude of ascending node respectively, that we know already to be constant, L depends on a and the mass of the system, which are constant as well, and G and H are respectively the total angular momentum and its vertical component, both conserved.

Being Delaunay's elements a conjugate set of variables they satisfy the following Hamilton equations:

$$\frac{\mathrm{d}L_j}{\mathrm{d}t} = -\frac{\partial\mathcal{H}}{\partial l_j}, \quad \frac{\mathrm{d}l_j}{\mathrm{d}t} = \frac{\partial\mathcal{H}}{\partial L_j} \tag{2.42}$$

$$\frac{\mathrm{d}H_j}{\mathrm{d}t} = -\frac{\partial\mathcal{H}}{\partial h_j}, \quad \frac{\mathrm{d}h_j}{\mathrm{d}t} = \frac{\partial\mathcal{H}}{\partial H_j} \tag{2.43}$$

$$\frac{\mathrm{d}G_j}{\mathrm{d}t} = -\frac{\partial\mathcal{H}}{\partial g_j} \tag{2.44}$$

$$\frac{\mathrm{d}g_j}{\mathrm{d}t} = \frac{\partial\mathcal{H}}{\partial G_j} \tag{2.45}$$

where $j = 1, 2$ for the inner and the outer orbit respectively.

When we deal with hierarchical triple systems we have two well defined Keplerian orbits. The Hamiltonian of the system can be decomposed into two Keplerian Hamiltonians and a coupling term expressed as a power series in $\alpha = a_1/a_2$ (as in Naoz et al.

(2013)). We can express it in Delaunay's elements, stopping the summation at second order in α. In order to do so we express the total Hamiltonian as the sum of the Hamiltonian of the two body problem of the inner and outer orbit (like in Eq. (2.41)), and the perturbing function R in (2.37), also expressed in Delaunay's elements:

$$\mathcal{H} = -\frac{\mathcal{G}^2 M_1^2 \mu_1^3}{2L_1^2} - \frac{\mathcal{G}^2 M_2^2 \mu_2^3}{2L_2^2} - 8\beta \left(\frac{L_1^4}{L_2^6}\right) \left(\frac{r}{a_1}\right)^2 \left(\frac{a_2}{R_3}\right)^3 (3\cos^2\psi - 1), \tag{2.46}$$

where

$$\beta = \frac{\mathcal{G}^2}{16} \frac{(m_1+m_2)^7 m_3^7}{(m_1 m_2)^3 (m_1+m_2+m_3)^3}. \tag{2.47}$$

We are interested in the long-term dynamics of the triple system, so we want to eliminate from the Hamiltonian in (2.46) all the short-period terms that depend on l_1 and l_2. This can be done both by a coordinate transformation as in Naoz et al. (2013) or actually averaging over the inner and outer orbital period as done in Murray & Dermott (1999). The result is the quadrupole-level Hamiltonian

$$\mathcal{H}_2 = C\left[\left(2+3e_1^2\right)\left(3\cos^2 i_{\rm tot} - 1\right) + 15 e_1^2 \sin^2 i_{\rm tot} \cos(2g_1)\right], \tag{2.48}$$

where

$$C = \beta \frac{L_1^4}{L_2^3 G_2^3}, \tag{2.49}$$

and $i_{\rm tot}$ is the relative inclination of the orbits. We specify (2.48) for a coplanar configuration, obtaining

$$\mathcal{H}_{2,\rm copl} = 2C\left(2+3e_1^2\right). \tag{2.50}$$

At this point the only missing bit is to compute the derivatives in (2.45) for $j = 1, 2$, resulting into

$$\dot{\omega}_1 = \frac{\partial \mathcal{H}_{2,copl}}{\partial G_1} = 12\frac{C}{L_1}\sqrt{1-e_1^2}, \tag{2.51}$$

$$\dot{\omega}_2 = \frac{\partial \mathcal{H}_{2,copl}}{\partial G_2} = 12\frac{C}{G_2}\left(1+\frac{3}{2}e_1^2\right). \tag{2.52}$$

These are the precession rates of the inner and outer orbit in a coplanar hierarchical triple and we will use these relations in Part III. Similar procedures result in the secular evolution of different osculating elements.

2.2.4 Secular evolution in misaligned configuration

An additional interesting illustration of the secular evolution of osculating orbital elements occurs within tilted hierarchical triple systems. Besides being interesting on their own, these results prepare the ground for a discussion of tilt evolution in circum-binary discs. We will, thus, stress here the qualitative dynamics of tilted hierarchical triples (mainly based on works by Naoz et al. (2013) and Aly et al. (2015)) and we will extend this to accretion discs in Section 4.2.3.

Let's consider a system made of a binary orbited by a third body and analyse the effect of the binary gravitational potential truncated at the quadrupole order (similarly to what we did in more details in Section 2.2.3). Let the binary mass be $M = m_a + m_b$, with m_a the primary mass and m_b the secondary mass, and a its semi-major axis. We define the binary mass ratio as $q = m_b/m_a$. The monopole order of the gravitational potential represents a single star of mass M in the center of mass of the binary, resulting in a Keplerian motion for the third body m_c. The quadrupole order is the lowest order deviation from a single central star.

As in Section 2.2.2, we define $\mathbf{r} = \mathbf{r}_1 - \mathbf{r}_2$ the binary separation and we write the specific angular momentum $\mathbf{h}$ in the center of mass frame of reference:

$$\mathbf{h} = \frac{\mu}{M}\mathbf{r} \times \dot{\mathbf{r}}, \tag{2.53}$$

where $\mu = m_a m_b / M$ is the binary reduced mass.

From Equation (2.8), we derive the eccentricity vector of the binary:

$$\mathbf{e} = \frac{\dot{\mathbf{r}} \times \mathbf{h}}{\mathcal{G}M} - \frac{\mathbf{r}}{r}, \tag{2.54}$$

with $\mathcal{G}$ the gravitational constant (check section 2.1 for the geometrical interpretation of $\mathbf{e}$). We recall that $\mathbf{h}$ and $\mathbf{e}$ are both conserved for a binary orbit. The eccentricity vector $\mathbf{e}$ lies along the semi-major axis pointing towards the pericenter. Consequently, it is perpendicular to $\mathbf{h}$. The magnitude of the eccentricity vector and angular momentum are linked by (2.18).

The third body of mass m_c follows a circular orbit, characterised by its radius R and its angular momentum $\mathbf{l}$, which is perpendicular to the third body orbital plane and its magnitude is $l = \sqrt{\mathcal{G}(M + m_c)R}$. The tilt angle of the third body orbit with respect to the binary orbit is $\beta = \arccos \hat{\mathbf{l}} \cdot \hat{\mathbf{h}}$, where $\hat{\mathbf{l}}$ and $\hat{\mathbf{h}}$ are versors pointing in the direction of $\mathbf{l}$ and $\mathbf{h}$, respectively. It can be shown that, at the quadrupole order, only angular momentum is exchanged between the binary and the third body orbit, while energy is separately conserved.

The quadrupole interaction energy between the binary and the third body, obtained with a double average over the binary and the third body orbits is (Naoz et al. 2013; Aly et al. 2015):

$$\langle E_{\rm quad} \rangle = -\frac{m_c \omega^2 a^2 q}{8(1+q)^2} \left[6e^2 - 1 + 3(1-e^2)(\hat{\mathbf{l}} \cdot \hat{\mathbf{h}})^2 - 15e^2(\hat{\mathbf{l}} \cdot \hat{\mathbf{e}})^2 \right], \tag{2.55}$$

where $\omega = \sqrt{\mathcal{G}(M + m_c)/R^3}$ is the frequency of the third body orbit and $e = |\mathbf{e}|$.

Let us call $\mathbf{\Theta}$ the binary quadrupole torque onto the third body average over the two orbits. It can be shown that

$$\mathbf{\Theta} = \frac{3\omega q}{4(1+q)^2} \frac{a^2}{r^2} \left[5e^2(\hat{\mathbf{l}} \cdot \hat{\mathbf{e}})\hat{\mathbf{e}} - (1-e^2)(\hat{\mathbf{l}} \cdot \hat{\mathbf{h}})\hat{\mathbf{h}} \right]. \tag{2.56}$$

Thus, we can express the evolution of the third body angular momentum as:

$$\dot{\mathbf{l}} = \mathbf{\Theta} \times \mathbf{l}. \tag{2.57}$$

In addition, since from Equations (2.55) and (2.56) we notice that $\mathbf{\Theta} \propto \partial \langle E_{\rm quad} \rangle / \partial \hat{\mathbf{l}}$, also the following relation holds:

$$\frac{\mathrm{d}\hat{\mathbf{l}}}{\mathrm{d}t} \cdot \frac{\partial \langle E_{\rm quad} \rangle}{\partial \hat{\mathbf{l}}} = 0 \tag{2.58}$$

In the limit of $m_c \ll M$ and avoiding extreme binary eccentricities, the binary orientation and eccentricity are constant. Under these assumptions, Equation (2.58) shows that the third body angular momentum direction variation always lies along constant energy curves and Equation (2.57) implies $\mathbf{l}\cdot\hat{\mathbf{l}} = 0$. Consequently, the third body angular momentum is simply precessing along constant energy curves.

Isolated extrema points of $\langle E_{\mathrm{quad}}\rangle$ are stable, non-precessing third-body orbit configurations. In particular, from the expression of $\langle E_{\mathrm{quad}}\rangle$ in Eq. (2.55), we have isolated minima in $\hat{\mathbf{l}} = \pm\hat{\mathbf{h}}$ and isolated maxima in $\hat{\mathbf{l}} = \pm\hat{\mathbf{e}}$ (except for $e = 0$, where we loose the $\hat{\mathbf{l}}\cdot\hat{\mathbf{e}}$ term).

The two minima correspond to coplanar configurations ($\beta = 0$), rotating or counter-rotating with the binary orbits. In such configurations, the third-body orbit lies on the same plane as the inner binary orbit. In circular binaries, these are the only accessible non-precessing orientations. Different orientations of the third body angular momentum have as solutions an orbit precessing around the binary angular momentum direction $\hat{\mathbf{h}}$ (with sense depending on the sign of β).

For an eccentric binary, we also have the two maxima points. They correspond to perpendicular orbits with $\beta = \pi/2$ (with opposite rotation senses) orbiting around the eccentricity vector direction. In such configurations, the third-body orbit lies on a plane perpendicular to the binary orbit. As for orbits near the two minimum points, deviations from the perpendicular orientation of the third body angular momentum result in third body orbits precessing around the eccentricity vector direction $\hat{\mathbf{e}}$.

There are two additional polar configurations in which $\hat{\mathbf{l}} = \pm\hat{\mathbf{k}}$, with $\hat{\mathbf{k}} = \hat{\mathbf{h}}\times\hat{\mathbf{e}}$. These two additional solutions are unstable and small deviations from them make the orbit fall into one of the four stable solutions. The energy of these two solutions is

$$\langle E_{\mathrm{quad}}\rangle_{\mathrm{unstable}} = -\frac{m\omega^2 a^2 q}{8(1+q)^2}\left[6e^2 - 1\right], \tag{2.59}$$

since $\hat{\mathbf{l}}\cdot\hat{\mathbf{e}}$ and $\hat{\mathbf{l}}\cdot\hat{\mathbf{h}}$ are both null if $\hat{\mathbf{l}} = \hat{\mathbf{k}}$. For $0 < e < 1$, the regions of precession around $\hat{\mathbf{h}}$ and around $\hat{\mathbf{e}}$ are separated by the energy curves with $\langle E_{\mathrm{quad}}\rangle = \langle E_{\mathrm{quad}}\rangle_{\mathrm{unstable}}$. Orbits with energy above this threshold precess around the binary angular momentum, while below this energy they precess around the binary eccentricity vector. Thus, the condition for a third body to precess around the eccentricity vector of an eccentric binary is:

$$(1-e^2)(\hat{\mathbf{l}}\cdot\hat{\mathbf{h}})^2 - 5e^2(\hat{\mathbf{l}}\cdot\hat{\mathbf{e}})^2 < 0. \tag{2.60}$$

Which can be written in terms of orbital elements of the third body orbit (Zanazzi & Lai 2018):

$$(1-e^2)\cos^2\beta - 5e^2\sin^2\beta\sin^2\phi < 0, \tag{2.61}$$

where the longitude of ascending node ϕ is referred to the direction of the binary eccentricity vector $\hat{\mathbf{e}}$ (see Sec. 2.1 for a discussion about binary orbital elements). The previous condition results in a critical tilt above which we have polar orbits given by[1] (Cuello & Giuppone 2019):

$$\beta_{\mathrm{crit}}(e_{\mathrm{b}},\phi) = \arcsin\sqrt{\frac{1-e_{\mathrm{b}}^2}{1-5e_{\mathrm{b}}^2\cos\phi^2 + 4e_{\mathrm{b}}^2}}. \tag{2.62}$$

The two different regimes are well summarised by the plot in Fig. 2.5 from Martin & Lubow (2017). The curves in the right panel of Fig. 2.5 trace test particle circular orbits

---

[1] for a counterrotating orbit $\beta_{\mathrm{crit}}(e_{\mathrm{b}},\phi) = \pi - \arcsin\sqrt{\frac{1-e_{\mathrm{b}}^2}{1-5e_{\mathrm{b}}^2\cos\phi^2+4e_{\mathrm{b}}^2}}$

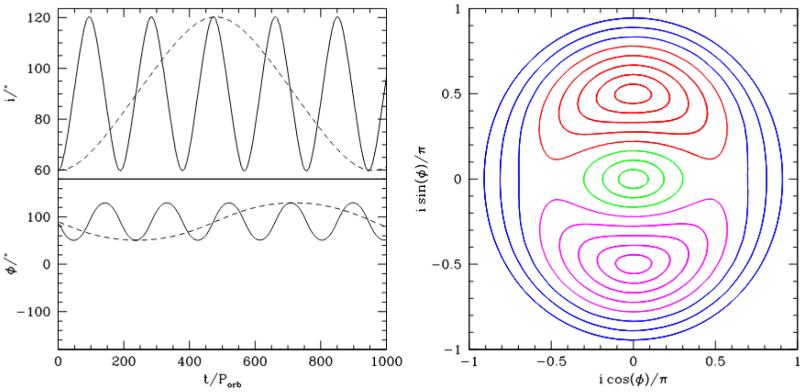

Figure 2.5: Oscillations of mutual inclination i and longitude of the ascending node ϕ for a body orbiting a binary system. On the left panel, different curves are the evolution with time (in units of the inner binary period) of i and ϕ for different semimajor axis systems (wider outer orbits lead to longer oscillation periods). On the right panel, orbits of misaligned triple stellar systems the same semimajor axes but different inclinations. Green and blue curves are prograde and retrograde circulating orbits (inclination below the critical angle for polar alignment). Red and purple curves are prograde and retrograde librating orbits (inclination above critical angle). Figure from Martin & Lubow (2017).

orbiting the same eccentric binary in the $i\cos\phi - i\sin\phi$ phase space. Each particle has the same separation from the binary center of mass but different initial inclinations. Particles that start along the green and blue curves evolve following those curves. The center of these curves is $i = 0$, thus particles are precessing around the binary angular momentum. Along such orbits, i is constant and ϕ is spanning $360°$. Above the critical angle for polar alignment particles start following red (purple) curves for prograde (retrograde) polar orbits. Prograde particles are precessing around the eccentricity vector **e** and the center of prograde curves is $i = 90°$ and $\phi = 90°$. Retrograde particles are precessing around $-$**e** and the center of prograde curves is $i = 90°$ and $\phi = -90°$. Along such orbits, the inclination and longitude of the ascending node are bound in intervals inside which they oscillate. The left panel shows the evolution of i and ϕ for two polar particles with different semi-major axes. There it is clear that the inclination and the longitude of the ascending node are oscillating around $90°$, hence the orbit is librating rather than processing. Tilting the third-body orbit even more, we go back to the precession regime for retrograde orbits (blue curves).

2.3 Simulating multiple stellar systems with the code PHANTOM

In this section, I present how I implemented the setup for generic hierarchical systems in the hydrodynamical code PHANTOM. PHANTOM is a Smoothed Particle Hydrodynamics code designed for astrophysical applications, details on the SPH method and on its implementation in PHANTOM can be found in the Appendix in Chap. B.

In order to simulate generic hierarchical stellar system configurations in the work I carried out during my PhD (Ceppi et al. 2022, 2023, Toci et al., under review; Alaguero et al., to be submitted), I implemented in PHANTOM the possibility to run hydrodynamical

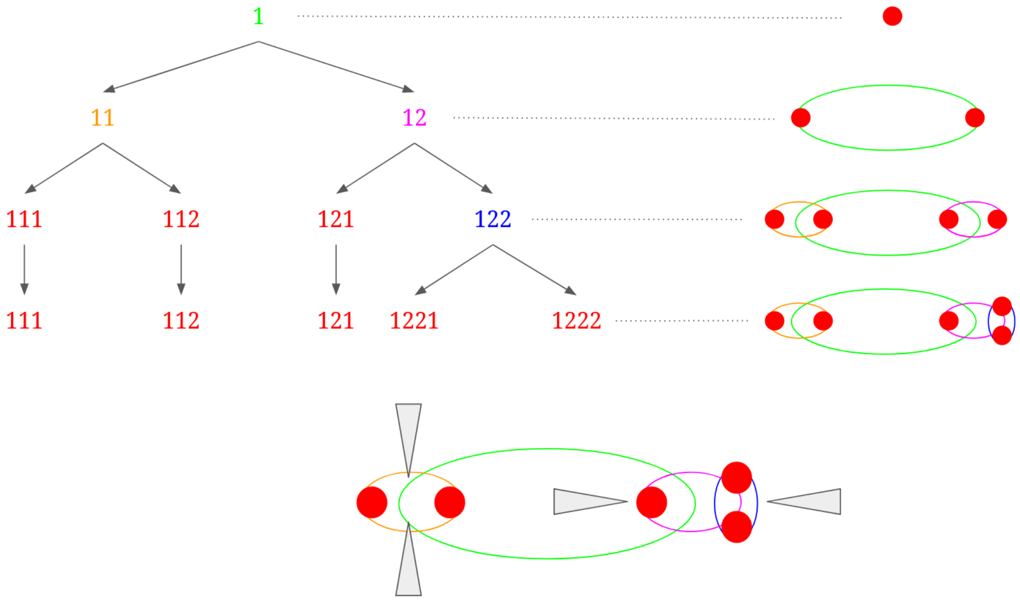

Figure 2.6: Schematical representations of the steps the algorithm takes to build a GG Tauri-like hierarchical quintuple stellar systems. Red labels represent stars in the system, other colours represent hierarchical levels with their associated orbit. Bottom sketch: discs can orbit single stars or hierarchical levels.

simulations of hierarchical multiple stellar systems with accretion discs orbiting their hierarchical levels. Even if I applied this setup for accretion disc physics, the N-body part of this algorithm is not limited to accretion disc physics application and it is already used in hydrodynamical simulations in different fields of astrophysics like in the study of AGB outflows (e.g. Malfait et al, to be submitted).

The orbital arrangements of observed multiple stellar systems tend to be hierarchical, as different configurations are unstable and have shorter life-times. In the case of a hierarchical system, the first approximation for each hierarchical level is the exact two-body orbit. Indeed, for each hierarchical level at each instant, we can neglect the perturbations due to the presence of additional bodies and compute the orbital elements of the elliptical orbits that the bodies' center of mass belonging to that hierarchical level would follow. These elements are called osculating elements. For example, in the case of a hierarchical triple, the set regarding the inner binary describes the orbit that the inner bodies would follow if the third body instantaneously disappeared. The set referring to the third body describes the orbit that it would follow if the inner binary was reduced to a single body with the total mass of the binary in its center of mass.

The first piece of information needed is the hierarchy structure of the system. This information can be nicely encoded in a string format, following the convention used by Reipurth et al. (2014). In the proposed nomenclature, binary graphs are used to describe hierarchical systems (see Fig. 2.6). The position of each sub-system in the graph is coded with a level label. The outermost pair is at the first hierarchical level in the graph (level '1', for the quintuple stellar system GG Tauri it represents the orbit followed by the centers of mass of GG Tauri A and GG Tauri B). This level can be decomposed into its two binary components (in GG Tauri, the two subsystems GG Tauri A and GG Tauri

B orbits). To label the more massive subsystem, we added a '1' to the parent level label, resulting in '11'. While, the lighter is associated with the label '12'. This top-down notation can continue to the deepest levels of the system. At the end of the process, each star has an associated label and each hierarchical level has a label as well. In a hierarchical triple system with a third body heavier than the inner binary, the third body label is '11', the inner binary primary star is labelled '121', the secondary '122' and '12' represent the inner binary hierarchical level as a whole.

Having the codenames associated with each star of the system allows the code to retrieve the hierarchical position of each star. Figure 2.6 shows how the string '121, 122, 111, 1121, 1122' encodes the structure of the protostellar system GG Tauri.

The basic process needed for iteratively produce the desired system is the splitting of a sink particle (which are used to represent stars in PHANTOM, see Bate et al. 1995) in a pair of gravitationally bounded sink particles. The initial sink is substituted with a binary of the same mass as the substituted sink. The center of mass of the inner binary follows the orbit of the substituted sink.

Starting from a single sink, we obtain a binary system. Splitting one of the two binary sinks, we obtain a hierarchical triple system and so on. For example, the process of building the GG Tauri stellar system, sketched in Fig. 2.6, is to split a single sink to form the binary made by GG Tauri A and GG Tauri B, then split both binary stars to obtain GG Tauri Aa-Ab and GG Tauri Ba-Bb, and lastly split GG Tauri Bb to obtain GG Tauri Bb1-Bb2. For each split, the information needed are the hierarchical level orbit osculating elements. After the initial setup, the N-body dynamics of the system is solved as described in Section 2.8.5 in Price et al. (2018b).

At each splitting, the initial position and velocity of the two binary bodies are computed by means of the Thiele-Innes elements (Binnendijk 1960). Thiele-Innes elements are computed in terms of the Campbell elements through the following relations:

$$\begin{aligned}\mathbf{P} =&(\cos\omega\cos\Omega - \sin\omega\cos i\sin\Omega,\\ &\cos\omega\sin\Omega + \sin\omega\cos i\cos\Omega,\\ &\sin\omega\sin i)\ ,\end{aligned} \tag{2.63}$$

$$\begin{aligned}\mathbf{Q} =&(-\sin\omega\cos\Omega - \cos\omega\cos i\sin\Omega,\\ &-\sin\omega\sin\Omega + \cos\omega\cos i\cos\Omega,\\ &\cos\omega\sin i)\ ,\end{aligned} \tag{2.64}$$

$$A = \cos E - e\ , \tag{2.65}$$

$$B = \sqrt{1-e^2}\sin E\ , \tag{2.66}$$

where ω, Ω, i, a and e are the argument of the pericenter, the argument of the ascending node, the inclination, the semi-major axis and the eccentricity of the binary orbit, respectively, and E is the eccentric anomaly. With Eq. (2.63)-(2.66) we can compute the rectangular coordinates and velocities of a given initial condition as:

$$(x, y, z) = a(A\mathbf{P} + B\mathbf{Q}), \tag{2.67}$$

$$(v_{\rm x}, v_{\rm y}, v_{\rm z}) = -a\dot{E}(\sin E\mathbf{P} - \sqrt{1-e^2}\cos E\mathbf{Q}), \tag{2.68}$$

where $\dot{E}$ is the time derivative of the eccentric anomaly. The eccentric anomaly E and its derivative $\dot{E}$ are computed from the true anomaly of the orbit.

Note that we can use the code associated with each subsystem to set useful information about the subsystem orbit and the surrounding environment. Again, taking GG Tauri as an example, the hierarchical triple system GG Tauri A is made by the stars ′111′, ′1121′ and ′1122′. GG Tauri A is identified by code ′11′, which is the prefix of each star belonging to GG Tauri A. After the splitting process, GG Tauri A is not a sink particle anymore, however, we can associate to code ′11′ all the properties of the GG Tauri A subsystem (such as center of mass position and velocity and system mass). Thus, after the sink-splitting step, each star or subsystem in the hierarchical system can be surrounded by an accretion disc orbiting the subsystem center of mass. Indeed, for each star and subsystem, we have code associated with the property needed to put the disc in orbit.

CHAPTER 3

Stellar multiplicity

The large parameter space in which multiple stellar systems live produces a wide set of different configurations. When looking at individual multiple stellar systems, the key ingredients driving the evolution are not always the same. Some configurations are prone to strong dynamical evolution, while others are less chaotic. Some strongly influence the surrounding environment, while others are too wide to affect it. This variety is supported also by the different formation mechanisms that possibly form multiple stellar systems inside molecular clouds. A way to build a general picture of multiple stellar system formation is to look at statistical properties of multiple stellar system populations. In this chapter, I present what we know about the occurrence of multiple stellar systems in stellar populations (Sec. 3.1), the distribution of relevant parameters in forming multiple stellar systems (namely, eccentricity and the angle they form with their surrounding disc plane in Sec. 3.2-3.3), the different mechanisms in which they form (Sec. 3.4) and how the characteristics of the surrounding environment may affect their properties (Sec. 3.5).

3.1 Observed stellar multiplicity

We can describe the level of multiplicity of a multiple stellar system population by defining the *multiplicity fraction* as:

$$MF = \frac{B + T + Q + ...}{S + B + T + Q + ...}, \tag{3.1}$$

where S, B, T, Q and so on are the number of single, binary, triple, quadruple stellar systems and so on in the population, respectively.

As we discuss in the following chapters, binaries and systems with more than two stars behave qualitatively in different ways. Thus, we can also compute the fraction of systems with more than two stars in the population by defining the *triple/high-order fraction* as:

$$THF = \frac{T + Q + ...}{S + B + T + Q + ...}. \tag{3.2}$$

In the following sections, measurements of these fractions in stellar populations with different ages are presented. For the field stellar population, statistics are detailed enough to be broken in system mass and size subclasses. Nevertheless, the general picture suggests that multiplicity increases with primary mass (i.e. more massive systems are more frequently multiple stellar systems) and reduces with age. Indeed, Class 0 populations present about two times more multiple stellar systems than Class I, which in turn has a

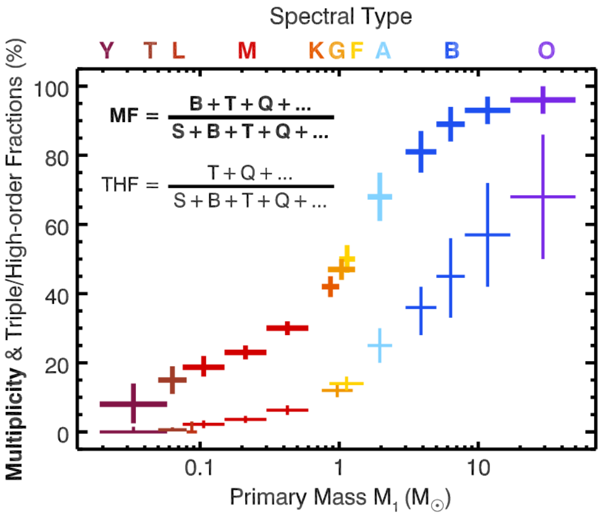

Figure 3.1: Multiplicity fraction and triple/high-order fraction for different primary mass classes in field multiple stellar systems, defined in (3.1) and (3.2), respectively. Multiple stellar systems are common, and half of the stellar systems are multiple from solar mass primaries on. Systems with more than two stars are a significant fraction of multiple systems, especially in A, B and O classes. Data are collected from different surveys by Offner et al. (2022).

higher fraction than main sequence populations. However, these results are more solid for intermediate separations (100-1000 au), while a detailed analysis of separation ranges suggests that this is not true for close binary systems, which probably form also thanks to the system evolution and for wide binaries which are more prone to be disrupted.

3.1.1 Multiplicity as a function of the mass in evolved stellar populations

In Figure 3.1 we report measured and bias-corrected multiplicity fraction (MF) and triple/high-order fraction (THF) versus primary mass from different surveys of field stellar systems (i.e., Fontanive et al. 2018; Burgasser 2007; Close et al. 2003; Allen et al. 2007; Winters et al. 2019; El-Badry et al. 2019; Raghavan et al. 2010; Tokovinin 2014; De Rosa et al. 2014; Murphy et al. 2018; Moe & Kratter 2018; Moe & Di Stefano 2017; Sana et al. 2012, 2014), collected by Offner et al. (2022). Let's summarize the relationship between the multiplicity of stellar systems and the mass of the primary star in detail.

In the brown dwarf regime, completeness correction is challenging, but surveys confirm an increasing multiplicity fraction with mass. In this regime, the multiplicity fraction is approximately 8% for early-Y/late-T dwarfs, rising to around 20% for early-T/L dwarfs (Close et al. 2003; Allen et al. 2007; Burgasser 2007; Fontanive et al. 2018). The THF in this mass range is below 3%.

Moving to M-dwarf primaries, Winters et al. (2019) provided a comprehensive assessment of multiplicity statistics within a 25-pc volume-limited sample. Taking the more complete 20-pc subset of the survey, Offner et al. (2022) split the sample into three mass intervals and observed an increase in the multiplicity fraction and triple fraction with primary mass within the M-dwarf regime, from approximately 20% to 30% and from 2% to 6%, respectively.

Moving further, about half of FGK primaries, which corresponds to the Sun-like regime, have a companion, and around 13% of systems in this category are triple or higher-order systems (Raghavan et al. 2010; Tokovinin 2014).

Expanding our considerations to heavier primaries, surveys of A-stars reveal a binary frequency that increases to approximately 68% (Moe & Kratter 2021). B-stars exhibit multiplicity fractions that continue to rise with primary mass, reaching up to 93%, while nearly the entire population of O-stars has companions (Moe & Di Stefano 2017). Concurrently, the triple and higher-order fraction increases to 25%, 57%, and 68%, respectively.

3.1.2 Multiplicity as a function of the mass in young stellar objects

In order to have insights into the evolution of the multiplicity of a stellar population with time, we report findings about multiplicity fractions for forming stellar systems.

Spectroscopic surveys of Class II/III T Tauri stars unveiled a fraction of close binary systems that aligns with their counterparts in the main sequence field, as supported by studies such as Mathieu (1994); Melo (2003); Elliott et al. (2014); Prato (2007); Kounkel et al. (2019). These observations emphasise that the characteristics of main sequence close binary systems, including their primary mass dependence and separation distribution, are primarily established during the T Tauri stage.

On the other hand, adaptive optics and speckle imaging surveys of T Tauri stars in star-forming regions such as Taurus, Chamaeleon, Ophiuchus, and Scorpius reveal an excess of companions within the separation range of 10 to 200 AU. These findings are corroborated by studies conducted by Ghez et al. (1993); Reipurth & Zinnecker (1993); Leinert et al. (1993); Ghez et al. (1997); Kraus et al. (2011); Tokovinin & Briceño (2020).

However, when we extend our focus to wider separations, within the range of 100 to 10,000 au, the binary fraction becomes sensitive to the stellar density of the surrounding environment. The densely populated Orion Nebula Cluster demonstrates a deficit of wide companions (Scally et al. 1999; Köhler et al. 2006; Reipurth et al. 2007; Duchêne et al. 2018; Jerabkova et al. 2019). Environments with intermediate density, such as Upper Scorpius and the Orion OB1 association, exhibit binary fractions consistent with those found in the field (Brandner et al. 1996; Kraus et al. 2008; Kounkel et al. 2016; Tokovinin & Briceño 2020; Tokovinin et al. 2020). Conversely, low-density star-forming regions like Taurus and Chamaeleon exhibit a slight surplus of wide companions (Ghez et al. 1993; Reipurth & Zinnecker 1993; Leinert et al. 1993; Ghez et al. 1997; Köhler & Leinert 1998; Connelley et al. 2008; Kraus et al. 2011; Joncour et al. 2017). These findings collectively indicate that the majority of wide binary systems face dynamic disruption in extremely dense regions, and the field population comprises a mixture of individuals from low, intermediate, and high-density environments.

Interestingly, within the same star-forming region, there is tentative evidence for the opposite trend between the wide binary fraction and the surrounding stellar density. Across separations ranging from 100 to 1,000 au, Kounkel et al. (2016) observed that young stars in sub-regions with higher spatial stellar density displayed a slightly higher wide binary fraction. Recent ALMA observations of Class 0/I protostars in Orion, as reported by Tobin et al. (2022), appear to confirm this result.

Moving to more massive systems, various high-resolution imaging surveys have provided insights into the binary properties of Herbig Ae/Be stars and massive Young Stellar Objects. While, as inferred from spectroscopic data, the close binary fraction for these stars typically falls within the range of 10% to 30% (Corporon & Lagrange 1999; Apai et al. 2007; Sana et al. 2017), notably lower than what is observed for main sequence stars in the field. The wide binary fraction for Herbig Ae/Be stars and massive YSOs typically ranges from 30% to 60% (Kouwenhoven et al. 2005; Baines et al. 2006; Wheelwright et al. 2010; GRAVITY Collaboration et al. 2018; Pomohaci et al. 2019), in agreement with their counterparts in the field.

One possible explanation for the lack of close binary systems in this context is that the close binary population of field stars within this mass range may result from the hardening of intermediate separation systems. This hardening process occurs over a Myr timescale, which implies that 1 Myr old stellar systems may exhibit a lack of close companions (Ramírez-Tannus et al. 2021). Alternatively, it is suggested that Herbig Ae/Be stars and massive Young Stellar Objects with close companions might have shorter disc lifetimes compared to those in wider orbital configurations. As a result, young massive stars with discs tend to have fewer close companions, given the same age.

Given the abundance of companions surrounding Young Stellar Objects compared to field stars, it's clear that the majority of stellar systems originate as multiple systems. However, over time, subsequent dynamical processes tend to decrease the overall multiplicity fraction, especially for low-mass and wider binary systems that have lower binding energies (Kroupa 1995).

By taking into account the Initial Mass Function of primary stars in our analysis, only 35% of newly formed main sequence stellar systems are multiple systems (Kroupa et al. 2013; Offner et al. 2022). Nevertheless, it's worth noting that a significant fraction of main sequence stars are part of multiple systems when considering that multiples involve two or more stars. For example, in the M-Dwarfes class, 49% of stars are single, 28% are part of binary systems, and 7% are components of triples and higher-order multiples. Accounting for the Initial Mass Function, we conclude that 58% of main sequence stars belong to multiple stellar systems. This fraction raises significantly increasing the stellar mass and reducing the population age.

3.1.3 Protostellar Multiplicity Statistics

Thanks to instruments like ALMA and VLA, uniform and unbiased surveys of multiplicity in nearby star-forming regions are now achievable, pushing the limit of our knowledge of multiplicity statistics even closer to the formation epoch. In particular, observations of Perseus, Ophiuchus and Orion regions have been collected with uniform sensitivities and resolutions (Tobin et al. 2016; Encalada et al. 2021; Tobin et al. 2020, 2022).

The overall protostellar population (Class 0, Class I and Flat Spectrum) in Orion and Perseus have a multiplicity frequency of $30\% \pm 3\%$ and $36\% \pm 6\%$, respectively. Focusing on Class 0 protostars, the measured multiplicity frequency is $38\% \pm 5\%$ and $47\% \pm 9\%$ in Orion and Perseus, respectively. These surveys have a comparable minimum separation set by the angular resolution, and the results are consistent despite different environmental conditions.Moving to Class I protostars, the measured multiplicity frequency in Orion and Perseus are $23\% \pm 4\%$ and $27\% \pm 9\%$, respectively. Compared to Class 0 protostars, the multiplicity frequency nearly halved. The decrease of multiple stellar systems, compared to Class 0, is significant with more than 3σ. Last, in Orion, where data about Flat Spectrum protostars are independently available, Flat Spectrum protostars have multiplicity frequency comparable to Class I.

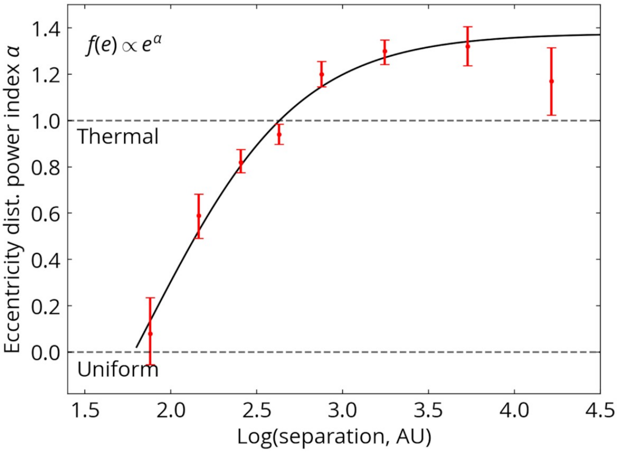

Figure 3.2: The parameter α of eccentricity distribution fitted on different binary semi-major axis classes. While binaries with about 100 au semi-major axis (the ones usually hosting circumbinary discs) show a uniform eccentricity distribution, wider binaries are more and more skewed towards eccentric orbits. Figure from Hwang et al. (2022).

3.2 Eccentricity distribution

Eccentricity, a fundamental orbital parameter in the study of orbital dynamics, offers critical insights into the mechanisms governing binary formation (Duquennoy & Mayor 1991; Duchêne & Kraus 2013). Additionally, the eccentricity distribution within stellar populations serves as a fossil record of their early dynamical evolution. Indeed, particularly for wide binary systems, the timescale for external gravitational interactions to become dynamically significant exceeds the age of the universe (Heggie 1975; Weinberg et al. 1987).

Under the sole influence of gravitational interaction, the eccentricity distribution reaches a stable state. After multiple N-body scatterings, once the population has dynamically relaxed, we expect the eccentricity distribution, denoted as $P(e)$, to follow a "thermal" distribution, characterised by $P(e) = 2e$ (Jeans 1919; Ambartsumian 1937; Heggie 1975).

Studies such as those conducted by Raghavan et al. (2010) and Duchêne & Kraus (2013) have explored the eccentricity distribution in relatively small binary systems with separations up to hundreds of astronomical units (AU). In these semi-major axis regimes, they generally observed distributions consistent with a random distribution, regardless of the system's mass.

For wider binary systems, Tokovinin (2020) found that binaries with separations in the range of greater than 10^3 au exhibit an eccentricity distribution that closely aligns with the thermal distribution. However, those with separations of less than 200 au tend to have less eccentric orbits. Furthermore, the eccentricity distribution becomes "superthermal" for systems with separations exceeding 10^4 AU.

Recently, Hwang et al. (2022) expanded on these findings by measuring the eccentricity distribution across a broad range of semi-major axes using high-precision astrometric data from *Gaia*. In line with previous works, they modelled the eccentricity distribution as $P(e) \propto e^{\alpha}$ and measured the α exponent. Their study confirmed previous research while extending the range of semi-major axes to around $10^{4.25}$ AU. Figure 3.2 shows the alpha parameter versus the system dimension. They found that for smaller systems, below 100 AU, the eccentricity distribution is ”sub-thermal” and approximately flat ($\alpha = 0$). Around 500 AU, the distribution transitions to thermal behaviour, characterised by $P(e) \propto e$ ($\alpha = 1$). For even wider systems, the eccentricity distribution becomes ”superthermal” with $\alpha > 1$. Below a period of 8 days, binaries undergo tidal circularisation, significantly reducing their average eccentricity.

3.3 Accretion disc misalignment distribution

The mutual inclination, denoted as β, between the orbital planes of binary systems and their circumbinary discs holds significant implications for our understanding of disc evolution and star formation. In general, we attribute the orientation of discs to the direction of the angular momentum vector of the material accreting from interstellar matter organized in filaments onto the disc (McKee & Ostriker 2007; André et al. 2010; Ward-Thompson et al. 2010). The orientation of this vector may evolve over time due to factors such as the relative motion between the system’s center of mass and the filament, turbulence or gravitational effects from nearby objects.

On the other hand, large-scale interstellar magnetic fields may play a role in maintaining the stability and direction of filaments for extended periods (Galli et al. 2006; Wang et al. 2011; Hennebelle 2013). While the magnetic fields impact on the process of star formation could be significant (Shu et al. 1987), their influence at scales less than 1000 au is still a matter of debate (Zhang et al. 2014). Additionally, their role during star formation might be complex and contingent on the system’s age (Targon et al. 2011; Chapman et al. 2013).

Determining the mutual inclination between an observed circumbinary disc and the binary’s orbit can be challenging. It necessitates knowledge of the binary’s orbital parameters, as well as precise observations of the circumbinary disc to establish its inclination and the longitude of the ascending node. Given these challenges, the number of protostellar systems for which the mutual inclination between the accretion disc and the orbital plane is constrained remains limited.

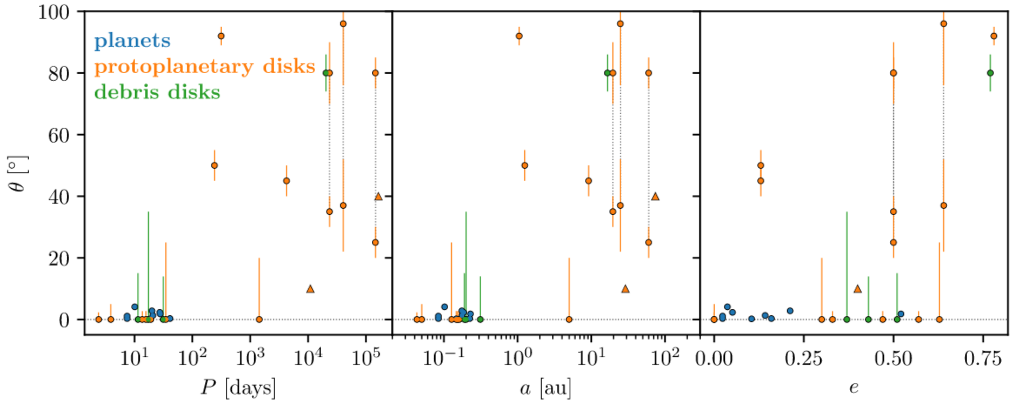

Figure 3.3: Measured mutual inclination distribution against orbital period P, semi-major axis a and orbital eccentricity e. The distribution of mutual inclination is shaped by the viscous evolution of discs towards coplanar and polar configurations (see Sec. 4.2.3.1 and 4.2.3.2). Figure from Czekala et al. (2019)

A recent effort by Czekala et al. (2019) compiled mutual inclinations of gaseous and debris discs from the literature, shedding light on this aspect of stellar systems. The gaseous discs in the surveys are the following. HD 98800B is a near equal-mass binary with a circumbinary disc in a polar orbit, with $\beta = 88.4° \pm 2°$ as measured by Kennedy et al. (2012). Czekala et al. (2019) measured a slightly different but compatible $\beta = 92° \pm 3°$. Both measurements agree with the disc being polar. The mutual inclination of the disc around HD 142527 B was initially reported as $\beta = 35° \pm 5°$ (Biller et al. 2012; Lacour et al. 2016; Boehler et al. 2017; Price et al. 2018a; Claudi et al. 2019), but improved orbital parameters suggest $\beta = 46° \pm 2°$ or $\beta = 76° \pm 3°$, depending on the value used for the longitude of the ascending node Balmer et al. (2022). For V892 Tau, recent data suggests $\beta = 5° \pm 4°$ based on orbital parameters provided by Long et al. (2021). In addition, using precise measurements and a hierarchical Bayesian model, Czekala et al. (2019) inferred mutual inclination angles for circumbinary discs in V4046 Sgr, AK Sco, DQ Tau, and UZ Tau E, yielding angles of $< 2.3°$, $< 2.7°$, $< 2.7°$, and $< 2.7°$, respectively. Figure 3.3 from Czekala et al. (2019) collects all these discs as orange points, along with known debris discs (in green) and planets in binary systems (in blue).

From this dataset, a pattern emerges: binary systems with orbital periods shorter than 10 days tend to exhibit circular orbits. This phenomenon is likely a result of dissipative forces causing the orbits to circularise. Furthermore, short-period binaries typically maintain a coplanar configuration with their surrounding circumbinary discs as a consequence.

Conversely, for circumbinary discs in orbit around long-period, eccentric binaries, the situation is more diverse. These systems can display a wide range of mutual inclinations, with some reaching up to $90°$. However, it's essential to note that while such variety exists, the majority of circumbinary discs still maintain a coplanar orientation with their host binary system. This tendency is particularly pronounced for discs orbiting pure binary systems, as discussed in Part III of this thesis.

3.4 Multiple stellar system formation mechanisms

A multiple stellar system is the result of two or more episodes of gravitational collapse and the subsequent gravitational bounding of the formed protostars. Two protostars can bond at different stages of their evolution. However, the hierarchical fragmentation of a molecular cloud itself is not able to form multiple stellar systems (Shu 1977; Larson 1972; Toci et al. 2018). Thus, different mechanisms must be responsible for their formation. Indeed, on top of gravity and pressure, turbulence and magnetic fields are involved in order to break the spherical asymmetry of a pure gravitational collapse.

In the following, we summarise different viable formation mechanisms for the formation of multiple stellar systems following the work done by Offner et al. (2022). It is important to stress from the beginning that each of these mechanisms leaves different imprints in the population of systems formed. Whether it is, for example, the spatial scale or the stellar masses, the distribution of properties of the whole multiple stellar systems population is the combination of subpopulations formed via different formation ways.

3.4.1 Core and filament fragmentation

Giant molecular clouds show substructures like filaments and cores on a scale of hundreds of AU. These overdensities suggest that a possible way of formation for multiple stellar systems is multiple gravitational collapses inside such overdensities. Indeed, the

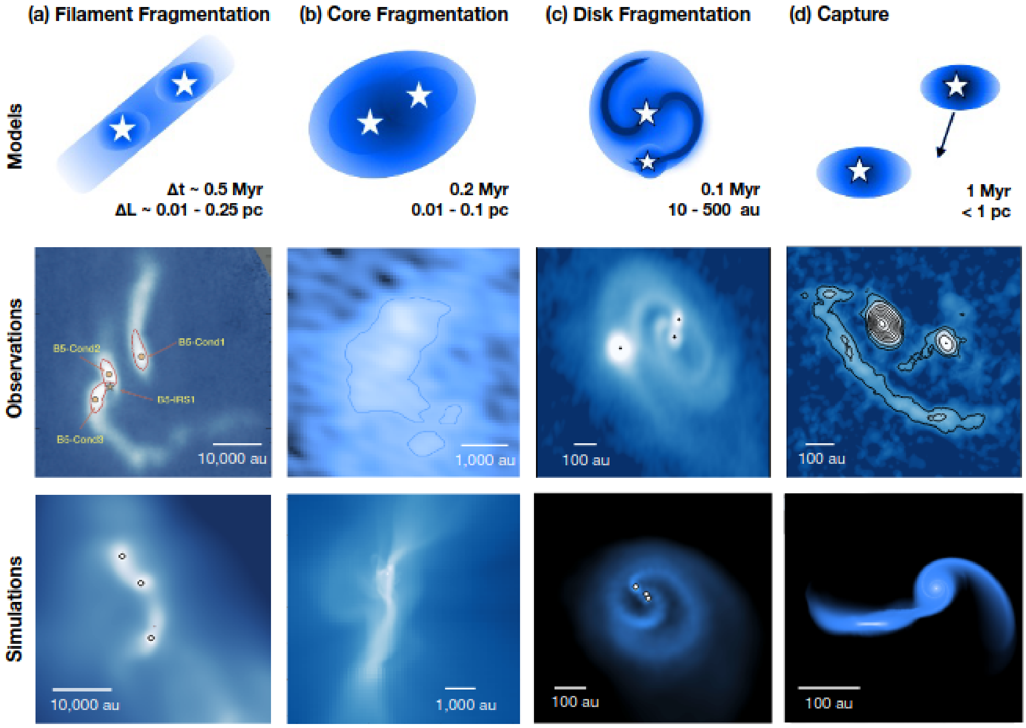

Figure 3.4: Different mechanisms for multiple stellar system formation. On the top row there is a sketch of the mechanism, on the central row there are observations of systems likely formed though it (Pineda et al. 2015; Kirk et al. 2017; Reynolds et al. 2021; Rodriguez et al. 2018) and on the bottom row there are numerical simulations reproducing similar multiple stellar systems (Guszejnov et al. 2021; Offner et al. 2016; Bate 2018; Muñoz et al. 2015). Figure form Offner et al. (2022)

presence of velocity and density gradients produced by rotation on turbulence promotes the fragmentation of the parent core, leading to the formation of bounded protostars (Larson 1972). At the same time, the turbulent nature of the environment provides similar inhomogeneities in velocity and density fields which can lead to the formation of multiple systems as well. Properties of the turbulence, such as its power spectrum, regulate the resulting distribution of masses and system sizes (Lee et al. 2020; Guszejnov & Hopkins 2015).

Gravitational collapse by itself is a scale-free mechanism, thus additional physics has to put a lower limit to the minimum spatial scale of systems forming via this mechanism. Likely, angular momentum, magnetic fields and tidal forces can provide such lower limit scale, all resulting in a minimum scale of about 10^2 au (Guszejnov et al. 2017; Haugbølle et al. 2018; Lee & Hennebelle 2018). At the same time, above 0.1 pc it is unlikely that forming protostar can bound. Thus, that is the upper limit for the scale of systems forming via gravitational collapse inside cores and filaments. Additionally, multiple systems formed like this have to consist of stars of similar age. Indeed, these processes are possible with big reservoirs of gas, which are available only at the onset of the cloud collapse. Numerical simulations and the study of the evolution of perturbations during the collapse suggest that only systems of two or three stars can form. Moreover, given the vast amount of gas available for accretion it is unlikely to form low-mass companions ($M \leq 0.08$ Solar masses, Fisher 2004).

3.4.2 Disc fragmentation

Gravitational fragmentation can also occur inside an already formed accretion disc. When gravity overcomes the support provided by thermal pressure, a portion of the disc can collapse and form independent objects gravitationally bound to the object the disc is orbiting around. This can lead to the formation of binaries and multiple stellar systems with more than two stars (e.g. if the disc is orbiting a binary). Discs prone to fragmentation are either massive (Adams et al. 1989; Shu et al. 1990; Bonnell 1994) or they radiate away heat very efficiently (on a timescale about the orbital timescale Gammie 2001). The most typical situation in which a disc fragments is when material is accreting on the outer part of the disc. At 100s of au, the disc temperature is mainly set by the radiation of the central stars. While mass accumulates on the disc outer region (i.e. the infalling rate is higher than the accretion rate through the disc), the temperature does not increase. Eventually, the surface density will be high enough to overcome the pressure support (Kratter & Lodato 2016). These conditions (massive discs and infall) are likely met during the Class 0 phase, when discs are deeply embedded in cloud material. Given the vast amount of mass available, this process rarely results in low mass ratio binaries. Indeed, the rapid infall of surrounding mass onto the collapsing object usually leads to the formation of stellar mass companions. In addition, the subsequent accretion from the disc likely favours the newly born object in the disc, raising its mass even more at the expense of the central object (Bate & Bonnell 1997; Young & Clarke 2015, and see Sec. 4.2.4).

3.4.3 Capture, dynamical evolution and migration

Processes presented in previous sections are not able to account for configurations such as close binaries with semi-major axes of the order of the AU due to the typical size of hydrostatic cores, which are expected to collapse in single stars (Larson 1969). Such configurations can only be achieved with subsequent orbital evolution and/or the capture of external bodies. Indeed, the fragmentation of clouds and discs forms single stars at large distances. Even if, at the beginning, these bodies are gravitationally bound, their orbits can be unstable as discussed in Sec. 2.2. Without external interaction, these systems would usually break, ejecting lighter bodies. However, the surrounding environment (gas cloud in core collapse or the disc material in disc collapse) can dump the orbits and drive systems towards stability as routinely seen in numerical hydrodynamical simulations (Ostriker 1994; Bate 2012; Muñoz & Lai 2015; Cournoyer-Cloutier et al. 2021). In the absence of external material, unbound objects in high stellar density region can affect systems' orbit as well. Repeated N-body scatterings tend to soften soft binaries and harden hard binaries (Heggie 1975) and to increase the average eccentricity of the population (Weinberg et al. 1987, and Sec. 3.2). In addition, interaction with external bodies leads to the formation of new binaries by exchanging partners in the systems and ejection of formerly bound companions, usually shrinking the orbits due to the lost energy and angular momentum in the ejections (Valtonen & Karttunen 2006; Kratter 2011).

An even more dramatic orbital evolution after the multiple stellar system formation is due to migration. Surveys of young stellar objects and numerical simulations suggest that multiple stellar systems form very early on, before the natal cloud disperses. Surrounding gas, both bound to the system or in the surroundings, can shrink the system size. The former case is more significant in widely separated bound binaries. There, gas cloud mediates the torque needed to shrink the semi-major axis, along with accretion onto the stars (Bate & Bonnell 1997; Ostriker et al. 1999; Stahler 2010). The latter case is more significant in binaries sharing the same circum-binary disc. Seminal work by Lubow & Artymowicz (1996) found inward migration due to the torque between the binary and the surrounding disc. Recently, more complete numerical simulations accounting also for the torque generated by circumstellar disc and accretion showed that outward migration can happen in specific regions of the disc and binary parameter space (Satsuka et al. 2017; Muñoz et al. 2019).

Secular evolution, discussed in Sections 2.2.3 and 2.2.4, can also lead to very close binary systems. Particularly, the dissipation of Kozai-Lidov cycles (Lidov 1962; Kozai 1962) can lead to binary periods of less than 10 days. This secular evolution, typical of misaligned triple stellar systems, consists in a periodic exchange of angular momentum between different hierarchical levels which makes the eccentricity and the mutual inclination of orbits to oscillate with time. When very high eccentricities are generated, the pericenter of the smaller orbits is pushed to separations close enough for tidal interaction to circularise the orbit dumping the oscillation and shrinking the system (Dabringhausen et al. 2022). This process well matches the observational fact that closest binaries are often found in high-order multiple stellar systems (Tokovinin et al. 2006). However, this mechanism is limited to misaligned triples. Coplanar very close binaries still need gas dissipation to be driven to close separation (Moe & Kratter 2018).

3.5 Impact of environment on multiplicity

Today advanced numerical techniques allow the numerical integration of the collapse of massive molecular clouds over large dynamic ranges and including several physical processes. Such calculations provide insights into the relationship between multiplicity, environmental properties and physical processes. Indeed, contrary to the stellar initial mass function, which is insensitive to environment properties (Offner & Arce 2014), multiplicity is affected by the environment in which multiple stellar systems are forming.

As we already stated in the previous sections, a possible channel of formation for multiple stellar systems is the fragmentation of discs. Cold discs are more prone to collapse as the pressure support is lower. The presence of radiative heating from protostars affects this channel of formation. Indeed, even low-mass stars influence gas within hundreds of au, heating it and reducing fragmentation. This mainly affects the formation of brown dwarfs (Offner et al. 2009; Bate 2012). The suppression of fragmentation due to radiation is present also at the molecular cloud level. However, there, protostars form further apart and the influence of radiation is lower (Guszejnov et al. 2017).

Protostellar outflows launched by accreting protostars inject energy and momentum in the cloud environment, reducing the overall star formation efficiency (Bally 2016). Additionally, numerical simulations suggest that the presence of protostellar outflows can explain differences between stellar initial mass function and core mass function (Offner & Chaban 2017; Guszejnov et al. 2021; Mathew & Federrath 2021). However, numerical simulations with and without protostellar outflows do not show significant differences in multiplicity fraction.

Another possible way of contrasting the gravitational collapse of gas is through magnetic field. Indeed, the presence of magnetic fields provides additional pressure support along with the thermal one. This results in a lower fragmentation rate and higher stellar masses (Padoan et al. 2014; Guszejnov et al. 2021). Numerical simulations suggest that strong magnetic fields favour multiple stellar system formation (Cunningham et al. 2018; Lee et al. 2019). This can be due to the fact that magnetic fields introduce asymmetries, preventing spherical collapse and promoting turbulent fragmentation of cores (Offner et al. 2016). Also, in numerical simulations less high-order multiple stellar systems form, which usually end up ejecting stars and, consequently, raising the single star population.

When it comes to its impact on multiple stellar system formation, turbulence is a less investigated property of molecular clouds. Turbulence does affect the gas distribution and star formation rate (Padoan et al. 2014; Federrath 2015) while leaving stellar initial mass function unaffected (Offner & Arce 2014; Guszejnov et al. 2021). Guszejnov et al. (2017) proposed an approximated semi-analytical model of turbulence accounting only for gravity (i.e. ignoring additional effects such as magnetic field) finding agreement with mass ratio and multiplicity distributions as a function of the stellar mass, while failing at reproducing separation distributions.

Metallicity also affects the cooling of gas in the cloud and discs. Indeed, in optically thin gas (typical of star forming cores), a lower metallicity reduces cooling via metal lines. Conversely, in optically thick discs, a lower metallicity can promote cooling by lowering the gas opacity. The impact of metallicity in molecular cloud collapse simulations is investigated by (Bate 2019), that runs four simulations with different metallicity from 0.01 to 3 solar metallicity. Again, the stellar initial mass function resulted to be independent of metallicity. However, calculations with lower metallicity fragmented more both in cores and filaments, and in accretion discs because of the thickness of the gas. Even if there is an increasing trend for multiplicity fraction with decreasing metallicity, values measured in (Bate 2019) with different metallicities are all compatible at 1σ.

CHAPTER 4

Accretion discs

In this chapter, we explore accretion discs' fluid dynamics, thermodynamics, and the nature of viscosity. We examine the governing equations related to mass, momentum, and energy conservation within these systems. Furthermore, we discuss the implications of turbulence and angular momentum transport.

According to modern theories, stars form as the result of the turbulent collapse and fragmentation of molecular cloud cores inside giant molecular clouds. This, in turn, results in the formation of single and multiple systems. When the seed of a star - called protostar - is formed inside a core, gas is accreted onto this central object. Due to angular momentum conservation, an accretion disc surrounding the protostar forms. In these discs, by means of dissipative processes modelled as a viscous torque, the angular momentum is carried at large radii and gas can accrete onto the stars. I present the 'classical disc theory' (e.g. Frank et al. 2002) for circumsingle discs in Sec. 4.1.

When a disc orbits around a binary system, the tidal interaction between the two stars and the disc allows angular momentum exchange. This can result in gap and cavity formation in the disc, whose detailed structure depends on the binary parameters. In order to bridge the gap cleared by the binary and to allow accretion, stars drag accretion streamers from the inner edge of the disc. I discuss the angular momentum exchanges between binaries and circumbinary discs, along with their equilibrium configurations and how mass accretes onto the binary stars in Sec. 4.2.

4.1 Circumsingle discs

Fluid dynamics equations govern the evolution of a gaseous accretion disc:

$$\frac{\partial \rho}{\partial t} + (\mathbf{v} \cdot \nabla)\rho = -\rho \nabla \cdot \mathbf{v}; \tag{4.1}$$

$$\frac{\partial \mathbf{v}}{\partial t} + (\mathbf{v} \cdot \nabla)\mathbf{v} = -\frac{\nabla p}{\rho} - \nabla \Phi + \frac{\nabla \cdot \boldsymbol{\sigma}}{\rho}; \tag{4.2}$$

$$\frac{\partial u}{\partial t} + (\mathbf{v} \cdot \nabla)u = -\frac{p}{\rho}\nabla \cdot \mathbf{v} - L. \tag{4.3}$$

Equation (4.1) represents mass conservation, where ρ is the mass density of the fluid and $\mathbf{v}$ is the velocity field of the fluid.

Equation (4.2) represents the conservation of angular momentum, where p is the fluid pressure, Φ is the gravitational potential and $\boldsymbol{\sigma}$ is the viscous stress tensor. The third term on the right-hand side of equation (4.2) accounts for the acceleration due to viscous forces acting on the fluid. In Cartesian coordinates, the stress tensor σ_{ij} has the following form:

$$\sigma_{ij} = \eta \left[\frac{\partial v_i}{\partial x_j} + \frac{\partial v_j}{\partial x_i} - \frac{2}{3}(\nabla \cdot \mathbf{v})\delta_{ij} \right] + \zeta(\nabla \cdot \mathbf{v})\delta_{ij}. \tag{4.4}$$

In the stress tensor, the η term has zero trace and, consequently, it vanishes for uniform compression. Thus, it corresponds to shear viscosity. The ζ term acts in the presence of compression and it represents bulk viscosity.

Finally, equation (4.3) is the energy conservation, where u is the specific internal energy and L is the specific heat flux.

Classical accretion disc theory assumes:

- Azimuthal symmetry: gradients in ϕ direction are null;
- Thin disc: at a given radius R the geometrical height of the disc H is much smaller than R ($H/R \ll 1$);
- Negligible disc self-gravity: the impact of disc gravity on itself has negligible impact on disc dynamics, thus the gravitational potential Φ can be approximated as the stellar gravitational potential;
- Negligible bulk viscosity: the primary contribution to viscous forces comes from the shearing term, the bulk viscosity is neglected.

The natural frame of reference given the system geometry is a cylindrical coordinate system, centred on the central protostar and with the z-axis perpendicular to the disc. Given the assumption of a thin, light and axisymmetric disc, equations become dependent only on the radial coordinate R and time t, with no dependency on z and ϕ coordinates. As $H/R \ll 1$, fluid properties can be integrated in the direction perpendicular to the disc, allowing us to consider quantities per unit surface instead of per unit volume. This effectively reduces the system to a two-dimensional geometry.

By integrating the continuity equation (4.1) over the z direction, we obtain the continuity equation for the surface density Σ

$$\frac{\partial \Sigma}{\partial t} = -\frac{1}{R}\frac{\partial}{\partial R}\left(R \Sigma v_R\right), \tag{4.5}$$

where v_R represents the radial component of the velocity of the gas and $\Sigma(R,t)$ is defined as:

$$\Sigma(R,t) = \int_{-\infty}^{+\infty} \rho(R,z,t)\mathrm{d}z. \tag{4.6}$$

Regarding momentum conservation in equation (4.2), in a circular shearing flow the only non-vanishing component of the stress tensor $\boldsymbol{\sigma}$ is in the $R\phi$ direction, expressed as:

$$\sigma_{R\phi} = \eta R \Omega', \tag{4.7}$$

where $\Omega' = \partial\Omega/\partial R$ represents the radial derivative of the gas angular velocity.

In the following sections, we project the Navier-Stokes equation onto the three cylindrical coordinate directions for additional insights on accretion disc physics.

4.1.1 Vertical equilibrium

In our model, we assume that velocities in the z direction are negligible and viscous forces only have components in the $R\phi$ direction. Thus, the projection of the Navier-Stokes equation (4.2) along z direction results in the following expression:

$$\frac{1}{\rho}\frac{\partial p}{\partial z} = -\frac{\partial \Phi}{\partial z}. \tag{4.8}$$

This equation is called the vertical hydrostatic equilibrium condition. It represents the balancing between the vertical component of the gravitational force and the vertical pressure gradient.

Assuming a barotropic equation of state, we can express the vertical pressure gradient as:

$$\frac{\partial p}{\partial z} = \frac{\partial p}{\partial \rho}\frac{\partial \rho}{\partial z} = c_\mathrm{s}^2\frac{\partial \rho}{\partial z}, \tag{4.9}$$

where $c_\mathrm{s}^2 = \partial p/\partial \rho$ represents the square of the sound speed in the gas.

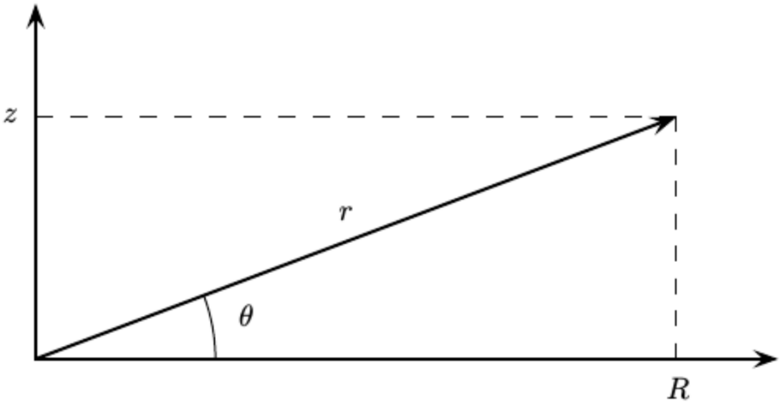

Figure 4.1: Geometry involved in the computation of the disc vertical structure.

The assumptions of negligible disc self gravity and of thin disc approximation enable us to simplify the expression for the vertical gravitational force as:

$$\frac{\partial \Phi}{\partial z} = \frac{\mathcal{G}M_*}{r^2}\sin(\theta) \approx \frac{\mathcal{G}M_*}{r^2}\frac{z}{r} \approx \frac{\mathcal{G}M_*}{R^3}z = \Omega_\mathrm{K}^2 z. \tag{4.10}$$

Here, M_* represents the mass of the central protostar, θ is the angle between the position vector and the disc plane (as illustrated in Figure 4.1) and $\Omega_\mathrm{K}(R) = \sqrt{\mathcal{G}M_*/R^3}$ is the Keplerian angular velocity, that is the angular velocity of a body in a circular orbit of radius R.

With these assumptions and assuming a vertically isothermal disc (no vertical temperature gradients), the condition of hydrostatic equilibrium can be rewritten as

$$c_\mathrm{s}^2\frac{\partial \rho}{\partial z} = -\rho\Omega_\mathrm{k}^2 z. \tag{4.11}$$

Integration of this equation in the z direction provides us with the vertical mass distribution, which takes the form of a Gaussian distribution:

$$\rho = \rho_0 e^{-z^2/2H^2}, \tag{4.12}$$

where ρ_0 is the density at $z = 0$ and $H = c_\mathrm{s}/\Omega_\mathrm{k}$. We define the thickness of the disc as H, that is the length scale of the vertical Gaussian distribution in (4.12).

Using the definition of H and the thin disc condition, we can derive the relationship

$$\frac{H}{R} = \frac{c_\mathrm{s}^2}{v_\mathrm{K}^2} \ll 1, \tag{4.13}$$

that implies $c_\mathrm{s} \ll v_\mathrm{K}$, with v_k the Keplerian linear velocity. This means that the orbital velocity of the gas has to be highly supersonic. Furthermore, we can assume from observation that accretion processes occur on a longer timescale than dynamical processes. Consequently, we have the following ordering for the velocities in the disc:

$$v_\mathrm{R} \ll c_\mathrm{s} \ll v_\phi. \tag{4.14}$$

4.1.2 Radial equilibrium

We now consider the radial projection of the Navier-Stokes equation (4.2). On the left-hand side, the advection term reduces to

$$(\mathbf{v} \cdot \nabla)\mathbf{v}|_R = -\frac{v_\phi}{R}, \tag{4.15}$$

and, due to the condition in equation (4.14), we can neglect the time derivative of the velocity radial component.

On the right-hand side, we have contributions from the pressure and gravitational potential radial gradient, but again no contribution from the viscosity stress tensor. Therefore, we arrive at the following equation:

$$\frac{v_\phi}{R} = \frac{1}{\rho}\frac{\partial p}{\partial R} + \frac{\partial \Phi}{\partial R}. \tag{4.16}$$

Assuming a barotropic equation of state, we can express the pressure gradient as:

$$\frac{1}{\rho}\frac{\partial p}{\partial R} = \frac{c_\mathrm{s}^2}{\rho}\frac{\partial \rho}{\partial R} = \frac{c_\mathrm{s}^2}{R}\frac{\partial \ln \rho}{\partial \ln R}. \tag{4.17}$$

Multiplying equation (4.16) by R, using equation (4.17) and recalling that

$$\frac{\partial \Phi}{\partial R} = \frac{\mathcal{G} M_*}{R^2} = \frac{v_\mathrm{K}^2}{R}, \tag{4.18}$$

we can express equation (4.16) as:

$$v_\phi^2 = v_\mathrm{K}^2 \left(1 + \frac{c_\mathrm{s}^2}{v_\mathrm{K}^2}\frac{\partial \ln \rho}{\partial \ln R}\right). \tag{4.19}$$

This equation reveals that, at first order, the orbital velocity of the gas is Keplerian, and thus equation (4.16) is the centrifugal balance condition. However, there is a second order correction term in H/R due to the radial pressure gradient that contributes to the centripetal force. This second-order term is negative, because we expect that the radial derivative of ρ to be negative, and it implies a sub-Keplerian orbital velocity for the gas component of the disc. For thin discs this correction is negligible and the disc can usually be considered to follow circular Keplerian orbits.

Interestingly, equation (4.19) implies that there exists a relative azimuthal velocity between the gas and massive bodies in the disc, as massive objects are not affected by pressure gradients. This difference in velocity has important consequences for the viscous interaction between gas and dust within the disc.

4.1.3 Azimuthal equilibrium

In the azimuthal direction ϕ of the Navier-Stokes equation, where pressure and gravity have no components, the only force in action is shear viscosity between adjacent rings. In our equations, we generally express viscosity through the kinematic viscosity coefficient $\hat{\nu} = \eta/\rho$. When we express our equations per unit surface we take into account $\hat{\nu}$ as its vertical average weighted on the density ρ, that is

$$\nu = \frac{1}{\Sigma}\int_{-\infty}^{+\infty} \hat{\nu}\rho \mathrm{d}z = \frac{1}{\Sigma}\int_{-\infty}^{+\infty} \eta \mathrm{d}z \tag{4.20}$$

The Navier-Stokes equation (4.2) along the ϕ direction reads as

$$\Sigma\left(\frac{\partial v_\phi}{\partial t} + \frac{v_\phi v_\mathrm{R}}{2R}\right) = \frac{1}{R^2}\frac{\partial}{\partial R}\left(R^3\Sigma\nu\Omega'\right). \tag{4.21}$$

Multiplying the previous equation by R and using the surface density continuity equation (4.5) yelds

$$\frac{\partial}{\partial t}(\Sigma R v_\phi) + \frac{1}{R}\frac{\partial}{\partial R}(R v_\phi \Sigma R v_\mathrm{R}) = \frac{1}{R}\frac{\partial}{\partial R}(R^3\nu\Sigma\Omega'). \tag{4.22}$$

Equation (4.22) represents a continuity equation for the superficial angular momentum density $L = \Sigma R v_\phi$. The difference between the advected angular momentum and the time derivative of L corresponds to the angular momentum variation caused by the torque due to the shear viscosity. Equation (4.22) also illustrates that thanks to viscosity, the angular momentum is carried throughout the disc, with each ring losing angular momentum from its inner and outer boundaries. If $\nu = 0$ there is no torque, thus no angular momentum transport.

From equation (4.22) we can derive the torque exerted by an external ring onto an internal one at radius R:

$$G(R) = 2\pi\nu\Sigma R^3\Omega'. \tag{4.23}$$

The torque $G(R)$ acting on the internal ring is negative, implying that angular momentum is transferred from internal to external radii. This torque vanishes for rigid rotation, as expected.

Assuming that the gas orbital velocity is nearly Keplerian, we can compute the radial velocity of the gas by combining equations (4.5) and (4.22), resulting in

$$v_\mathrm{R} = \frac{3}{R^{1/2}\Sigma}\frac{\partial(R^{1/2}\nu\Sigma)}{\partial R}. \tag{4.24}$$

Substituting the previous equation in equation (4.22) we obtain an equation for the time evolution of the surface density Σ of the disc, that is

$$\frac{\partial \Sigma}{\partial t} = \frac{3}{R}\frac{\partial}{\partial R}\left[R^{1/2}\frac{\partial}{\partial R}\left(R^{1/2}\nu\Sigma\right)\right]. \tag{4.25}$$

Two interesting points can be derived from this equation. Firstly, we see that with no viscosity (i.e. $\nu = 0$) there is no disc evolution. Secondly, equation (4.25) has the form of a diffusion equation with a diffusion time scale

$$t_\nu = \frac{R^2}{\nu}. \tag{4.26}$$

Its value has significant implications for the timescales of disc evolution and the efficiency of angular momentum transport within these systems.

4.1.4 Steady state accretion rate

In a stationary condition, each derivative with respect to time is null. We can exploit this in Eq. (4.5) and (4.22), which are the vertically integrated continuity equations for mass surface density and angular momentum surface density, respectively. By integrating them over the azimuthal direction (i.e. multiplying by 2π, given the azimuthal symmetry) we obtain

$$\frac{1}{R}\frac{\partial}{\partial R}(2\pi v_R \Sigma R) = 0 \tag{4.27}$$

and

$$\frac{1}{R}\frac{\partial}{\partial R}(2\pi v_R \Sigma R^2 \Omega) = \frac{1}{R}\frac{\partial}{\partial R}(2\pi \nu \Sigma R^3 \Omega'). \tag{4.28}$$

To solve these equations, we need to define two constants: the mass and the angular momentum flux. The mass flux is the mass accretion rate onto the central star, which is $\dot{M} = -2\pi R\Sigma v_R$. The angular momentum flux can be written as $\dot{J} = 2\pi\Sigma v_R R^3\Omega$. Under the so called "no torque condition", we can assume there is a radius $R_{\rm in}$ near the star at which $\partial\Omega/\partial R = 0$ and the viscous torque vanishes. This radius has to exist, given that near the star the angular velocity of the disc has to drop to connect to the stellar rotation velocity which has to be smaller than $\Omega_{\rm K}$ for stability reasons. Thus,

$$\dot{J} = \dot{J}\Big|_{R=R_{\rm in}} = 2\pi\Sigma v_R R_{\rm in}^3\Omega(R_{\rm in}) = -\dot{M}R_{\rm in}^2\Omega_{\rm in}. \tag{4.29}$$

From Eq. (4.28) we see also that

$$\dot{J} = \dot{M}\Omega R^2 - 2\pi\nu\Sigma R^3\Omega', \tag{4.30}$$

where the first term of the right hand side is an advection term while the second term is a torque. Given Eq. (4.29), we obtain the following relationship:

$$\nu\Sigma = \frac{\dot{M}}{3\pi}\left(1 - \sqrt{\frac{R_{\rm in}}{R}}\right)^{-1}, \tag{4.31}$$

which, far from the central star (where $R \gg R_{\rm in}$) becomes

$$\dot{M} = 3\pi\nu\Sigma. \tag{4.32}$$

Given that we are in a stationary situation, $\dot{M}$ is constant and thus, also $\nu\Sigma$ is a constant. Interestingly, this equation relates crucial disc properties, like viscosity, with the accretion rate.

4.1.5 Viscosity and α prescription

Viscosity is a crucial component of our disc model as it plays a fundamental role in driving angular momentum transport and energy dissipation, ultimately governing the evolution of accretion discs and the mass accretion onto the central protostar. Additionally, the transport and dissipation of energy set the temperature profile of the disc, influencing its emission properties.

However, we have yet to address the nature of the viscosity invoked to describe accretion disc evolution. This is a critical issue because not knowing the nature of viscosity impedes our ability to study its magnitude and the timescales of phenomena associated with it.

To shed light on this issue, let's consider a scenario where the only source of viscosity in the disc is collisional viscosity, the primary source of viscosity in terrestrial fluids. Collisional viscosity arises from the exchange of fluid particles between fluid elements due to their random motion. Different fluid elements possess different mean velocities, leading to energy and angular momentum exchange.

The magnitude of collisional viscosity, denoted as $\nu_{\rm coll}$, should be of the order of the product of the typical velocity of fluid particles ($\approx c_{\rm s}$) with their mean free path λ. In mathematical terms:

$$\lambda = \frac{1}{n\sigma_{\rm coll}} = \frac{\mu m_{\rm p}}{\rho\sigma_{\rm coll}} \approx \frac{\mu m_{\rm p}}{\Sigma\sigma_{\rm col}} H, \tag{4.33}$$

where $n = \mu m_{\rm p}/\rho$, with $\mu m_{\rm p}$ representing the mean molecular mass and $\rho \approx \Sigma/H$.

We can define the viscous timescale as $t_\nu = R^2/\nu_{\rm coll}$ as done in equation (4.26), with $\nu_{\rm coll} = \lambda c_{\rm s}$, and by comparing it with the dynamical timescale $t_{\rm dyn} = \Omega^{-1}$, we obtain

$$\frac{t_\nu}{t_{\rm dyn}} = \Omega\frac{R^2}{\nu_{\rm coll}} = \left(\frac{\Sigma\sigma_{\rm coll}}{\mu m_{\rm p}}\right)\left(\frac{H}{R}\right)^{-2}. \tag{4.34}$$

If we assume that the collisional cross section is of the order of the size of a molecule of H_2, we have $\sigma_{\rm coll} \approx 10^{-16}$ cm^2. Moreover, being the gas mainly composed of H_2 molecules, we have $\mu \approx 2$. In a disc of mass $M_{\rm d} = 0.005$ solar masses, disc thickness $H/R \approx 0.1$ and a radius of $R_{\rm out} = 50$ AU, we have $\Sigma \approx M_{\rm d}/R^2_{\rm out} \approx 10$ g/cm^2. Using equation (4.34) with $m_{\rm p} \approx 10^{-24}$ g we obtain

$$\frac{t_\nu}{t_{\rm dyn}} \approx 10^{11}. \tag{4.35}$$

The dynamical timescale of a disc is at least of the order of a year. Thus, this estimate tells us that disc evolution driven solely by collisional viscosity has a timescale longer that the age of the universe. This clearly demontrates that the fluid within the disc is not collisional, despite the observed viscous behaviour of discs.

This points to the idea that the nature of disc viscosity cannot be attributed to microscopic interaction between fluid elements. At the same time it gives us a clue of what the nature of this viscosity could be. Indeed, equation (4.34) expresses the Reynolds number of the disc, that measures the tendency of a fluid to be turbulent. A high Reynolds number means that the fluid in an accretion disc is prone to be turbulent and this opens new ways for fluid elements to interact over larger distances compared to the mean free path. These macroscopic interactions between fluid elements can act as a viscosity source greater than the collisional one by several orders of magnitude.

Balbus & Hawley (1998) showed the conditions under which turbulence behaves as an effective viscosity term described by the stress tensor in the Navier-Stokes equation.

Turbulence, in the presence of correlations between the radial and azimuthal components of fluctuating fields (e.g., velocity, magnetic field, or gravitational field), can extract angular momentum and energy from the mean field and transport them through fluctuations.

We thus have two primary ways to evaluate the viscosity in an accretion disc. The first approach involves observations: we observe accretion discs and we measure ν through their properties. This is similar to what we have done in order to exclude collisional viscosity as the source of viscosity in discs. The second approach is theoretical: we identify an instability that can lead to turbulence and with numerical experiments we measure the correlation between the azimuthal and radial components of its fluctuating field.

While the nature of viscosity in protoplanetary discs remains largely unknown, Shakura & Sunyaev (1973) introduced a useful parameterization to estimate its magnitude and compare theoretical models with observations. In its simpler interpretation, this parameterization is based on dimensional analysis, expressing viscosity as the product of a velocity scale (c_s) and a length scale (H). Where c_s is the speed of sound and H is the thickness of the disc. The result is:

$$\nu = \alpha c_\mathrm{s} H. \tag{4.36}$$

Firstly we notice that $\alpha \leq 1$. Indeed, the typical turbulent velocity cannot be grater than c_s, as perturbations would quickly dissipate through shocks. On the other hand, if we suppose isotropic turbulence, the length scale is limited to the disc thickness H.

We stress the fact that with this prescription we have not gone any deeper in understanding what the nature of viscosity is, we have only condensed all our ignorance in the α parameter.

From the previous example about collisional viscosity we see that the expected α parameter is

$$\alpha_\mathrm{coll} = \frac{\nu_\mathrm{coll}}{c_\mathrm{s} H} \approx \frac{\lambda}{H} = \frac{\mu m_\mathrm{p}}{\Sigma \sigma_\mathrm{coll}} \approx 10^{-9}. \tag{4.37}$$

As previously mentioned, this is too small compared to the observed α parameter in protoplanetary discs. Estimates based on recent high angular resolved surveys conducted with the Atacama Large Millimeter/submillimeter Array (ALMA) found α to be of the order of 5×10^{-4} (Dullemond et al. 2018).

4.1.6 Temperature profile

To accrete on the central star, the material has to lose both angular momentum and gravitational energy. We saw in Sec. 4.1.3 how angular momentum is carried towards larger radii via the viscous torque. As for gravitational energy, it has to be dissipated by dissipative processes producing heat. Thus, in addition to external radiation, also internal processes heat up the disc. In the following we presents two regimes in which we are able to compute the temperature profile fo the disc given the source providing the heating. Such temperature profiles are useful in setting up the temperature profile of accretion discs hydrodynamical simulations.

4.1.6.1 Active disc temperature profile

In Sec. 4.1.3 we derived the net torque over an annulus, i.e. $\partial G/\partial R$, where G is the torque applied by an annulus over the one adjacent to it. By multiplying the net torque by Ω we obtain the work done by viscous forces over a ring of width $\mathrm{d}R$. We finally divide by $2\pi R$ to obtain the work done per unit surface P, that is

$$P = \frac{1}{2\pi R}\Omega\frac{\partial G}{\partial R} = \frac{1}{2\pi R}\frac{\partial}{\partial R}(G\Omega) - \frac{G\Omega'}{2\pi R}. \tag{4.38}$$

The power per unit surface P has two contributions. The first, positive, represents the transport of energy because, when integrated, it gives contribution only at boundaries. The second, negative, is a proper dissipation term. Interestingly, viscosity, besides diffusing angular momentum, also transports energy over the disc.

The dissipated energy per unit surface is, thus,

$$D(R) = \frac{G\Omega'}{2\pi R} = \nu\Sigma(R\Omega')^2. \tag{4.39}$$

Which, assuming Keplerian rotation, reads:

$$D(R) = \frac{9}{4}\nu\Sigma\Omega^2. \tag{4.40}$$

By integrating the previous equation over the disc and assuming a stationary disc (i.e. using Eq. (4.31) to express $\nu\Sigma$), we obtain the rate of energy dissipated by the disc:

$$L_{\mathrm{disc}} = \int_{R_{\mathrm{in}}}^{R_{\mathrm{out}}} D(R)2\pi R\mathrm{d}R = \int_{R_{\mathrm{in}}}^{R_{\mathrm{out}}} \frac{3}{2}\frac{\mathcal{G}M}{R^2}\left(1-\sqrt{\frac{R_{\mathrm{in}}}{R}}\right)\dot{M}\mathrm{d}R = \frac{1}{2}\frac{\mathcal{G}M}{R_{\mathrm{in}}}\dot{M}, \tag{4.41}$$

which basically is the gravitational energy to be dissipated for bringing mass from infinity to R_{in} at a rate $\dot{M}$.

Under the assumption that the source of disc heating is mainly the dissipated gravitational energy, we can derive the temperature profile of such disc, called "active disc".

A surface element dissipation rate at radius R can be equated to the energy emitted by a black body of temperature T_{s}, multiplied by two because the disc is emitting from both surfaces:

$$2\sigma_{\mathrm{SB}}T_{\mathrm{s}}^2 = \frac{3}{4\pi}\frac{\mathcal{G}M}{R^3}\dot{M}\left(1-\sqrt{\frac{R_{\mathrm{in}}}{R}}\right), \tag{4.42}$$

where σ_{SB} is the Stefan-Boltzmann constant.

From previous equation we can derive the superficial temperature profile:

$$T_{\mathrm{s}} = \left[\frac{3}{8\pi\sigma_{\mathrm{SB}}}\frac{\mathcal{G}M}{R^3}\dot{M}\left(1-\sqrt{\frac{R_{\mathrm{in}}}{R}}\right)\right]^{1/4}. \tag{4.43}$$

For $R \gg R_{\mathrm{in}}$ the radial dependency of the surface temperature T_{s} is like

$$T_{\mathrm{s}} \approx T_0\left(\frac{R}{R_0}\right)^{-3/4}. \tag{4.44}$$

4.1.6.2 Passive disc temperature profile

Typically, the main source of heating in protoplanetary discs is external (e.g. the central star) rather than internal heating. Indeed, the disc surface is exposed to the central star radiation because the disc geometry is generally flared, that is the aspect ratio H/R increases with R. The general problem of radiative transfer in passive protoplanetary discs is complicated and usually solved numerically. However, under the following assumptions we can derive a radial temperature profile (Chiang & Goldreich 1997).

First, we assume the disc to be in local thermal equilibrium, i.e. radiation is absorbed and emitted by the dust suspended in the disc at the same rate, even if on different wavelengths. We also consider regions where $R \gg R_*$ so that we are allowed to treat the star as point-like. Given that the energy absorbed and emitted by a surface element ΔA of the disc is the same, we write

$$2\left(\frac{L_*}{4\pi R^2}\right)\alpha\Delta A = 2\sigma_{\mathrm{SB}}T_{\mathrm{s}}^4\Delta A, \tag{4.45}$$

where on the left hand side we have the rate of absorption of the stellar radiation (L_*), with α the flaring angle of the disc so that, for small angles, $\alpha\Delta A$ is the projection of ΔA perpendicular to the incident light direction. On the right hand side there is the radiation emitted by the surface element at a temperature T_{s}. Writing $L_* = 4\pi R_*^2\sigma_{\mathrm{SB}}T_*^4$, we can express the radial temperature profile as

$$T_{\mathrm{s}}^4 = \alpha^{1/4}\left(\frac{R_*}{R}\right)^{1/2} T_*. \tag{4.46}$$

4.2 Circumbinary discs

Systems with two or more stars are typically arranged in hierarchical configurations (see section 2.2.2) and can in principle host discs around each star of the system and around each hierarchical level. The existence and the dimensions of these discs depend mainly on the mass ratio and orbital parameters of the hierarchical level to which they belong, and on the availability of gas in the regions of interest.

In this section, we focus on phenomena occurring in the simplest multiple stellar system: a binary. It makes sense to start from a binary configuration because we already saw that binary orbits are the fundamental bricks of higher multiple systems, and we expect that a hierarchical system leads to a small correction to the binary behaviour described in this section on short timescales.

The presence of multiplicity in an accretion environment allows a tidal interaction between the stellar system and the gas discs surrounding it. This interaction has been firstly studied in the context of protoplanets embedded in circumstellar discs by Lynden-Bell & Pringle (1974) and successively developed by Lin & Papaloizou (1979a), Lin & Papaloizou (1979b) and Lin & Papaloizou (1986).

The tidal interaction between a disc of gas and a binary system allows the stellar and the gaseous component to mutually exchange angular momentum through a tidal torque that induce modifications to both the disc structure and the binary orbital parameters. Goldreich & Tremaine (1980) were the first to show this backreaction on the multiple system in the case of protoplanets.

This orbital parameters evolution surely affects the multiplicity of the population destabilising systems with more than two stars. In Tokovinin (2008) the author shows that the two main features not well reproduced by pure N-body stellar cluster evolution are the eccentricities and the period ratios of multiple systems. These are the two parameters that influence stability the most in hierarchical systems. This suggests that the accretion processes and viscous interactions are important in the earliest phase of multiple systems dynamical evolution. Indeed, the more accretion phenomena are efficient in destabilising hierarchical systems the more old populations orbital parameters distribution has to be shifted towards more stable eccentricity and semi-major axis ranges.

4.2.1 Tidal torque and the impulse approximation

We start studying the interaction between a binary and an accretion disc through a useful approximation, called "impulse approximation". Our aim is to compute the angular momentum exchange between the binary and the disc and we will follow the approach of Lin & Papaloizou (1979a). We assume that the mass ratio of the binary $q \ll 1$ and we consider a disc coplanar with the orbital plane.

Assuming that $q \ll 1$ allows us to consider the secondary star in Keplerian motion around the primary, and to neglect the motion of the primary. In the impulse approximation, we ignore the hydrodynamics of the gas and we study the interaction between the secondary star and a gas test particle that is orbiting in circular motion around the primary star. The only hydrodynamical effect allowed is the viscous interaction that is efficient enough to guarantee that the test particles after being deflected reach again a circular Keplerian orbit before the next encounter. We assume also that the encounters between the gas particle and the secondary are impulsive: the duration of the gravitational interaction is short compared to the orbital period and the deflection is small. Even with these simplifications, the impulse approximation leads to results in agreement with more sophisticated models, as shown in Lin & Papaloizou (1979b).

Let us consider a secondary star of mass M_s orbiting the primary star of mass M_p with a semimajor axis a, and a gas particle of mass μ orbiting the primary at radius $R = a + p$, where $p << a$ is the impact parameter of the encounter. In the frame of reference of the secondary the gas flows at distance p from the secondary with a velocity $v = v_\mathrm{gas} - v_\mathrm{s}$, where v_gas and v_s are the orbital velocity of the gas particle and of the secondary respectively. Figure 4.2 represents the encounter.

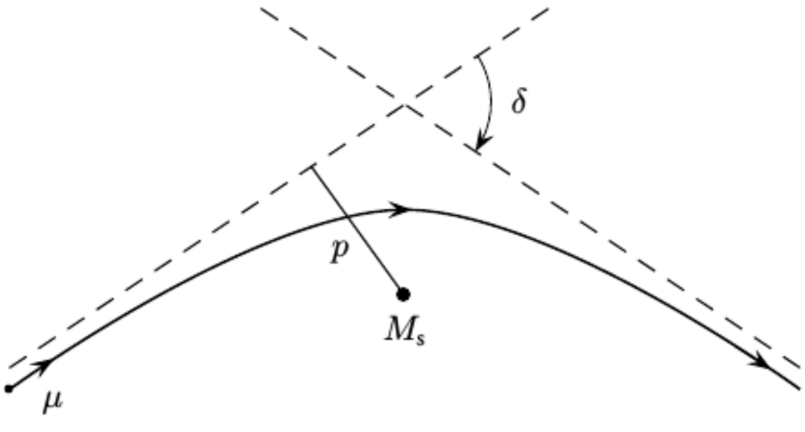

Figure 4.2: Deflection of a gas particle orbit caused by the encounter with the secondary.

From classical mechanics results, it can be shown that the angle δ by which the gas particle is deflected during the encounter respects

$$\mathrm{cotan}\frac{\delta}{2} = \frac{pv^2}{\mathcal{G}M_\mathrm{s}}. \tag{4.47}$$

This corresponds to the Rutherford scattering formula, as expected.

Given the impulsive nature of the interaction, we can consider the gravitational force always acting perpendicular to the velocity of the gas particle. Thus, the module of the velocity will be conserved and only the direction of the velocity will be affected. The deflection cause the particle to gain a small radial velocity and to reduce the tangential velocity. Indeed, after the encounter the particle radial velocity is $v \sin\delta$ and the tangential velocity reduces to $v\cos\delta$. If we suppose that the particle's orbital radius is not modified by the encounter and we approximate $R \approx a$, the encounter reduces the specific angular momentum of the gas particle by an amount

$$\Delta j_\mathrm{g} = av(\cos\delta - 1) = -\frac{2av}{\mathrm{cotan}^2(\delta/2)}, \tag{4.48}$$

where in the last passage we exploited the relation $\cos\delta - 1 \approx -2\tan^2(\delta/2)$, that holds for small δ. Using equations (4.47) we can finally write

$$\Delta j_\mathrm{g} = -\frac{2a(\mathcal{G}M_\mathrm{s})^2}{p^2v^3}. \tag{4.49}$$

It worth noting that if the gas particle orbits outside the secondary orbit, its relative velocity $v < 0$ and thus $\Delta j_\mathrm{g} > 0$. This means that in encounters gas outside the orbital radius of the secondary gains angular momentum, while gas inside looses angular momentum. The secondary thus tends to repel the gas around it.

The gas particle goes into an encounter every

$$\Delta t = \frac{2\pi}{|\Omega_\mathrm{K}(R) - \Omega_\mathrm{K}(a)|} \approx \frac{4\pi}{3}\frac{a}{\Omega_\mathrm{s}p}\mathrm{sgn}(p), \tag{4.50}$$

where Ω_K is the Keplerian angular velocity and $\Omega_\mathrm{s} = \Omega_\mathrm{K}(a)$. The resulting torque exerted by the secondary onto the gas per unit mass is

$$\Lambda_\mathrm{t,g} = \frac{\Delta j_\mathrm{g}}{\Delta t} = -\mathrm{sgn}(v)\frac{3}{2\pi}\frac{\mathcal{G}^2M_\mathrm{s}^2}{pv^3}\Omega_\mathrm{s}. \tag{4.51}$$

Using the fact that $p \ll a$ we can write

$$v = (a+p)\Omega_\mathrm{K}(a+p) - a\Omega_\mathrm{K}(a) \approx -\frac{3}{2}\Omega_\mathrm{K}(a)p. \tag{4.52}$$

Substituting the previous into equation (4.51) gives

$$\Lambda_\mathrm{t,g} = -\mathrm{sgn}(a-R)\frac{4}{9\pi}q^2\Omega_\mathrm{s}^2a^2\left(\frac{a}{p}\right)^4. \tag{4.53}$$

The previous equation express the specific torque exerted by the secondary onto the gas, that is the angular momentum variation of the gas particle. We are interested also in the transfer from the gas to the secondary. However, the gravitational force in this configuration is a central force and thus it conserves the total angular momentum. From this it must be that $\Delta j_\mathrm{g} + \Delta j_\mathrm{s} = 0$, or in terms of torque, that

$$\Lambda_\mathrm{t,s} = -\Lambda_\mathrm{t,g} = \mathrm{sgn}(a - R)\frac{4}{9\pi}q^2\Omega_\mathrm{s}^2 a^2 \left(\frac{a}{p}\right)^4 . \tag{4.54}$$

The equation (4.54) holds only for $p \approx 0$, around which we expanded $\Omega_\mathrm{K}(a + p)$. However, Lin & Papaloizou (1979b) showed that (4.54) is valid also for $p \neq 0$. This allows us to integrate (4.54) over all the possible impact parameters in order to obtain the total torque exerted by the disc on the secondary. Assuming azimuthal symmetry:

$$\begin{aligned} T &= \int_{R_\mathrm{in}}^{R_\mathrm{out}} \Lambda_\mathrm{t,s}(R)\Sigma(R)2\pi R\mathrm{d}R = \\ &= \int_{p_\mathrm{min}}^{p_\mathrm{max}} \Lambda_\mathrm{t,s}(a+p)\Sigma(a+p)2\pi(a+p)\mathrm{d}p \approx \\ &\approx \int_{p_\mathrm{min}}^{p_\mathrm{max}} \Lambda_\mathrm{t,s}(a)\Sigma(a)2\pi a\mathrm{d}p, \end{aligned} \tag{4.55}$$

where we have to choose the integral boundary. For p_max we can extend the integration to $+\infty$ as there the integral vanishes. For p_min we can take it to be the radius r_L of the Roche Lobe of the secondary. Indeed, near the secondary gas starts orbiting around the secondary and thus stops scattering and the angular momentum exchange vanishes. For small values of the mass ratio q, the Roche Lobe reduces to $r_\mathrm{L} = a(q/3)^{1/3}$.

With these boundaries the integral in (4.55) gives

$$T = \frac{8}{9}q^2\Omega_\mathrm{s}^2 a^7 \Sigma \int_{r_\mathrm{L}}^{+\infty} \frac{\mathrm{d}p}{p^4} = \frac{8}{9}q\Omega_\mathrm{s}^2 a^4 \Sigma. \tag{4.56}$$

We showed that the tidal interaction tends to push the gas away from the secondary. This effect alone would open a gap in the disc at the secondary radius. However, in section 4.1.3 we also showed the tendency of the gas to spread due to viscous interaction, thus viscous discs tend to diffuse and refill the gap opened by tidal torques. Gaps form depending on which of these processes dominates over the other.

We compare the magnitude of these two contrasting processes defining a time-scale for the angular momentum transfer between the disc and the secondary τ_t, and compare it with the viscous time scale

$$\tau_\nu = \frac{R^2}{\nu} \tag{4.57}$$

as defined in section 4.1.3. In order to do this, we divide an angular-momentum-scale of the disc $(\pi a^2 \Sigma \cdot A\Omega_\mathrm{s} \cdot a)$ by the tidal torque T computed in equation (4.56). The tidal time-scale results:

$$\tau_\mathrm{t} = \frac{\pi a^4 \Sigma \Omega_\mathrm{s}}{T} = \frac{9\pi}{8}\frac{a^4\Sigma\Omega_\mathrm{s}}{q\Omega_\mathrm{s}^2 a^4 \Sigma} = \frac{9\pi}{8q\Omega_\mathrm{s}}. \tag{4.58}$$

We can define a gap-opening criterion imposing that $\tau_\mathrm{t} < \tau_\nu$. Given the time-scales in (4.57) and (4.58) this reduces to:

$$q > \left(\frac{\Omega_\mathrm{s} R^2}{\nu}\right)^{-1} \equiv \mathrm{Re}. \tag{4.59}$$

A secondary will be able to open a gap in the disc around the primary when the mass ratio of the binary exceeds the local Reynolds number.

4.2.2 Disc truncation

The process of gap formation described in the previous section is an example of how a multiple stellar system shapes the discs that surround it. Typically the dimension of the discs depends on the tidal interaction. For example, when the gap-opening criterion is verified the secondary truncates the circumprimary disc, determining its inner radius. The limitation of $q \ll 1$ however restricts its application to mainly star-planet systems.

In general, tidal truncation can occur via two main mechanisms. The first one is due to the exchange of angular momentum between the disc and the binary at certain resonant locations (Lynden-Bell & Kalnajs 1972). The second one generally occurs for circular orbits and is based on non-resonant phenomena that can occur at each radius and not only at resonant ones.

4.2.2.1 Resonant interaction

In this section, we briefly discuss the general approach to the problem of predicting the size of a resonantly truncated disc. For the detailed mathematical approach, we refer to Artymowicz & Lubow (1994), where the authors determine the gap-opening criteria for eccentric binaries with no restriction on mass ratios.

The general approach in order to study the interaction between a binary and the gas consists in decomposing the perturbation of the gravitational potential due to the secondary in Fourier modes $\phi_{m,l}$ of the form $\exp[i(m\theta - l\Omega_{\rm b}t)]$ where l is the time harmonic number, $m \geq 0$ is the azimuthal number and $\Omega_{\rm b} = (\mathcal{G}M/a^3)^{1/2}$ binary orbital frequency, with M the total mass of the binary. The evolution and effects of perturbations induced in the disc are then computed by means of the linearised hydrodynamic equations.

This approach shows that the exchange of angular momentum in these resonant interactions can occur only at particular resonant locations in the disc. At these locations, a frequency of the satellite perturbation matches a characteristic frequency within the disc and the disc responds with the excitation of a density wave. These density waves carry energy and angular momentum, which dissipate through shocks.

For each disc in the system (circumstellar or circumbinary) and for each harmonic $\phi_{m,l}$ two types of resonances are possible. The first type is called corotation resonance and occurs when

$$\Omega(R) = \Omega_{\rm p} = \frac{l}{m}\Omega_{\rm b}, \tag{4.60}$$

where $\Omega(R)$ is the angular velocity of the gas at radius R. The second type is called Lindblad resonances, which are a set of resonances that appear when the gas orbital velocity and the pattern speed differ by a submultiple of the epicyclic frequency κ. That is when

$$\Omega(R) = \Omega_{\rm p} \pm \frac{\kappa(R)}{m}. \tag{4.61}$$

If we neglect the small difference between the Keplerian angular velocity $\Omega_{\rm K}$ and the orbital angular velocity of the gas due to pressure gradients, we can assume that

$$\Omega^2(R) = d\frac{\mathcal{G}M}{R^3}, \tag{4.62}$$

where $M = M_1 + M_2$ is the mass of the binary and $d = 1$ in the circumbinary disc case, $d = M_1/M$ in the case of circumprimary disc and $d = M_2/M$ in the case of circumsecondary disc. With this approximation we can consider $\kappa(R) = \Omega_{\rm K}(R)$ and thus the resonant radii are given by

$$r_{\rm CR} = \left(\frac{m}{l}\right)^{\frac{2}{3}} d^{\frac{1}{3}} a, \tag{4.63}$$

$$r_{\rm LR} = \left(\frac{m \pm 1}{l}\right)^{\frac{2}{3}} d^{\frac{1}{3}} a, \tag{4.64}$$

where the $+$ sign corresponds to the outer Linblad resonances and the $-$ sign corresponds to the inner Linblad resonances.

4.2.2.2 Non resonant interaction

In usual circular binaries, when the reduced mass $\mu = (M_1 M_2)/(M_1 + M_2) > 0.1$ the resonant radii in equations (4.63) and (4.64) are outside the Roche Lobes of the stars. When this happens the discs cannot be resonantly truncated and two main non-resonant truncation mechanisms can operate. The first one concerns the density perturbation of the disc due to the binary motion and was first considered by Papaloizou & Pringle (1977). In their article they study the density perturbation due to the secondary in absence of dissipation and found that they are in phase with the secondary. When dissipation is considered, however, it introduces a phase lag in the perturbation. This phase lag introduces non axisymmetric components in the density perturbation that lead to a tidal torque on the secondary, that results in an angular momentum exchange between the disc and the binary. Papaloizou & Pringle (1977) compute analytically this tidal torque and identify the truncation radius as the radius at which tidal torques dominate viscous ones.

It is interesting that in this mechanism both torques depend on viscosity (in fact the magnitude of the lag and thus of the tidal torque depends on how much viscous the disc is) and in consequence, the truncation radius does not depend on viscosity, as it cancels out in the comparison between the two torques. Note that this is the opposite of what happens in resonant mechanisms and in the impulse approximation, where tidal torques are independent of viscosity, and thus viscosity affects the disc size as ν does not cancel out in the torques comparison.

The second mechanism of non resunant disc truncation was first considered by Paczynski (1977) and more recently by Pichardo et al. (2005), and is due to the orbit intersection of test particles in the restricted three body problem. Test particle orbits are a very good approximation of streamlines in accretion discs with very small pressure and viscosity. In regions where test particles orbits intersect (an thus streamlines) high dissipative shocks have to occur and thus there we could expect a depletion of gas.

Paczynski (1977) numerically finds, in the case of a binary with circular orbits and small q, that orbits close to the Roche Lobe of a star in a binary always intersect each others (as shown in Figure 4.3) and thus he predicts the last non-intersecting orbit to be the outer radius of the circumstellar disc.

More recently Pichardo et al. (2005) relaxed the Paczynski (1977) assumption on circularity and mass ratio and numerically predicted the tidal truncation radius due to orbit crossing for a number of eccentricity and mass ratio values. They fitted a power law in both eccentricity e and mass ratio q for the truncation radius (i=1 for the primary and i=2 for the secondary), obtaining

$$R_i = R_{{\rm Egg},i} \cdot 0.733 \cdot (1-e)^{1.20} q^{0.07}, \tag{4.65}$$

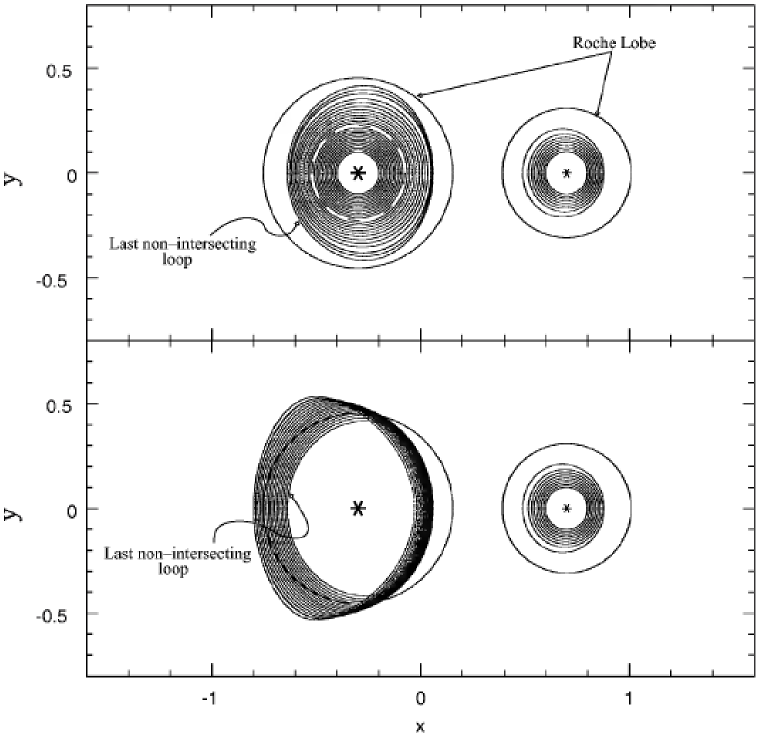

Figure 4.3: Test particle orbits for a circular binary and a mass ratio $q = 0.2$. Top panel: orbits plotted up to the position of the last non-intersecting loop (that defines the circumstellar gaseous disc). Bottom panel: orbits plotted starting from the first intersecting loop. (From Pichardo et al. (2005))

where $R_{\mathrm{Egg},i}$ is the Eggleton's estimate for the Roche Lobe average radius as in Eggleton (1983):

$$R_{\mathrm{Egg},i} = a\frac{0.49q_i^{2/3}}{0.6q_i^{2/3} + \ln\left(1 + q_i^{1/3}\right)}, \tag{4.66}$$

where $q_1 = \frac{M_1}{M_2}$ and $q_2 = \frac{M_2}{M_1}$.

4.2.3 Equlibrium configurations

Observations of protostellar circumbinary discs showed the existence of configurations in which there is a misalignment between the binary orbital plane and the disc plane. In Sec. 3.3 we presented the state-of-the-art knowledge about the distribution of such misalignment, where we saw that disc misalignment spans from nearly coplanar discs to discs perpendicular to the orbital plane (polar discs).

Misalignment could arise from different mechanisms, both at the onset of stellar formation and in subsequent evolutionary stages. Giant molecular clouds, where stars and discs form, are turbulent. Discs forming in a turbulent environment can be misaligned with the central binary (Offner et al. 2010; Bate 2012). In case the disc surrounding a binary star formed after the binary formation process via accretion of surrounding material, the accreting material is likely misaligned with the binary orbital plane leading to the formation of a misaligned disc (Bate et al. 2010).

Given a misaligned disc, we can naively expect that dissipation will drive the disc towards a configuration coplanar to the binary orbital plane. Indeed, that is the minimum energy configuration for a given density distribution. This is indeed what happens in the majority of the disc parameter space region and it is discussed in Sec. 4.2.3.1.

When the disc is orbiting an eccentric binary, however, it can align perpendicularly to the binary orbital plane if the initial misalignment is sufficiently high. This mechanism, called 'polar alignment', results from the 3 body dynamics discussed in Sec. 2.2.4 and is discussed in Sec. 4.2.3.2.

4.2.3.1 Coplanar equilibrium

Let's consider a binary with masses m_a and m_b and semi-major axis a. The second-order gravitational potential Φ in cylindrical coordinates centered in the binary center of mass averaged over the binary orbit has been computed by Facchini et al. (2013):

$$\Phi(R,z) = -\frac{\mathcal{G}M}{R} - \frac{\mathcal{G}M\eta a^2}{4R^3} + \frac{\mathcal{G}Mz^2}{2R^3} + \frac{9}{8}\frac{\mathcal{G}M\eta a^2 z^2}{R^5}, \tag{4.67}$$

where $\eta = m_\mathrm{a}m_\mathrm{b}/(m_\mathrm{a}+m_\mathrm{b})^2$ and $M = m_a + m_b$.

A misaligned test particle orbiting in this gravitational potential field undergoes nodal precession. That is, the angular momentum vector of the particle precesses around the binary angular momentum vector (see Sec. 2.2.4).

The precession frequency of the test particle is

$$\Omega_\mathrm{p}(R) = \frac{3}{4}\frac{\sqrt{\mathcal{G}M}\eta a^2}{R^{7/2}}. \tag{4.68}$$

Given that Ω_p depends on the radius, a disc of non-interacting particles would undergo differential precession. If, however, we consider a gaseous disc, viscosity tends to keep the disc together depending on the disc thickness and viscosity. In the typical protostellar disc regime, discs are warm enough to efficiently communicate in the radial direction through pressure-induced bending waves, allowing the disc to avoid warping. Thus, a protostellar disc is generally able to hold itself together and it precesses as a solid body (Papaloizou & Terquem 1995; Larwood & Papaloizou 1997; Lubow & Ogilvie 2000).

The disc precession frequency ω_p can be computed by averaging Ω_p over the angular momentum surface density at radius R, that is $L(R) = \Sigma R^2\Omega$. Thus,

$$\omega_\mathrm{p} = \frac{\int_{R_\mathrm{in}}^{R_\mathrm{out}} \Omega_p(R)L(R)2\pi R\mathrm{d}R}{\int_{R_\mathrm{in}}^{R_\mathrm{out}} L(R)2\pi R\mathrm{d}R}. \tag{4.69}$$

In addition, because of viscosity, the disc tends to align to the binary orbital plane, with an alignment timescale that is of the order of the viscous time (Papaloizou & Terquem 1995; Larwood et al. 1996; Bate et al. 2000) eventually reaching the coplanar equilibrium configuration. In particular, Bate et al. (2000) found that the timescale needed for dissipation of the disc tilt can be expressed as

$$t_\mathrm{alignment} \propto \omega_\mathrm{p}^{-1}\alpha^{-1}\left(\frac{H}{R}\right)^2\frac{\Omega_\mathrm{out}}{\omega_\mathrm{p}}, \tag{4.70}$$

where α is the α-viscosity parameter discussed in Sec. 4.1.5, Ω_out is the disc orbital velocity at the disc outer edge and H/R is the disc aspect ratio.

4.2.3.2 Polar equilibrium

A test particle orbiting an eccentric binary, under the conditions discussed in Sec. 2.2.4, precesses around the binary eccentricity vector, which is a vector lying on the semi-major axis and pointing towards the pericenter of the binary orbit (Farago & Laskar 2010). Aly et al. (2015) and Martin & Lubow (2019) numerically showed that also accretion discs can undergo polar alignment. In addition, Lubow & Martin (2018) studied the stability of the polar configuration, analytically describing the process of polar alignment for viscous accretion discs.

Lubow & Martin (2018) applied the same procedure used in Lubow & Ogilvie (2000), but to a nearly polar disc. They found that, at the lowest order, the frequency of the disc oscillation is given by

$$\omega = \frac{3\sqrt{5}}{4} e_{\mathrm{b}} \sqrt{1+4e_{\mathrm{b}}^2}\,\frac{m_a m_b}{M^2} \left\langle \left(\frac{a}{R}\right)^{7/2} \right\rangle \Omega_{\mathrm{b}}, \tag{4.71}$$

where the angular brackets represent an angular momentum weighted average. Here e_{b} is the binary eccentricity and Ω_{b} is the binary frequency. Thus,

$$\left\langle \left(\frac{a}{R}\right)^{7/2} \right\rangle = \frac{\int_{R_{\mathrm{in}}}^{R_{\mathrm{out}}} \Sigma R^3 \Omega (a/R)^{7/2} \mathrm{d}R}{\int_{R_{\mathrm{in}}}^{R_{\mathrm{out}}} \Sigma R^3 \Omega \mathrm{d}R}. \tag{4.72}$$

Given an initial tilt i_0, the disc inclination evolves as

$$i(t) = i_0 \sqrt{\frac{1+9e_{\mathrm{b}}^2 + (1-e_{\mathrm{b}}^2 \cos 2\omega t)}{2(1+4e_{\mathrm{b}}^2)}}. \tag{4.73}$$

In the presence of dissipation, tilt and nodal oscillations are dumped and the disc eventually settles on a polar orbit. Lubow & Martin (2018) showed that, for a fixed disc structure, small departures from the polar state decay on a timescale

$$t_{\mathrm{decay}} \propto \frac{(H/R)^2 \Omega_{\mathrm{b}}}{\alpha \omega^2} \propto \frac{(H/R)^2 M^2}{\alpha e_{\mathrm{b}}^2 (1+4e_{\mathrm{b}}^2) m_a^2 m_b^2 \Omega_{\mathrm{b}}}. \tag{4.74}$$

We can appreciate the process of polar alignment in the same way in which we described polar orbits in the $i\sin(\phi) - i\cos(\phi)$ plane for three body systems. In Fig. 4.4, a circumbinary disc starts with an inclination i and longitude of ascending node ϕ suitable for polar alignment. Instead of oscillating in close orbits, as in the case without dissipation, the curve on the right panel shrinks towards the equilibrium configuration ($i = \pi/2$, $\phi = \pi/2$). This is due to the dumping in the synchronous oscillations of i and ϕ shown in the left panels of the figure.

4.2.4 Accretion dynamics

The mass of a protobinary (or higher multiplicity system) formed in the collapse of a molecular cloud core is initially only a fraction of the total core mass. Indeed, the higher angular momentum gas starts to orbit the stars forming an accretion disc, which slows down the mass accretion onto the stars. Surveys of mass ratios of binary systems have shown the tendency of binary populations to flatten their mass ratio distribution with stellar age (De Rosa et al. 2014). This can be a result of the competition between the

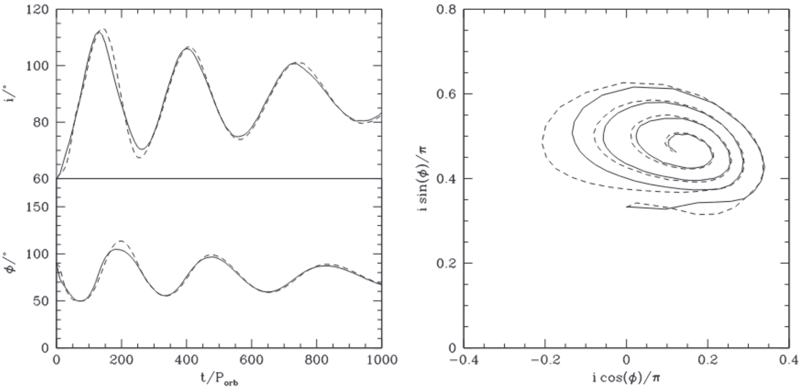

Figure 4.4: Evolution of disc tilt i and longitude of the ascending node ϕ in a disc undergoing nodal liberation. On the left panel i and ϕ are plotted against time. On the right panel the disc evolution is plotted on the $i\sin(\phi) - i\cos(\phi)$ plane. Figure from Martin & Lubow (2019).

primary and the secondary in accreting mass from the circum-binary disc. In general, numerical studies agree with the tendency for the secondary to accrete the majority of the disc mass. This tendency to form high mass ratio binaries is found in cluster level numerical simulation (e.g. Bate 2009) as well as in the study of isolated binary with different numerical techniques (e.g. three-dimensional Smoothed Particle Hydrodynamics in Bate & Bonnell (1997) and Dotti et al. (2010), and two-dimensional grid codes in de Val-Borro et al. (2011), Farris et al. (2014)).

This is in line with the shorter distance between the inner edge of the disc and the secondary Roche Lobe, and with the lower relative velocity between the accreting gas and the secondary.

In Young & Clarke (2015), the authors show that the general tendency of a binary to raise its mass ratio depends also on gas temperature. They found that, independently of the mass ratio, raising the temperature of the accreting gas raises the fraction of gas accreting onto the primary. Gerosa et al. (2015) proposed a parametrisation of the competitive accretion trend based on a set of simulations of black holes binaries in Farris et al. (2014). The temperature parameter on which Young & Clarke (2015) studied the variation of the competitive accretion is the sound speed normalised to the orbital speed of the binary, that is

$$c = c_{\rm s}/\sqrt{\frac{\mathcal{G}M}{a}}, \tag{4.75}$$

where $\mathcal{G}$ is the gravitational constant, M the mass of the binary and a its semi-major axis. This parameter is also the aspect ratio of the disc at radius a.

The parametrisation in Gerosa et al. (2015) fits numerical trends of the ratio of the accretion rate of the primary on the total accretion rate through the λ_1 and $\lambda_2 = 1 - \lambda_1$ factors defined as

$$\lambda_i = \frac{\dot{M}_i}{\dot{M}_{\rm tot}}, \tag{4.76}$$

where $\dot{M}_1$ and $\dot{M}_2$ are the accretion rates of respectively the primary and the secondary, and $\dot{M}_{\rm tot}$ is the total accretion rate (i.e. $\dot{M}_{\rm tot} = \dot{M}_1 + \dot{M}_2$, note that the λ_i are not independent as by definition $\lambda_1 + \lambda_2 = 1$). This parametrisation reads:

$$\begin{aligned} \lambda_1^{\mathrm{P}} &= \frac{q}{1+q}, \text{ and} \\ \lambda_2^{\mathrm{P}} &= \frac{1}{1+q}, \end{aligned} \tag{4.77}$$

where q is the binary mass ratio.

The λ factors measure how the mass accreted at a certain time is distributed between the primary and the secondary. From their mean values, one can derive the tendency of mass equalisation, that is how much the mass ratio varies from the initial value and if it grows or it decreases.

When more than two stars are at play, also the interaction between the infalling gas and inner hierarchical level binaries has to be taken into account. In Part II of this thesis I investigate differential accretion in hierarchical triple systems (Ceppi et al. 2022).

Part II

Accretion rates in multiple stellar systems

CHAPTER 5

Accretion rates in hierarchical triple systems with discs

This chapter is based on the paper "Accretion rates in hierarchical triple systems with discs" by Simone Ceppi, Nicolás Cuello, Giuseppe Lodato, Cathie Clarke, Claudia Toci, Daniel J. Price, published on Monthly Notices of the Royal Astronomical Society, Volume 514, Issue 1, pp.906-919, in July 2022.

Surveys of star forming regions indicate that multiple stellar systems are common in young populations (Reipurth et al. 2014; Duchêne & Kraus 2013). Among Class 0 and Class I stars (younger than 1 Myr) the multiplicity fraction ranges between 40% and 70% (Connelley et al. 2008; Chen et al. 2013), while in evolved populations is around 20% (Duquennoy & Mayor 1991). In addition, molecular cloud simulations show that protostars are likely to form as part of multiple stellar systems and that their surrounding discs experience dramatic dynamical interactions with neighbour stars (Bate 2009, 2018). Thus, multiple stellar systems with discs are expected to be common in star forming regions. This is also confirmed by surveys of Class 0 systems, as in Tobin et al. (2016).

After the initial collapse of a molecular cloud core, the majority of the mass available to the forming stellar system is confined by angular momentum conservation in the disc and slowly accretes onto the stars (Bonnell & Bate 1994). The tidal torque between the central multiple system and the surrounding disc allows the exchange of angular momentum between the disc and the stellar system (Lin & Papaloizou 1979b; Goldreich & Tremaine 1980). The gravitational torque exerted by the multiple system on the circum-multiple disc is thought to suppress the surface density in the surrounding of the stars. Indeed, a high enough angular momentum exchange between the system and the surrounding material is able to open a central cavity in the disc (Artymowicz & Lubow 1996). However, thanks to the asymmetries of the gravitational potential and to the three dimensional nature of the problem, accretion of gas onto the stars is not suppressed. Indeed, the stars of the system pull streamers of gas from the inner edge of the cavity. These streamers bridge the lower density region between the disc inner edge and the stellar system allowing the gas to flow towards the stars (Artymowicz & Lubow 1996; Farris et al. 2014; Ragusa et al. 2016). There, inner accretion discs around the single stars process the infalling gas that eventually is accreted.

An example is the well known GG Tauri A (Keppler et al. 2020; Phuong et al. 2020). GG Tau A is a triple (Di Folco et al. 2014) stellar system surrounded by a circum-triple accretion disc. The stars carved a central cavity, where we observe streamers and filaments of gas. Another multiple system that shows cavities and nested discs separated by low density regions is the GW Orionis triple stellar system (Kraus et al. 2020; Bi et al. 2020). Other similar examples are the binary BHB 2007 (Alves et al. 2019), in which a complex structure of filaments supply gas from the circum-binary disc to the circum-stellar discs and L1448 IRS3B (Reynolds et al. 2021), that is really young multiple stellar system in formation.

In general, systems with more than two stars are unstable and their evolution eventually leads to the ejection of one body of the system (Valtonen & Karttunen 2006). The only stable configurations observed are made of nested binary orbits and are called hierarchical configurations. For example, a hierarchical triple system is made of a binary orbited at distance by a third body. In order to preserve the stability of the system, the third body needs to orbit the binary at a distance of several time the binary semi-major axis (see Mardling & Aarseth (2001) for a stability criterion).

How accreting mass from the circum-multiple disc distributes itself around the individual stars plays a key role in the star formation scenario. Indeed, both the evolution of the stellar system masses and the supply of gas around the stars to form inner discs (and possibly inner planets) strongly depend on the competition between the stars in having access to the gas stored in the disc. The study of these processes allows us also to link the properties of the observed evolved population of binaries to their initial conditions in which they initially born (Bate 2000). The fraction of mass accreted by each star of the system depends on the system orbital parameters, in particular on the mass ratio , as shown by Farris et al. (2014). In addition, other less studied system parameters play a role in the mass distribution among the system stars, for example the infalling gas temperature (Young et al. 2015; Young & Clarke 2015) and the gas viscosity (Duffell et al. 2020).

This process, known as differential accretion, has been widely studied in binaries. Different numerical (SPH and grid) methods show that the secondary star of the binary should accrete most of the disc mass (e.g. in Bate & Bonnell 1997; Farris et al. 2014; Young et al. 2015). This is due to the lower relative velocity between the secondary and the disc material orbiting at the inner edge, and to the lower distance between the secondary orbit and the inner edge of the disc. However, there are exceptions to this general behaviour when the system orbit is very eccentric. Indeed, in this case, Dunhill et al. (2015) showed that discs around binaries with mass ratio lower than unity can temporary accrete more mass onto the primary and Muñoz & Lai (2016) showed that unitary mass ratio binaries can temporary break the symmetry expected in their accretion rates. Both these exceptions are due to the precession of the eccentric cavity carved by the stellar system.

As of today, however, little is known about differential accretion in hierarchical systems. In this chapter we investigate to which extent the accretion trends of binary systems remain valid for hierarchical triples. In doing so, we propose a model to describe the deviations of the stellar accretion rates in triple systems. We also discuss the possibility to reveal unresolved hierarchical triple systems from their accretion rates and the difficulty in constraining the orbital parameters of the unresolved small binary.

The chapter is organised as follows: in Sec. 5.1 we describe the systems setup we considered and their initial conditions. In Sec. 5.2 we present our results. We discuss the results of the simulations sets in Sec. 5.3 and we give our conclusions in Sec. 5.4.

5.1 Hydrodynamical simulations

We performed gas simulations of coplanar multiple systems embedded in an outer coplanar accretion disc using the 3D Smoothed Particle Hydrodynamics code PHANTOM (Price

Table 5.1: Hydrodynamical simulations sets. All binary orbits (wider and smaller) are circular and coplanar with the disc. The semi-major axis of each wide orbit is $a_{\rm wide} = 10$ au. All small binary have a unitary mass ratio $q_{\rm small} = 1$.

Set 1	$\frac{a_{\rm small}}{a_{\rm wide}}$	$q_{\rm wide}$	split star
$b2$	-	0.2	-
$b4$	-	0.4	-
$b65$	-	0.65	-
$ts2$	0.1	0.2	secondary
$ts4$	0.1	0.4	secondary
$ts65$	0.1	0.65	secondary
$tp2$	0.1	0.2	primary
$tp4$	0.1	0.4	primary
$tp65$	0.1	0.65	primary
Set 2			
$ts2a15$	0.15	0.2	secondary
$ts2a05$	0.05	0.2	secondary
$ts4a18$	0.18	0.4	secondary
$ts4a15$	0.15	0.4	secondary
$ts4a05$	0.05	0.4	secondary
$ts65a20$	0.2	0.65	secondary
$ts65a15$	0.15	0.65	secondary
$ts65a05$	0.05	0.65	secondary
Set 3			
$tp2a20$	0.2	0.2	primary
$tp2a05$	0.05	0.2	primary
$tp4a20$	0.2	0.4	primary
$tp4a05$	0.05	0.4	primary
$tp65a20$	0.2	0.65	primary
$tp65a05$	0.05	0.65	primary

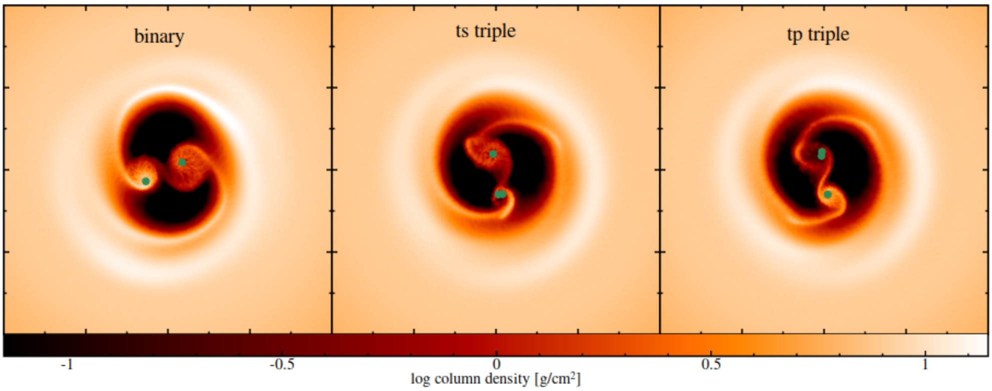

Figure 5.1: Snapshots of three selected high resolution simulation of Set 1 showing the gas density in logarithmic scale. Green dots are the sink particles. All the three simulations have $q_{\rm wide} = 0.65$. On the first column there is the binary. The central column shows the triple system obtained by splitting the secondary star of the binary (ts type). On the right column is shown the triple obtained by splitting the primary star of the binary (tp type). All snapshots are taken at 55 wide binary orbits.

et al. 2018b).

We perform three sets of simulations. Set 1 consists of nine simulations made of three binary systems and six hierarchical triple systems. The three binaries have mass ratio $q_{\rm wide} = M_{\rm s}/M_{\rm p} = 0.2$, 0.4 and 0.65 respectively, where $M_{\rm s}$ is the mass of the lighter star and $M_{\rm p}$ the mass of the heavier one. Initially, the binaries are circular and have a semi-major axis $a_{\rm wide} = 10$ au. From each binary we derived two hierarchical triple systems. The first kind of triples (labelled as ts) is built by splitting the secondary star of the binary, while the second kind of triples (labelled tp) is built by splitting the primary. In order to build the hierarchical triple systems, the binary stars are split into a circular binary with the same total mass of the split star, with a semi-major axis $a_{\rm small} = 1$ au and a mass ratio $q_{\rm small} = 1$[1]. This set of simulations aims at understanding the effect of the mass ratio on the accretion trends. Table 5.1 contains the orbital configuration of each of these systems, and Fig. 5.1 shows the gas surface density after 50 wide binary orbits for each simulation.

The simulations of Set 2 are devoted to explore the dependency of the triple system accretion rates on the small binary semi-major axis. In Set 2 we consider hierarchical triple systems where we split the secondary star. We start from the $ts2$, $ts4$ and $ts65$ simulations from Set 1 and we vary the small binary semi-major axis as reported in Table 5.1.

Finally, in Set 3 we focus on hierarchical triple systems where we split the primary star. We start from the $tp2$, $tp4$ and $tp65$ simulations from Set 1 and we vary the small binary semi-major axis as reported in Table 5.1.

The total stellar mass of each binary and triple system is 3 $M_\odot$. Each system is surrounded by the same coplanar gas disc that initially extends from $R_{\rm in} = 2\,a_{\rm wide}$ to $R_{\rm out} = 10\,a_{\rm wide}$ with a mass equal to 0.03 $M_\odot$. The disc is modelled using 10^6 SPH par-

---

[1] For more information about how we implemented in the PHANTOM code the possibility to simulate hierarchical triple systems, see Section 2.3.

ticles , resulting in a smoothing length about 0.1 times the disc scale height. The initial gas surface density profile is

$$\Sigma(R) = \Sigma_{\rm in} \left(\frac{R}{R_{\rm in}}\right)^{-p} \left(1 - \sqrt{\frac{R_{\rm in}}{R}}\right), \tag{5.1}$$

with $\Sigma_{\rm in} = 69.4$ g cm^{-2} and $p = 1$. We assume a locally isothermal equation of state centered in the center of mass of the system. The sound speed profile follows

$$c_{\rm s}(R) = c_{\rm s}(R_{\rm in}) \left(\frac{R}{R_{\rm in}}\right)^{-q}, \tag{5.2}$$

with $q = 0.25$. This results in a disc aspect ratio given by

$$\frac{H}{R} = \frac{H_0}{R_0} \left(\frac{R}{R_{\rm in}}\right)^{(1/2-q)}. \tag{5.3}$$

We set $H_0/R_0 = 0.1$ at $R = a_{\rm wide}$, as in Farris et al. (2014) and Young & Clarke (2015).

Disc viscosity is implemented via the artificial viscosity method that is standard in SPH (Lucy 1977; Gingold & Monaghan 1977), which can be related to the Shakura & Sunyaev (1973) α-viscosity as found by Lodato & Price (2010). As differential accretion depends on viscosity, we set $\alpha_{\rm SS} = 0.1$, by setting $\alpha_{\rm AV} \approx 9$, to match the values chosen by previous works, in particular by Farris et al. (2014) and Duffell et al. (2020).

Stars are simulated as sink particles (Price et al. 2018b; Bate et al. 1995). Sink particles are particles that interact only via gravity with other sink particles and SPH particles. They are evolved via a second-order Leapfrog integrator, as described in chapter 2.8.5 of Price et al. (2018b). Sinks are allowed to accrete SPH particles and to store the accreted particles angular momentum and mass. The accretion of a gas particle can occur when it enters the accretion radius of a sink. To be accreted, the gas particle has to be gravitationally bound to the sink and its angular momentum has to be sufficiently low. In order to reliably resolve the accretion rates, the accretion radius of each sink is set to 0.1 au. This radius is at most ~ 0.04 times the wide binary secondary Roche lobe radius, depending on the binary mass ratio (Eggleton 1983).

All our simulations were evolved for 100 wide binary orbits, that correspond to half a viscous time-scale at the disc inner edge $R_{\rm in} \approx 2a_{\rm wide}$, which can be expressed as (Lynden-Bell & Pringle 1974; Hartmann et al. 1998):

$$t_\nu \approx \frac{4}{9}\frac{R^2}{\nu}\bigg|_{R_{\rm in}}, \tag{5.4}$$

with $\nu = \alpha H c_{\rm s}$. We can write

$$\nu = \alpha H^2 \Omega = \alpha \left(\frac{H}{R}\right)^2 \Omega_{\rm wide} \sqrt{R a_{\rm wide}^3}, \tag{5.5}$$

where Ω is the Keplerian frequency and $\Omega_{\rm wide}$ is the binary orbital frequency. Using Eq. (5.5) at $R = R_{\rm in}$, the viscous time in unit of binary orbits is

$$t_\nu|_{R_{\rm in}} \approx \frac{8}{9\sqrt{2}\pi}\frac{1}{\alpha(H/R)^2}\frac{2\pi}{\Omega_{\rm wide}}. \tag{5.6}$$

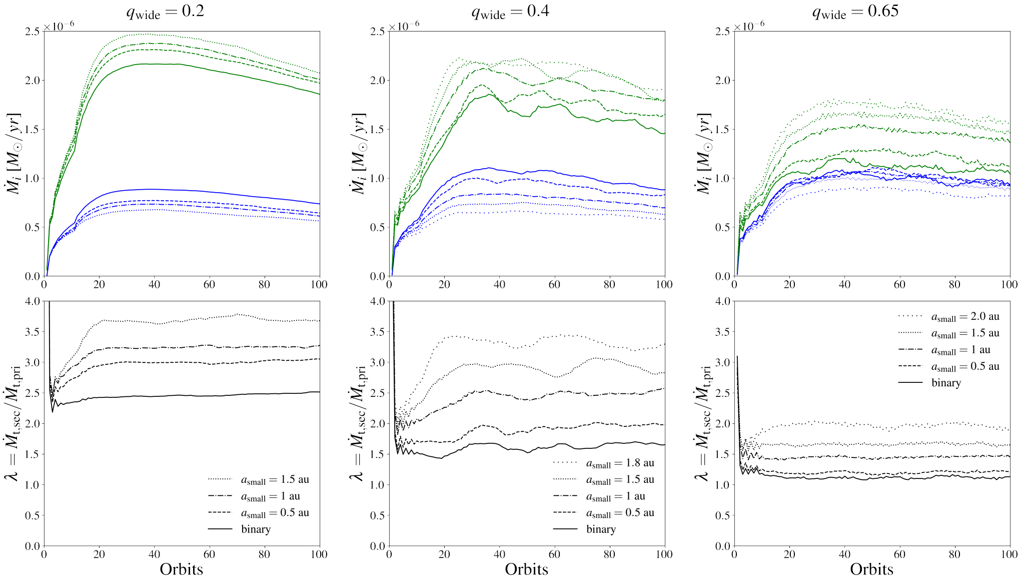

Figure 5.2: Moving averaged accretion rates and $\lambda = (\dot{M}_{\mathrm{t,sec1}} + \dot{M}_{\mathrm{t,sec2}})/\dot{M}_{\mathrm{t,pri}}$ factors measured in the *ts* triple simulations (Set 2). For each wide orbit mass ratio q_{wide}, on the upper panel are plotted the accretion rate of the secondary (green) and primary (blue) star. On the lower panel are plotted the ratio between the accretion rates. The solid line refers to the associated binary, from which the triples are generated. Each different line style refer to different small binary semi-major axis. The secondary accretion rate for triple system is the sum of the accretion rates of the small binary stars.

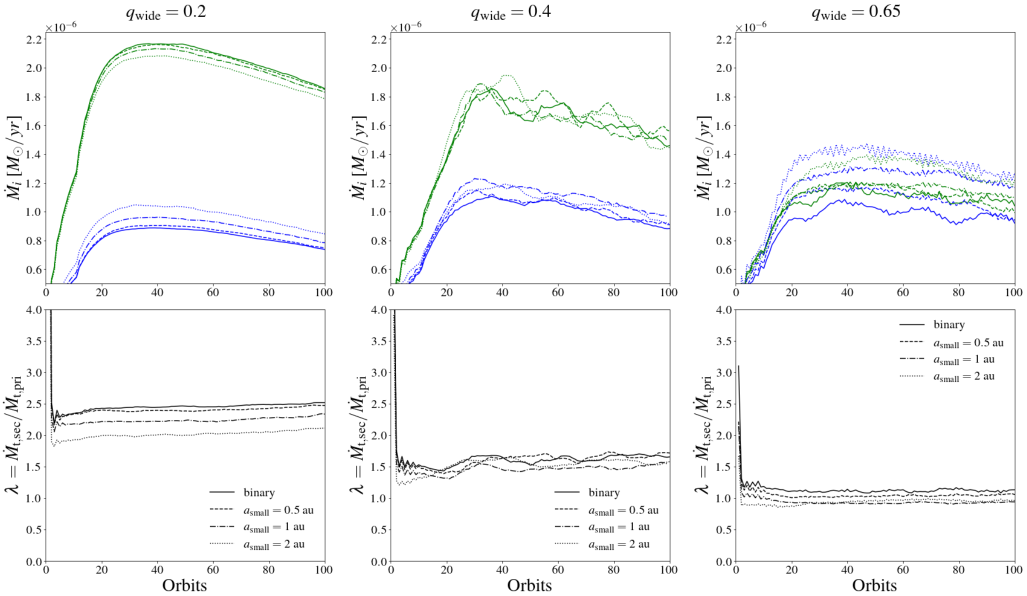

Figure 5.3: Moving averaged accretion rates and $\lambda = \dot{M}_{\rm t,sec}/(\dot{M}_{\rm t,pri1} + \dot{M}_{\rm t,pri2})$ factors measured in the *tp* triple simulations (Set 3). For each wide orbit mass ratio $q_{\rm wide}$, on the upper panel are plotted the accretion rate of the secondary (green) and primary (blue) star. On the lower panel are plotted the ratio between the accretion rates. The solid line refers to the associated binary, from which the triples are generated. Each different line style refer to different small binary semi-major axis. The primary accretion rate for triple system is the sum of the accretion rates of the small binary stars.

With our choice of α and H/R the viscous time is approximately 200 binary orbits. We discuss the tests we made on longer integration time in Appendix A.

The main observable to be measured in this work is the accretion rate of each star during the simulation. The accretion rates of the simulations conducted in this work are shown in the first row of Fig. 5.2 and Fig. 5.3. We are not interested in the absolute value of the accretion rates but in their ratio. The ratio between the stellar accretion rates cancel out the decreasing trend shown in Figs. 5.2 and 5.3 because the gas mass distributes with the same proportion between stars, in agreement with what found in Muñoz et al. (2020). In the second row of each mass ratio in Fig. 5.2 and Fig. 5.3 these ratios display a constant trend with an initial transient phase shorter than 20 orbits, showing that differential accretion quickly reaches a steady state.

The accretion rates measured in this work are reported for each orbit, as in Fig. 5.2 and Fig. 5.3. To compute the accretion rates in the n-th orbit we integrate the $\dot{M}(t)$ over the orbital period P, thus

$$\dot{M}_n = \int_{t_n}^{t_n+P} \frac{\dot{M}(t)}{P} \mathrm{d}t, \tag{5.7}$$

where t_n is the initial time of the n-th orbit. We then averaged with a moving average over 11 orbits (i.e. 4 orbits of the cavity inner edge), so that

$$\langle \dot{M}_n \rangle = \frac{\sum_n^{n+10} \dot{M}_i}{11}. \tag{5.8}$$

The ratios between the stellar accretion rates with their errors (as in Fig. 5.4) are computed discarding the initial transient orbits.

5.2 Numerical results

5.2.1 Binary systems differential accretion

The ratio between the stellar accretion rates is the key observable in the binary systems differential accretion problem. Let us define this factor as:

$$\lambda_\mathrm{b} = \frac{\dot{M}_\mathrm{b,sec}}{\dot{M}_\mathrm{b,pri}}, \tag{5.9}$$

where $\dot{M}_\mathrm{b,sec}$ and $\dot{M}_\mathrm{b,pri}$ are the moving averaged accretion rates of the secondary and primary star, respectively (defined in Eq. (5.8)). The λ_b ratio measures how evenly the accreting mass distributes over the binary stars. If λ_b is larger than unity, this means more material is being accreted by the secondary. We simulate three binary systems (with $q_\mathrm{wide} = 0.2, 0.4, 0.65$, simulations $b2, b4, b65$) in order to consistently compare the hierarchical triple simulations with their binary counterparts. Fig. 5.4 shows with green dots the λ factors measured in our Set 1 of 3D SPH binary simulations.

The λ_b factor depends on the parameters of the system. In particular λ_b depends on the mass ratio of the binary, as pointed out by Farris et al. (2014). In addition, λ_b depends also on the infalling gas properties (Young et al. 2015; Young & Clarke 2015). For a given mass ratio, warmer discs raise the primary accretion rate, pushing λ_b towards unity. This is due to the fact that warmer gas streamers have a wider range of trajectories to reach the primary star. In addition, warmer gas around the secondary star crosses the Roche lobe more easily, reaching the primary Roche lobe. Last, Duffell et al. (2020) showed that

$\lambda_{\rm b}$ depends also on gas viscosity. In particular, they found that for less viscous discs the value of $\lambda_{\rm b}$ tends towards unity.

Recently two parametrisations for $\lambda_{\rm b}(q)$ were proposed. The first one in Kelley et al. (2019) (hereafter K19 parametrisation), that updates the one proposed by Gerosa et al. (2015) and is built by fitting the Farris et al. (2014) binary simulation set. The second one in Duffell et al. (2020) (hereafter D20 parametrisation), who simulate binary accretion discs slowly modifying the binary mass ratio during the simulation in order to span $\lambda_{\rm b}(q)$ continuously. These works, based on different 2D grid numerical techniques, resulted in two different parametrisations (see green curves in Fig. 5.4). In order to be able to compare our binary simulations with the D20 and K19 parametrisations, we used the same disc thickness and viscosity of previous works, even if higher than the typical protostellar disc viscosity (Hartmann et al. 1998; Dullemond et al. 2018).

As shown in Fig. 5.4, our binary simulations are in fairly good agreement with the parametrisations proposed in the literature. In particular, we found the same accretions trends described by previous works. Indeed, the secondary star always accretes most of the mass. Moreover, the higher the binary mass ratio, the lower the value of $\lambda_{\rm b}$ (as expected). In addition, if we reduce the thickness of our disc, $\lambda_{\rm b}$ tends to the D20 parametrisation. The discrepancies can be due to the different numerical technique we used. In particular, our simulations are 3D as opposed to the 2D ones by Duffell et al. (2020) and Farris et al. (2014), and the disc height profile could vary between simulations away from the inner cavity edge.

We fit our binary data points with the following one-parameter function:

$$\lambda_{\rm b} = C + \frac{1-C}{q_{\rm wide}} \ , \tag{5.10}$$

that accounts for the $q_{\rm wide}^{-1}$ dependency found in previous studies (Gerosa et al. 2015; Duffell et al. 2020) and that approaches unity when $q_{\rm wide}$ approaches unity. Indeed, for symmetry reasons we expect a unitary mass ratio binary to evenly accrete mass onto the two binary stars. Our best fit for the C parameter results in $C = 0.63$. Contrary to K19 and D20 parametrisations, our formula is obtained from a set of 3D simulations and it is shown in Fig. 5.4 (green solid curve).

5.2.2 Hierarchical triples differential accretion

For a quantitative comparison with the $\lambda_{\rm b}$ factor measured in binaries, we introduce an analogous ratio for hierarchical triples: $\lambda_{\rm t}$. If the small binary of the triple system is lighter than the single body (i.e. in the ts type triples) we define $\lambda_{\rm t}$ as the ratio between the sum of the accretion rates of the small binary stars ($\dot{M}_{\rm t,sec1} + \dot{M}_{\rm t,sec2}$) over the accretion rate of the single star ($\dot{M}_{\rm t,pri}$):

$$\lambda_{\rm t} = \frac{\dot{M}_{\rm t,sec1} + \dot{M}_{\rm t,sec2}}{\dot{M}_{\rm t,pri}}. \tag{5.11}$$

If instead the small binary is heavier than the single body (i.e. in the tp triple case) we define $\lambda_{\rm t}$ as the ratio between the accretion rate of the single star ($\dot{M}_{\rm t,sec}$) over the sum of the accretion rates of the small binary stars ($\dot{M}_{\rm t,pri1} + \dot{M}_{\rm t,pri2}$):

$$\lambda_{\rm t} = \frac{\dot{M}_{\rm t,sec}}{\dot{M}_{\rm t,pri1} + \dot{M}_{\rm t,pri2}}. \tag{5.12}$$

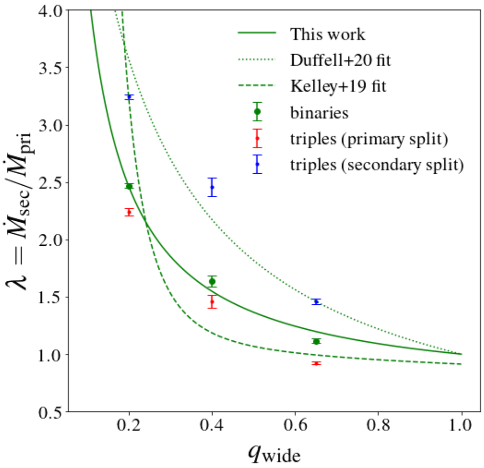

Figure 5.4: Set 1 simulations $\lambda = \dot{M}_{\rm sec}/\dot{M}_{\rm pri}$ values. Green dots are binary simulations. Red dots are triples obtained by splitting the primary star of the binary. Blue dots are triples obtained by splitting the secondary star. The solid green curve is the fit proposed in this work in Eq. (5.10). Dotted and dashed green curves are the Duffell et al. (2020) and Kelley et al. (2019) parametrisations, respectively.

In other words, the $\lambda_{\rm t}$ factor of a hierarchical triple system is defined considering the system as a binary in which the small binary is treated as a single body, with an accretion rate equal to the sum of the accretion rate of the small binary stars.

Accordingly, we define $q_{\rm wide}$ (the mass ratio of the wide orbit) for the ts and the tp triples case. In the former case we define

$$q_{\rm wide} = \frac{M_{\rm t,sec1} + M_{\rm t,sec2}}{M_{\rm t,pri}}, \tag{5.13}$$

where $M_{\rm t,sec1}$ and $M_{\rm t,sec2}$ are the mass of the small binary primary and secondary respectively, and $M_{\rm t,pri}$ is the mass of the single body. In the latter case we define

$$q_{\rm wide} = \frac{M_{\rm t,sec}}{M_{\rm t,pri1} + M_{\rm t,pri2}}, \tag{5.14}$$

where $M_{\rm t,pri1}$ and $M_{\rm t,pri2}$ are the mass of the small binary primary and secondary respectively, and $M_{\rm t,sec}$ is the mass of the single body. In Fig. 5.4 we show, for each $q_{\rm wide}$ in Set 1, the $\lambda_{\rm t}$ factors of the triple simulations, along with the $\lambda_{\rm b}$ factor of their associated binaries.

The differential accretion in hierarchical triple is set by the combination between the binary differential accretion and the effects induced by the presence of the small binary. Thus, in order to isolate the contributions of the small binary to differential accretion we compared each hierarchical triple simulations with their associated binary. In order to do this, we associated to each binary system discussed in Sec. 5.2.1 (i.e. each b simulation) two hierarchical triple systems, obtaining the nine simulations of Set 1 (see Tab. 5.1). The two associated triples are built by substituting the primary or the secondary binary star with a small binary, obtaining, respectively, the tp and ts triple simulations (refer to Section 2.3 for the details on how we implemented this substitution in the PHANTOM code). The triple obtained by splitting the secondary star can be viewed as a massive body orbited by a lighter binary (ts type). If instead the primary is split, the system consists of a massive binary orbited by a third lighter body (tp type). The substituting small binary is circular, has a mass ratio $q_{\rm small} = 1$ and has a semi-major axis $a_{\rm small} = 0.1\,a_{\rm wide}$, where $a_{\rm wide}$ is the semi-major axis of the wide binary orbit. The mass of the substituting small binary is equal to the substituted star. With this process we built up the simulation Set 1, discussed in Sec. 5.1.

As shown in Fig. 5.4, in the parameter space region explored by this simulation set, ts and tp simulations raise their small binary accretion rate with respect to their single counterpart in the associated binary system. As a consequence, ts simulations raise their λ value while tp simulations lower it. In addition, ts triples shift λ more than tp triples. In Fig. 5.2 and Fig. 5.3 we report the accretion rates and λ factors of every simulation of this work. The binary (solid curve) and the $a_{\rm small} = 1$ au ts and tp simulations (dashed curves) show how the accretion rates of the single stars contribute in shifting the λ factors. From the single accretion rates data, we see that the small binary always increases its accretion rate while the tertiary star lowers it. However, the split affects the single star only for lower mass ratios. Indeed, in the $q_{\rm wide} = 0.65$ case the accretion rate of the single body does not change significantly. This implies that the total accretion rate of the $q = 0.65$ triple systems is not conserved with respect to the binary case. Given that the total accretion rate of the system is set by viscous accretion, it should not be different for different stellar systems surrounded by the same disc. Thus, we conclude that the $q_{\rm wide} = 0.65$ systems have not reached steady-state. However, we show in Appendix A that 100 outer binary orbits are enough to measure λ factors in reliable manner.

5.2.3 Dependency on $a_{\rm small}$ and prescription for accretion rate deviations in triples

How much accretion rates deviate from the binary case depends on the orbital configuration of the hierarchical triple, in particular on its small binary mass $M_{\rm b}$ and on its small binary semi-major axis $a_{\rm small}$. Indeed, Figs. 5.5 and 5.6 show how much the triple $\lambda_{\rm t}$ factor deviates from the associated binary $\lambda_{\rm b}$ factor as a function of $a_{\rm small}$ for Set 2 (ts type triples, see Sec. 5.1) and Set 3 simulation (tp type triples, see Sec. 5.1), respectively.

The change in the accretion rate of a multiple system star is linked to a variation of the net flux of mass in its Roche lobe. Indeed, in the steady state regime all the mass that enters the Roche lobe is eventually accreted by the star(s) inside the lobe. This implies that the mechanisms that modify the accretion rate of a body have to act on the scale of its Roche lobe. Two physics phenomena can be invoked in order to describe these deviations: the augmented geometrical cross-setion of the small binary and the angular momentum exchange between the small binary and the surrounding gas.

On the one hand the small binary interacts with the surrounding gas through a geometrical cross-setion that is proportional to the area of the small binary orbit A,

$$A \propto a_{\rm small}^2. \tag{5.15}$$

Thus, we expect that the larger geometrical cross-setion of the small binary raises its accretion rate with respect to the corresponding single star in the associated binary system.

On the other hand, we expect the small binary torque onto the surrounding gas to obstruct the accretion of material onto the small binary stars. In the impulse approximation (Lin & Papaloizou 1979b) we can estimate the torque exerted by the small binary onto the surrounding gas. If we suppose the small binary mass ratio $q_{\rm small} \ll 1$, the density of tidal torque exerted by the small binary onto a fluid element at distance p from the

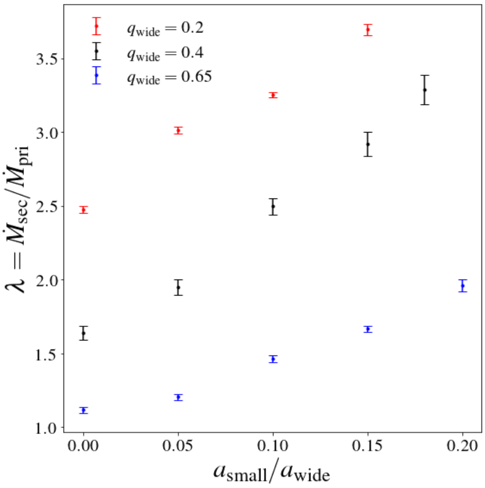

Figure 5.5: $\lambda = \dot{M}_{\rm sec}/\dot{M}_{\rm pri}$ factors for Set 2 triples. Different colours refer to different mass ratio of the wide orbit $q_{\rm wide}$. $a_{\rm small}/a_{\rm wide} = 0$ points are the associated binary simulations.

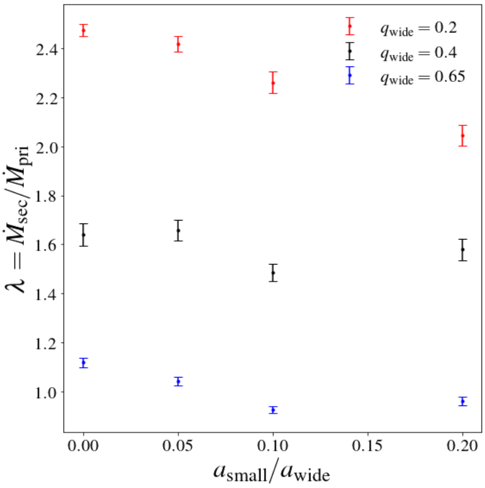

Figure 5.6: $\lambda = \dot{M}_{\rm sec}/\dot{M}_{\rm pri}$ factors for Set 3 triples. Different colours refer to different mass ratio of the wide orbit $q_{\rm wide}$. $a_{\rm small}/a_{\rm wide} = 0$ points are the associated binary simulations.

secondary star can be approximated by

$$\tau = f q_{\rm small}^2 \Omega_{\rm small}^2 a_{\rm small}^2 \left(\frac{a_{\rm small}}{p} \right)^4 , \tag{5.16}$$

where $\Omega_{\rm small}$ is the small binary frequency and f is a dimensionless normalisation factor. Even if this approximation holds for low mass ratio binaries only, it gives us insights about how the specific torque scales with the small binary properties. We can assume that p is approximately equal to distance between the inner binary stars and the small binary Roche lobe edge, thus $p \propto R_{\rm Roche}$. Hence, writing explicitly the binary frequency in Eq. (5.16) we obtain

$$\tau \propto M_{\rm b} \frac{a_{\rm small}^3}{R_{\rm Roche}^4}, \tag{5.17}$$

where $M_{\rm b}$ is the small binary mass.

Taking into account the torque scaling and the geometrical cross-setion, we propose a parametrisation to describe the competition between these mechanisms in modifying the accretion rate of the triple small binary with respect to the corresponding single star in the associated binary system. With this prescription we also test the relative efficiency of different contributions to the deviations. Deviations are measured by means of the accretion ratio between the accretion rate of the small binary in the triple ($\dot{M}_{\rm t,sec} = \dot{M}_{\rm t,sec1} + \dot{M}_{\rm t,sec2}$) over the accretion rate of the corresponding binary star ($\dot{M}_{\rm b,sec}$). We then fit the accretion ratios with the following prescription:

$$\frac{\dot{M}_{\rm t,sec}}{\dot{M}_{\rm b,sec}} = 1 + \Gamma_\tau \frac{(a_{\rm small}/a_{\rm wide})^3}{(R_{\rm Roche}/a_{\rm wide})^4} + \Gamma_{\rm A} \left(\frac{a_{\rm small}}{a_{\rm wide}} \right)^2 , \tag{5.18}$$

where Γ_τ and $\Gamma_{\rm A}$ are parameters to be fitted and relate to the torque and the geometrical cross-setion, respectively. In Eq. (5.18) we assume the geometrical term to scale with the small binary cross-setion ($\propto a_{\rm small}^2$), and the torque term to scale as in Eq. (5.17) ($\propto a_{\rm small}^3/R_{\rm Roche}^4$). We thus expect that for small semi-major axis the cross-setion contribution to the accretion rate will dominate the accretion. Meanwhile, for wide semi-major axis the torque term will be more relevant. In addition, we expect that the torque parameter Γ_τ will be proportional to the small binary mass (as in Eq. (5.17)), while the geometrical cross-setion will depend only on the geometry of the orbits and not on the mass. However, the efficiency of each term depends on Γ_τ and $\Gamma_{\rm A}$.

5.2.3.1 Secondary split accretion ratios

In order to test the parametrisation for the accretion rate deviation due to the splitting, we simulate a second set of hierarchical triples. The aim of this set is to explore different regimes for the accretion ratio varying the semi-major axis of the small binary.

We started from the ts triples of Set 1 (with $a_{\rm small} = 1$ au) and we simulated the same ts hierarchical triple but with a semi-major axis of the small binary of $a_{\rm small} = 0.5$ and 1.5 au. We also exploited the wider stable range of semi-major axis for high $q_{\rm wide}$ hierarchical triples (Mardling & Aarseth 2001) in order to simulate even wider small binaries for $q_{\rm wide} = 0.4$ (for which we also simulate $a_{\rm small} = 1.8$ au) and 0.65 systems (with $a_{\rm small} = 2$ au). The accretion rates of this simulation set (called Set 2, see Sec. 5.1) are plotted in Fig. 5.2 and their average $\lambda_{\rm t}$ factors are reported in Fig. 5.5.

In order to apply the prescription in Eq. (5.18), we compute the ratio between the accretion rate of the small binary ($\dot{M}_{\rm t,sec}$) over the accretion rate of the secondary star

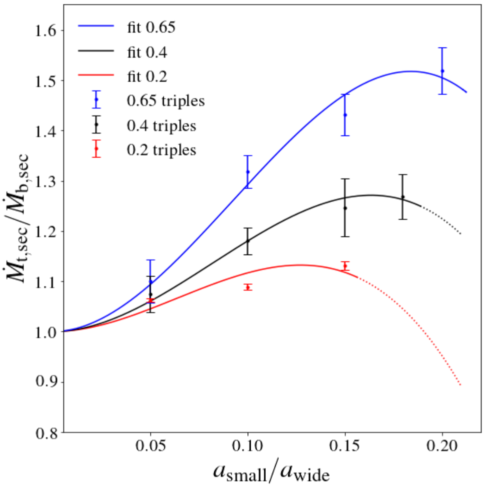

Figure 5.7: Set 2 deviations in the small binary accretion rate as a function of the small binary semi-major axis. These simulations are obtained by splitting the secondary star of the three binaries of Set 1. The dots are the ratios between the accretion rate of the small binary ($\dot{M}_{\mathrm{t,sec}}$) and the accretion rate of the secondary star in the associated binary system ($\dot{M}_{\mathrm{b,sec}}$). The curves are obtained by fitting the three parameters of our prescription (Eq. (5.18)) for each mass ratio of the wide orbit (0.2, 0.4, 0.65 for red, black and blue curves respectively). The dotted part of each curve denotes the semi-major axes range for which the hierarchical triples are unstable.

in the associated binary system ($\dot{M}_{\mathrm{b,sec}}$). When the repulsing effect of the binary torque contributes more than the geometrical cross-section to the accretion rate deviation, we expect this accretion ratio to be less than one. On the contrary, when the cross-section dominates, the ratio will be larger than one. Fig. 5.7 shows $\dot{M}_{\mathrm{t,sec}}/\dot{M}_{\mathrm{b,sec}}$ varying the small binary semi-major axis.

Widening the inner binary, each q_{wide} data set in Fig. 5.7 follows a similar trend: a steep raise for smaller small binary semi-major axes, followed by lower deviations for larger small binary semi-major axes. Accretion ratios clearly depend on q_{wide}, that in turn depends on the small binary mass. Indeed, for a given small binary semi-major axis, more massive small binaries systematically correspond to higher deviations in the accretion rate. Thus, the extent of the deviation depends on the split star mass. In the explored semi-major axes range, the accretion ratios are always higher than unity. Thus, the geometrical cross-section contribution to the deviation is greater than the torque contribution in each triple we considered.

In order to study how Γ_τ and Γ_{A} depend on the small binary mass, we separately fit the data point of each mass ratio (i.e. the blue, black and red points in Fig. 5.7) with the prescription in Eq. (5.18). We thus obtain for each mass ratio the values of Γ_τ and Γ_{A} that best fit our data. These values are plotted in Fig. 5.8. The parameter Γ_τ scales linearly with the small binary mass M_{b}, as expected from Eq. (5.17). Also Γ_{A} depends on the small binary mass, in contrast with what we expect from a purely geometric cross-section. The dependency of Γ_{A} on M_{b} can be due to a gravitational focusing effect. Indeed, without gravitational focusing, gas with an impact parameter higher than a_{small} skips the small binary geometric cross-section. On the contrary, in the gravitationally

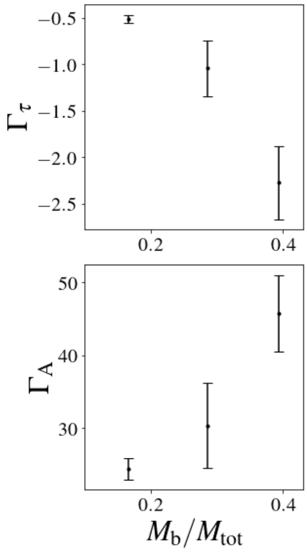

Figure 5.8: Best fit Γ parameters for our prescription (Eq. (5.18)) as a function of the small binary mass. M_b and M_tot are the mass of the inner binary and of the system, respectively.

focused limit, gas with an impact parameter higher than a_small can enter the cross-section of the small binary. This is because the relative velocity between the gas and the binary is lower than the escape velocity from it. In this limit, more massive binaries have a larger effective cross-section, as noticed in the plot.

5.2.3.2 Primary split accretion ratios

We study how the accretion rate varies as a function of the orbital parameters of the triple when splitting the primary star. Primary and secondary stars are expected to accrete gas from the disc inner edge in different ways. On the one hand, the secondary has access to the gas stored in the disc mainly by pulling streamers directly from the inner edge. These streamers fill the secondary star Roche lobe (and to a lesser extent the cavity) with gas, allowing gas to fall onto the secondary star. On the other hand, the primary star pulls less massive streamers than the secondary, particularly for low mass ratios. Thus, the primary provides less gas directly from the disc, resulting in lower accretion rates. Another viable way for gas to reach the primary star is by means of the L1 point between the Roche lobes of the two binary stars. The more gas crosses the L1 point towards the primary, the higher its accretion rate at the expenses of the secondary star. As said, in hotter discs the accretion rate of the two stars are more even also thanks to this gas exchange (Young et al. 2015).

Raising the mass ratio q_wide, these differences level out and the primary becomes more and more independent from the secondary in filling its Roche lobe with gas. As a result, the closer q_wide is to unity, the more the primary and secondary star accrete mass in a similar way. On the contrary, away from $q_\mathrm{wide} = 1$ we expect the primary to be in a gas-poor environment, which prevents it from efficiently accreting mass. We expect these differences to result in different differential accretion deviations when splitting the primary star, rather than the secondary. Indeed, the split of the primary can either raise the mass that crosses L1 or raise the mass that falls onto the small binary from the inner edge. Thus, we tested the primary split configurations in Set 3.

In Set 3, we simulate a set of tp hierarchical triples, based on the tp simulations of Set 1 (with $a_{\rm small} = 1$ au), varying the small binary semi-major axis ($a_{\rm small} = 0.5, 2$ au, see Sec. 5.1). Fig. 5.3 shows the accretion rates of Set 3 simulations and Fig. 5.6 shows their average $\lambda_{\rm t}$ factors.

The greater λ factor deviations are observed in the $q_{\rm wide} = 0.2$ systems (Fig. 5.6). The deviations are due to an enhanced flow through the L1 point, indeed, as shown in Fig. 5.3, the raise in the accretion rate of the small binary is at the expenses of the accretion rate of the third body. Fig. 5.6 also shows that wider small binaries more easily capture mass from the third body Roche lobe, further reducing their λ factor.

Hierarchical triples with $q_{\rm wide} = 0.4$ and 0.65 show smaller or no deviations due to the splitting. Indeed, in Fig. 5.2 their λ factors reduce up to 0.9 times the binary λ factor. Thus, for higher mass ratios of the outer orbit the small binary is less efficient in stealing mass from the third body Roche lobe. In addition, and contrary to the $q_{\rm wide} = 0.2$ case, wider small binary semi-major axes affect the deviations in λ only modestly, as the impact of the geometrical cross-section is limited by the availability of mass in the surrounding of the small binary.

In light of this, the deviation observed in triples obtained by splitting the primary star cannot be captured by the effects described in Eq. (5.18). In Fig. 5.9 we show the ratios between the accretion rate of the small binary over the accretion rate of its single counterpart in the associated binary system. Only for high $q_{\rm wide}$ we recover the trend observed in Fig. 5.7, as the small binary starts to accrete more similarly to the secondary star of a binary, for which Eq. (5.18) holds.

It is important to notice that the accretion rate of primaries and tp triples small binaries are not fully resolved (as discussed in Appendix A). Thus, the numerical results of this section have to be treated with caution. These results are still relevant as we report the *relative* deviations due to the splitting measured for different choices of orbital parameters and we never rely on the absolute values that we measure in our simulations.

5.3 Accretion in hierarchical triple systems

5.3.1 Deviations of triple differential accretion from the associated binary system

We have shown that hierarchical triples embedded in accretion discs have a peculiar way to distribute disc mass between the stars of the system. The ground state of differential accretion in hierarchical triples is based on the binary dynamics. Indeed, to a first approximation the wide orbit of the hierarchical triple mimics a binary system and it accretes mass in the same way, favouring the lighter body of the system. However, at smaller scales the influence of the triple system small binary has to be taken into account. The small binary-gas interaction changes the accretion rates of the three stars in relative terms (changing the proportion in which mass distributes among the stars, as shown in Fig. 5.4). Having a larger geometrical cross-setion, the small binary increases its accretion rate. This geometrical mechanism competes with the tendency of the small binary gravitational torque to repel the surrounding gas out of its Roche lobe. This competition gives the peculiar shape of the deviations in the accretion rate of the small binary as a function of its semi-major axis, as shown in Figs. 5.7 and 5.8.

This mechanism generally shifts the triple system $\lambda_{\rm t}$ factor in favour of the small binary. However, how much $\lambda_{\rm t}$ deviates from the associated binary $\lambda_{\rm b}$ factor depends also on the mass ratio of the triple system wide orbit ($q_{\rm wide}$). Indeed, lower mass ratios

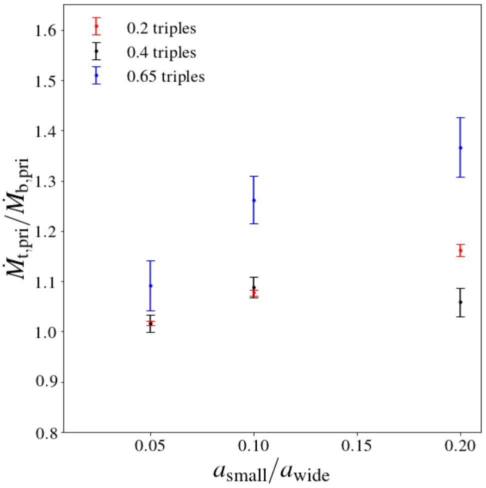

Figure 5.9: Set 3 deviations in the small binary accretion rate as a function of the small binary semi-major axis. These simulation are obtained by splitting the primary star of the three binaries of Set 1. The dots are the ratio between the accretion rate of the small binary ($\dot{M}_{\rm t,pri} = \dot{M}_{\rm t,pri1} + \dot{M}_{\rm t,pri2}$) and the accretion rate of the primary star in the associated binary system ($\dot{M}_{\rm b,pri}$).

show higher deviations from the associated binary, both when the small binary is lighter or heavier than the third body. Moreover, the triples obtained by splitting the secondary star of a binary result in higher deviations, compared to triples obtained by splitting the primary star (see Sec. 5.2.3.2).

5.3.2 Differential accretion in hierarchical triples

The main consequence of differential accretion in binary systems is a tendency to equalise system masses. Indeed, as discussed in previous works (Farris et al. 2014; Kelley et al. 2019; Duffell et al. 2020), with enough mass at disposal the higher accretion rate of the secondary star pushes the mass ratio of the system towards unity.

In this work we found that a hierarchical triple system in which the small binary is lighter than the third body raises the wide binary mass ratio $q_{\rm wide}$ more effectively than its associated binary system. Indeed, in the parameter space explored, the hierarchical triple $\lambda_{\rm t}$ factor (defined in Eq. (5.11)) is higher than the $\lambda_{\rm b}$ factor of its associated binary (defined in Eq. (5.9)).

For a quantitative comparison, the $q_{\rm wide} = 0.65$ configuration (the one with the lowest $\lambda_{\rm t}$ among Set 1) has a $\lambda_{\rm t} \approx 1.3\lambda_{\rm b}$, when splitting the secondary star of the associated binary. Even if we account only for the mass equalisation due to the triple mechanism (i.e. if we consider $\lambda_{\rm b} = 1$) we found that the small binary accretion rate is 1.3 times higher than the primary one. The binary differential accretion mechanism alone allows to obtain such a disequilibrium in the accretion rates only for q_B lower than 0.35 or 0.75 for Kelley et al. (2019) and Duffell et al. (2020) parametrisations (respectively), as shown in Fig. 5.4. For wider small binary semi-major axes or lower wide orbit mass ratios, the triple differential accretion mechanism is even more efficient. In addition, the disequilibrium between the stellar accretion rates in triples is at play even if $q_{\rm wide} \approx 1$, where binary differential accretion is turned off.

We also remind that binary prescriptions strongly depend on the circum-binary gas properties and we do not know how they behave in actual protostellar discs conditions. On the contrary, we showed that the larger than unity $\lambda_\mathrm{t}/\lambda_\mathrm{b}$ ratio is due to the increased cross-setion of the small binary, which solely depends on the geometry of the orbits. Thus, we expect this ratio to be independent of the disc conditions. This difference is important because Duffell et al. (2020) showed that binary differential accretion is turned off in low viscosity regimes, where they found $\lambda \approx 1$ independently of the mass ratio. If this result is confirmed, we expect binary differential accretion to be turned off for low viscosity protostellar discs. But, if the larger than unity $\lambda_\mathrm{t}/\lambda_\mathrm{b}$ ratio is preserved (as we expect), the differential accretion in hierarchical triples constitutes the only viable mechanism to equalise the stellar masses.

Assuming $\lambda_\mathrm{b} = 1$, as in protostellar disc condition independently of q (Duffell et al. 2020) or as in more viscous discs around high q systems, we can explicitly study the evolution of q with time in the binary and in the hierarchical triple case. Under the approximation of a constant accretion rate (e.g. due to an infall that replenishes the outer part of the disc) we obtain the following differential equation for q:

$$\frac{\mathrm{d}q}{\mathrm{d}t_\mathrm{acc}} = \frac{q+1}{\lambda(q)+1}\left(\lambda(q) - q\right), \tag{5.19}$$

where $t_\mathrm{acc} = (\dot{M}_\mathrm{tot}/M_\mathrm{tot})t$ is the time in unit of the mass doubling time of the system, with $\dot{M}_\mathrm{tot}$ and M_tot the total system accretion rate and mass respectively. Solving Eq. (5.19) we obtain the times needed by a hierarchical triple and by a binary (τ_t and τ_b, respectively) in order to reach a given wide orbit mass ratio q_wide starting from the same initial mass ratios q_0. Fig. 5.10 shows $\tau_\mathrm{t}/\tau_\mathrm{b}$ as a function of the final wide orbit mass ratio q_wide for three different initial mass ratio q_0. We assume $\lambda(q_\mathrm{wide}) = 1$ for binaries and $\lambda(q_\mathrm{wide}) = 1.3$ for triples, that is the triple λ factor we expect from the $\lambda_\mathrm{t}/\lambda_\mathrm{b}$ ratio measured in our simulations, as discussed in the previous paragraphs. The equalising time for hierarchical triples (i.e. the time needed to reach $\lambda(q_\mathrm{wide}) = 1$) is nearly an order of magnitude lower than the binary equalising time, in particular for high q_wide systems.

A more subtle difference between the two mechanisms is the final equilibrium point of the wide orbit mass ratio q_wide. Indeed, from Eq. (5.19) we see that the equilibrium point for q_wide is at $q_\mathrm{wide} = \lambda$. Thus, because i) binary differential accretion prescriptions tends to unity for increasing q_wide and ii) symmetry reasons suggest that an equal mass binary has $\lambda_\mathrm{b} = 1$, binaries stall at mass ratio $q_\mathrm{wide} = 1$. Conversely, for a triple with a small binary heavier than the single body, we expect a λ_t lower than unity due to the raise in the small binary accretion rate. Thus, hierarchical triple systems stall at a mass ratio q_wide smaller than unity as well. The extent of this equilibrium shift depends on the specific orbital parameters of the system, which are responsible of the the shift in λ_t. This work suggests an equilibrium point for triple systems of $q_\mathrm{wide} \approx 0.9$. Indeed, $\lambda_\mathrm{t}/\lambda_\mathrm{b}$ measured in our triple systems with small binary heavier than the single star is approximately 0.9. Thus, we expect that around $q_\mathrm{wide} = 1$, where $\lambda_\mathrm{b} \approx 1$ as well, $\lambda_\mathrm{t} = 0.9$.

5.3.3 Multiplicity signatures in differential accretion

In principle, with a perfect knowledge of binary differential accretion and of its dependency on the binary mass ratio q_wide, on the gas viscosity and temperature, we could be able to infer from an observed λ_b in a binary system the presence of an unresolved small binary. Indeed, in case of binary accretion rates not in line with the binary theory, we

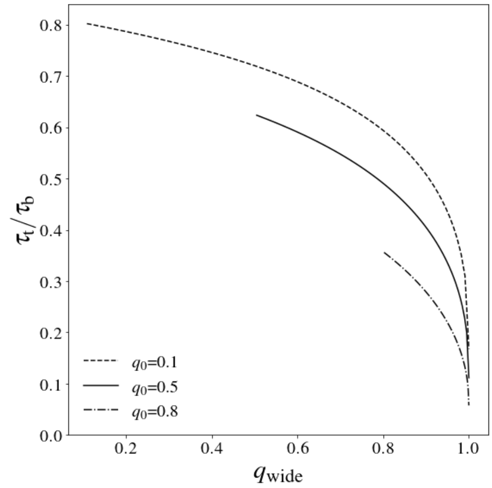

Figure 5.10: Ratio of the times needed in order to reach a certain $q_{\rm wide}$ by a triple ($\tau_{\rm t}$) and by a binary ($\tau_{\rm b}$). Different curves refer to different initial mass ratios q_0. Curves are obtained by solving Eq. (5.19) with $\lambda(q_{\rm wide}) = 1$ for binaries and $\lambda(q_{\rm wide}) = 1.3$ for triples.

could invert the relation proposed in Eq. (5.18) in order to obtain the $a_{\rm small}$ of a possible unresolved small binary. However, up to now binary prescriptions do not take into account dependencies other than $q_{\rm wide}$[2].

In addition, the disc conditions explored in this work (and in the main works on this topic in the literature) are halfway between the compact object accretion discs (that are thinner than the aspect ratio used) and protoplanetary discs (that are orders of magnitude less viscous), and thus do not represent either cases. Moreover, we limited our investigation to: i) circular wide and small binary orbits, ii) to equal masses small binaries and iii) to coplanar configurations. This allowed us to simplify the problem and observe the specific signatures of the geometrical and torque effects described in this work.

We expect the mechanism proposed in this work to be at play in more complex configurations as well. However, its efficiency will be surely affected. This is mainly due to the dependency of both the accretion rate and the small binary torque on the orbital parameters of a given multiple system. In particular, the eccentricity and the mutual inclinations between the orbital planes and the discs are likely to play a major role since they can induced tilt oscillations and precession, which would translate into phase-dependent accretion rates along the orbit. A known example of a system where an highly eccentric binary shows phase-modulated accretion rates is discussed in Dunhill et al. (2015), where they show that for a limited amount of time it is possible for the primary to accrete more mass than the secondary.

Given these limitations, the only remaining case that at the moment could highlight an unresolved small binary in an accreting binary system is a system where a $\lambda < 1$ is observed. In that case no binary configuration can reproduce this behaviour (except with an high eccentricity) and the only explanation that can be addressed to solve the puzzle

---

[2] Although in Young & Clarke (2015) a trend related to temperature is suggested, further studies are needed to constrain an effective parametrisation.

should be a massive unresolved small binary, whose geometrical cross-setion counterbalances the tendency of binary differential accretion to favour the secondary single star. However, in our simulations even such configurations hardly push under 1 the ratio between the accretion rates, as can be seen in Fig. 5.3 and discussed in Sec. 5.2.3.2. Although in principle this should be possible for mass ratios greater than the ones explored in this work, the parameter space region where significant signatures of an hidden small binary could appear remains small.

Thus, the goal to exploit the deviation of the observed $\lambda_{\rm t}$ in a triple system from the $\lambda_{\rm b}$ expected in its associated binary system is complicated by these additional dependencies and at the moment we cannot disentangle deviations due to different mechanisms, that change λ without the need to invoke an higher multiplicity.

5.4 Conclusions

In this chapter we presented hydrodynamical simulations of discs in hierarchical triple systems. We focus on the accretion process from the circum-triple disc onto the individual stars of the system. In particular, we studied how the presence of the small binary affects the accretion rates of the individual stars.

We performed a set of simulations in order to span different hierarchical triple system configurations using the SPH code PHANTOM. We proposed a semi-analytical prescription (given by Eq. (5.18)) able to describe the data we obtained in our simulations.

Our main findings are the following:

1. Differential accretion in hierarchical triple systems can be explained by the interplay between two contrasting mechanisms: 1) the increased geometrical cross-setion between gas and small binary, and 2) its angular momentum exchange with it. These two mechanisms are superimposed on the binary differential accretion process.

2. The small binary torque is too weak to counterbalance the increased accretion rate of the small binary due to the larger cross-section, except for very wide small binary semi-major axes ($a_{\rm small}$) that result in unstable hierarchical triples. Thus, in the vast majority of the stable hierarchical triple parameters space the small binary accretes more mass than if it would be a single star of the same mass. As a result, if the hierarchical triple small binary is heavier than the third body, the standard differential accretion scenario (whereby the secondary accretes more of the mass) is hampered. Reciprocally, if the small binary is lighter than the third body, the standard differential accretion scenario is enhanced.

3. Hierarchical triple systems with a small binary lighter than the single star equalise their masses nearly an order of magnitude quicker than binary systems. Conversely, in triples with a small binary heavier than the single star mass equalisation is slowed down. In contrast with binaries, the equilibrium mass ratio for triple systems is lower than 1.

In conclusion, the mass ratio in accreting hierarchical triple stellar systems evolves differently compared to binaries. These differences, during the disc lifetime, are expected to produce characteristic mass ratio distributions, which could possibly be observed through ongoing and future surveys. Further observational data will help to test and further constrain the proposed accretion model for triple stellar systems. At any rate, the orbital parameters and initial masses play a crucial role in determining the final stellar mass ratios in high-order multiple stellar systems.

Part III

Polar alignment in multiple stellar systems

CHAPTER 6

Precession and polar alignment of accretion discs in triple (or multiple) stellar systems

This chapter is based on the paper "Precession and polar alignment of accretion discs in triple (or multiple) stellar systems" by Simone Ceppi, Cristiano Longarini, Giuseppe Lodato, Nicolás Cuello, Stephen H. Lubow, published on Monthly Notices of the Royal Astronomical Society, Volume 520, Issue 4, pp.5817-5827, in April 2023.

Star formation takes place in clustered environments, where pre-stellar objects dynamically interact with each other, forming the seeds of multiple stellar systems (Clarke et al. 2000; Reipurth et al. 2014; Offner et al. 2022). Surveys of star forming environments (McKee & Ostriker 2007), as well as numerical simulations (Bate 2009; Bate et al. 2010; Bate 2018), show that stars form from a sequence of accretion episodes, for which the angular momentum is randomly oriented. In such a scenario, at least some accretion discs are expected to be misaligned to the stellar orbital plane. Recently, observations have confirmed these theoretical predictions (Czekala et al. 2019). For example, the systems GG Tau (Köhler 2011b; Aly et al. 2018; Keppler et al. 2020), KH 15D (Chiang & Murray-Clay 2004; Lodato & Facchini 2013), HD142527 (Casassus et al. 2013; Price et al. 2018a) and GW Ori (Kraus et al. 2020; Bi et al. 2020; Smallwood et al. 2021) exhibit high relative misalignments.

The dynamics of misaligned circumbinary discs dynamics has been actively studied during the last few decades, both theoretically (Papaloizou & Pringle 1983; Papaloizou & Lin 1995; Ogilvie 1999; Bate et al. 2000; Nixon et al. 2012, 2013) and numerically (Facchini et al. 2013; Aly & Lodato 2020). An inclined gas disc around a circular binary tends to precess around the binary angular momentum vector. If the disc sound crossing time is short enough (i.e. the inner part of the disc communicates its precession to the disc outer edge efficiently, Papaloizou & Lin 1995) the disc rigidly precesses with a frequency given by Bate et al. (2000) (see also Lodato & Facchini 2013). In addition, because of viscosity, the disc tends to align to the binary orbital plane, with an alignment timescale that is of the order of the viscous time (Papaloizou & Terquem 1995; Larwood et al. 1996; Bate et al. 2000; Lubow & Ogilvie 2000) eventually reaching the coplanar equilibrium configuration. Also, misalignment in circumbinary discs affects dust dynamics (Longarini et al. 2021; Aly et al. 2021), creating substructures such as rings.

When the binary system is eccentric an additional stable configuration is possible. Aly et al. (2015) and Martin & Lubow (2017) showed that a circumbinary disc around an

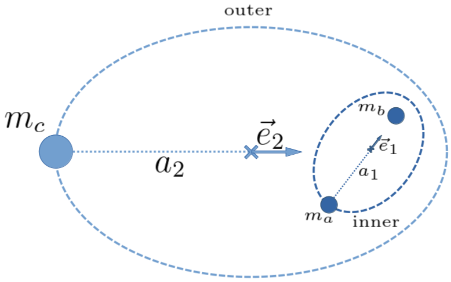

Figure 6.1: Hierarchical triple system sketch (not to scale). Light blue refers to the outer orbit, dark blue to the inner one. Dashed curves, crosses and arrows are the orbit, center of mass and eccentricity vector of the hierarchical level considered.

eccentric binary tends to align its angular momentum vector to the eccentricity vector of the stellar system, leading to a polar configuration. This mechanism happens if the initial inclination is above a critical value, that is a decreasing function of the eccentricity. Polar alignment is likely to occur for high initial inclination, high eccentricity (Martin & Lubow 2018), cold and low mass discs (Martin & Lubow 2019).

Although we would expect to see several accretion discs in a polar configuration, only a few have been observed up to now. One is the disc orbiting HD98800 B (Kennedy et al. 2019). Also, 99 Her is a debris disk in a polar configuration (Kennedy et al. 2012) that likely evolved from a gaseous accretion disc (Smallwood et al. 2020). In addition, recently Kenworthy et al. (2022) showed that the light curve of an eclipse in V773 Tau multiple stellar system can be explained with the presence of a highly inclined disc. Interestingly, HD98800 B (as well as V773) is not a pure binary system (for which the polar alignment theory has been developed), but it resides inside a hierarchical quadruple stellar system. A recent study by Martin et al. (2022) finds that the high multiplicity of HD98800 does not prevent polar alignment of the circumbinary disc.

As in the case of HD98800, young multiple stellar systems often comprise more than two stars arranged in hierarchical configurations (Duchêne & Kraus 2013; Moe & Di Stefano 2017). A hierarchical configuration is made of nested binary orbits in which each semi-major axis is much larger than the semi-major axes of its subsystems. This semi-major axes hierarchy allows an analytic perturbative analysis of the orbital evolution that results in a periodic exchange of angular momentum between the orbits. As a result, hierarchical systems show periodic oscillations in the orbital shape and orientation (Naoz et al. 2013). Given this secular orbital evolution, the possibility of polar discs in systems with more than two stars needs to be further investigated.

In this chapter, we study whether discs in hierarchical systems can align polarly or if they fail to catch up with the secular evolution of the orbit. In section 6.1 we present the analytical framework under which we derive an additional criterion for the possibility of polar alignment of circumbinary discs in hierarchical systems. In Section 6.2 we numerically test the analytical findings of Section 6.1. In Section 6.3 we discuss the results of sections 6.1 and 6.2. We conclude in Section 6.4.

6.1 Polar configuration stability in systems with more than two stars

6.1.1 Disc polar alignment in systems with more than two stars

We describe the orientation of a generic misaligned orbit around a central binary with the tilt angle, β, and the longitude of the ascending node (relative to the eccentricity vector direction), Ω. The β and Ω angles describe the direction of the specific orbital angular momentum vector ($\mathbf{l}$) relative to the central binary angular momentum ($\mathbf{l}_b$) and eccentricity vector ($\mathbf{e}_b$). The frame of reference is defined by the instantaneous direction of the binary angular momentum and eccentricity vector with axes $\mathbf{e}_b$, $\mathbf{e}_b \times \mathbf{l}_b$ and $\mathbf{l}_b$. We define β and Ω via the following relation:

$$\mathbf{l} = (\sin\Omega\sin\beta, \cos\Omega\sin\beta, \cos\beta). \tag{6.1}$$

By virtue of this definition, β is the angle between the circumbinary orbit orbital plane and the binary orbital plane, while Ω is the angle between the direction of the binary eccentricity vector and the circumbinary orbit ascending node. Using these angles, we can describe the orientation of the orbital plane of a third body around a binary, as well as the orientation of a circumbinary accretion disc. In the latter case, β and Ω can be functions of the disc radius R. In the following, we suppose the accretion disc to precess as rigid body, with a tilt and longitude of the ascending node independent of R.

Analytical studies of the restricted three body problem in Farago & Laskar (2010) showed that an inclined test particle orbiting an eccentric binary system undergoes two alternative kinds of precession. In the first kind, the angular momentum vector of the particle precesses around the angular momentum vector of the binary. For a circular orbit binary, this kind of particle orbit, known as a circulating orbit, maintains a constant angle between the particle orbital plane and the binary orbital plane (i.e. a constant tilt β), while the longitude of the ascending node Ω spans 2π with a typical frequency, given for example by Lodato & Facchini (2013) (see their eq. 12). For an eccentric orbit binary, the tilt angle β and nodal precession rate vary in time by an amount that depends on the binary eccentricity (Smallwood et al. 2019). In the second kind of precession, the angular momentum of the particle precesses around the eccentricity vector of the binary. In this case, which is a librating orbit, β oscillates around 90 degrees, while Ω oscillates around a fixed value. The orbit of the test particle belongs to the first or the second kind of orbit depending on the angles β and Ω, and on the eccentricity of the central binary e_{b}. If the tilt of the particle is larger than a critical angle $\beta_{\mathrm{crit}}(e_{\mathrm{b}}, \Omega)$ the particle will precess around the binary eccentricity vector, otherwise around the binary angular momentum vector. For an orbit co-rotating with the central system, the critical angle for polar alignment is[1] (Farago & Laskar 2010; Cuello & Giuppone 2019)

$$\beta_{\mathrm{crit}}(e_{\mathrm{b}}, \Omega) = \arcsin\sqrt{\frac{1-e_{\mathrm{b}}^2}{1-5e_{\mathrm{b}}^2\cos\Omega^2+4e_{\mathrm{b}}^2}}. \tag{6.2}$$

A gaseous disc around an eccentric binary follows a similar evolution, except that, due to viscous dissipation, the orbital plane of the disc decays towards one of the two equilibrium configurations. Orbits precessing around the binary angular momentum tend to become coplanar (aligned with the binary orbital plane), while orbits precessing around the eccentricity vector decay towards a polar configuration (perpendicular to

---

[1] for a counterrotating orbit $\beta_{\mathrm{crit}}(e_{\mathrm{b}}, \Omega) = \pi - \arcsin\sqrt{\frac{1-e_{\mathrm{b}}^2}{1-5e_{\mathrm{b}}^2\cos\Omega^2+4e_{\mathrm{b}}^2}}$

the orbital plane). Disc polar alignment in circumbinary discs has been studied in many previous works both analytically and numerically (e.g. Aly et al. 2015; Martin & Lubow 2019; Lubow & Martin 2018; Cuello & Giuppone 2019; Zanazzi & Lai 2018).

Numerical simulations of the collapse of a molecular cloud show that the stellar and accretion disc formation process is very chaotic. In particular, we expect a randomly distributed initial misalignment between the stellar systems orbital planes and the discs orbiting them (Bate 2018). Also, from analytical investigations we expect no correlation between the disc and the binary initial angular momentum (Toci et al. 2018). Misaligned discs can result also from stellar flybys, which can generate an inclination up to 60° (Xiang-Gruess 2016; Cuello et al. 2023). Thus, even if the conditions for polar alignment should be easily met, up to now we observed only one polarly aligned disc and it orbits around the inner binary of a hierarchical quadruple system (i.e. HD 98800, Kennedy et al. 2019; Zúñiga-Fernández et al. 2021). In addition, the vast majority of observed misaligned discs (particularly highly misaligned ones, that could undergo polar alignment) are found around systems with more than two stars (Czekala et al. 2019).

In general, stable stellar systems with more than two stars are arranged in nested binary orbits in which each semi-major axis is much larger than the semi-major axes of its subsystems. These configurations are called hierarchical and are the only ones that guarantee long-lasting stability to the stellar system. For example, fig. 6.1 sketches a triple system in a hierarchical configuration. Each hierarchical system level can be approximated to zeroth order by a binary system. Doing so, we could study polar alignment of discs around systems with more than two stars with the formalism developed by Lubow & Martin (2018). This crude approximation, however, completely neglects the perturbative term introduced in the gravitational potential by the presence of more than two stars. Taking into account this term means to reduce the hierarchical system to a hierarchical triple system. The exchange of angular momentum between the hierarchical levels of the system triggers further dynamical mechanisms such as Kozai-Lidov oscillations (von Zeipel 1910; Kozai 1962; Lidov 1962; Naoz 2016; Hamers 2021).

In a hierarchical triple system, we can analytically compute the evolution of the binary orbital parameters of both the inner and outer orbit. Due to their mutual torques, we expect these osculating orbital elements to evolve with time on a secular timescale. In particular, the eccentricity vector direction, along which highly inclined discs would like to align their angular momentum, varies with time.

In coplanar hierarchical triple systems, we can analytically compute the precession frequency of the outer and inner orbit eccentricity vector. At the same time, a nearly polar aligned disc has a typical tilt oscillation frequency that is its nodal libration frequency (Lubow & Martin 2018). In the triple case the secular evolution of the orbital parameters shifts the polar orbit position with time, possibly undermining the stability of the polar configuration. In particular, if the nodal libration frequency is not high enough, the disc will not be able to track the evolving stable polar orbit, failing to remain polarly aligned.

In a hierarchical triple system we have two possible accretion discs orbiting a multiple stellar system: the first one orbiting the inner binary of the triple and the second one orbiting the outer orbit of the triple system. In the next sections we discuss the timescales involved in the two cases and the stability of the polar orbit around both the outer (Sec. 6.1.2) and the inner (Sec. 6.1.3) orbit.

6.1.2 Polar alignment in the circum-triple disc

Let us consider a coplanar hierarchical triple as in the sketch of Fig. 6.1. The masses of the inner binary stars are m_a and m_b, for the primary and the secondary respectively,

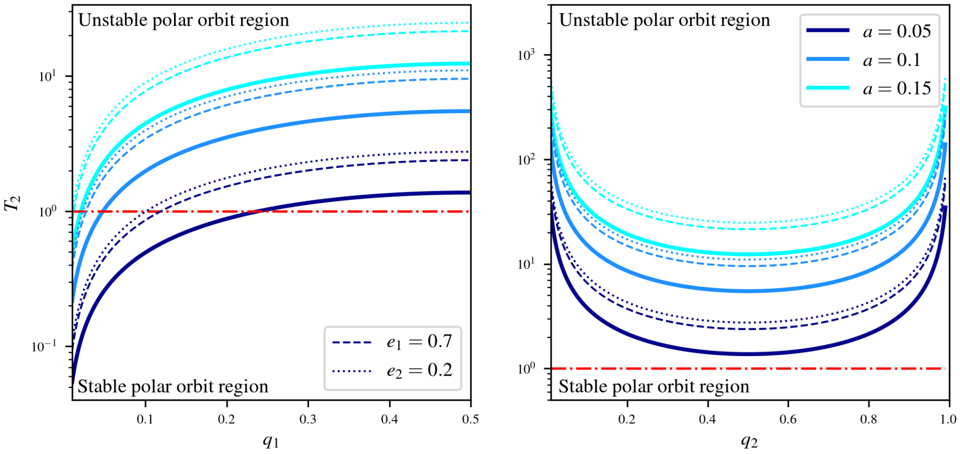

Figure 6.2: Dependency of T_2 (see sec. 6.1.2) on mass ratios, semi-major axes ratio, and eccentricities. When T_2 is smaller than unity (dash dotted red line) polar alignment is possible, conversely for $T_2 > 1$ it is not. On the left panel, T_2 is plotted as a function of the inner binary mass ratio q_1 (fixing q_2 to 0.5), while on the right one as a function of the outer binary mass ratio q_2 (fixing q_1 to 0.5). The thicker lines refer to $e_2 = 0.5$ and $e_1 = 0$. The dotted and dashed lines show how increasing e_1 to 0.7 (fixing $e_2 = 0.5$) and lowering e_2 to 0.2 (fixing $e_1 = 0$) affect T_2, respectively. Different colors refer to different semi-major axes ratios.

while m_c is the mass of the external third body. In addition, we define q_1, e_1, a_1 and Ω_1 (q_2, e_2, a_2 and Ω_2) the mass ratio, eccentricity, semi-major axis, and Keplerian frequency of the inner (outer) orbit. To zeroth order, the outer orbit of the triple is equivalent to the orbit of its associated binary, defined as the binary composed of m_c and a single star of mass $m_a + m_b$ placed in the inner binary centre of mass. Thus, instantaneously, m_c orbits the centre of mass of the inner binary along the same orbit as the one the associated binary would trace.

A nearly polar disc orbiting a pure binary undergoes nodal libration with the following theoretical frequency (Lubow & Martin 2018):

$$\omega_{\rm pa} = \frac{3\sqrt{5}}{4} e_{\rm b}\sqrt{1+4e_{\rm b}^2}\,\frac{M_1 M_2}{(M_1+M_2)^2}\left\langle\left(\frac{a_{\rm b}}{R}\right)^{\frac{7}{2}}\right\rangle\Omega_b, \tag{6.3}$$

where e_b is the binary orbit eccentricity, M_1 and M_2 are the binary masses, Ω_b the binary Keplerian frequency and angular bracket notes the average of the ratio between the binary semi-major axis a_b and the disc radius R, weighted over the angular momentum of the disc at radius R.

We apply Eq. (6.3) to the outer orbit case, as instantaneously it can be approximated by its associated binary. As for the masses, $M_1 = m_c$ and $M_2 = m_a + m_b$. For the eccentricity $e_b = e_2$ and for the orbital frequency $\Omega_b = \Omega_2$. We also compute the average weighted over the angular momentum assuming a Keplerian velocity field and that the disc extends from $R_{\rm in}$ to $R_{\rm out}$ with a density profile $\Sigma(R) \propto R^{-1}$. By doing so, we obtain:

$$\omega_{\rm pa,2} = \frac{9\sqrt{5}}{16} e_2\sqrt{1+4e_2^2}\,q_2(1-q_2)\left(\frac{a_2}{R_{\rm in}}\right)^{\frac{7}{2}}\frac{1-x_{\rm o}^{-2}}{x_{\rm o}^{3/2}-1}\Omega_2, \tag{6.4}$$

where $x_\mathrm{o} = R_\mathrm{out}/R_\mathrm{in}$ and $q_2 = m_c/(m_a + m_b + m_c)$ is the outer orbit mass ratio.

The librating behaviour happens due to the precession of the disc angular momentum around the eccentricity vector of the triple outer orbit. However, the triple outer orbit eccentricity vector $\mathbf{e}_2$ precesses with time due to the perturbation of the inner binary. The precession rate for the outer orbit can be analytically computed from the Hamiltonian of the stellar system with a perturbative approach (e.g. Murray & Dermott 2000; Naoz et al. 2013):

$$\omega_{e_2} = \frac{3}{4}a^2 q_1(1-q_1)\frac{1+\frac{3}{2}e_1^2}{(1-e_2^2)^2}\Omega_2 \tag{6.5}$$

where $a = a_1/a_2$ is the ratio between the inner and the outer orbit semi-major axis and $q_1 = m_b/(m_a + m_b)$ is the inner orbit mass ratio. This means that a polarly aligned disc around the outer orbit of a hierarchical triple system oscillates around a stable orbit that precesses with time with a frequency ω_{e_2}. Thus, in order for the disc to stay "attached" to the moving eccentricity vector, the condition for libration should be unaffected by the binary precession, meaning that $\omega_{\mathrm{pa},2} > \omega_{e_2}$.

To check the stability of small oscillations around the precessing polar configuration, we define the dimensionless quantity $T_2 = \omega_{e_2}/\omega_{\mathrm{pa},2}$: when $T_2 < 1$, polar alignment takes place; conversely, if $T_2 > 1$, it does not. The value of T_2 is

$$T_2 = \frac{4}{3\sqrt{5}}a^2\left(\frac{R_\mathrm{in}}{a_2}\right)^{\frac{7}{2}}\frac{x_o^{3/2}-1}{1-x_o^{-2}}\frac{q_1(1-q_1)}{q_2(1-q_2)}\mathcal{F}_2(e_1,e_2), \tag{6.6}$$

where

$$\mathcal{F}_2(e_1,e_2) = \frac{1+\frac{3}{2}e_1^2}{(1-e_2^2)^2 e_2\sqrt{1+4e_2^2}}. \tag{6.7}$$

The T_2 factor scales quadratically with the semi-major axes ratio: thus, either widening the outer orbit or shrinking the inner one decreases T_2 (which favours polar alignment). The torque between the inner and the outer orbit depends on a. Hence, the lower the value of a, the lower the precession frequency (i.e. the slower the precession). In addition, T_2 depends on the inner and outer orbit eccentricities via the $\mathcal{F}_2$ term. This term diverges both for e_2 approaching unity and zero. In the former case, the precession frequency of the outer orbit diverges, making polar alignment impossible. In the latter case, the nodal libration frequency of a nearly polarly aligned disc reduces to zero. Indeed, as the outer binary becomes more circular, the process of polar alignment becomes less likely. A recent study by Lepp et al. (2023) examined the behavior of of circum-triple test particles and found a similar criteria as given by T_2. Their criteria differs from T_2 mainly at small e_2.

As for the mass ratios, polar alignment is difficult for high q_1 and for q_2 approaching zero or unity. Indeed, higher values of q_1 (i.e. nearly equal mass inner binaries) translate into higher precession frequencies. Meanwhile, very high and very low q_2 reduce the outer binary to a single star concentrating the mass in the third body or in the inner binary (respectively) thus reducing the torque on the disc to zero. Conversely, when q_1 tends to zero, the inner binary perturbation becomes negligible — slowing the precession. This favours polar alignment.

Figure 6.2 shows how T_2 depends on the system orbital parameters. In this plot we assume $R_\mathrm{in} = 1.5\ a_2$ (as expected in very inclined discs: Lubow et al. 2015; Miranda & Lai 2015) and $R_\mathrm{out} = 30\ a_2$, thus $x_\mathrm{o} = 30/1.5$. In the left panel, T_2 is plotted as a function of the inner binary mass ratio q_1 (fixing q_2 to 0.5, i.e. equal mass outer binary), while on the right one as a function of the outer binary mass ratio q_2 (fixing q_1 to 0.5, i.e.

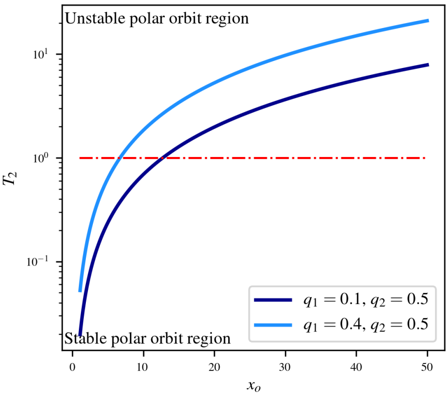

Figure 6.3: T_2 factor as defined in equation (6.6) as a function of the ratio between the outer and the inner disc radii x_o. We used the same parameters of the solid line in figure 6.2 with a semi-major axis ratio of 0.1. Different colors are different inner binary mass ratios. The outer binary mass ratio is fixed to 0.5, the most favourable to polar alignment.

equal mass inner binary). The thicker lines refer to a configuration in which $e_2 = 0.5$. Such outer orbit eccentricity avoids extreme values that are expected to undermine (also) the stability of the triple stellar system and it sets the easiest configuration for polar alignment to occur, being $e_2 = 0.5$ the minimum of $\mathcal{F}_2$. Moreover, for $0.2 < e_2 < 0.8$ the impact on $\mathcal{F}_2$ is of the order of 1. We also set $e_1 = 0$ to favour polar alignment as well. The dotted and dashed lines show how increasing e_1 to 0.7 (fixing e_2 to 0.5) and lowering e_2 to 0.2 (fixing e_1 to zero) affect T_2, respectively. The vast majority of the parameter space does not allow for polar alignment, as the curves are always above unity. The only exception is where the outer orbit is reduced to a two-body system, that is when q_1 tends to zero or for extremely small semi-major axis ratios a.

Last, the size of the disc also impacts the possibility of polar alignment. The more extended the disc the higher T_2, due to the lower nodal libration frequency of a radially extended disc. Figure 6.3 shows the dependence of T_2 on x_o. The two curves refer to two different inner binary mass ratios (the outer binary mass ratio is set to 0.5 the most favourable to polar alignment). Provided x_o is low enough ($\lesssim 10$), the circum-triple accretion disc can become polar. Depending on the semi-major axis and mass ratios, if the triple is not isolated and the disc is truncated from the outside, x_o can drop under that value, favouring the polar alignment of the disc.

6.1.3 Polar alignment in the inner circum-binary disc

The stability of the polar orbit for a disc orbiting the inner binary of a hierarchical triple system is determined by the inner binary eccetricity vector precession rate. In addition, Martin et al. (2022) showed that in this configuration also Kozai-Lidov oscillation of the disc (due to the interaction with the outer third body) could prevent circum-inner binary discs polar alignment. The disc Kozai-Lidov oscillation timescale can be computed by the theory of rigid disks (Larwood et al. 1996; Lubow & Ogilvie 2001) as done in Martin et al. (2014) (see their Eq. (4)). Using the same technique as in Equation (6.3), we obtain

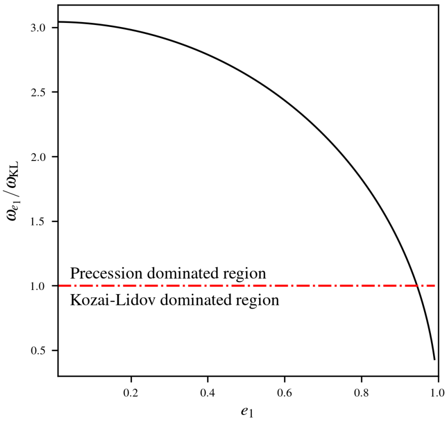

Figure 6.4: Ratio between the inner binary precession frequency and the disc Kozai-Lidov oscillation frequency. We use the same disc parameters as in Fig. 6.5 ($x_{\rm out} = 5/1.5$ and $R_{\rm in}/a_1 = 1.5$). The ratio is always above unity (red dash-dotted line) except for inner binary eccentricity near unity. Thus, in this configuration precession is always faster than disc Kozai-Lidov oscillation.

the following frequency for the circum-inner disc Kozai-Lidov oscillation:

$$\omega_{\rm KL} = \frac{3}{4}\frac{q_2}{1-q_2}a^3\left(1-e_2^2\right)^{-3/2}\left(\frac{R_{\rm in}}{a_1}\right)^{3/2}\frac{1-x_{\rm o}^{-2}}{x_{\rm o}^{3/2}-1}\Omega_1 \ . \tag{6.8}$$

Firstly, we compare the disc Kozai-Lidov oscillation timescale with the other relevant ones. We compute the nodal libration frequency of a nearly polar orbit around the inner binary of a hierarchical triple system ($\omega_{\rm pa,1}$) and the precession frequency of the inner binary eccentricity vector (ω_{e_1}), as we did for the outer orbit case in Section 6.1.2. We obtain:

$$\omega_{\rm pa,1} = \frac{9\sqrt{5}}{16}e_1\sqrt{1+4e_1^2}q_1(1-q_1)\left(\frac{a_1}{R_{\rm in}}\right)^{\frac{7}{2}}\frac{1-x_{\rm o}^{-2}}{x_{\rm o}^{3/2}-1}\Omega_1 \ , \tag{6.9}$$

and

$$\omega_{e_1} = \frac{3}{4}a^3\frac{q_2}{1-q_2}\sqrt{\frac{(1-e_1^2)}{(1-e_2^2)^3}}\Omega_1 \ . \tag{6.10}$$

Figure 6.4 shows the ratio between the precession frequency of the inner binary eccentricity vector ($\omega_{\rm e_1}$) and the disc Kozai-Lidov frequency of the circum-inner binary disc ($\omega_{\rm KL}$). This ratio solely depends on the eccentricity of the inner orbit e_1 and on the disc extent, as shown by Eqs. (6.8) and (6.10). In Figure 6.4 we use $x_{\rm out} = 5/1.5$ and $R_{\rm in}/a_1 = 1.5$. With such parameters, apart from $e_1 \sim 1$, precession is always faster than disc Kozai-Lidov oscillation. In general, for $\omega_{\rm KL} > \omega_{\rm e_1}$ we would need a combination of extremely eccentric inner binaries, small discs ($x_{\rm out} < 5/1.5$) and large disc cavities ($R_{\rm in}/a_1 > 2$). Thus, if polar alignment occurs because of a sufficiently slow precession of the inner binary, the disc Kozai-Lidov oscillation will not prevent polar alignment, since it is generally slower than precession. Having checked that, we go back to discussing the role of the inner binary precession. We define the corresponding $T_1 = \omega_{\rm e_1}/\omega_{\rm pa,1}$

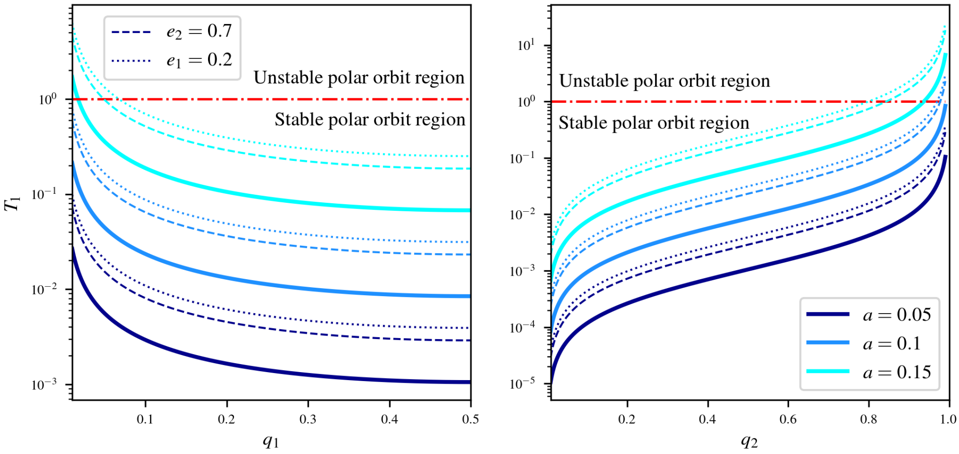

Figure 6.5: Dependency of T_1 (see sec. 6.1.3) on mass ratios, semi-major axes ratio and eccentricities. When T_1 is smaller than unity (dash dotted red line) polar alignment is possible, conversely for $T_1 > 1$ it is not. On the left panel, T_1 is plotted as a function of the inner binary mass ratio q_1 (fixing q_2 to 0.5), while on the right one as a function of the outer binary mass ratio q_2 (fixing q_1 to 0.5). The thicker lines refer to $e_2 = 0$ and $e_1 = 0.5$. The dotted and dashed lines show how lowering e_1 to 0.2 (fixing $e_2 = 0$) and raising e_2 to 0.7 (fixing $e_1 = 0.5$) affect T_1, respectively. Different colors refer to different semi-major axes ratios.

parameter for the inner binary as

$$T_1 = \frac{4}{3\sqrt{5}} a^3 \left(\frac{R_{\rm in}}{a_1}\right)^{\frac{7}{2}} \frac{x_o^{3/2}-1}{1-x_o^{-2}} \frac{q_2/q_1}{(1-q_1)(1-q_2)} \mathcal{F}_1(e_1, e_2), \tag{6.11}$$

with

$$\mathcal{F}_1(e_1, e_2) = \sqrt{\frac{1-e_1^2}{(1-e_2^2)^3} \frac{1}{e_1\sqrt{1+4e_1^2}}}, \tag{6.12}$$

The T_1 factor scales with the third power of the semi-major axes ratio. Thus, either widening the outer orbit or shrinking the inner one, results in an overall decrease of T_1. The precession frequency lowers (i.e. the precession is slower) with lower a because the torque between the inner and the outer orbit weakens. In addition, T_1 depends on the inner and outer orbit eccentricities via the $\mathcal{F}_1$ term. This term diverges for both e_2 approaching unity and e_1 approaching zero. In the former case, the precession frequency of the inner orbit diverges, making polar alignment impossible. In the latter case, the nodal libration frequency of the polar disc tends to zero. Again, as the inner binary becomes more circular, the process of polar alignment becomes less likely.

As for the mass ratios, polar alignment is made difficult for high values of q_2 and for q_1 approaching zero. Higher values of q_2 result in a higher precession frequency. Meanwhile, very low q_1 reduce the inner binary to a single star, reducing the torque on the disc to zero. Conversely, when q_2 tends to zero, the third outer body perturbation becomes negligible, which slows the precession and favours polar alignment.

Figure 6.5 shows how T_1 depends on the system orbital parameters. In this plot, we assume $R_{\rm in} = 1.5\ a_1$ and $R_{\rm out} = 5\ a_1$, thus $x_{\rm o} = 5/1.5$. In the left panel, T_1 is plotted as a function of the inner binary mass ratio q_1 (fixing q_2 to 0.5), while on the right one as a function of the outer binary mass ratio q_2 (fixing q_1 to 0.5). The thicker lines refer to a configuration in which $e_1 = 0.5$ and $e_2 = 0$. The dotted and dashed lines show how raising e_2 to 0.7 (fixing e_1 to 0.5) and lowering e_1 to 0.2 (fixing e_2 to zero) affect T_1, respectively.

A disc orbiting the innermost binary of a hierarchical system is able to go polar in the vast majority of the inner binary parameter space, contrary to an accretion disc around the outer orbit of a hierarchical system. Except for very small q_1 and very high q_2, the T_1 factor is always below unity no matter the eccentricities, semi-major axis ratio or mass ratios.

In the case of HD98800 we have precise measurements of the orbital parameters of both the inner orbits and of the outer orbit of the quadruple stellar system (Zúñiga-Fernández et al. 2021). If we approximate HD98800 A to a single body, the disc around HD98800 B measures a $T_{1,\mathrm{HD}} \approx 3 \times 10^{-4}$. This value is well below unity as expected, being the disc in a polar configuration.

6.2 Numerical simulations

We performed 3D numerical simulations using the Smoothed Particle Hydrodynamics (SPH) code PHANTOM (Price et al. 2018b), widely used in the astrophysical community to study gas and dust in protostellar environments (e.g. Dipierro et al. 2015; Mentiplay et al. 2019; Veronesi et al. 2020; Ragusa et al. 2020; Toci et al. 2020; Ballabio et al. 2021; Vericel et al. 2021) and for simulating the hydrodynamics of stellar systems with more than two stars embedded in accretion discs (e.g. Ragusa et al. 2017, 2021; Martin & Lubow 2019; Price et al. 2018a; Cuello et al. 2019; Poblete et al. 2019; Calcino et al. 2019; Smallwood et al. 2021; Ceppi et al. 2022). These simulations are designed to test the criteria presented in Sections 6.1.2 and 6.1.3 for polar alignment in discs orbiting a hierarchical triple outer (sec. 6.2.1) and inner (sec. 6.2.2) orbit.

6.2.1 Circum-triple disc simulations

Simulations **S1** and **S2** test the polar alignment of a disc around the outer orbit of a hierarchical triple (**S1**), compared to the same disc orbiting around the binary associated to the triple outer orbit (i.e. the binary with the same orbital parameters of the triple outer orbit and made of the third body and a star obtained by condensing the triple inner binary in its centre of mass, simulation **S2**). The triple system consists of a circular equal mass inner binary ($m_a = m_b = 0.5\ M_\odot$) orbited by a coplanar third star with mass equal to the inner binary mass ($m_c = m_a + m_b = 1\ M_\odot$). The semi-major axis of the inner binary is $a_1 = 1$ au. The semi-major axis and the eccentricity of the outer orbit are $a_2 = 10$ au and $e_2 = 0.5$. The outer and the inner orbital plane are coplanar. The associated binary system consists of a star of mass m_c orbited by a star of mass $m_a + m_b$. The eccentricity and semi-major axis of the binary are the same as the triple outer binary orbit.

Both the binary and triple system are orbited by the same gaseous accretion disc. The disc is initially tilted to the stellar orbital plane of $\beta = 70°$ and the longitude of the ascending node Ω equals 90°. Each simulated disc is made of 3×10^5 SPH particles, resulting in a vertical resolution of $\langle h/H \rangle \sim 0.24$. The total gas mass is initially the 1% of the stellar mass and the discs extend from $R_{\mathrm{in}} = 15$ au to $R_{\mathrm{out}} = 100$ au. The gas surface density is initially distributed with a power law profile

$$\Sigma(R) = \Sigma_{\rm in}\left(\frac{R}{R_{\rm in}}\right)^{-p}\left(1-\sqrt{\frac{R_{\rm in}}{R}}\right), \tag{6.13}$$

with $p = 1$ and $\Sigma_{\rm in} = 22.2$ g/cm^2. We adopt a locally isothermal equation of state $P = c_s^2\rho$, with

$$c_{\rm s}(R) = c_{\rm s}(R_{\rm in})\left(\frac{R}{R_{\rm in}}\right)^{-q}, \tag{6.14}$$

with $q = 0.25$. The resulting disc aspect ratio is given by

$$\frac{H}{R} = \frac{H_0}{R_0}\left(\frac{R}{R_{\rm in}}\right)^{1/4}, \tag{6.15}$$

with an $H_0/R_0 = 0.1$ at $R = R_{\rm in}$. Viscosity is implemented with the artificial viscosity method (Lucy 1977; Gingold & Monaghan 1977) resulting in a Shakura & Sunyaev (1973) α-viscosity (Lodato & Price 2010) with $\alpha_{\rm SS} \sim 0.01$ ($\alpha_{\rm AV} = 0.42$). In every simulation, stars are modelled as sink particles (Bate et al. 1995; Price et al. 2018b).

The initial tilt of the disc is well above the critical angle for polar alignment around a binary system, which is $\beta_{\rm crit}(e = 0.5, \Omega = 90°) \sim 40°$ (Farago & Laskar 2010). Thus, we expect the circumbinary disc in simulation **S2** to polarly align. Conversely, even if the outer orbit parameters in the hierarchical triple of simulation **S1** are the same as the binary in **S2**, $T_2 \sim 6 > 1$. Thus, we expect the disc not to align polarly.

Figure 6.6 shows radially averaged tilt (β, top panels) and longitude of the ascending node (Ω, bottom panels) profiles of the disc as a function of time. The two systems behave very differently: the circumbinary disc undergoes polar alignment, since the inclination oscillates around $\beta \sim 90°$ and the longitude of the ascending node librates, as expected for a disc going polar (Martin & Lubow 2019). On the other hand, the circum-triple disc aligns to the stellar orbital plane (i.e. the inclination decreases) and it precesses, with its longitude of the ascending node spanning 2π. There are two processes that make the longitude of the ascending node to precess: i) the eccentricity vector, to which the longitude of the ascending node refers, is precessing; ii) the disc itself is precessing, as an inclined circumbinary disc would around a pure binary. This can be seen computing the longitude of the ascending node referring to the initial eccentricity vector position. This absolute longitude of the ascending node is plotted as a dashed curve in Fig. 6.6. As expected, polar alignment does not occur in this case, since the precession rate of the eccentricity vector is larger than the polar alignment one.

The disc inclination, apart from the oscillating behaviour, is exponentially decaying towards the mid-plane. We fit the exponential decay to find the timescale of coplanar alignment, obtaining $\tau_{\rm cop} \sim 3.8 \times 10^4$ outer orbit periods. The timescale $\tau_{\rm cop}$ is of the order of the disc viscous timescale for this disc ($\sim 2 \times 10^4$ outer orbits). Bate et al. (2000) found that the alignment timescale (given by their equation (35), see also Lubow & Ogilvie (2000)) for a tilted disc is of the order of (or slightly longer than) the disc viscous timescale. This suggests that an accretion disc with $T_2 > 1$ orbiting the outer levels of a hierarchical system sees the central system as a circular binary. In fact, the evolution of the tilt angle of the circum-triple disc in simulation **S1** is similar to a circum-binary disc orbiting a low eccentric binary system (an exponentially decaying tilt and a precessing longitude of the ascending node). This is due to the fact that the disc sees the eccentricity vector of the central stellar system averaged over the precession period.

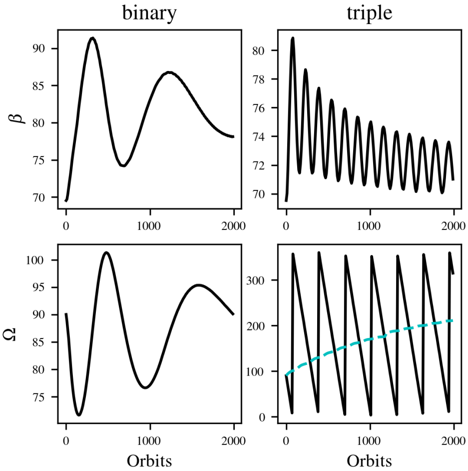

Figure 6.6: Radially averaged tilt (top row) and longitude of the ascending node (bottom row) of the circumbinary (left column, simulation **S2**) and circumtriple (right column, simulation **S1**) disc as a function of time. Dashed line is the longitude of the ascending node with respect to the initial semi-major axis direction, rather than the eccentricity vector. In the left column the circum-binary disc is aligning polarly. As expected due to the mass of the disc, the polar alignment inclination is less than 90 degrees.

In the right column the circum-triple disc is going coplanar, even if the orbital parameters of the triple outer orbit are the same as the binary orbital parameters.

6.2.2 Circum-binary disc simulation in a triple system

Simulation **S3** studies a disc orbiting the inner binary of a hierarchical triple system. The stellar system consists of an eccentric ($e_1 = 0.5$) equal mass inner binary ($m_a = m_b = 0.5\,M_\odot$) orbited by a third star with mass equal to the inner binary mass ($m_c = m_a + m_b = 1\,M_\odot$) in a circular orbit. The semi-major axis of the inner and outer binary are $a_1 = 1$ au and $a_2 = 20$ au respectively, and the inner and outer orbits are coplanar.

The inner binary is orbited by a circum-binary disc with an initial tilt of $\beta = 70°$ and a longitude of the ascending node of 90°. The disc is simulated with 3×10^5 SPH particles, resulting in a vertical resolution of $\langle h/H \rangle \sim 0.23$. The total gas mass is initially the 1‰ of the inner binary mass and the disc extends from $R_{\rm in} = 1.5$ au to $R_{\rm out} = 5$ au. The gas surface density profile is the same as in Eq. (6.13), with $\Sigma_{\rm in} = 2.7 \times 10^2\ {\rm g\,cm^{-2}}$, and the temperature and aspect ratio profiles are given by Eqs. 6.14 and 6.15. Viscosity and stars are implemented as in previous simulations, with $\alpha_{\rm SS} \sim 0.01$ ($\alpha_{\rm AV} = 0.44$).

The initial disc tilt is above the critical angle for polar alignment around a pure binary system. In addition, in this configuration $T_1 \sim 0.008 < 1$, which should translate into disc polar alignment (see Sect. 6.1.3).

Figure 6.7 shows radially averaged tilt (β, top panel) and longitude of the ascending node (Ω, bottom panel) profiles of the disc as a function of time. The tilt plot clearly shows that the disc oscillates around 90° with the amplitude being damped over time. The longitude of the ascending node is librating as well: thus, the disc is going polar as expected. However, the disc is librating around the eccentricity vector of the inner binary, which in turn is precessing with time. As a consequence, the disc angular momentum is precessing as well. This can be seen computing the disc longitude of the

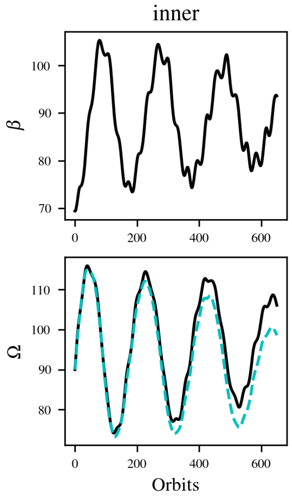

Figure 6.7: Radially averaged tilt (top row) and longitude of the ascending node (bottom row) of the circum-inner binary disc (simulation **S3**) as a function of time. Dashed line is the longitude of the ascending node with respect to the initial semi-major axis direction, rather than the eccentricity vector. The disc is aligning to a polar configuration. The libration timescale and the stationary inclination differ from the circumtriple disc due to the lower mass of the circuminner binary disc.

ascending node with respect to the initial semi-major axis direction, instead of referring to the inner binary eccentricity vector, which is precessing. This absolute longitude of the ascending node is plotted in the second row of Fig. 6.7 with a dashed curve. The absolute longitude of the ascending node is oscillating as the relative longitude of the ascending node, but its mean value is decreasing with time following the precession of the inner binary eccentricity vector.

6.3 Discussion

6.3.1 Polar alignment in hierarchical stellar systems

Hierarchical systems with more than two stars are common in a young stellar population (Duchêne & Kraus 2013; Moe & Di Stefano 2017), and they typically host discs orbiting their hierarchical levels. A significant fraction of misaligned stellar discs studied in the literature are orbiting or are inside systems with more than two stars (e.g. Phuong et al. 2020; Keppler et al. 2020; Kraus et al. 2020; Bi et al. 2020; Price et al. 2018a; Kennedy et al. 2019). By studying the observed misalignment distribution of discs in multiple stellar systems, we aim at obtaining information about their physical properties, their formation and early stage evolution. Properties of discs (e.g. size, viscosity) affect the evolution of the tilt angle which, in return, provides information about them. In order to extract information from the final observed tilt distribution, we need to understand the way in which it evolves and, possibly, the initial conditions of its evolution.

In particular, the fraction of discs in a polar configuration gives us insights about the fraction of highly-eccentric binary systems with highly-inclined discs. Remarkably, the time evolution towards a polar orbit is faster than the disc lifetime. So, in principle, the final outcome of the evolution process (i.e. the observed fraction of polar discs) directly traces the initial conditions (i.e. the outcome of star formation process). Indeed, the fraction of polarly aligned discs is related to how common the critical configuration is (i.e. a binary with eccentricity $e_{\rm b}$, orbited by a disc with tilt $\beta > \beta_{\rm crit}(e_{\rm b}, \Omega)$). However, we have to take into account that pure binary systems and systems with more than two stars have different critical conditions for polar alignment.

The analytical and numerical findings, reported in Sections 6.1 and 6.2, show that the secular evolution of the osculating orbital elements in hierarchical systems is a threat to disc polar alignment. In particular, a fast enough precession of the orbit eccentricity vector prevents the mechanism of polar alignment. Figures 6.2 and 6.5 show the T parameter discussed in Sections 6.1.2 and 6.1.3 (respectively) as a function of the relevant parameters of a hierarchical triple (the two mass ratios q_1 and q_2, the semi-major axis ratio a and the inner and outer orbit eccentricities e_1 and e_2). When T is larger than unity, the polar orbit is unstable — no matter how high the disc-orbit misalignment is. Under this condition, the pure binary criteria for polar alignment derived in the literature can not be applied to hierarchical systems.

Looking at the parameter space explored in Figure 6.2 and at the numerical results in section 6.2.1, discs orbiting the outer levels of hierarchical systems are generally not able to go polar. Indeed, the T parameter is always larger than unity, except for radially narrow discs and where the system is reduced to an actual binary system (i.e. for a mass ratio of the inner binary (q_1) approaching zero and for very small semi-major axis ratios (a)). Thus, regardless of the mutual inclination, a misaligned radially extended disc orbiting an outer level of a hierarchical system always evolves towards a coplanar configuration. Since the eccentricity vector is quickly precessing, the disc evolves as orbiting a circular orbit given that the eccentricity vector is averaged over a precession period.

In a circum-binary disc in an hierarchical system, however, polar alignment is possible as the T factor is generally below unity (see Figs. 6.5 and 6.7). As the precession of the inner binary eccentricity vector is slow enough for the polar disc to follow it, the disc remains locked to the eccentricity vector, precessing with it and conserving the polar configuration. Note that the disc precession happens on the eccentricity vector precession timescale and not on the typical nodal precession timescale for a tilted circum-binary disc (Bate et al. 2000; Lodato & Facchini 2013). Superimposed to this precession, the longitude of the ascending node is librating as well, due to the precession of the disc angular momentum vector around the inner binary eccentricity vector.

The evolution of the osculating elements in hierarchical systems further affects the polar alignment process in such systems. The critical angle for polar alignment significantly depends on Ω, that is relative to the central orbit eccentricity vector (see eq. 7.4). Given that this vector in hierarchical system precesses with time, Ω is constantly spanned with time. Thus, regardless of the initial Ω value, the triple configuration will precess, eventually exploring the Ω related to the lowest critical angle. Therefore, even if the initial Ω results in a configuration where $\beta < \beta_{\rm crit}$ (so no polar alignment for a pure binary configuration), the triple configuration will polarly align as soon as the Ω precession allows it to fullfill the condition $\beta > \beta_{\rm crit}(\Omega, e_{\rm b})$. Thus, given the eccentricity of the orbit, the critical angle for polar alignment in hierarchical systems is always the one with $\Omega = 90^\circ$ (the lower one).

Up to now, we only discussed hierarchical stellar systems with inner and outer orbits coplanar to each other. When the inner and the outer orbit of a hierarchical triple are misaligned, the secular evolution of the osculating orbital parameters is even more complex. Indeed, not only the argumentum of periapsis precesses with time, but also

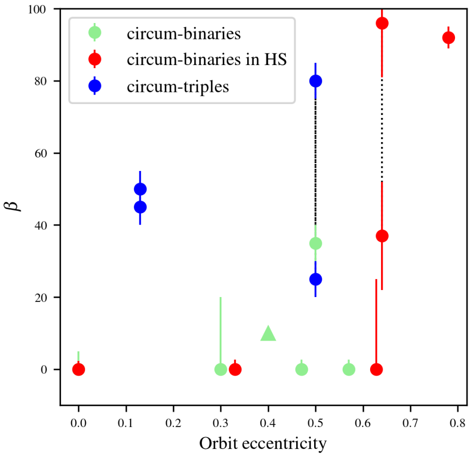

Figure 6.8: Disc-orbit misalignment of circumbinary discs in Tables 3 and 4 in Czekala et al. (2019) as a function of the central system eccentricity. Green dots are accretion discs orbiting pure binary systems, blue dots are accretion discs orbiting an outer hierarchical level of a hierarchical system, red dots are accretion discs orbiting the innermost hierarchical level of a hierarchical system (HS). The triangle represents the lower limit on the mutual inclination of R Cra. Dotted lines connect the two degenerate solutions for HD 142527, SR 24N, and GG Tau A systems.

Kozai-Lidov oscillations of the stellar orbits occur. Thus, the eccentricity of each hierarchical level orbit and the mutual inclination between the hierarchical orbital planes oscillate with time. However, at least for a circular outer orbit, the Kozai-Lidov oscillation frequency is similar to the precession frequency of the inner binary orbit we derived in Eq. (6.10) (Naoz 2016; Antognini 2015). Therefore, the T parameter is still reliable to predict the possibility of polar alignment in the inner orbit of misaligned hierarchical triples. However, a thorough analysis of this problem is needed, especially regarding the possibility of polar alignment in misaligned hierarchical triples circum-outer orbit accretion discs and we defer this to subsequent work. An aspect of crucial importance is that Kozai-Lidov oscillations can trigger polar alignment in misaligned hierarchical systems. Indeed, in the oscillation the orbits eccentricities raise (lowering the critical angle) and the orbital inclinations oscillation makes also the tilt of the disc to change. This can trigger polar alignment in configurations with a lower-than-unity T parameter, but a low initial orbit-disc misalignment.

We thus expect polar alignment to still be possible only around the innermost level of hierarchical systems even for misaligned multiple systems, where it can be even promoted by Kozai-Lidov oscillations and the Ω precession.

6.3.2 Observed tilt distribution of discs around binaries and hierarchical systems

Figure 6.8, originally reported by Czekala et al. (2019), collects all protoplanetary discs in the literature orbiting in multiple stellar systems for which we know the inclination between the disc and the system orbital plane. Each point in the plot represents a disc orbiting a pair of bound stars, either in a pure binary system or in a higher multiplicity system. Green dots refer to discs orbiting in a pure binary system, blue dots refer to discs

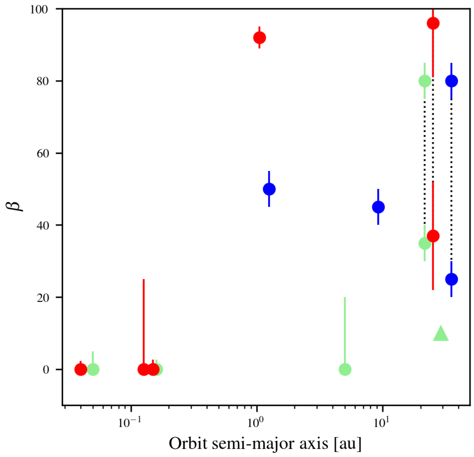

Figure 6.9: Disc-orbit misalignment of circumbinary discs in Tables 3 and 4 in Czekala et al. (2019) as a function of the orbit semi-major axis. Legend is the same as figure 6.8.

that have more than two stars orbiting in their cavity (i.e. the outer level of hierarchical systems) and red dots refer to discs orbiting a binary with external companions outside the disc (i.e. the innermost level of hierarchical systems). The dots connected by dotted vertical lines are two possible solutions for the mutual inclination due to a 180° ambiguity in the longitude of the ascending node of the system due to lack of radial velocity information.

The three populations show different tilt distribution. Discs orbiting pure binary systems (green dots) are mostly coplanar, hence there are no polarly aligned discs. This mismatches with the theoretical expectation. If the initial tilt distribution is nearly randomly distributed, we expect a wider scatter in the distribution because the population should be slowly going coplanar on a tilt evolution timescale comparable to the viscous timescale (Bate et al. 2000; Lubow & Ogilvie 2000). This could be due to a lower average tilt in the initial population or to a faster than expected tilt evolution (e.g. due to an higher than expected viscosity). In addition, we lack the expected small population of polarly aligned discs (resulting from the fraction of discs initially more tilted than the critical angle for polar alignment in binaries). Hence, either the conditions for polar alignment are less populated than expected or external factors reduce the stability of the polar configuration (e.g. the interaction with the environment).

The tilt distribution of circum-binary discs in hierarchical systems is more articulated. We have a small fraction of polarly aligned discs (i.e. the disc in HD98800B and possibly in SR 24N), although there are less discs in this populations than in the pure binaries one. This is in agreement with our analytical findings (polar configuration is stable in such systems) and suggests that the conditions for polar alignment are more likely for those systems than in pure binaries. This is also in line with what discussed in section 6.3.1: phenomena that are typical of systems with more than two stars could be able to foster polar alignment. First, polar alignment for such configurations could be triggered by Kozai-Lidov oscillations of the hierarchical system. Second, by varying the longitude of the ascending node, the precession of the orbit eccentricity vector allows the disc to always reach the configuration in which the critical angle for polar alignment is minimum. We defer the study of the impact of these mechanisms on polar alignment to future works. Additionally, depending on the stellar system parameters (such as binary mass, semi-major axis, eccentricity) general relativity could limit the possibility of polar alignment for extended discs (Lepp et al. 2022). Thus, the presence of an additional external companion truncating the disc from the outside could facilitate polar alignment for circum-inner binary discs as well. The rest of the population is nearly coplanar. Thus, discs that do not go polar evolve as in the pure binary case.

It is worth noting that also the binary separation plays a role in the degree of alignment of circum-binary discs (see figure 6.9). Indeed, short period binaries (no matter if isolated or with an external companion) present coplanar discs. The inclination distribution of that region of the parameter space could be affected also by the short period binary formation mechanisms that drive initially wider binaries to shrink. Still, wider binaries inclination distributions present the same trends discussed in the previous paragraph (i.e. highly misaligned discs around inner binaries and more coplanar discs around pure binaries).

Even though the statistics are low, in the population of discs orbiting more than two stars there are no coplanar discs, neither highly misaligned (possibly polar) ones. Indeed, the highest blue point refer to the degenerate solution with an high inclination for the GG Tau A circum-triple disc. All the hydrodynamical models of GG Tau A in the literature favour the mildly inclined solution (Aly et al. 2018; Keppler et al. 2020; Cazzoletti et al. 2017). Thus, the correct tilt for GG Tau A is around 30 degrees despite the uncertainty in the astrometry and the highest blue point should be discarded. The lack of polar discs agrees with our analytical findings. The lack of coplanar discs constrasts with our results in discs orbiting coplanar hierarchical systems. Indeed, we found that circum-triple discs evolve as orbiting a circular binary (due to the fast precession of the eccentricity vector). In addition, gived that they form via the same mechanisms, we expect the same initial tilt distribution for discs in pure binaries and in hierarchical systems. If the initial condition and the evolution are similar, then *why is the tilt distribution of pure binaries and systems with more than two stars so different?*

We suggest the answer lies in the orbital dynamics of systems with more than two stars. This kind of systems have access to a richer dynamical evolution compared to pure binary systems. As previously discussed their orbital parameters and orbital orientation evolve with time on a shorter timescale compared to the disc lifetime. In particular, misaligned hierarchical systems vary their inclinations with time. Specifically, let us consider a hierarchical triple system orbited by a low-misaligned accretion disc. Looking at the pure binary population, on the long run the disc should become coplanar with the triple orbital plane. If the inner and outer orbit of the triple are misaligned, however, we expect their mutual inclination to evolve with time due to Kozai-Lidov oscillations. Thus, the inclination of the outer orbit will oscillate as well. As a consequence, the mutual inclination between the circum-triple disc and the triple outer orbit will oscillate with time, even if the disc had enough time to align to the stellar plane. Thus, the observed misalignment in the systems with more than two stars population is possibly the result of these stellar orbit evolution processes, and not the outcome of accretion disc evolution. This implies that the misaligned configurations we observe in systems with more than two stars are not stable — or slowly evolving — configurations. Indeed, because we are taking a snapshot of an oscillating stellar orbital plane, we happen to be observing a tilted disc by pure chance.

6.4 Conclusions

In this chapter we showed that the requirement on the parameters of a circum-binary disc for going polar are necessary but not sufficient when dealing with hierarchical systems. A crucial additional requirement is that the eccentricity vector precession timescale of the system orbited by the accretion disc has to be longer than the disk libration timescale. We derived an analytical criterion to be satisfied in order for a disc to go polar around the outer levels of a hierarchical system (Eq. (6.6)) and around the innermost hierarchical level (Eq. (6.11)).

We found that discs orbiting the outer level of a hierarchical system can hardly polarly align. Except for radially narrow discs and very small mass and semi-major axis ratios, the precession of the outer orbit eccentricity vector is always faster than the nodal libration. Conversely, discs orbiting the innermost level of a hierarchical system are able to go polar as the precession of the inner eccentricity vector is slower than polar alignment. Smoothed particle hydrodynamics simulations confirm these results and surveys of circumbinary accretion discs are also in agreement — even though statistics are still poor.

In addition, we found that the inclination of an accretion disc orbiting a hierarchical system evolves as if it was orbiting a circular binary. The disc sees the central system eccentricity vector averaged over the precession period. This is in contrast with the fact that pure binary systems and systems with more than two stars host different disc populations. The former presents discs mostly coplanar with the stellar orbital plane with little spread in the tilt distribution. The latter consists of misaligned discs with a wider spread in tilt distribution. We suggest that the scatter in misalignment observed in system with more than two stars is due to the secular oscillation of hierarchical systems orbital parameters, that continuously vary the stellar orbital plane orientation, rather than to the evolution of the accretion discs.

In conclusion, this work shows that when analysing the population of discs around binaries it is important to separate pure binaries from binaries inside hierarchical systems. Indeed, the misalignment distributions of pure binaries and systems with more than two stars tell us different stories. The former is the result of viscous disc evolution, while the second one is related to N-body orbital parameter oscillations. This additional complexity can be a precious tool to deeper investigate the impact of multiplicity on accretion disc evolution and planet formation, and, in general, to better understand the formation of multiple stellar systems. The increasing statistics of this population will allow us also to better measure the fraction of polar discs and the distribution of mutual inclination in the two populations. This is an important test for our theory. Indeed, the final distribution have to be the result of the initial conditions we derived with models, plus the theoretical expected evolution. A mismatch between the predicted and the observed populations would highlight missing pieces in the theory of disc formation and evolution.

Part IV

The population of polarly aligned discs and the initial distribution of binary orbital parameters

CHAPTER 7

Probing initial distributions of orbital eccentricity and disc misalignment via polar discs

This chapter is based on the paper "Probing initial distributions of orbital eccentricity and disc misalignment via polar discs" by Simone Ceppi, Nicolás Cuello, Giuseppe Lodato, Cristiano Longarini, Daniel J. Price, Daniel Elsender and Matthew R. Bate, published on Astronomy & Astrophysics, Volume 681, in January 2024

The tilt of an accretion disc orbiting an eccentric binary has two alternative equilibrium configurations. If the mutual inclination (initial disc tilt with respect to the stellar orbital plane) is below a critical angle for polar alignment (Farago & Laskar 2010; Zanazzi & Lai 2018; Cuello & Giuppone 2019) the disc is expected to nodally precess, and align to the stellar orbital plane due to viscous dissipation (Bate et al. 2000; Lubow & Ogilvie 2000). If the initial mutual inclination is higher than the critical angle for polar alignment, Aly et al. (2015) and Martin & Lubow (2017) showed that the circumbinary disc angular momentum vector precesses around the binary orbit eccentricity vector. Due to viscous dissipation, the disc evolves to a polar configuration in which the mutual inclination is around 90° (depending on disc parameters, see Martin & Lubow 2019).

Ceppi et al. (2023) showed that, in the general case of a disc in a multiple stellar system, if the disc is orbiting more than two stars the polar alignment mechanism is highly suppressed[1]. Conversely, if the disc is orbiting a pair of stars with additional bodies outside the disc, polar alignment is at least as likely as in the pure circumbinary disc case.

The properties of multiple stellar systems are already used to find insights into the physics driving stellar and planet formation evolution. The available statistics on multiple stellar systems supports that the vast majority of stars are born in a multiple stellar system and that stellar multiplicity increases with stellar mass (Larson 1972; Duchêne & Kraus 2013; Offner et al. 2022). These are crucial constraints for numerical experiments on the collapse of molecular clouds (Bate et al. 2002; Krumholz et al. 2012; Bate 2018, 2019; Mathew & Federrath 2021; Mathew et al. 2023; Lebreuilly et al. 2023). Orbital parameter distributions, such as the semi-major axis distribution (Duquennoy & Mayor 1991; Raghavan et al. 2010), or the binary mass ratio distribution (Moe & Di Stefano

---

[1] Polar alignment could still occur under the right conditions (e.g. very small semi-major axis ratios or for very small discs). Ceppi et al. (2023) derived an analytical criterion to assess the stability of the polar configuration in triples (see also the criterion obtained by Lepp et al. 2023).

2017; El-Badry et al. 2019) also help to constrain formation mechanisms. The presence of more than two stars is expected to change the shape of these distributions, encoding additional information about the dependence on multiplicity (Smith et al. 1997; Ceppi et al. 2022; Offner et al. 2022).

In this chapter, we show that, from the current distribution of mutual misalignment and eccentricity — like the one in Czekala et al. (2019) — and with increased statistics, we are able to constrain the distributions of eccentricity and inclination between orbital planes and discs at birth. Such distributions, in turn, depend on which physical properties are more significant in the formation process of these objects. In addition to dynamical interactions between stars (Bate et al. 2002; Bate 2018; Elsender et al. 2023), the presence and the strength of magnetic fields (Price & Bate 2007; Wurster et al. 2019; Zhao et al. 2020; Lebreuilly et al. 2021), different metallicities (Elsender & Bate 2021) and the level of turbulence in the cloud (Bate et al. 2010; Walch et al. 2012) may play a significant role in setting the initial properties of disc and star populations.

The chapter is organised as follows: In Section 7.1 we present a model to compute the fraction of polar discs and the mean eccentricity of stellar orbits hosting polar discs. By applying this method to a population of hierarchical systems and of pure binaries, we derive the relationship between the initial and evolved distributions of system properties. Finally, in Section 7.2 we constrain the initial conditions for both populations. In Section 7.3 we discuss our results and we give our conclusions in Section 7.4.

7.1 Initial conditions and polar disc population

7.1.1 Polar disc fraction and mean polar systems eccentricity

As soon as the condition for polar alignment is satisfied, an accretion disc starts oscillating around the polar configuration. The disc dissipates the oscillation on a fraction of the viscous timescale (Lubow & Martin 2018; Zanazzi & Lai 2018). Thus, it is reasonable to assume that all discs able to go polar in the initial population will do so. Then, if we neglect the impact of subsequent external interactions, the fraction of polarly aligned discs we observe in a given evolved population is directly linked to the initial conditions (eccentricity and misalignment distributions) in a forming population.

In this section, we build a toy model to estimate the expected fraction of polar discs and their eccentricity distribution in an evolved young stellar population (Class II).

Given the observed and theoretically predicted preference for low mutual inclinations (e.g. Czekala et al. (2019); Elsender et al. (2023)), we describe the initial distribution of mutual inclination with a normalised exponential distribution:

$$P_\beta(\beta) = \frac{1}{N_\beta} \exp\left(-\frac{\beta}{\sigma_\beta}\right), \tag{7.1}$$

where β is the mutual inclination, σ_β is a parameter that regulates the shape of the distribution and N_β normalises the distribution over the support considered, i.e. from $\beta = 0$ to $\pi/2$.

The initial distribution of eccentricity is described by a normalised power law distribution:

$$P_{\mathrm{e}}(e) = \frac{1}{N_{\mathrm{e}}} e^{\alpha}, \tag{7.2}$$

where e is the orbital eccentricity, α is a parameter regulating the distribution shape and N_{e} normalises the distribution over $e = 0$ to 1. This is in line with surveys of eccentricities (Duquennoy & Mayor 1991; Raghavan et al. 2010; Hwang et al. 2022) and it allows for a thermal distribution ($P(e) \propto e$) that can be produced by repeated N-body interactions (Jeans 1919; Ambartsumian 1937; Heggie 1975).

Thus, the two-dimensional probability density function for the initial condition is given by:

$$P(e, \beta) = P_{\mathrm{e}}(e) P_{\beta}(\beta). \tag{7.3}$$

For an orbit co-rotating with the central system, the critical angle for polar alignment is[2] (Farago & Laskar 2010; Zanazzi & Lai 2018; Cuello & Giuppone 2019)

$$\beta_{\mathrm{crit}}(e, \Omega) = \arcsin \sqrt{\frac{1 - e^2}{1 - 5e^2 \cos \Omega^2 + 4e^2}}. \tag{7.4}$$

where e is the orbital eccentricity and Ω is the disc longitude of the ascending node.

Supposing that all discs above β_{crit} go polar and neglecting subsequent external interactions, we can integrate over the initial mutual inclination above β_{crit}, to obtain the distribution of polar discs as a function of system eccentricity $P_{\mathrm{pol}}(e)$. At this stage, we consider $\Omega = \pi/2$ and we will fix $P_{\mathrm{pol}}(e)$ to take into account a distribution of longitude of the ascending node in Sec. 7.1.2. Thus,

$$P_{\mathrm{pol}}(e) = \int_{\beta_{\mathrm{crit}}(e, \frac{\pi}{2})}^{\pi/2} P(e, \beta) \mathrm{d}\beta. \tag{7.5}$$

Integrating P_{pol} over the eccentricity we obtain the expected fraction of polar discs (F_{p}) in an evolved population, that is the ratio between the number of polar discs and the total number of discs in the population:

$$F_{\mathrm{p}} = \int_0^1 P_{\mathrm{pol}}(e) \mathrm{d}e. \tag{7.6}$$

Additionally, from P_{pol} we can compute the mean eccentricity of stellar systems hosting polar discs, i.e.:

$$\langle e \rangle = \int_0^1 e P_{\mathrm{pol}}(e) \mathrm{d}e. \tag{7.7}$$

Integrals in Eqs. (7.6) and (7.7) are challenging to solve due to the dependencies of β_{crit}. In the next section we present two assumptions to remove the Ω dependency in the case of hierarchical systems and pure binaries. By doing so, we only deal with the eccentricity dependence in these integrals.

7.1.2 Taking into account the longitude of ascending node

Figure 7.1 shows how the critical angle β_{crit} in Eq. (7.4) depends on the longitude of the ascending node (Ω) for different orbital eccentricities. Let us take the subpopulation of circumbinary discs with a given mutual misalignment β_{sp} orbiting pure binaries with a given orbital eccentricity e_{sp}. We have a Ω_{crit} so that the critical angle for polar alignment $\beta_{\mathrm{crit}}(e_{\mathrm{sp}}, \Omega_{\mathrm{crit}}) = \beta_{\mathrm{sp}}$. All discs with $\Omega < \Omega_{\mathrm{crit}}$ (dotted line in Figure 7.1) will not polar align. All discs with a $\Omega > \Omega_{\mathrm{crit}}$ (dashed line) will polar align.

---

[2] for a counterrotating orbit $\beta_{\mathrm{crit}}(e_{\mathrm{b}}, \Omega) = \pi - \arcsin \sqrt{\frac{1 - e_{\mathrm{b}}^2}{1 - 5e_{\mathrm{b}}^2 \cos \Omega^2 + 4e_{\mathrm{b}}^2}}$

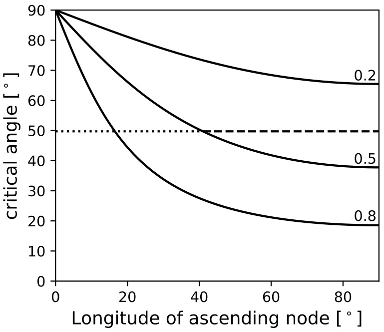

Figure 7.1: Critical angle for polar alignment as a function of the disc longitude of the ascending node for a fixed binary eccentricity ($e = 0.2, 0.5, 0.8$). Given a mutual inclination (e.g. $50°$) and an eccentricity (e.g. $e = 0.5$), the dashed (dotted) line is the Ω interval in which the disc will go perpendicular (coplanar) to the orbital plane.

If we suppose a uniformly distributed Ω, the fraction of discs that will polar align is the ratio between the length of the dashed curve and the width of the Ω interval (i.e. $\pi/2$).Thus, the fraction f of discs that will polarly align is:

$$f(e_{\rm sp}, \beta_{\rm sp}) = 1 - \frac{2}{\pi}\Omega_{\rm crit}(e_{\rm sp}, \beta_{\rm sp}). \tag{7.8}$$

In the case of a binary population, we have to take into account the factor $f(e, \beta)$. To compute the distribution of polar discs with respect to orbital eccentricity, Equation (7.5) becomes:

$$P_{\rm pol}(e) = \int_{\beta_{\rm crit}(e)}^{\pi/2} P(e, \beta) f(e, \beta) {\rm d}\beta. \tag{7.9}$$

In circumbinary discs in hierarchical systems, the precession of the eccentricity vector drives the polar alignment process (Ceppi et al. 2023). The orbit precesses on a shorter timescale than the timescale for coplanar alignment. Hence, precession could lower the critical angle for polar alignment to its minimum value because the system quickly explores the Ω for which the critical angle is minimum. This is true only if, while the system is exploring different longitudes of the ascending node, the tilt of the disc does not decrease significantly. Otherwise, the polar alignment of the disc would still be favoured compared to binary systems but the initial longitude of the ascending node would nevertheless be relevant. If we suppose this hypothesis to hold, for discs orbiting the inner binary of a triple what really matters is the minimum critical angle no matter the longitude of ascending node. Independent of Ω, if the disc inclination is higher than the minimum critical angle (the one for $\Omega = 90°$) the disc will polar-align. Therefore, for triples $\beta_{\rm crit}(e, \Omega) = \beta_{\rm crit}(e, \Omega = 90°)$. Thus, Eq. (7.5) can be written as

$$\begin{aligned} P_{\rm pol}(e) &= \int_{\beta_{\rm crit}(e)}^{\pi/2} P(e, \beta) {\rm d}\beta = \\ &= -P_{\rm e}(e)\frac{\sigma_\beta}{N_\beta}\left[\exp\left(-\frac{\pi/2}{\sigma_\beta}\right) - \exp\left(-\frac{\beta_{\rm crit}(e)}{\sigma_\beta}\right)\right]. \end{aligned} \tag{7.10}$$

With the previous assumptions, we are left only with the eccentricity dependence both for binaries and hierarchical systems.

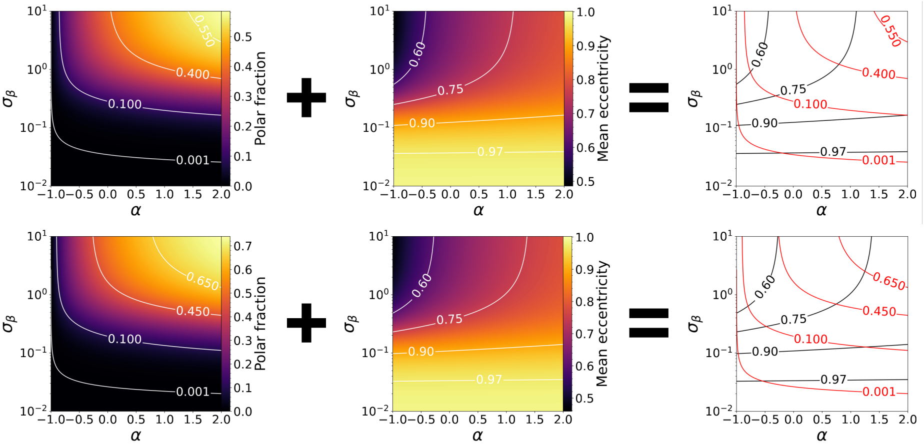

Figure 7.2: Fraction of polar discs ($F_{\rm p}$, leftmost column) and mean orbital eccentricity of systems hosting polar discs ($\langle e\rangle$, central column) for binary system population (top row) and triple system population (bottom row). As shown by the rightmost column, each point of the $\alpha - \sigma_\beta$ parameter space is uniquely characterized by a pair of $F_{\rm p}$ and $\langle e\rangle$ (crossing of two contour lines, red contour for polar fraction, black contour for mean eccentricity).

7.1.3 Polar fraction and mean eccentricity for multiple systems

Given a pair of values α and σ_β — the parameters of the distributions of eccentricity and mutual angle, respectively — we are now able to compute the expected polar disc fraction of an evolved population and the mean eccentricity of systems hosting a polar disc with Equations (7.6) and (7.7), respectively. For pure binaries and hierarchical systems, the polar disc distributions are given by Eqs. (7.9) and (7.10), respectively.

We semi-analytically computed these integrals over the α–σ_β parameter space for the initial distributions. The parameter α ranges between -1 and 2, while σ_β ranges between 0.01 and $+\infty$. The left panels in Figure 7.2 show how the fraction of expected polar discs in an evolved population $F_{\rm p}$ depends on α and σ_β for binary and hierarchical systems. In general, the binary population is less prone to host polar discs compared to systems with more than two stars. This is due to the different $\beta_{\rm crit}$ we used to describe the two populations. The higher the probability of having high eccentricity or mutual inclination, the more likely it is to find configurations with a high mutual inclination and orbital eccentricity which go polar more easily. Thus, $F_{\rm p}$ increases for higher α or σ_β.

The central panels in Figure 7.2 show the mean eccentricity of orbits hosting polar discs ($\langle e\rangle$) over the α–σ_β parameter space for binaries and hierarchical systems. The binary polar population tends to have higher $\langle e\rangle$, again due to the f factor (Eq. (7.8)). Indeed, the Ω interval allowing polar alignment is larger for more eccentric systems. Thus, we have more polar discs around highly eccentric systems. Lowering σ_β raises $\langle e\rangle$. Indeed, higher eccentricity values are required in regions where systems are mildly misaligned. Conversely, lowering α means lowering $\langle e\rangle$. The less likely is to have very eccentric systems in the initial population, the less eccentric the polar population will be.

Each pair of α–σ_β uniquely connects to a pair of $F_{\rm p} - \langle e\rangle$. This can be seen with contour lines in the right panel of Figure 7.2. A given pair of polar fraction $F_{\rm p}$ and mean eccentricity $\langle e \rangle$ contour lines cross only at one point of the α–σ_β parameter space. Thus, we are able to numerically invert the α–σ_β and $F_\mathrm{p} - \langle e \rangle$ coordinate systems to obtain plots in Figure 7.3. This plot showcases how α and σ_β depend on F_p and $\langle e \rangle$. Doing so, once we have constrained F_p and $\langle e \rangle$ from observations in a population we can constrain α and σ_β in the initial condition.

7.1.4 Measurement of polar fraction and mean eccentricity

Statistics on mutual inclinations between discs and stellar orbital planes are fairly scarce at the moment. Even if it is relatively easy to measure the disc inclination with respect to the sky plane, constraining the stellar orbital inclination is challenging. Thus, in the most recent literature surveys (Czekala et al. 2019; Zurlo et al. 2023) the sample size is around 15 discs. Among these discs, only one accretion disc is confirmed in a polar configuration: HD 98800B (Kennedy et al. 2012; Zúñiga-Fernández et al. 2021). Additionally, two discs are likely polar[3] (HD 142527, Balmer et al. (2022), and SR 24 N, Fernández-López et al. (2017)). Another notable example is 99 Her, which is a polar debris disc that likely evolved from a polar accretion disc (Smallwood et al. 2020). HD 98800B and SR 24N have additional companions outside the circumbinary disc. The semimajor axis ratios for the two systems are about 0.02 and 0.01 for HD 98800 and SR 24, respectively. The presence of additional bodies could possibly affect the process of polar alignment, for example, exciting Kozai-Lidov oscillations in the disc. However, the outer orbits of these triples are too wide to drastically impact the inner disc (Martin et al. 2014).

In the following, we show that the two different prescriptions for Ω in binaries and hierarchical systems with more than two stars result in similar values for the mean eccentricity, and in minor differences in terms of polar fraction distributions compared to the current uncertainties we have in surveys. Thus, here we do not distinguish between binaries and hierarchical systems in the sample.

We estimate the mean eccentricity of systems hosting polar discs averaging over confirmed polar systems (HD98800B), systems that are likely polar (SR24 N and HD142527) and the polar debris disc 99 Her. We obtain an average eccentricity of $\langle e \rangle^\mathrm{obs} = 0.67 \pm 0.11$.

To evaluate the polar disc fraction, if we take into account the single confirmed polar system (HD98800B) we end up with a polar fraction of 0.08. If, however, we include also the additional two likely polar systems (SR24 N and HD142527) the fraction raises up to 0.25. We take the average of these two values as a very rough estimate for the polar fraction, with their standard deviation as an error. The result is $F_\mathrm{p}^\mathrm{obs} = 0.17 \pm 0.08$. This fraction should be considered as an upper limit. In a sample of well-measured discs and orbital planes inclinations, there is a bias towards systems in which those quantities of interest are measured properly (for example because they are promising polar discs).

In the following, we use $F_\mathrm{p}^\mathrm{obs}$ and $\langle e \rangle^\mathrm{obs}$ as references for exploring the parameter space of the initial conditions.

7.2 Mapping observations onto the parameter space

For a binary (triple) population, Figures 7.3a and 7.3b (7.3c and 7.3d) show α and σ_β, respectively, as a function of $\langle e \rangle$ and F_p.

White regions are regions where no α and σ_β pair results in the given pair of $\langle e \rangle$ and F_p. In the following, we check which initial distribution is more likely to form the observed polar-aligned disc population in binaries and triples.

---

[3] There is a degeneracy of 180° in the orbital longitude of the ascending node (Czekala et al. 2019).

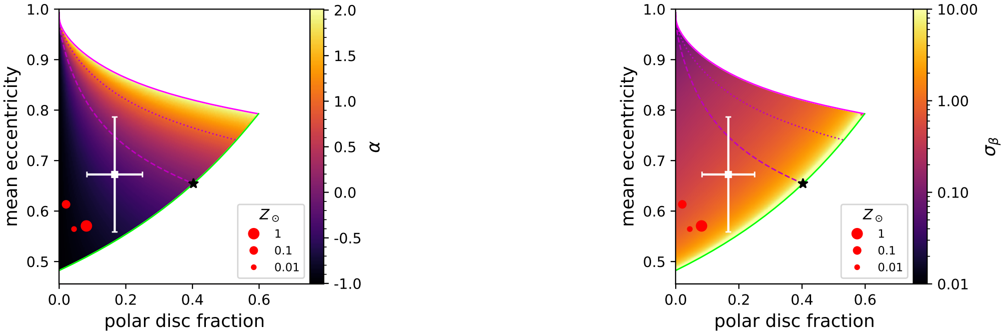

(a) α as a function of $\langle e\rangle$ and F_{p} for polar binary population.

(b) σ_β as a function of $\langle e\rangle$ and F_{p} for polar binary population.

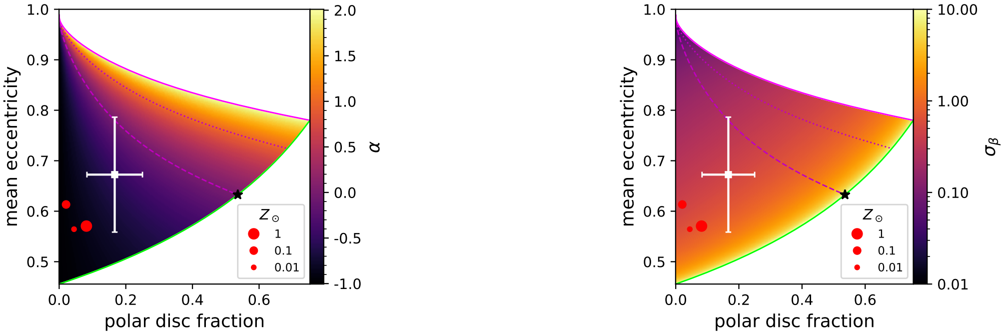

(c) α as a function of $\langle e\rangle$ and F_{p} for polar triple population.

(d) σ_β as a function of $\langle e\rangle$ and F_{p} for polar triple population.

Figure 7.3: α (left) and σ_β (right) as a function of $\langle e\rangle$ and F_{p} for binary (top) and triple (bottom) populations. White regions are $F_{\mathrm{p}} - \langle e\rangle$ pairs that cannot be generated by any $\alpha - \sigma_\beta$ pair. Purple curves are the parameter space region in which $\alpha = 2, 1, 0$ for solid, dotted and dashed, respectively. Green curves are the parameter space region in which $\sigma_\beta = \infty$. Black star is the solution for randomly distributed mutual inclination and eccentricity. White box point with error bars is the $F_{\mathrm{p}}^{\mathrm{obs}}$ and $\langle e\rangle^{\mathrm{obs}}$ observation values derived in section 7.1.4. Red circle points are $F_{\mathrm{p}} - \langle e\rangle$ pairs measured in the four Bate (2019) molecular cloud collapse simulations with different metallicities.

7.2.1 Randomly distributed initial condition

The first assumption we test is flat distributions in both orbital eccentricity and mutual inclination. This corresponds to taking the limit for σ_β approaching infinity and $\alpha = 0$ in Eqs. (7.1) and (7.2) respectively. The assumptions are: i) star formation at the molecular cloud level gives no preferential orbital eccentricity; ii) there is no preferred mutual inclination at the onset of stellar and disc formation.

Under these assumptions, we can compute analytically both the polar fraction and the mean eccentricity of the triple polar population, solving Eqs. (7.6) and (7.7) respectively with $P_\mathrm{e} = 1$ and $P_\beta = 2/\pi$. The results are $F_\mathrm{p}^\mathrm{tri} = 0.54$ and $\langle e \rangle^\mathrm{tri} = 0.63$.

For the binary population, we numerically integrate Eq. (7.9) since the f factor makes the integral not analytically solvable. Results for binaries are $F_\mathrm{p}^\mathrm{bin} = 0.40$ and $\langle e \rangle^\mathrm{bin} = 0.65$. We find these points in Fig. 7.3 at the crossing of the green and the dashed purple curves, marked with a star. Indeed, green and dashed purple curves are the limit for σ_β approaching infinity and $\alpha = 0$, respectively. In surveys, we find a polar fraction $F_\mathrm{p}^\mathrm{obs} = 0.17 \pm 0.08$ and a mean eccentricity $\langle e \rangle^\mathrm{obs} = 0.67 \pm 0.11$ (see Section 7.1.4). Even if the mean eccentricity in this configuration is compatible with the observed one, the observed polar fraction is not compatible with the expected polar fraction for a binary/triple population.

These circumbinary discs form around young stars due to accretion of surrounding gas and circularisation. Assuming that there is no correlation between the forming system's and the disc' angular momenta, then rather than assuming a flat distribution of mutual inclination, we expect $P_\beta = \sin\beta$. In this case, we can take advantage of Eq. (16) in Aly et al. (2015) which gives the fraction of configurations undergoing polar precession for a randomly distributed Ω, thus applicable to the binary population. Integrating over the eccentricity we obtain an expected $F_\mathrm{p}^\mathrm{bin} = 1 - \tanh(2/\sqrt{5})/\pi \approx 0.54 > 0.4$. This estimate is higher than the one previously computed given that, in this case, higher inclinations are favoured compared to coplanar configurations. Likewise, for the triple population, we analytically solve Eq. (7.6) with $P_\beta = \sin\beta$, obtaining $F_\mathrm{p}^\mathrm{tri} = (5 - \sqrt{5})/4 \approx 0.69 > 0.54$.

This result implies that non-uniform distributions — either in mutual inclination and/or orbital eccentricity — are needed to explain the observed polar population (or that many polar discs have been missed, which seems unlikely).

7.2.2 Correlated orbit-disc mutual inclinations

The first hypothesis we relax is the random initial distribution of mutual misalignment. We are still bound to move along the dashed purple curve in Figures 7.3b and 7.3d (where $\alpha = 0$). Over this restricted parameter space region, $\langle e \rangle$ has a lower limit given by the $\sigma_\beta = \infty$ case (i.e. 0.65 and 0.63 for binaries and triples, respectively), while F_p can span values from 0 to the $\sigma_\beta = \infty$ case (i.e. 0.40 and 0.54 for binaries and triples, respectively). The restricted parameter space region is compatible with $\langle e \rangle^\mathrm{obs}$ and $F_\mathrm{p}^\mathrm{obs}$. In particular, observations constrain σ_β to range between 0.25 and 0.78 for binaries and between 0.17 and 0.43 for triples which implies a narrow β distribution around $\beta = 0$, i.e. close to aligned orbit-disc systems should be more common at birth. Such correlation between the angular momenta of the disc and of the binary/triple orbit is needed to describe the observed polar population, under the assumption of randomly distributed initial orbital eccentricities.

7.2.3 Non-flat initial conditions

We now allow α and σ_β to explore the whole parameter space to fully exploit the information contained in the measurement of $\langle e \rangle$ and F_p. The observed mean eccentricity and polar fraction select a region of possible values of α and σ_β highlighted by the error bars in Fig. 7.3. For binaries, we obtain $\alpha \leq 0.6$ and $0.26 \leq \sigma_\beta \leq 1.8$. As for the triples, $\alpha \leq 0.46$ and $0.23 \leq \sigma_\beta \leq 1.87$.

Again, the small statistics suggest the presence of a correlation between the angular momenta of the discs and stellar systems. As for the eccentricity, even if it is still marginally compatible with a random distribution, present data suggest a decreasing function ($\alpha < 0$). Indeed, with a flat or slightly increasing eccentricity distribution, we would expect an higher mean eccentricity or an higher polar fraction.

7.3 Discussion

7.3.1 Constraining initial conditions in multiple stellar systems

Our analysis suggests that, to be compatible with present data about polar discs, initial distributions both for mutual inclinations and eccentricities have to be non-uniform. While we expect the angular momenta of forming discs and multiple systems to be correlated, the distribution of eccentricities we find does not completely match with observational results from surveys of evolved multiple stellar systems.

The observed evolved eccentricity distribution ranges from a uniform distribution ($\alpha = 0$) for orbits with semi-major axis of the order of 100 AU (Raghavan et al. 2010), up to an (increasing) thermal distribution ($\alpha = 1$) for 500 AU and becomes even steeper for larger systems (Duquennoy & Mayor 1991; Tokovinin 2020; Hwang et al. 2022). Conversely, we find an α between -1 and 0.6, pointing towards a slightly decreasing distribution, only marginally compatible with a uniform one.

First, we have to consider that we do not observe systems hosting circum-multiple discs with semi-major axis larger than about 100 AU (e.g. Czekala et al. 2019) nor numerical simulations form them (e.g. Elsender et al. 2023), thus we are interested in comparing our results with this range of semi-major axis in which α is closer to our findings (systems of $\sim$ 200 AU have $\alpha \sim 0.6$). In addition, gravitational interactions tend to raise the average eccentricity of the population. However, the thermalisation of the distribution could be only partially explained with gravitational interaction during cluster evolution which should act for much longer in order to push α from 0 to 1 (Heggie 1975; Weinberg et al. 1987). Thus, depending on the thermalisation timescale, we could reconcile our findings with observed distributions.

In addition, the orbital eccentricity can evolve through interactions between the binary and the circumbinary disc. For example, D'Orazio & Duffell (2021) numerically show that the hydrodynamical interaction with a coplanar disc could lead to preferred values of binary eccentricity. Even if it is not clear if this result is compatible with eccentricity surveys, the fact that our model does not take into account that the eccentricity of observed systems could be systematically different from the initial condition is also something to investigate in the future. To the best of our knowledge, there are no studies regarding this effect on misaligned circumbinary discs.

7.3.2 Comparison with cluster formation simulations

Nowadays, it is possible to perform detailed numerical simulations of the collapse of molecular clouds. In such simulations, the initial conditions of the cloud are set (e.g.

amount of turbulence, strength of magnetic fields, metallicity), and regulate the distribution of the parameters of the population of the forming protosystems. By tuning the properties of the cloud, one could aim at reproducing the measured distribution of inclination and eccentricity. This would result in an indirect measurement of the molecular cloud properties.

In this work, we applied this analysis to the molecular cloud collapse simulations by Bate (2019). We measured α and σ_β in the newly born protostellar systems population by fitting the synthetic $P_{\rm pol}$ (Eq. (7.5)) resulting from the simulation. We computed the expected $F_{\rm p}$ and $\langle e \rangle$ with Equations (7.6) and (7.7), respectively. Finally, we compared the values of $F_{\rm p}$ and $\langle e \rangle$ obtained from the simulations with the ones measured in observations (see Section 7.1.4).

The simulation set consists of four molecular clouds collapsing with four different metallicities (see details in Elsender & Bate 2021). We note that the higher the metallicity, the steeper the eccentricity distribution becomes. The steep decrease in eccentricity does not fit well with the same functional form as the observed distributions, on which we based our parameterisation. Thus, we are able to satisfactorily fit the three lower metallicities only.

The three red dots in Figure 7.3 represent the computed $F_{\rm p}$ and $\langle e \rangle$ for 3 different realisations of the same cloud but with different metallicities. The metallicity has an impact both on the eccentricity and mutual inclination distribution, hence the scatter in Figure 7.3. However, it appears to have too little impact on the properties of the population.

Regardless of the metallicity, the resulting polar disc fractions all are generally too low compared to observations. Given that the distribution of misalignment angles from the calculations of Bate (2019) and the observed systems are in good agreement (Elsender et al. 2023), this mismatch must be due to the lack of eccentric orbits in the simulations (possibly due to the simulations being too dissipative). We note however that, as discussed in Section 7.1.4, the proposed observational value has to be considered as an upper limit. In other words, we cannot currently completely rule out such small polar disc fractions from observations.

Finally, this analysis would benefit from numerical simulations producing distributions of mutual inclination and eccentricity, but for different sets of initial conditions (e.g. different amount of turbulence or magnetic field strength) — such as Bate (2019) with metallicity. This would lead to more robust predictions and better constraints for the polar disc population. Provided accurate measurements of $F_{\rm p}$ and $\langle e \rangle$, the method illustrated here constitutes a powerful way to infer the initial conditions in molecular clouds from disc populations.

7.4 Conclusions

We showed how to measure the correlation between the inclination of accretion discs and of forming stellar multiple systems (i.e. the distribution of mutual inclination) and the distribution of orbital eccentricity of such stellar systems at the onset of star and disc formation. Using our model, we were able to compute the two fundamental parameters describing the initial distributions of disc-orbit mutual inclination (σ_β) and orbital eccentricity (α). The only required measurements are the fraction of polar discs in a disc population ($F_{\rm p}$) and the mean eccentricity of systems hosting polar discs ($\langle e \rangle$). Despite the low statistics available, we find that:

1. The observed disc population is not compatible with a randomly distributed ini-

tial distribution of mutual misalignment – there must be a preference for aligned systems;

2. The orbital eccentricity is marginally compatible with a random distribution as observed in field stellar systems with semi-major axis below 100 au. The observed increasing eccentricity for wider orbits is still compatible with present data up to ~ 200 au. However, our model suggests a slight initial preference for circular orbits. We will investigate in future works if this discrepancy is compatible with the eccentricity evolution of young multiple stellar systems.

The limitation of this proof-of-concept toy model lies in the simplified distributions taken to describe the initial conditions. This simplification allowed us to describe the distributions with only two parameters, facilitating the computation of the relations between $\alpha - \sigma_\beta$ and $F_\mathrm{p} - \langle e \rangle$ pairs, the parameter space discussion, and the comparison with data. This gives no degeneracy in the model and a strictly two dimensional parameter space. A better observational constraint on the polar disc fraction would improve the robustness of this method. Also, the impact of the interaction with a polar disc on the eccentricity of the binary system has to be investigated further.

In conclusion, by measuring the polar disc fraction and the distribution of mutual inclinations, we showed that it is possible to infer the initial eccentricity and mutual inclination distributions of binaries and triples at birth. This will shed light on formation processes within molecular clouds that affect the population of binary and triple stars.

Part V

Conclusions

Summary and conclusions

In this thesis, we delved into the pivotal role of multiple stellar systems, particularly those with more than two and three stars, in shaping the formation and evolution of stellar populations. While these systems are the predominant playground for stellar and planetary formation, they are often regarded as complex exceptions, especially in comparison to the more extensively studied single stellar system configurations. The models and evolution theories developed over the past six decades have significantly enhanced our comprehension of accretion disc physics. However, it is essential to acknowledge that these models are typically idealised, as the majority of stars reside in multiple stellar systems. Furthermore, even stars observed as single entities may have been part of a multiple stellar system in the past or undergone temporary interactions with additional bodies, such as during flybys.

Theoretical challenges in modelling multiple stellar systems are mirrored by observational limitations, with multiplicity often concealed within disc cavities and hidden by surrounding material. Nevertheless, advancements in observational instruments are steadily revealing multiple stellar systems within discs, while astrometry is becoming more sensitive. The present capabilities offer us the opportunity to develop a comprehensive theory for disc and planet formation in multiple stellar systems and prepare our models for forthcoming observational data.

Throughout this thesis, I underlined the significance of taking into account multiple stellar systems in models of stellar and planetary formation. Ignoring the influence of multiplicity restricts the range of configurations for which our theories hold. Despite the added complexity, multiple stellar systems provide a unique way for a more profound understanding of the overall stellar and planet formation processes. The broader parameter space and diverse mechanisms inherent to these systems yield an abundance of observables that probe various aspects of ongoing physical processes, from gas hydrodynamics to dust dynamics and evolution. Importantly, these observables are indicative of fundamental hydrodynamical properties governing stellar and planet formation across diverse systems, not just those with two or more stars.

In particular, this thesis challenges the oversimplification of reducing the dynamics of multiple stellar systems with more than two stars to two-body system dynamics. It asserts the critical importance of accounting for the secular evolution of these systems and highlights additional phenomena inherent to multiple stellar systems that can elucidate observations, providing otherwise inaccessible insights in stellar formation physics.

- **In Part II** of this thesis, I presented the work I carried out in Ceppi et al. (2022) about how accreting mass distributes over the stars of a stellar system with more than two stars (a.k.a. differential accretion). We found that the presence of an additional body affects the way in which mass distributes over the stars and that this deviation can be interpreted with simple geometrical cross-section and gravitational interaction considerations. This is an example of an overlooked mechanism which can give us crucial insights into the way in which stars grow and evolve. Particularly, the key feature called 'twin peak' (i.e. an excess of unitary mass ratio binaries in surveys of multiple stellar systems mass ratios, Moe & Di Stefano 2017; El-Badry et al. 2019) is often justified by invoking this mechanism which should push binaries towards equalising their masses. Even if there are successful models which explain such feature Tokovinin & Moe (2020), there are hints that the picture could still be incomplete. For example, Torniamenti et al. (2021) showed the presence of a similar peak via a physically informed pairing of stars from the initial stellar mass function. In addition, the mass needed for this process to work (which is of the order of the stellar mass) is puzzling, given the mass available in the circumbinary discs modelled around such stellar systems. With the results of this work, higher accretion rates and faster equalisation times support the idea that the peak could be the result of multiple stellar systems accretion history. A definitive answer on what is the origin of the shape of multiple stellar systems mass ratio surveys can advance our understanding regarding their complex evolution.

- **In Part III**, I generalised the criteria for disc polar alignment in binary systems to multiple stellar systems with more than two stars. I showed that the conditions for a disc to librate in a pure binary system are necessary but not sufficient conditions when more than two stars are at play. In particular, the secular evolution of the system hierarchical levels has to be taken into account. The precession of the eccentricity vector, around which the disc angular momentum precesses in the polar configuration, can be too fast for the polar alignment process to occur. In Ceppi et al. (2023) I found that, generally, a disc orbiting a pair of stars with additional companions outside the disc is able to polarly align. Conversely, a disc orbiting more than two stars is not able to polarly align given that the eccentricity vector precesses too quickly. Even if this is true in the vast majority of the parameter space, there are specific configurations that contradict this general rule (see Figs. 6.5-6.2). These findings are crucial because, besides showing that ignoring the higher multiplicity of a hierarchical system can lead to wrong results, most of the multiple stellar systems with discs we observe with high mutual angles (i.e. possibly in a polar configuration) consist of more than two stars. In addition, once we realised that multiplicity matters in describing mutual inclination distributions, we found that different sub-populations of mutual inclination surveys are characterised by a specific hierarchical configuration. Indeed, discs orbiting pure binary systems (with or without external companions) mainly show either very high or nearly coplanar inclinations. Conversely, discs orbiting more than two stars mainly present mildly misaligned configurations. This suggests that multiplicity has a role in shaping such surveys and it changes the story these surveys are telling, opening new lines of research discussed in the future perspective below.

- **In Part IV**, I took advantage of the process of polar alignment to constrain statistical properties of the initial distribution of orbital parameters at the onset of binaries and multiple stellar system population formation. Given the faster timescale with which polar discs settle in a polar configuration and the sharp criterion that makes a disc librate instead of precessing, the population of polar discs in Class II somehow retains information about the distributions of the parameters at the epoch in which polar alignment was triggered. In particular, it is possible to retrieve information about the distribution of parameters polar alignment criteria are sensible to: the mutual inclination distribution and the eccentricity distribution. In Ceppi et al. (2024) I developed a simple toy model able to retrieve such information from the fraction of polar discs in a multiple stellar system population and the mean eccentricity of orbits hosting polar discs. Although the model will benefit from additional refinements (as discussed below in future developments), even now we can constrain initial distributions otherwise virtually inaccessible due to how much embedded in the natal cloud very young populations are. The constraints will be tighter by observationally improving the measurements of the fraction of polar discs and the mean eccentricity of the polar system population.

During my PhD, I worked together with other scientists to foster the approach I showcased in this thesis on multiple stellar systems study. In the following, I briefly mention the **works in which I had a prominent role** and which I think better represents the strength of this approach in order to investigate multiple stellar systems.

- In Rigliaco et al. (2023), we modelled a Herbig Ae/Be multiple stellar system T CrA, in the Corona Australis star-forming region. This system is interesting as scattered light images reveal the presence of a complex environment around it, composed of bright orbiting material at very high inclinations, along with a dark lane linked to the inner part of the outer disc mid-plane, and streamer that are tracing infalling material from the surrounding environment. The light curve suggests that the binary period is 29.6 yr. The system configuration consists of different geometrical planes. The orbit of the binary star is perpendicular to the outflows and is nearly edge-on. The disk is itself seen edge-on but with a different position angle.

  We worked both on SPHERE and ALMA observations of the system. In particular, I contributed with a full hydrodynamical model of the system along with radiative transfer simulation to obtain synthetic images to be compared with the available data. Moreover, both through simulations and with analytical considerations I analysed the accretion rates onto the stars, affected by the different inclinations of orbital and disc planes. Numerical simulations and the theoretical modelling of this multiple stellar system led to a deeper understanding of the system properties, stellar configuration, and the observed disc features.

- In Toci et al., under review, we tackled a longtime debate about the hierarchical triple system GG Tauri A and the size and shape of the cavity of its surrounding circumtriple disc. Despite numerous observational attempts, a comprehensive understanding of the geometry of the GG Tau A system is still lacking. Indeed, current astrometry is not capable of breaking the degeneracy between coplanar and misaligned orbits between the outer orbit of GG Tau A and its circumtriple disc. We investigated through detailed gas and dust hydrodynamical simulations both the coplanar and misaligned orbits finding that the best match between the position of the stars, the cavity size, and the dust ring size of GG Tau A is obtained with the misaligned configuration. Indeed, on a short timescale, it presents a circular cavity and dust ring as in the observations. However, no matter the disc misalignment, the cavity size and its eccentricity quickly grow on longer timescales and the model anymore reproduces the correct morphology. Why GG Tauri A disc cavity did not already develop an eccentric cavity remains to be investigated. Indeed, despite the success of our model in describing the system on short timescales, GG Tauri A is challenging. Some some mechanism must be at play in order to form the observed circular cavity, while avoiding the eccentricity growth observed in numerical simulations.

- In Alaguero et al., to be submitted, we investigated the (possibly) triple stellar system V892 Tau. The system is characterised by a binary orbited by a circumbinary disc plus a third companion (V892 Tau NE), which poor astrometry does not constrain if its orbit is bound or unbound. In this study, we focused on the emission and the kinematical signatures in the circumbinary disc to check if those signatures could be due to the interaction with a bound companion, and which kind of orbit the companion should follow in order to better reproduce them. First, we modelled the system as a pure circumbinary disc. However, a large fraction of the observed features could not be explained without taking into account the third body (Long et al. 2021). In Alaguero et al. we found, via a numerical investigation, that an eccentric inclined orbit of V892 Tau NE is the configuration better matching the observations. We successfully reproduced the disc extent and inclination with respect to the inner binary plane. As a matter of fact, the third body's misaligned orbit makes the disc oscillate and precess with time leading to a long-lived misalignment. Finally, the dissipation effects at play force the disc to eventually settle on a close to coplanar but slightly misaligned configuration, compatible with recent observation.

The quest for a complete understanding of multiple stellar systems formation and evolution is still ongoing, along with the formation of planets in such intricate environments. However, the past track of theory developments, to which this thesis integrates and further develops, is proof of the importance of stellar multiplicity in this field. Multiple stellar systems operate as sophisticated laboratories that we are still learning to handle properly. The methods I developed in this thesis, constitute promising tools to investigate the detailed physics of stellar and planet formation in multiple systems.

Further developments on this topic are the refinement of the models proposed. In this context, I think that a more thorough exploration of the implications of the polar alignment mechanism in young multiple systems would be particularly relevant.

- I found that differential accretion works differently in systems with more than two stars. Indeed, in the context of hierarchical systems, even in simple coplanar circular configurations it is not for granted that the lightest bodies accrete more mass (Ceppi et al. 2022). An additional interesting aspect of the problem, which we only slightly developed in that paper, is whether material even has stable configurations to settle into when orbiting the inner binary of a hierarchical triple. Indeed, the circum-inner binary disc is internally truncated by the binary (about 1-3 binary semi-major axes a_{tmin}) and externally limited by the Roche lobe size of the inner binary ($R_{\rm L}$). Thus, it is not granted that, even in a stable hierarchical system where $R_{\rm L} > a_{\rm in}$, there is enough space for the disc to be stable. Understanding which configurations are able to hold inner discs allows us also to predict which configurations are able to host planets, which necessarily need discs to assemble. Additionally, it would be relevant to add dust to the equation to complete the study of where there could be conditions for planet formation in multiple stellar systems.

- On top of the analytical criterion for polar alignment in hierarchical systems, the work I carried out in Ceppi et al. (2023) suggests a possible paradigm shift in interpreting the distribution of mutual angles in multiple stellar systems with discs.

Indeed, my study highlights the primary role that multiplicity has in shaping this distribution. In other words, depending whether systems are pure binaries or multiple stellar systems, the resulting distributions are significantly different. In particular, the population of mildly misaligned discs was previously interpreted as composed of discs which were on their way to dissipating the mutual inclination with their hosting stellar systems. Given that a vast portion, if not all, of the observed discs in that sub-population is actually composed of discs orbiting more than two stars, a more appealing interpretation is related to the dynamics of tilted multiple stellar systems. Indeed, we know that hierarchical triple systems with misaligned inner and outer orbits can undergo inclination oscillations via the Kozai-Lidov mechanism Lidov (1962); Kozai (1962). Given that the inclination oscillation timescale is much shorter than the timescale on which the disc could react, the tilt we are observing is likely a transitory configuration (due to an oscillating outer orbit inclination rather than a slowly decreasing tilt inherited from the initial system configuration). This would explain why virtually no pure binaries, nor discs orbiting the innermost hierarchical level of hierarchical systems show such a range of misalignment. Indeed, most of them show either very low (nearly coplanar) or very high (possibly polar) configurations. Therefore, a thorough investigation of the disc dynamics in Kozai-Lidov oscillating hierarchical systems is needed. Remarkably, it is not possible yet to establish the possible equilibrium configurations of any given multiple system based on the initial conditions. If future studies confirm the lack of mildly misaligned discs orbiting pure binaries, this could be a hint that we have to better study the timescales on which mutual inclination is dissipated and/or the initial distribution of mutual inclination between discs and binary orbit. In this case, nearly all binaries have had time to reduce the initial misalignment up to the coplanar configuration, which suggests an evolutionary timescale faster than the viscous timescale.

- The work done in Ceppi et al. (2024) aims at better constraining the initial distribution of misalignment at the onset of stellar formation. The preliminary work I carried out in the paper can be significantly improved by refining the model and with better statistics. For the sake of clarity, we developed a toy-model which depends only on two parameters so that we could lighten the computational effort and easily represent the workflow. However, more complex models could be built, especially for representing the initial distribution of eccentricity and mutual inclination. These distributions can be more sophisticated, with more complex functions depending on more parameters in order to be more flexible in retrieving the initial distribution. This will certainly increase the computational demand of the model and could lead to degenerate solutions. However, if this effort is complemented with higher statistics about polar discs, it will lead to more precise estimates of the parameters predicted by the model. Thanks to this, we could robustly measure distributions of mutual inclination and eccentricity for entire populations of very embedded multiple stellar systems. Reliable estimates of the initial mutual inclination distribution are key for the development discussed for the work on disc dynamics in multiple stellar systems undergoing Kozai-Lidov oscillations. Moreover, with (simulated and observed) molecular cloud collapse simulation sets spanning different values of molecular cloud properties (such as turbulence or magnetic fields), we could measure the impact that such properties have on the resulting synthetic population. Matching the synthetic population parameter distributions with the ones predicted by our model would eventually constrain molecular cloud properties at the origin of the overall stellar formation process in a robust manner.

The work done in this thesis is nothing more than small steps towards a comprehensive understanding of multiple stellar systems formation and evolution physics. The pivotal role of multiple stellar systems in the formation of stars, planets and everything teeming with life on them is more than ever evident. We just need to turn our gaze away from the Solar System and look at our nearest stellar system (α Centauri), the one closer to look at and maybe to reach in the future, to contemplate a triple stellar system. Along with present and future data on early stages of stellar formation, the hunt for planets with more than one sun is already on, with the BEBOP program (Martin et al. 2019) and it is only at its beginning (e.g. PLATO program Rauer et al. 2014). As scientists, we have to be prepared.

Appendices

APPENDIX A

Numerical tests

A.1 Accretion rate dependency on accretion prescription and spatial resolution

The accretion rate onto the stars of each stellar system is the main observable measured in this work. In the following sections we detail the numerical tests we performed to check that the measured accretion rates are reliable. In the first section we discuss how the accretion rates depend on the accretion prescription we used in our simulations. In the second section we test if the measured accretion rates are fully resolved in our numerical simulations.

A.1.1 Accretion prescription

Given that we used sink particles, there is only one possible numerical choice when setting the simulation: the sink radius $R_{\rm sink}$. SPH particles inside a sphere of radius $0.8\,R_{\rm sink}$ are automatically accreted onto the sink. The other particles inside a sphere of radius $R_{\rm sink}$ are accreted only if they are both gravitationally bound to the sink and have a sufficiently low angular momentum (Price et al. 2018b; Bate et al. 1995). In all our simulations, we set all the accretion radii equal to 0.1 au. This radius is roughly 4% of the smallest Roche lobe radius around secondary stars in binaries (that is the smallest Roche lobe radius around small binaries in triples).

To test how the choice of sink radii affects stellar accretion, we ran two additional simulations doubling and halving all sink radii of our reference simulation (the $ts2$ triple in Set 1). We integrated these two configurations for 100 outer orbit periods and we compared the accretion rates with the reference simulation.

Fig. A.1 shows the accretion rates and λ factors of test simulations, along with the reference one. We found that deviations from the reference simulation due to different sink radii are lower than 2%. The deviations due to the splitting we measure in this work are at least one order of magnitude higher, particularly in triples with the small binary lighter than the third body (compare Fig. A.1 with Fig. 5.2). Since the accretion rates are not affected by the choice of the accretion radius, we conclude that our sink particles measure stellar accretion properly.

A.1.2 Spatial resolution

To model accretion onto the stars in a realistic way, we simulate the entire circum-triple disc. This choice limits our ability to carefully model the formation and evolution of circumstellar discs. The simulations presented in this work barely resolve inner discs in the cavity of the circum-tripe disc. These discs do form within the cavity but with a

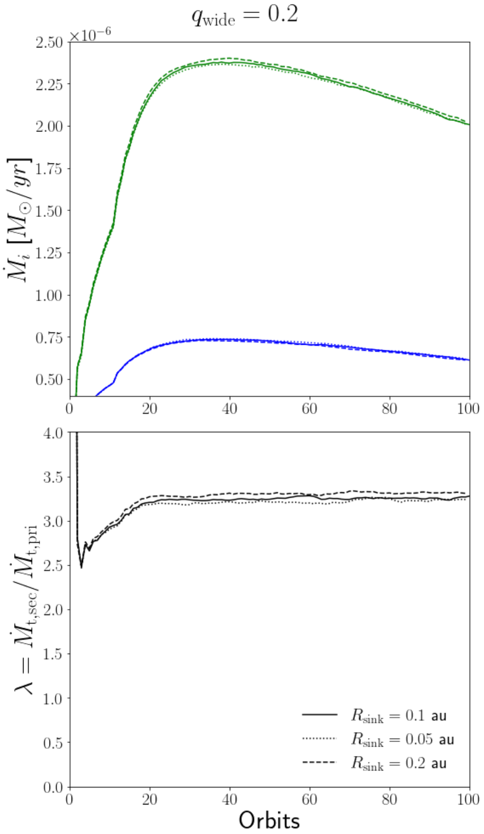

Figure A.1: Accretion rates and $\lambda = (\dot{M}_{\rm t,sec1} + \dot{M}_{\rm t,sec2})/\dot{M}_{\rm t,pri}$ factors measured in the triple simulations run to test the accretion prescription. On the upper panel are plotted the accretion rate of the secondary (green) and primary (blue) star. On the lower panel are plotted the ratio between the accretion rates. The solid line refers to the reference simulation $ts2$. Each different line style refer to different sink radii. The secondary accretion rate for triple system is the sum of the accretion rates of the small binary stars.

limited spatial resolution. Indeed, the spatial resolution in the immediate surrounding of the stars is about 20% of the Roche lobe radius (that is the spatial scale of the expected circum-stellar discs).

The net flux of mass through the Roche lobe boundary around each stars is the quantity that sets the individual accretion rates. The formation of discs inside the Roche lobes can introduce a delay during the disc formation phase. However, the mass that enters a given lobe will eventually fall onto the star. Indeed, mass cannot accumulate indefinitely in the Roche lobe. Here we wish to investigate whether the numerical resolution is high enough to ensure that the accretion rates onto the stars are well resolved.

To test the resolution of our simulations we ran two additional simulation: we multiplied by 4 and divided by 2 the number of particles in the $ts2$ reference simulation, obtaining a higher resolution simulation of 4 millions particles and a lower resolution simulation with 500k particles. We ran the higher resolution simulation for 40 outer orbit periods and the lower resolution simulation for 100 orbits. Their accretion rates and λ factors are shown in Fig. A.2.

The simulations show that the accretion rate of secondaries are fully resolved: the simulations at higher and lower resolution exhibit the same accretion rates as the reference simulation. We note that the accretion rate of the primary grows with resolution. This implies that the circum-primary disc material is not fully resolved. Hence, we conclude that our results based on secondary splitting and the resulting accretion rate deviations are not affected by resolution issues. However, the measured λ factors (both in binaries and in triples) are slightly overestimated, due to the underestimation of the primary accretion rate. The configuration we tested is the most affected by this issue, as it is the one with the lower primary accretion rate. Here, the λ factor is overestimated by $\approx 8\%$. It is worth highlighting that the ratio of λ factors constitutes a more reliable quantity given that we are comparing binary and triple simulations *at the same resolution*. However, our results about primary splitting (Sec. 5.2.3.2) have to be dealt with more caution. Our results are still relevant in the sense that – instead of discussing individual accretion rates – we report the relative deviations measured for different choices of orbital parameters.

A.2 Integration time

Our simulations in sets 1, 2, and 3 last 100 outer orbit periods. As discussed in section 5.1, this time span is half a viscous timescale at the inner edge of the disc. Thus, by the end of the simulation, the circum-triple disc has not reached steady-state. Given the number of simulations required to perform the analysis made in this work, modelling the entire disc viscous evolution is beyond our computational ability. Moreover, note that the configuration considered here, where the mass reservoir in the evolving disc is limited, will not actually settle into a steady state even for longer times. However, in this work we are interested in the way in which mass distributes from the circum-multiple disc over the stellar system stars. This is well measured by the ratio of the stellar accretion rate. In all the simulations we run, these ratios show an initial transient of less than 20 binary orbits – regardless of the multiplicity and of the orbital parameters of the system, before settling down into quasi equilibrium. To further test this, we ran the three $q_{\rm wide} = 0.65$ simulations in Set 1 for longer integration times. Fig. A.3 shows the accretion rates and the λ factors measured in these simulations. We find that, independently on the total accretion rate, mass divides between the sinks in the same way (i.e. we measure a constant λ factor) until the gas smoothing length in the surrounding of the small binary exceeds the small binary semi-major axis. This happens around 250 orbits and

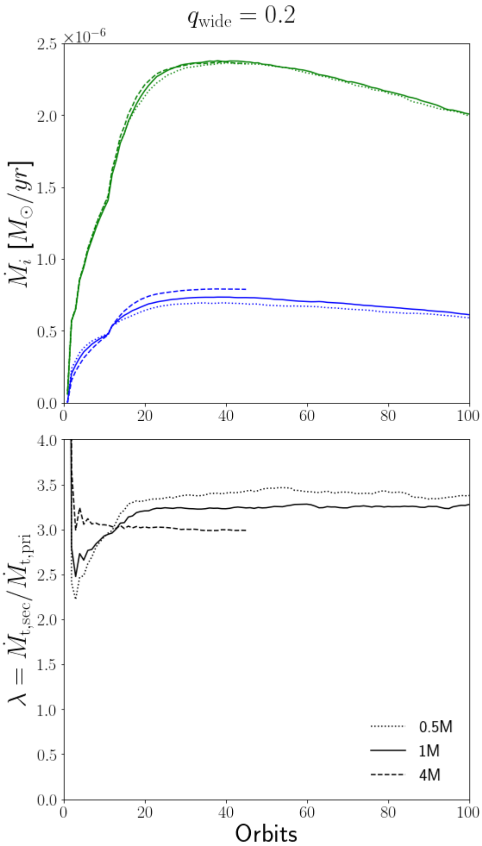

Figure A.2: Accretion rates and $\lambda = (\dot{M}_{\text{t,sec1}} + \dot{M}_{\text{t,sec2}})/\dot{M}_{\text{t,pri}}$ factors measured in the triple simulations run to test the resolution. On the upper panel are plotted the accretion rate of the secondary (green) and primary (blue) star. On the lower panel are plotted the ratio between the accretion rates. The solid line refers to the reference simulation $ts2$. Dotted and dashed line refer to the lower and higher resolution simulations, respectively. The secondary accretion rate for triple system is the sum of the accretion rates of the small binary stars.

it is a purely numerical effect caused by the loss of resolution around the small binary. Thus, even if the total accretion rate will evolve towards the steady-state, we expect the accretion rate ratios to remain constant. This allowed us to reliably measure the λ factors even if our simulations have not reached a steady-state.

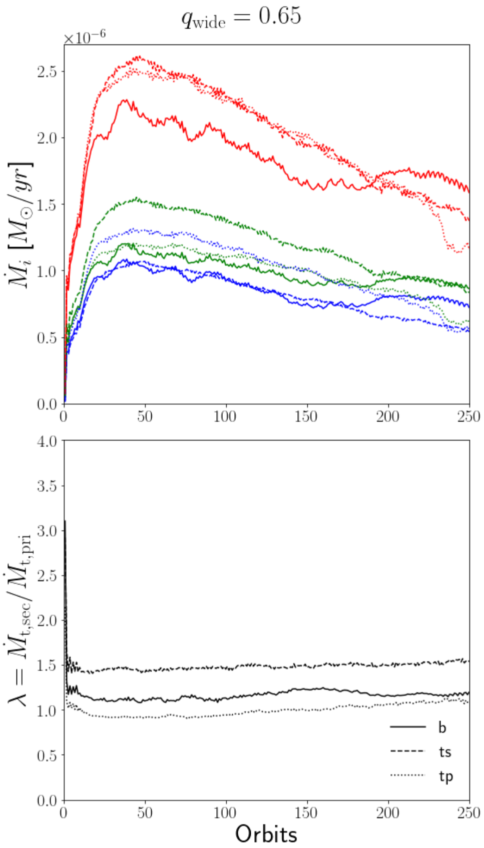

Figure A.3: Accretion rates and $\lambda = (\dot{M}_{\mathrm{t,sec1}} + \dot{M}_{\mathrm{t,sec2}})/\dot{M}_{\mathrm{t,pri}}$ factors measured in the triple simulations run to test longer integration times. On the upper panel are plotted the total accretion rate of the system (red) and the accretion rate of the secondary (green) and primary (blue) star. On the lower panel are plotted the ratio between the accretion rates (secondary over primary). The solid, dashed and dotted lines refer to the binary ($b65$), ts triple ($ts65$) and tp triple ($tp65$) simulations, respectively. The secondary (primary) accretion rate for ts (tp) triple system is the sum of the accretion rates of the small binary stars.

APPENDIX B

Smoothed Particle Hydrodynamics

Smoothed Particle Hydrodynamics (SPH) is a numerical method built on a Lagrangian scheme firstly developed for the study of astrophysics systems involving fluid dynamics (Gingold & Monaghan 1977; Lucy 1977).

In this chapter we discuss the basis of SPH, with the aim of better understand their implementation in the code used to carry out simulations in this thesis, PHANTOM.

The first part is devoted to show how the equations of hydrodynamics are computed on a set of particles that discretize the simulated fluid. We start from computing the density of the fluid considering a discrete set of particles. This is a first example of kernel interpolation, and later it will be also the base onto which build the SPH scheme, as in Price (2012).

B.1 Density calculation and equations of motion

The first step in a numerical simulation is to discretise the physical quantities that describe the system in order to treat them numerically. The basis of SPH (as for others numerical approaches to hydrodynamics) lies in the way chosen to rebuild continuum physical quantities from their discrete description. Different approaches are related to different possible ways of describing a fluid.

The first approach is the Eulerian description. In this view we consider a small volume, fixed in space, through which the fluid flows, carrying its physical properties. The variables that describe the fluid (e.g. density ρ, temperature T) are function of the time and of the position of the considered volume (e.g $\rho(t, \mathbf{r})$). In this view changes in physical quantities are time derivatives at fixed position.

The second one is the Lagrangian description in which we consider a specific fluid element with its physical properties. The variables that describe the fluid are function of the time and of the considered fluid element (e.g $\rho(t, \mathbf{a})$, where $\mathbf{a}$ is a label for that particular fluid element). In this view any changes in physical quantities is time derivatives at a fixed fluid element.

B.1.1 Computing density

If we want to compute the density $\rho(\mathbf{r})$ at a certain time from a set of point masses of mass m, we can create (in line with the Eulerian description) a mesh and separate the point masses in the cells. A basic way to compute the density of a cell is to divide the mass it contains by its volume (fig 1a).

Limitations to this approach are its dependency from the geometry of the mesh and the lack of conservation of physical quantities. It also easily over-sample sparse region and under-sample dense one.

Another possibility is to not construct a mesh, but to compute the density at a point **r** sampling the local mass distribution. For example one can build a sphere of radius R (with R fixed or tuned to contain a fixed number $N_{\rm nb}$ of neighbour particles) and define

$$\rho(\mathbf{r}) = \frac{\sum_{b=1}^{N_{\rm nb}} m_b}{\frac{4}{3}\pi R^3}. \tag{B.1.1}$$

Thereby we have no dependency on the geometry of the mesh, and we tune our sampling on the density needs.

However this approach is often very noisy, due to the fact that a particle crossing the sphere surface, even if away from **r**, can affect significantly ρ.

A way to reduce this problem is to weight the impact of a particle on the density computation in **r** with its distance from **r** itself. This leads to the third approach, a weighted summation on the particles, that is the SPH approach we present in the next section.

B.1.2 The SPH way to compute density

The third way to compute $\rho(\mathbf{r})$ is by a weighted summation over the mass of the nearest $N_{\rm nb}$ particles around **r**. So

$$\sum_{b=1}^{N_{\rm nb}} m_b W(\mathbf{r} - \mathbf{r}_b, h), \tag{B.1.2}$$

where W is a generic function (called *smoothing kernel*) that weights the impact of a particle to the sum, in respect of how far the particle is, compared to a scale length h called *smoothing length.*

Since conservation of total mass implies that $\int_V \rho dV = \sum_{b=1}^{N_{\rm part}} m_b$, with $N_{\rm part}$ the total number of particles, W has to be normalised:

$$\int_V W(\mathbf{r} - \mathbf{r}_b, h) dV = 1. \tag{B.1.3}$$

A good smoothing kernel needs to grant:

1) A weighting that is positive, decreases monotonically with relative distance and has smooth derivatives;

2) Symmetry with respect to $\mathbf{r} - \mathbf{r}_b$, thus W has to depend on $|\mathbf{r} - \mathbf{r}_b|$;

3) A bell shape in order to limit the impact of far away particles on the summation.

In order to fullfill the above requests, the first choice that comes to mind is the Gaussian

$$W(\mathbf{r} - \mathbf{r}_b, h) = \frac{\sigma}{h^d} exp\left[-\frac{(\mathbf{r} - \mathbf{r}_b)^2}{h^2}\right], \tag{B.1.4}$$

where d is the number of spatial dimension and σ a normalisation factor that depends on d.

The main problem with a Gaussian kernel is that its strictly positive everywhere in space, and this leads to account for the contribution of all the particles of the system, with a consequent computational cost that scales with $N_{\rm part}^2$, with $N_{\rm part}$ the number of particles of the system.

This behaviour can be fixed setting the Gaussian-like kernel to zero outside of a certain radius (that is to create two sets of particles, one with particles inside a certain number of h that count in the computation of ρ, and one outside that do not contribute), with the advantage that the computational cost reduces to $O(N_{\rm nb}N_{\rm part})$ and the disadvantage to make the density estimate more noisy.

B.1.3 Setting the smoothing length

We turn now our attention in how to set the smoothing length h, noting that it is free to be a function of time and space. It make sense to have h depends on the position because in our system we want an even resolution and the same h can be too wide for dense region or uselessly short (contain no neighbour) for sparse one. Moreover the evolution in time of the system changes the optimal smoothing length for the same spot.

That's why it worth to relate the smoothing length in **r** to the local density of particles and write

$$h(\mathbf{r}) \propto n(\mathbf{r})^{-1/d}, \tag{B.1.5}$$

with

$$n(\mathbf{r}) = \sum_b W(\mathbf{r} - \mathbf{r}_b, h). \tag{B.1.6}$$

If we consider particles with the same mass, $n(\mathbf{r})$ (from which h depends) becomes proportional to $\rho(\mathbf{r})$, that in turn depends on h. So we now have two equations that have to be solved[1] simultaneously to compute $h(\mathbf{r})$, namely

$$\rho(\mathbf{r}_a) = \sum_b m_b W(\mathbf{r}_{ab}, h) \tag{B.1.7}$$

and

$$h(\mathbf{r}_a) = \eta \left(\frac{m_a}{\rho_a} \right)^{1/d}, \tag{B.1.8}$$

where we computed the quantities at the position $\mathbf{r}_a$ of the particle **a**, and introduced the notation $\mathbf{r}_{ab} \equiv \mathbf{r}_a - \mathbf{r}_b$.

B.1.4 Density and equations of motion

We now show that the interpolation of the density described above (Eq. B.1.7), along with its gradient, can be the pillar onto which build the SPH algorithm.

We begin from the discrete Lagrangian that controls the dynamics of the particles. With T the kinetic energy and V the thermal energy we can write

$$L = T - V = \sum_b m_b \left[\frac{1}{2}\mathbf{v}_b^2 - u_b\left(\rho_b, s_b\right) \right], \tag{B.1.9}$$

where u is the specific internal energy, wrote as a function of density and entropy, and **v** the velocity of the particle.

Note that even without considering this Lagrangian as the discrete version of the continuum hydrodynamics one (it can be shown that it is, e.g. Eckart (1960)), it's symmetries and thus conservation properties will be inherited by its consequent equations of motion.

Through the least action principle we can retrieve the Euler-Lagrange equation,

$$\frac{d}{dt}\left(\frac{\partial L}{\partial \mathbf{v}} \right) - \frac{\partial L}{\partial \mathbf{r}} = 0. \tag{B.1.10}$$

Before to compute the derivatives in (B.1.10), we must stop to stress two important assumption we made retrieving it:

---

[1] with a root-finding method like Newton-Raphson or Bisection.

1. We assumed that the Lagrangian in (B.1.9) is differentiable, in order to use Euler-Lagrange equations;

2. We are not considering the discrete time integration in the Euler-Lagrange equation.

The first assumption exclude any chance to treat discontinuity in our system without special consideration (e.g. as discussed in section B.2, introducing viscosity).

The second remind us that the choice of a particular integration scheme influence the numerical properties of our simulation (e.g. lack of exact conservation of quantities, with a non symplectic integrator)

We can now insert the Lagrangian in the Euler-Lagrange equation, obtaining the equations of motion:

$$\frac{\partial L}{\partial \mathbf{v}_a} = m_a \mathbf{v}_a; \tag{B.1.11}$$

and

$$\frac{\partial L}{\partial \mathbf{r}_a} = -\sum_b m_b \left.\frac{\partial u_b}{\partial \rho_b}\right|_s \frac{\partial \rho_b}{\partial \mathbf{r}_a}. \tag{B.1.12}$$

These equations are computed at the position of particle **a** and assuming that entropy s is constant, so implying no dissipation.

We derive the $[\partial u_b/\partial \rho_b]_s$ term in (B.1.12) from the first thermodynamic principle cast per unit mass,

$$du = Tds + \frac{P}{\rho^2} d\rho, \tag{B.1.13}$$

where u is the specific internal energy, Tds is the heat added to the system per unit mass and $P/\rho^2 d\rho$ is the work on the fluid per unit mass[2].

From (B.1.13) we see that the change in specific thermal energy at constant entropy reads

$$\left.\frac{\partial u_b}{\partial \rho_b}\right|_s = \frac{P_b}{\rho_b^2}. \tag{B.1.14}$$

Moreover, in section B.1.6 we compute the $\partial \rho_b/\partial \mathbf{r}_a$ derivative in equation (B.1.12), that is the gradient of the density at particle b respect to the position of particle a. There we show that substituting into (B.1.12) the equation (B.1.14) and the density gradient in (B.1.26) gives us the SPH equations of motion

$$\frac{d\mathbf{v}_a}{dt} = -\sum_b m_b \left[\frac{P_a}{\Omega_a \rho_a^2} \frac{\partial W(\mathbf{r}_{ab}, h_a)}{\partial \mathbf{r}_a} + \frac{P_b}{\Omega_b \rho_b^2} \frac{\partial W(\mathbf{r}_{ab}, h_a)}{\partial \mathbf{r}_a} \right], \tag{B.1.15}$$

that for a constant smoothing length reduces to

$$\frac{d\mathbf{v}_a}{dt} = -\sum_b m_b \left(\frac{P_a}{\rho_a^2} + \frac{P_b}{\rho_b^2} \right) \nabla_a W(\mathbf{r}_{ab}, h_a). \tag{B.1.16}$$

From the latter equations we can stress again the dissipationless nature of SPH, computing the time derivatives of the total linear momentum or total angular momentum,

---

[2] PdV is the work done *by* the system, so $\frac{P}{mN}\, dV$ is the work done per unit mass, with N and m the number and the mass of particles respectively, but V/N is the volume of a particle, that is m/ρ. So $\frac{dV}{N} = m\, d\frac{1}{\rho} = -\frac{m}{\rho^2} d\rho$. Thus the work done *on* the system per unit mass is $\frac{P}{\rho^2} d\rho$.

respectively $\sum_a m_a \mathbf{v}_a$ and $\sum_a \mathbf{r}_a \times m_a \mathbf{v}_a$, and obtaining *exactly* zero. These conservation properties follows from the symmetries of the Lagrangian and of the SPH density estimate (B.1.7) in it, as stated by Noether's theorem.

It remains to determine how energy evolves. In the absence of dissipation, from equation (B.1.14), we can derive

$$\frac{du_a}{dt} = \frac{P_a}{\rho_a^2} \frac{d\rho_a}{dt}. \tag{B.1.17}$$

Deriving the (B.1.7) to express the time derivative of the density we obtain an SPH equation for the evolution of the specific internal energy u, namely

$$\frac{du_a}{dt} = \frac{P_a}{\Omega_a \rho_a^2} \sum_b m_b \left(\mathbf{v}_a - \mathbf{v}_b\right) \cdot \nabla_a W \left(\mathbf{r}_{ab}, h_a\right). \tag{B.1.18}$$

B.1.5 Kernel interpolation

The process shown in section B.1.2 in order to compute density from a set of point masses scattered in space is a special case of the general process of interpolating a quantity $A(\mathbf{r})$ at any point in space from quantities defined only on a set of discrete point $\{\mathbf{r}_\mathrm{b}\}$ (that, in the density example, are the positions of the particles).

The general theory of interpolation starts from the identity

$$A\left(\mathbf{r}\right) = \int A\left(\mathbf{r}'\right) \delta\left(\mathbf{r} - \mathbf{r}'\right) d\mathbf{r}' \tag{B.1.19}$$

where A is scalar variable and δ the Dirac delta function.

Than we approximate the δ function with a first order approximation function W with finite width h, writing

$$A\left(\mathbf{r}\right) = \int A\left(\mathbf{r}'\right) W\left(\mathbf{r} - \mathbf{r}', h\right) d\mathbf{r}' + O(h^2), \tag{B.1.20}$$

where W has to be normalised in space and has to tend to a delta for small h. The function W is the smoothing kernel introduced for the computing of the density.

To finally recover the form of an interpolated quantity, $\langle A(r) \rangle$, we discretise the equation (B.1.20) on a finite set of points (the particles), by replacing the integral with a summation, and the mass element $\rho d\mathbf{r}$ with the particle mass m, obtaining

$$\langle A\left(\mathbf{r}\right) \rangle \approx \sum_b m_b \frac{A_b}{\rho_b} W(\mathbf{r} - \mathbf{r}_b, h), \tag{B.1.21}$$

that no wonder reduces to (B.1.7) for $A = \rho$.

In order to construct the SPH-style hydrodynamic equations that have to be solved to simulate our system we have to define the vector operators that appear in the hydrodynamic equations.

For example we can define the gradient of the function $A(\mathbf{r})$ taking the gradient of (B.1.21), that results in

$$\nabla \langle A\left(\mathbf{r}\right) \rangle \approx \sum_b m_b \frac{A_b}{\rho_b} \nabla W(\mathbf{r} - \mathbf{r}_b, h), \tag{B.1.22}$$

that has the noticeable property of depending on the gradient of the kernel function (that we know, and we chosen wisely) and not from the gradient of A (that we don't know).

The same can be done for vector quantities (e.g. $\nabla \cdot \mathbf{A}(\mathbf{r})$, $\nabla \times \mathbf{A}(\mathbf{r})$), we report the computation of $\nabla \cdot \mathbf{A}(\mathbf{r})$, as it will be useful in section B.1.7:

$$\nabla \cdot \mathbf{A}(\mathbf{r}) \approx \sum_b m_b \frac{\mathbf{A}_b}{\rho_b} \cdot \nabla W(\mathbf{r} - \mathbf{b}_b, h) . \tag{B.1.23}$$

Also, from this example is straight to show that the approximation done in the δ approximation in (B.1.20) are not negligible, as from (B.1.22) it's clear that the defined gradient of a function A doesn't reduce to zero for a constant A.

It became necessary to find smart ways to define operators, rather than the bare definition above. For example, for the gradient, it's meaningful (given that the gradient of a constant is not zero) to write

$$\nabla A = \nabla(1 \cdot A) = \nabla A + A\nabla 1 \tag{B.1.24}$$

So we can redefine the definition (B.1.22) of the gradient in $\mathbf{r}_a$ with

$$\begin{aligned}
&\nabla \langle A(\mathbf{r}_a)\rangle \equiv \nabla A(\mathbf{r}_a) - A_a \nabla 1 = \\
&= \sum_b m_b \frac{A_b}{\rho_b} \nabla W(\mathbf{r}_{ab}, h) - \sum_b m_b \frac{A_a}{\rho_b} \nabla W(\mathbf{r}_{ab}, h) = \\
&= \sum_b m_b \frac{A_{ab}}{\rho_b} \nabla W(\mathbf{r}_{ab}, h).
\end{aligned} \tag{B.1.25}$$

In principle we can now write hydrodynamics equations in the SPH way sobstituting the SPH version of operators in them and implement them in a code.

B.1.6 SPH equations of motion

We have to compute the $\partial\rho_b/\partial\mathbf{r}_a$ derivative in equation (B.1.12), that is the gradient of the density at particle b respect to the position of particle a. In order to compute this gradient we take the gradient of the density estimate, giving

$$\frac{\partial \rho_b}{\partial \mathbf{r}_a} = \frac{1}{\Omega_b} \sum_c m_c \frac{\partial W(\mathbf{r}_{bc}, h_b)}{\partial \mathbf{r}_a} (\delta_{ba} - \delta_{ca}) , \tag{B.1.26}$$

where δ is the Dirac delta and Ω_b is a term to account for the gradient of the smoothing length (as it depends on ρ), defined as

$$\Omega_a = \left[1 - \frac{\partial h_a}{\partial \rho_a} \sum_b m_b \frac{\partial W(\mathbf{r}_{ab}, h_a)}{\partial h_a} \right] . \tag{B.1.27}$$

Using equation (B.1.8) to compute h, give us

$$\frac{\partial h}{\partial \rho} = -\frac{h}{\rho d} . \tag{B.1.28}$$

Using (B.1.14) and (B.1.26) in (B.1.12), and some algebra, gives us the SPH equations of motion

$$\frac{d\mathbf{v}_a}{dt} = -\sum_b m_b \left[\frac{P_a}{\Omega_a \rho_a^2} \frac{\partial W(\mathbf{r}_{ab}, h_a)}{\partial \mathbf{r}_a} + \frac{P_b}{\Omega_b \rho_b^2} \frac{\partial W(\mathbf{r}_{ab}, h_a)}{\partial \mathbf{r}_a} \right] , \tag{B.1.29}$$

that for a constant smoothing length reduces to

$$\frac{d\mathbf{v}_a}{dt} = -\sum_b m_b \left(\frac{P_a}{\rho_a^2} + \frac{P_b}{\rho_b^2} \right) \nabla_a W(\mathbf{r}_{ab}, h_a). \tag{B.1.30}$$

B.1.7 SPH equations and kernel interpolation

We have constructed three equations into which is condensed the physics that rules our particles (through the Lagrangian defined in Eq. B.1.9), the thermodynamics of our system (Eq. B.1.13) and our choice of how to compute density (Eq. B.1.7).

Theses equations are:

$$\rho(\mathbf{r}_a) = \sum_b m_b W(\mathbf{r}_{ab}, h); \quad h(\mathbf{r}_a) = \eta \left(\frac{m_a}{\rho_a} \right)^{1/d}, \tag{B.1.31}$$

$$\frac{d\mathbf{v}_a}{dt} = -\sum_b m_b \left[\frac{P_a}{\Omega_a \rho_a^2} \frac{\partial W(\mathbf{r}_{ab}, h_a)}{\partial \mathbf{r}_a} + \frac{P_b}{\Omega_b \rho_b^2} \frac{\partial W(\mathbf{r}_{ab}, h_a)}{\partial \mathbf{r}_a} \right], \tag{B.1.32}$$

$$\frac{du_a}{dt} = \frac{P_a}{\Omega_a \rho_a^2} \sum_b m_b \mathbf{v}_{ab} \cdot \nabla_a W\left(\mathbf{r}_{ab}, h_a\right). \tag{B.1.33}$$

To recognise that these are the SPH (or interpolated) version of the not yet mentioned continuum hydrodynamics equations (continuity, Euler and energy respectively), we have to recall the definitions of vector operator given in B.1.5.

We can take as an example the density estimate. Taking the time derivative, with constant smoothing length, we have

$$\frac{d\rho_a}{dt} = \sum_b m_b \mathbf{v}_{ab} \cdot \nabla_a W\left(\mathbf{r}_{ab}, h\right), \tag{B.1.34}$$

that consist in two terms.

Comparing the first one,

$$\mathbf{v}_a \cdot \sum_b m_b \frac{\rho_b}{\rho_b} \nabla_a W(\mathbf{r}_{ab}, h), \tag{B.1.35}$$

with the definition of the gradient in (B.1.22) make us recognize it as $\mathbf{v} \cdot \nabla \rho$.

For the second, comparing with the divergence definition in (B.1.23), we have

$$\sum_b m_b \frac{\rho_b \mathbf{v}_b}{\rho_b} \cdot \nabla_a W(\mathbf{r}_{ab}, h) \approx \nabla \cdot (\rho \mathbf{v}). \tag{B.1.36}$$

Putting things together, we retrieve the continuity equation, namely

$$\frac{d\rho}{dt} = \mathbf{v} \cdot \nabla \rho - \nabla \cdot (\rho \mathbf{v}) = -\rho \nabla \cdot \mathbf{v}. \tag{B.1.37}$$

The need of differentiability of the Lagrangian (thus of density and thermal energy) and the above-requested absence of dissipation (taking entropy as constant) imply the need of special care in intrinsic dissipative situation, as we discuss in the next section.

B.2 Artificial viscosity

The non dissipative SPH formulation force us to introduce an artificial viscosity (Monaghan 1997) to deal with situation where dissipation is required. First of all to treat shocks, where we have an increase of entropy, and to prevent interpenetration of particles.

The problems with shocks arise from the assumption of differentiability of the Lagrangian made in the previous sections. This problem emerge[3] as the shocked quantities varies on a not resolved scale (typically a mean free path of the gas particles), leading to an apparent discontinuity on the large scale.

To deals with shocks we can smooth them over a small number of smoothing lengths in order to maintain the shock appearance on a large scale, while keeping finite gradients and preserving the correct behavior away from the shock. In other words making the shock no longer discontinuous on the small scale (Price 2008).

For this purpose we have to modify the stress tensor, that until now consists only in the isotropic pressure term, adding a dissipation term to diffuse these discontinuities.

A possible[4] way (shown by Monaghan (1997)) to achieve this, is to introduce a dissipative artificial viscosity term in addition to the pressure term, of the form

$$q_a^{\mathrm{AV}} = \begin{cases} \frac{1}{2}\alpha_a^{\mathrm{AV}}\rho_a v_{\mathrm{sig},a}\left|\mathbf{v}_{ab}\cdot\hat{\mathbf{r}}_{ab}\right|, & \mathbf{v}_{ab}\cdot\hat{\mathbf{r}}_{ab} < 0 \\ 0 & \mathbf{v}_{ab}\cdot\hat{\mathbf{r}}_{ab} \geq 0 \end{cases} \tag{B.2.1}$$

with

$$v_{\mathrm{sig},a} = c_{\mathrm{s},a} + \beta^{\mathrm{AV}}\left|\mathbf{v}_{ab}\cdot\hat{\mathbf{r}}_{ab}\right|. \tag{B.2.2}$$

The β^{AV} parameter was originally added to prevent particle penetration in high Mach number shocks (Monaghan 1989).

A switch has to be added to reduce dissipation away from shocks, while providing as little dissipation as possible and in the meantime resolving the shock. This is done by evolving α^{AV} in time (Morris & Monaghan 1997) and only at the shock location.

Although in this thesis we have not dealt with shock situations, we dealt with the artificial viscosity technique. This is because the artificial viscosity modification of the Euler equation links to the Navier-Stokes viscosity terms and so it can be used to represent a physical viscosity in the whole disc (Lodato & Price 2010).

Actually, from the study of second-order derivatives in SPH formulation (Español & Revenga 2003), it can be shown that

$$-\sum_b \frac{m_b}{\rho_b}\left(\mathbf{A}_{ab}\cdot\hat{\mathbf{r}}_{ab}\right)\frac{F_{ab}}{|r_{ab}|} = \frac{1}{5}\nabla\left(\nabla\cdot\mathbf{A}\right) + \frac{1}{10}\nabla^2\mathbf{A}, \tag{B.2.3}$$

where we defined $\nabla_a W(\mathbf{r}_{ab}, h) \equiv F_{ab}\hat{\mathbf{r}}_{ab}$.

The comparison of this expression with the Euler equation (B.1.15) with the addition of artificial viscosity stress tensor term (neglecting the non linear term) show that the artificial viscosity term can be written as

$$\left(\frac{d\mathbf{v}}{dt}\right)_{AV} \approx \alpha^{\mathrm{AV}} v_{\mathrm{sig}}\left|r_{ab}\right|\left(\frac{1}{5}\nabla\left(\nabla\cdot\mathbf{v}\right) + \frac{1}{10}\nabla^2\mathbf{v}\right), \tag{B.2.4}$$

---

[3] in SPH and real physical systems.

[4] also the way implemented in PHANTOM.

an so it mimics an actual Navier-Stokes viscosity with

$$\nu^{\mathrm{AV}} \approx \frac{1}{10}\alpha^{\mathrm{AV}} v_{\mathrm{sig}} \left| r_{ab} \right| , \tag{B.2.5}$$

and

$$\frac{\zeta^{\mathrm{AV}}}{\rho} \approx \frac{1}{6}\alpha^{\mathrm{AV}} v_{\mathrm{sig}} \left| r_{ab} \right| . \tag{B.2.6}$$

In order to use artificial viscosity as a Shakura & Sunyaev (1973) viscosity, we have to slightly modify the request made above for shock capture with the following (Lodato & Price 2010):

1. Viscosity should be applied for both approaching and receding particles,
2. The β^{AV} term in the signal velocity should be dropped such that $v_{\mathrm{sig}} = c_{\mathrm{s}}$,
3. q^{AV} should be multiplied by a factor $h/\left| r_{ab} \right|$, similar to Monaghan (1992), and
4. The Morris & Monaghan (1997) switch should not be used, so α^{AV} should be treated as a constant.

These conditions result in rewriting q_a^{AV} as

$$q_a^{\mathrm{AV}} = \frac{1}{2}\alpha^{\mathrm{AV}} \rho_a c_{\mathrm{s},a} \left| \mathbf{v}_{ab} \cdot \hat{\mathbf{r}}_{ab} \right| \frac{h}{\left| r_{ab} \right|}, \tag{B.2.7}$$

giving

$$\nu^{\mathrm{AV}} \approx \frac{1}{10}\alpha^{\mathrm{AV}} c_{\mathrm{s}} h, \tag{B.2.8}$$

and

$$\frac{\zeta^{\mathrm{AV}}}{\rho} \approx \frac{1}{6}\alpha^{\mathrm{AV}} c_{\mathrm{s}} h. \tag{B.2.9}$$

This allows us to write the α_{SS} parameter of Shakura in terms of artificial viscosity as:

$$\alpha_{\mathrm{SS}} \approx \frac{1}{10}\alpha^{\mathrm{AV}} \frac{\langle h \rangle}{H}, \tag{B.2.10}$$

where $\langle h \rangle$ is the azimuthally averaged smoothing lenght.

Equations above show two main complication in using artificial viscosity to represent real viscosity:

1. The physical α_{SS} viscosity vary through the disc, and with the resolution;
2. We introduce a large unwanted bulk viscosity coefficient.

In the physics of accretion disc the second point it's not so influent since the $\nabla \cdot \mathbf{v}$ is not large and usually counterbalance the high coefficient.

Bibliography

Adams, F. C., Ruden, S. P., & Shu, F. H. 1989, *Astrophys. J.*, 347, 959

Allen, P. R., Koerner, D. W., McElwain, M. W., Cruz, K. L., & Reid, I. N. 2007, *Astron. J.*, 133, 971

Alves, F. O., Caselli, P., Girart, J. M., et al. 2019, Science, 366, 90

Aly, H., Dehnen, W., Nixon, C., & King, A. 2015, *Mon. Not. R. Astron. Soc.*, 449, 65

Aly, H., Gonzalez, J.-F., Nealon, R., et al. 2021, *Mon. Not. R. Astron. Soc.*, 508, 2743

Aly, H. & Lodato, G. 2020, *Mon. Not. R. Astron. Soc.*, 492, 3306

Aly, H., Lodato, G., & Cazzoletti, P. 2018, Monthly Notices of the Royal Astronomical Society, 480, 4738

Aly, H., Lodato, G., & Cazzoletti, P. 2018, *Mon. Not. R. Astron. Soc.*, 480, 4738

Ambartsumian, V. A. 1937, , 14, 207

André, P., Men'shchikov, A., Bontemps, S., et al. 2010, *Astron. Astrophys.*, 518, L102

Andrews, S. M., Huang, J., Pérez, L. M., et al. 2018, *Astrophys. J. Lett.*, 869, L41

Antognini, J. M. O. 2015, *Mon. Not. R. Astron. Soc.*, 452, 3610

Apai, D., Bik, A., Kaper, L., Henning, T., & Zinnecker, H. 2007, *Astrophys. J.*, 655, 484

Artymowicz, P. & Lubow, S. H. 1994, in Circumstellar Dust Disks and Planet Formation, ed. R. Ferlet & A. Vidal-Madjar, Vol. 10, 339

Artymowicz, P. & Lubow, S. H. 1996, *Astrophys. J. Lett.*, 467, L77

Baines, D., Oudmaijer, R. D., Porter, J. M., & Pozzo, M. 2006, *Mon. Not. R. Astron. Soc.*, 367, 737

Balbus, S. A. & Hawley, J. F. 1998, Reviews of Modern Physics, 70, 1

Ballabio, G., Nealon, R., Alexander, R. D., et al. 2021, *Mon. Not. R. Astron. Soc.*, 504, 888

Bally, J. 2016, , 54, 491

Balmer, W. O., Follette, K. B., Close, L. M., et al. 2022, *Astron. J.*, 164, 29

Bate, M. R. 2000, *Mon. Not. R. Astron. Soc.*, 314, 33

Bate, M. R. 2009, *Mon. Not. R. Astron. Soc.*, 397, 232

Bate, M. R. 2012, *Mon. Not. R. Astron. Soc.*, 419, 3115

Bate, M. R. 2018, *Mon. Not. R. Astron. Soc.*, 475, 5618

Bate, M. R. 2019, *Mon. Not. R. Astron. Soc.*, 484, 2341

Bate, M. R. & Bonnell, I. A. 1997, *Mon. Not. R. Astron. Soc.*, 285, 33

Bate, M. R., Bonnell, I. A., & Bromm, V. 2002, *Mon. Not. R. Astron. Soc.*, 336, 705

Bate, M. R., Bonnell, I. A., Clarke, C. J., et al. 2000, *Mon. Not. R. Astron. Soc.*, 317, 773

Bate, M. R., Bonnell, I. A., & Price, N. M. 1995, *Mon. Not. R. Astron. Soc.*, 277, 362

Bate, M. R., Lodato, G., & Pringle, J. E. 2010, *Mon. Not. R. Astron. Soc.*, 401, 1505

Bi, J., van der Marel, N., Dong, R., et al. 2020, *Astrophys. J. Lett.*, 895, L18

Biller, B., Lacour, S., Juhász, A., et al. 2012, *Astrophys. J. Lett.*, 753, L38

Binnendijk, L. 1960, Properties of double stars; a survey of parallaxes and orbits.

Boehler, Y., Weaver, E., Isella, A., et al. 2017, *Astrophys. J.*, 840, 60

Bonnell, I. A. 1994, *Mon. Not. R. Astron. Soc.*, 269, 837

Bonnell, I. A. & Bate, M. R. 1994, *Mon. Not. R. Astron. Soc.*, 271, 999

Brandner, W., Alcala, J. M., Kunkel, M., Moneti, A., & Zinnecker, H. 1996, *Astron. Astrophys.*, 307, 121

Burgasser, A. J. 2007, *Astrophys. J.*, 659, 655

Calcino, J., Price, D. J., Pinte, C., et al. 2019, *Mon. Not. R. Astron. Soc.*, 490, 2579

Casassus, S., van der Plas, G. M., Perez, S., et al. 2013, *Nature*, 493, 191

Cazzoletti, P., Ricci, L., Birnstiel, T., & Lodato, G. 2017, Astronomy & Astrophysics, 599, A102

Ceppi, S., Cuello, N., Lodato, G., et al. 2022, *Mon. Not. R. Astron. Soc.*, 514, 906

Ceppi, S., Cuello, N., Lodato, G., et al. 2024, arXiv e-prints, arXiv:2401.03767

Ceppi, S., Longarini, C., Lodato, G., Cuello, N., & Lubow, S. H. 2023, *Mon. Not. R. Astron. Soc.*, 520, 5817

Chapman, N. L., Davidson, J. A., Goldsmith, P. F., et al. 2013, *Astrophys. J.*, 770, 151

Chen, X., Arce, H. G., Zhang, Q., et al. 2013, *Astrophys. J.*, 768, 110

Chiang, E. I. & Goldreich, P. 1997, *Astrophys. J.*, 490, 368

Chiang, E. I. & Murray-Clay, R. A. 2004, *Astrophys. J.*, 607, 913

Clarke, C. J., Bonnell, I. A., & Hillenbrand, L. A. 2000, in Protostars and Planets IV, ed. V. Mannings, A. P. Boss, & S. S. Russell, 151

Claudi, R., Maire, A. L., Mesa, D., et al. 2019, *Astron. Astrophys.*, 622, A96

Close, L. M., Siegler, N., Freed, M., & Biller, B. 2003, *Astrophys. J.*, 587, 407

Connelley, M. S., Reipurth, B., & Tokunaga, A. T. 2008, *Astron. J.*, 135, 2526

Corporon, P. & Lagrange, A. M. 1999, *Astron. Astrophys. Supp. Ser.*, 136, 429

Cournoyer-Cloutier, C., Tran, A., Lewis, S., et al. 2021, *Mon. Not. R. Astron. Soc.*, 501, 4464

Cuello, N., Dipierro, G., Mentiplay, D., et al. 2019, *Mon. Not. R. Astron. Soc.*, 483, 4114

Cuello, N. & Giuppone, C. A. 2019, *Astron. Astrophys.*, 628, A119

Cuello, N., Ménard, F., & Price, D. J. 2023, European Physical Journal Plus, 138, 11

Cunningham, A. J., Krumholz, M. R., McKee, C. F., & Klein, R. I. 2018, *Mon. Not. R. Astron. Soc.*, 476, 771

Czekala, I., Chiang, E., Andrews, S. M., et al. 2019, *Astrophys. J.*, 883, 22

Dabringhausen, J., Marks, M., & Kroupa, P. 2022, *Mon. Not. R. Astron. Soc.*, 510, 413

De Rosa, R. J., Patience, J., Wilson, P. A., et al. 2014, *Mon. Not. R. Astron. Soc.*, 437, 1216

de Val-Borro, M., Gahm, G. F., Stempels, H. C., & Pepliński, A. 2011, *Mon. Not. R. Astron. Soc.*, 413, 2679

Di Folco, E., Dutrey, A., Le Bouquin, J. B., et al. 2014, *Astron. Astrophys.*, 565, L2

Dipierro, G., Price, D., Laibe, G., et al. 2015, *Mon. Not. R. Astron. Soc.*, 453, L73

D'Orazio, D. J. & Duffell, P. C. 2021, *Astrophys. J. Lett.*, 914, L21

Dotti, M., Volonteri, M., Perego, A., et al. 2010, *Mon. Not. R. Astron. Soc.*, 402, 682

Duchêne, G. & Kraus, A. 2013, , 51, 269

Duchêne, G., Lacour, S., Moraux, E., Goodwin, S., & Bouvier, J. 2018, *Mon. Not. R. Astron. Soc.*, 478, 1825

Duffell, P. C., D'Orazio, D., Derdzinski, A., et al. 2020, *Astrophys. J.*, 901, 25

Dullemond, C. P., Birnstiel, T., Huang, J., et al. 2018, *Astrophys. J. Lett.*, 869, L46

Dunhill, A. C., Cuadra, J., & Dougados, C. 2015, *Mon. Not. R. Astron. Soc.*, 448, 3545

Duquennoy, A. & Mayor, M. 1991, *Astron. Astrophys.*, 500, 337

Eckart, C. 1960, Physics of Fluids, 3, 421

Eggleton, P. & Kiseleva, L. 1995, *Astrophys. J.*, 455, 640

Eggleton, P. P. 1983, *Astrophys. J.*, 268, 368

El-Badry, K., Rix, H.-W., Tian, H., Duchêne, G., & Moe, M. 2019, *Mon. Not. R. Astron. Soc.*, 489, 5822

Elliott, P., Bayo, A., Melo, C. H. F., et al. 2014, *Astron. Astrophys.*, 568, A26

Elsender, D. & Bate, M. R. 2021, *Mon. Not. R. Astron. Soc.*, 508, 5279

Elsender, D., Bate, M. R., Lakeland, B. S., Jensen, E. L. N., & Lubow, S. H. 2023, *Mon. Not. R. Astron. Soc.*, 523, 4353

Encalada, F. J., Looney, L. W., Tobin, J. J., et al. 2021, *Astrophys. J.*, 913, 149

Español, P. & Revenga, M. 2003, , 67, 026705

Facchini, S., Lodato, G., & Price, D. J. 2013, *Mon. Not. R. Astron. Soc.*, 433, 2142

Farago, F. & Laskar, J. 2010, *Mon. Not. R. Astron. Soc.*, 401, 1189

Farris, B. D., Duffell, P., MacFadyen, A. I., & Haiman, Z. 2014, *Astrophys. J.*, 783, 134

Federrath, C. 2015, *Mon. Not. R. Astron. Soc.*, 450, 4035

Fernández-López, M., Zapata, L. A., & Gabbasov, R. 2017, *Astrophys. J.*, 845, 10

Fisher, R. T. 2004, *Astrophys. J.*, 600, 769

Fontanive, C., Biller, B., Bonavita, M., & Allers, K. 2018, *Mon. Not. R. Astron. Soc.*, 479, 2702

Frank, J., King, A., & Raine, D. J. 2002, Accretion Power in Astrophysics: Third Edition

Galli, D., Lizano, S., Shu, F. H., & Allen, A. 2006, *Astrophys. J.*, 647, 374

Galli, P. A. B., Loinard, L., Bouy, H., et al. 2019, *Astron. Astrophys.*, 630, A137

Gammie, C. F. 2001, *Astrophys. J.*, 553, 174

Gerosa, D., Veronesi, B., Lodato, G., & Rosotti, G. 2015, *Mon. Not. R. Astron. Soc.*, 451, 3941

Ghez, A. M., McCarthy, D. W., Patience, J. L., & Beck, T. L. 1997, *Astrophys. J.*, 481, 378

Ghez, A. M., Neugebauer, G., & Matthews, K. 1993, *Astron. J.*, 106, 2005

Gingold, R. A. & Monaghan, J. J. 1977, *Mon. Not. R. Astron. Soc.*, 181, 375

Goldreich, P. & Tremaine, S. 1980, *Astrophys. J.*, 241, 425

GRAVITY Collaboration, Karl, M., Pfuhl, O., et al. 2018, *Astron. Astrophys.*, 620, A116

Guszejnov, D., Grudić, M. Y., Hopkins, P. F., Offner, S. S. R., & Faucher-Giguère, C.-A. 2021, *Mon. Not. R. Astron. Soc.*, 502, 3646

Guszejnov, D. & Hopkins, P. F. 2015, *Mon. Not. R. Astron. Soc.*, 450, 4137

Guszejnov, D., Hopkins, P. F., & Krumholz, M. R. 2017, *Mon. Not. R. Astron. Soc.*, 468, 4093

Hamers, A. S. 2021, *Mon. Not. R. Astron. Soc.*, 500, 3481

Hartmann, L., Calvet, N., Gullbring, E., & D'Alessio, P. 1998, *Astrophys. J.*, 495, 385

Haugbølle, T., Padoan, P., & Nordlund, $A. 2018, Astrophys. J., 854, 35$

Heggie, D. C. 1975, *Mon. Not. R. Astron. Soc.*, 173, 729

Hennebelle, P. 2013, *Astron. Astrophys.*, 556, A153

Hoyle, F. 1960, , 1, 28

Hwang, H.-C., Ting, Y.-S., & Zakamska, N. L. 2022, *Mon. Not. R. Astron. Soc.*, 512, 3383

Jeans, J. H. 1919, *Mon. Not. R. Astron. Soc.*, 79, 408

Jerabkova, T., Beccari, G., Boffin, H. M. J., et al. 2019, *Astron. Astrophys.*, 627, A57

Joncour, I., Duchêne, G., & Moraux, E. 2017, *Astron. Astrophys.*, 599, A14

Kelley, L. Z., Haiman, Z., Sesana, A., & Hernquist, L. 2019, *Mon. Not. R. Astron. Soc.*, 485, 1579

Kennedy, G. M., Matrà, L., Facchini, S., et al. 2019, Nature Astronomy, 3, 230

Kennedy, G. M., Wyatt, M. C., Sibthorpe, B., et al. 2012, *Mon. Not. R. Astron. Soc.*, 421, 2264

Kenworthy, M. A., González Picos, D., Elizondo, E., et al. 2022, *Astron. Astrophys.*, 666, A61

Keppler, M., Penzlin, A., Benisty, M., et al. 2020, *Astron. Astrophys.*, 639, A62

Kirk, H., Dunham, M. M., Di Francesco, J., et al. 2017, *Astrophys. J.*, 838, 114

Köhler, R. 2011a, *Astron. Astrophys.*, 530, A126

Köhler, R. 2011b, *Astron. Astrophys.*, 530, A126

Köhler, R. & Leinert, C. 1998, *Astron. Astrophys.*, 331, 977

Köhler, R., Petr-Gotzens, M. G., McCaughrean, M. J., et al. 2006, *Astron. Astrophys.*, 458, 461

Kounkel, M., Covey, K., Moe, M., et al. 2019, *Astron. J.*, 157, 196

Kounkel, M., Megeath, S. T., Poteet, C. A., Fischer, W. J., & Hartmann, L. 2016, *Astrophys. J.*, 821, 52

Kouwenhoven, M. B. N., Brown, A. G. A., Zinnecker, H., Kaper, L., & Portegies Zwart, S. F. 2005, *Astron. Astrophys.*, 430, 137

Kozai, Y. 1962, *Astron. J.*, 67, 591

Kratter, K. & Lodato, G. 2016, , 54, 271

Kratter, K. M. 2011, in Astronomical Society of the Pacific Conference Series, Vol. 447, Evolution of Compact Binaries, ed. L. Schmidtobreick, M. R. Schreiber, & C. Tappert, 47

Kraus, A. L., Ireland, M. J., Martinache, F., & Hillenbrand, L. A. 2011, *Astrophys. J.*, 731, 8

Kraus, A. L., Ireland, M. J., Martinache, F., & Lloyd, J. P. 2008, *Astrophys. J.*, 679, 762

Kraus, S., Kreplin, A., Young, A. K., et al. 2020, Science, 369, 1233

Kroupa, P. 1995, *Mon. Not. R. Astron. Soc.*, 277, 1507

Kroupa, P., Weidner, C., Pflamm-Altenburg, J., et al. 2013, in Planets, Stars and Stellar Systems. Volume 5: Galactic Structure and Stellar Populations, ed. T. D. Oswalt & G. Gilmore, Vol. 5, 115

Krumholz, M. R., Klein, R. I., & McKee, C. F. 2012, *Astrophys. J.*, 754, 71

Lacour, S., Biller, B., Cheetham, A., et al. 2016, *Astron. Astrophys.*, 590, A90

Larson, R. B. 1969, *Mon. Not. R. Astron. Soc.*, 145, 271

Larson, R. B. 1972, *Mon. Not. R. Astron. Soc.*, 156, 437

Larwood, J. D., Nelson, R. P., Papaloizou, J. C. B., & Terquem, C. 1996, *Mon. Not. R. Astron. Soc.*, 282, 597

Larwood, J. D. & Papaloizou, J. C. B. 1997, *Mon. Not. R. Astron. Soc.*, 285, 288

Lebreuilly, U., Hennebelle, P., Colman, T., et al. 2021, *Astrophys. J. Lett.*, 917, L10

Lebreuilly, U., Vallucci-Goy, V., Guillet, V., Lombart, M., & Marchand, P. 2023, *Mon. Not. R. Astron. Soc.*, 518, 3326

Lee, A. T., Offner, S. S. R., Kratter, K. M., Smullen, R. A., & Li, P. S. 2019, *Astrophys. J.*, 887, 232

Lee, Y.-N. & Hennebelle, P. 2018, *Astron. Astrophys.*, 611, A89

Lee, Y.-N., Offner, S. S. R., Hennebelle, P., et al. 2020, , 216, 70
Leinert, C., Zinnecker, H., Weitzel, N., et al. 1993, *Astron. Astrophys.*, 278, 129
Lepp, S., Martin, R. G., & Childs, A. C. 2022, *Astrophys. J. Lett.*, 929, L5
Lepp, S., Martin, R. G., & Lubow, S. H. 2023, *Astrophys. J. Lett.*, 943, L4
Lidov, M. L. 1962, , 9, 719
Lin, D. N. C. & Papaloizou, J. 1979a, *Mon. Not. R. Astron. Soc.*, 188, 191
Lin, D. N. C. & Papaloizou, J. 1979b, *Mon. Not. R. Astron. Soc.*, 186, 799
Lin, D. N. C. & Papaloizou, J. 1986, *Astrophys. J.*, 307, 395
Lin, D. N. C. & Pringle, J. E. 1976, in Structure and Evolution of Close Binary Systems, ed. P. Eggleton, S. Mitton, & J. Whelan, Vol. 73, 237
Lodato, G. & Facchini, S. 2013, *Mon. Not. R. Astron. Soc.*, 433, 2157
Lodato, G. & Price, D. J. 2010, *Mon. Not. R. Astron. Soc.*, 405, 1212
Long, F., Andrews, S. M., Vega, J., et al. 2021, *Astrophys. J.*, 915, 131
Longarini, C., Lodato, G., Toci, C., & Aly, H. 2021, *Mon. Not. R. Astron. Soc.*, 503, 4930
Lubow, S. H. & Artymowicz, P. 1996, in NATO Advanced Study Institute (ASI) Series C, Vol. 477, Evolutionary Processes in Binary Stars, ed. R. A. M. J. Wijers, M. B. Davies, & C. A. Tout, 53
Lubow, S. H. & Martin, R. G. 2018, *Mon. Not. R. Astron. Soc.*, 473, 3733
Lubow, S. H., Martin, R. G., & Nixon, C. 2015, *Astrophys. J.*, 800, 96
Lubow, S. H. & Ogilvie, G. I. 2000, *Astrophys. J.*, 538, 326
Lubow, S. H. & Ogilvie, G. I. 2001, *Astrophys. J.*, 560, 997
Lucy, L. B. 1977, *Astron. J.*, 82, 1013
Lynden-Bell, D. & Kalnajs, A. J. 1972, *Mon. Not. R. Astron. Soc.*, 157, 1
Lynden-Bell, D. & Pringle, J. E. 1974, *Mon. Not. R. Astron. Soc.*, 168, 603
Mardling, R. A. & Aarseth, S. J. 2001, *Mon. Not. R. Astron. Soc.*, 321, 398
Martin, D. V., Triaud, A. H. M. J., Udry, S., et al. 2019, *Astron. Astrophys.*, 624, A68
Martin, R. G., Lepp, S., Lubow, S. H., et al. 2022, *Astrophys. J. Lett.*, 927, L26
Martin, R. G. & Lubow, S. H. 2017, *Astrophys. J. Lett.*, 835, L28
Martin, R. G. & Lubow, S. H. 2018, *Mon. Not. R. Astron. Soc.*, 479, 1297
Martin, R. G. & Lubow, S. H. 2019, *Mon. Not. R. Astron. Soc.*, 490, 1332
Martin, R. G., Nixon, C., Lubow, S. H., et al. 2014, *Astrophys. J. Lett.*, 792, L33
Mathew, S. S. & Federrath, C. 2021, *Mon. Not. R. Astron. Soc.*, 507, 2448
Mathew, S. S., Federrath, C., & Seta, A. 2023, *Mon. Not. R. Astron. Soc.*, 518, 5190
Mathieu, R. D. 1994, , 32, 465
McCaughrean, M. J. & O'Dell, C. R. 1996, *Astron. J.*, 111, 1977
McKee, C. F. & Ostriker, E. C. 2007, , 45, 565
Melo, C. H. F. 2003, *Astron. Astrophys.*, 410, 269
Mentiplay, D., Price, D. J., & Pinte, C. 2019, *Mon. Not. R. Astron. Soc.*, 484, L130
Mikkola, S. 2008, in Multiple Stars Across the H-R Diagram, ed. S. Hubrig, M. Petr-Gotzens, & A. Tokovinin, 11
Miranda, R. & Lai, D. 2015, *Mon. Not. R. Astron. Soc.*, 452, 2396
Moe, M. & Di Stefano, R. 2017, *Astrophys. J. Suppl.*, 230, 15
Moe, M. & Kratter, K. M. 2018, *Astrophys. J.*, 854, 44
Moe, M. & Kratter, K. M. 2021, *Mon. Not. R. Astron. Soc.*, 507, 3593
Monaghan, J. J. 1989, Journal of Computational Physics, 82, 1
Monaghan, J. J. 1992, , 30, 543

Monaghan, J. J. 1997, Journal of Computational Physics, 136, 298

Morris, J. P. & Monaghan, J. J. 1997, Journal of Computational Physics, 136, 41

Muñoz, D. J., Kratter, K., Vogelsberger, M., Hernquist, L., & Springel, V. 2015, *Mon. Not. R. Astron. Soc.*, 446, 2010

Muñoz, D. J. & Lai, D. 2015, Proceedings of the National Academy of Science, 112, 9264

Muñoz, D. J. & Lai, D. 2016, *Astrophys. J.*, 827, 43

Muñoz, D. J., Lai, D., Kratter, K., & Miranda, R. 2020, *Astrophys. J.*, 889, 114

Muñoz, D. J., Miranda, R., & Lai, D. 2019, *Astrophys. J.*, 871, 84

Murphy, S. J., Moe, M., Kurtz, D. W., et al. 2018, *Mon. Not. R. Astron. Soc.*, 474, 4322

Murray, C. D. & Dermott, S. F. 1999, Solar system dynamics

Murray, C. D. & Dermott, S. F. 2000, Solar System Dynamics (Cambridge University Press)

Naoz, S. 2016, , 54, 441

Naoz, S., Farr, W. M., Lithwick, Y., Rasio, F. A., & Teyssandier, J. 2013, *Mon. Not. R. Astron. Soc.*, 431, 2155

Nixon, C., King, A., & Price, D. 2013, *Mon. Not. R. Astron. Soc.*, 434, 1946

Nixon, C., King, A., Price, D., & Frank, J. 2012, *Astrophys. J. Lett.*, 757, L24

Offner, S. S. R. & Arce, H. G. 2014, *Astrophys. J.*, 784, 61

Offner, S. S. R. & Chaban, J. 2017, *Astrophys. J.*, 847, 104

Offner, S. S. R., Dunham, M. M., Lee, K. I., Arce, H. G., & Fielding, D. B. 2016, *Astrophys. J. Lett.*, 827, L11

Offner, S. S. R., Klein, R. I., McKee, C. F., & Krumholz, M. R. 2009, *Astrophys. J.*, 703, 131

Offner, S. S. R., Kratter, K. M., Matzner, C. D., Krumholz, M. R., & Klein, R. I. 2010, *Astrophys. J.*, 725, 1485

Offner, S. S. R., Moe, M., Kratter, K. M., et al. 2022, arXiv e-prints, arXiv:2203.10066

Ogilvie, G. I. 1999, *Mon. Not. R. Astron. Soc.*, 304, 557

Ostriker, E. C. 1994, *Astrophys. J.*, 424, 292

Ostriker, E. C., Gammie, C. F., & Stone, J. M. 1999, *Astrophys. J.*, 513, 259

Paczynski, B. 1977, *Astrophys. J.*, 216, 822

Padoan, P., Federrath, C., Chabrier, G., et al. 2014, in Protostars and Planets VI, ed. H. Beuther, R. S. Klessen, C. P. Dullemond, & T. Henning, 77–100

Papaloizou, J. & Pringle, J. E. 1977, *Mon. Not. R. Astron. Soc.*, 181, 441

Papaloizou, J. C. B. & Lin, D. N. C. 1995, *Astrophys. J.*, 438, 841

Papaloizou, J. C. B. & Pringle, J. E. 1983, *Mon. Not. R. Astron. Soc.*, 202, 1181

Papaloizou, J. C. B. & Terquem, C. 1995, *Mon. Not. R. Astron. Soc.*, 274, 987

Phuong, N. T., Dutrey, A., Diep, P. N., et al. 2020, *Astron. Astrophys.*, 635, A12

Pichardo, B., Sparke, L. S., & Aguilar, L. A. 2005, *Mon. Not. R. Astron. Soc.*, 359, 521

Pineda, J. E., Offner, S. S. R., Parker, R. J., et al. 2015, *Nature*, 518, 213

Poblete, P. P., Cuello, N., & Cuadra, J. 2019, *Mon. Not. R. Astron. Soc.*, 489, 2204

Pomohaci, R., Oudmaijer, R. D., & Goodwin, S. P. 2019, *Mon. Not. R. Astron. Soc.*, 484, 226

Prato, L. 2007, *Astrophys. J.*, 657, 338

Price, D. J. 2008, Journal of Computational Physics, 227, 10040

Price, D. J. 2012, Journal of Computational Physics, 231, 759

Price, D. J. & Bate, M. R. 2007, *Astrophys. Space Sci.*, 311, 75

Price, D. J., Cuello, N., Pinte, C., et al. 2018a, *Mon. Not. R. Astron. Soc.*, 477, 1270

Price, D. J., Wurster, J., Tricco, T. S., et al. 2018b, , 35, e031

Raghavan, D., McAlister, H. A., Henry, T. J., et al. 2010, *Astrophys. J. Suppl.*, 190, 1

Ragusa, E., Alexander, R., Calcino, J., Hirsh, K., & Price, D. J. 2020, *Mon. Not. R. Astron. Soc.*, 499, 3362

Ragusa, E., Dipierro, G., Lodato, G., Laibe, G., & Price, D. J. 2017, *Mon. Not. R. Astron. Soc.*, 464, 1449

Ragusa, E., Fasano, D., Toci, C., et al. 2021, *Mon. Not. R. Astron. Soc.*, 507, 1157

Ragusa, E., Lodato, G., & Price, D. J. 2016, *Mon. Not. R. Astron. Soc.*, 460, 1243

Ramírez-Tannus, M. C., Backs, F., de Koter, A., et al. 2021, *Astron. Astrophys.*, 645, L10

Rauer, H., Catala, C., Aerts, C., et al. 2014, Experimental Astronomy, 38, 249

Reipurth, B., Clarke, C. J., Boss, A. P., et al. 2014, in Protostars and Planets VI, ed. H. Beuther, R. S. Klessen, C. P. Dullemond, & T. Henning, 267

Reipurth, B., Guimarães, M. M., Connelley, M. S., & Bally, J. 2007, *Astron. J.*, 134, 2272

Reipurth, B. & Zinnecker, H. 1993, *Astron. Astrophys.*, 278, 81

Reynolds, N. K., Tobin, J. J., Sheehan, P., et al. 2021, *Astrophys. J. Lett.*, 907, L10

Rigliaco, E., Gratton, R., Ceppi, S., et al. 2023, *Astron. Astrophys.*, 671, A82

Rodriguez, J. E., Loomis, R., Cabrit, S., et al. 2018, *Astrophys. J.*, 859, 150

Sana, H., de Mink, S. E., de Koter, A., et al. 2012, Science, 337, 444

Sana, H., Le Bouquin, J. B., Lacour, S., et al. 2014, *Astrophys. J. Suppl.*, 215, 15

Sana, H., Ramírez-Tannus, M. C., de Koter, A., et al. 2017, *Astron. Astrophys.*, 599, L9

Satsuka, T., Tsuribe, T., Tanaka, S., & Nagamine, K. 2017, *Mon. Not. R. Astron. Soc.*, 465, 986

Scally, A., Clarke, C., & McCaughrean, M. J. 1999, *Mon. Not. R. Astron. Soc.*, 306, 253

Shakura, N. I. & Sunyaev, R. A. 1973, in IAU Symposium, Vol. 55, X- and Gamma-Ray Astronomy, ed. H. Bradt & R. Giacconi, 155

Shu, F. H. 1977, *Astrophys. J.*, 214, 488

Shu, F. H., Adams, F. C., & Lizano, S. 1987, , 25, 23

Shu, F. H., Tremaine, S., Adams, F. C., & Ruden, S. P. 1990, *Astrophys. J.*, 358, 495

Smallwood, J. L., Franchini, A., Chen, C., et al. 2020, *Mon. Not. R. Astron. Soc.*, 494, 487

Smallwood, J. L., Lubow, S. H., Franchini, A., & Martin, R. G. 2019, *Mon. Not. R. Astron. Soc.*, 486, 2919

Smallwood, J. L., Nealon, R., Chen, C., et al. 2021, *Mon. Not. R. Astron. Soc.*, 508, 392

Smith, K. W., Bonnell, I. A., & Bate, M. R. 1997, *Mon. Not. R. Astron. Soc.*, 288, 1041

Stahler, S. W. 2010, *Mon. Not. R. Astron. Soc.*, 402, 1758

Targon, C. G., Rodrigues, C. V., Cerqueira, A. H., & Hickel, G. R. 2011, *Astrophys. J.*, 743, 54

Tobin, J. J., Looney, L. W., Li, Z.-Y., et al. 2016, *Astrophys. J.*, 818, 73

Tobin, J. J., Offner, S. S. R., Kratter, K. M., et al. 2022, *Astrophys. J.*, 925, 39

Tobin, J. J., Sheehan, P. D., Megeath, S. T., et al. 2020, *Astrophys. J.*, 890, 130

Toci, C., Galli, D., Verdini, A., Del Zanna, L., & Landi, S. 2018, *Mon. Not. R. Astron. Soc.*, 474, 1288

Toci, C., Lodato, G., Christiaens, V., et al. 2020, *Mon. Not. R. Astron. Soc.*, 499, 2015

Tokovinin, A. 2008, *Mon. Not. R. Astron. Soc.*, 389, 925

Tokovinin, A. 2014, *Astron. J.*, 147, 87

Tokovinin, A. 2020, *Mon. Not. R. Astron. Soc.*, 496, 987

Tokovinin, A. & Briceño, C. 2020, *Astron. J.*, 159, 15

Tokovinin, A. & Moe, M. 2020, *Mon. Not. R. Astron. Soc.*, 491, 5158

Tokovinin, A., Petr-Gotzens, M. G., & Briceño, C. 2020, *Astron. J.*, 160, 268

Tokovinin, A., Thomas, S., Sterzik, M., & Udry, S. 2006, *Astron. Astrophys.*, 450, 681

Torniamenti, S., Ballone, A., Mapelli, M., et al. 2021, *Mon. Not. R. Astron. Soc.*, 507, 2253

Valtonen, M. & Karttunen, H. 2006, The Three-Body Problem

Valtonen, M., Karttunen, H., Myllári, A., Orlov, V., & Rubinov, A. 2006, Stability limit for hierarchical three-body systems, 44

Vericel, A., Gonzalez, J.-F., Price, D. J., Laibe, G., & Pinte, C. 2021, *Mon. Not. R. Astron. Soc.*, 507, 2318

Veronesi, B., Ragusa, E., Lodato, G., et al. 2020, *Mon. Not. R. Astron. Soc.*, 495, 1913

von Zeipel, H. 1910, Astronomische Nachrichten, 183, 345

Vynatheya, P., Hamers, A. S., Mardling, R. A., & Bellinger, E. P. 2022, *Mon. Not. R. Astron. Soc.*, 516, 4146

Walch, S., Whitworth, A. P., & Girichidis, P. 2012, *Mon. Not. R. Astron. Soc.*, 419, 760

Wang, K., Zhang, Q., Wu, Y., & Zhang, H. 2011, *Astrophys. J.*, 735, 64

Ward-Thompson, D., Kirk, J. M., André, P., et al. 2010, *Astron. Astrophys.*, 518, L92

Weinberg, M. D., Shapiro, S. L., & Wasserman, I. 1987, *Astrophys. J.*, 312, 367

Wheelwright, H. E., Oudmaijer, R. D., & Goodwin, S. P. 2010, *Mon. Not. R. Astron. Soc.*, 401, 1199

Winters, J. G., Henry, T. J., Jao, W.-C., et al. 2019, *Astron. J.*, 157, 216

Wurster, J., Bate, M. R., & Price, D. J. 2019, *Mon. Not. R. Astron. Soc.*, 489, 1719

Xiang-Gruess, M. 2016, *Mon. Not. R. Astron. Soc.*, 455, 3086

Young, M. D., Baird, J. T., & Clarke, C. J. 2015, *Mon. Not. R. Astron. Soc.*, 447, 2907

Young, M. D. & Clarke, C. J. 2015, *Mon. Not. R. Astron. Soc.*, 452, 3085

Zanazzi, J. J. & Lai, D. 2018, *Mon. Not. R. Astron. Soc.*, 473, 603

Zhang, Q., Qiu, K., Girart, J. M., et al. 2014, *Astrophys. J.*, 792, 116

Zhao, B., Tomida, K., Hennebelle, P., et al. 2020, , 216, 43

Zúñiga-Fernández, S., Olofsson, J., Bayo, A., et al. 2021, *Astron. Astrophys.*, 655, A15

Zurlo, A., Gratton, R., Pérez, S., & Cieza, L. 2023, European Physical Journal Plus, 138, 411

Acknowledgments

What a wonderful journey, folks! It started semi-randomly and it went wildly. For sure, all the joy and fulfilment I collected along the way, and its wondrous conclusion are largely due to all the amazing people I met and travelled with. Here, I would like to thank them, sure that this list will be far from complete!

These three years have been wisely guided by Giuseppe and Nicolás. Giuseppe, your attention to detail and search for cleanness in scientific work have been inspiring and improved me as a scientist. I have felt completely free to explore my line of research following my curiosity, and you helped me to root it in my scientific results. Nico, you have been one of the most precious encounters of the past three years. You showed me how to be a better scientist and a better person. You supported me since the first meeting we had, through all the stages of my PhD until the last months, in which you selflessly aided me in choosing what to do with my life. You did show me what passion and inner strength are. Looking back, I realise you have been far more than a supervisor: you have been a mentor and a friend.

The work I carried out would not have had the same depth without the people I collaborated with in my papers. Daniel, it has been a joy to work with you both on my first and last paper. You taught me how to happily take things seriously, at work or in life. My stay in Melbourne has been so transformative also thanks to you and your inspiring care. Cathie, you have been my first point of contact with the research field outside of Milan and I could have never been so lucky. Your patience and kindness inspired me and I would wish for everyone to share a step of their research path with you. My last two scientific efforts pivoted in Santa Barbara with people I met there. Steve, Matthew and Dan, you are one of the key reasons my experience at KITP has been so impactful in my career.

Now it's time for my two conscript disc physicists and office fellows, Cristiano and Pietro. Cristiano, we shared a lot, both from a scientific and personal point of view. We literally travelled around the world together. You taught me to chase my dreams and always give my best, whether in relationships or scientific research. Pietro, you have been a reference point for these three years. You deeply enriched me, discussing life and physics and, to me, your sincerity, stillness and purity have been a guide.

Let's step into the other side of the astrophysics XXXVI cycle and of the office: the cosmologists. Marina, your generosity and attention to people made an immeasurable difference in these three years. Among all of your great skills and qualities, you are the one who appreciated most and shared my humour and this definitely shaped the office's atmosphere. Giovanni, you have been the reference point for either the most serious or most crazy funny stuff, that's a fantastic achievement of the *not* best PhD student of the school.

Last but not least, the first of the next generation and the last of the past one: Rossella, your kindness and your strength characterise you. I am sorry we have misled you, but now a bit of the XXXVI cycle spirit runs in your veins too.

My journey in scientific research started in another office: Claudia's office. Claudia, you are where everything started. That was a tough time, as we like to remember. Still, even behind a screen, you have overwhelmed me with your energy backing me up along those challenges. This journey started thanks to you and you have always been there since then. You taught me to never leave anyone behind and I greatly admire your strength in fighting for what you believe in and love.

Past colleagues and present collaborators and friends have been essential as well. Alessia, we know our relationship started on the wrong foot (even if I was not aware of that!). It's wonderful that it turned into a true friendship, that's been a precious turn of events. Alice, you are the one who first helped me join the group and your glowingness always strikes me. Antoine, you have been a wonderful companion during my Grenoble stays and a great colleague during work. Your dedication matches your friendliness and this mix made my Grenoble experiences. Benedetta, it could be said that you have been our first colleague. I am happy we shared a lot during the last months and became good friends. We passed through hard moments together and sharing part of this route with you lightened the steps. Martina, you passed to us the "baton" of the office and, even if away from there, you always have been part of it. Enrico, you are one of the most sincere, kind and fun colleagues I had and the first PhD student I met during my Bachelor's thesis. That was pure luck.

I cannot avoid spending two words for Gerrit and Alvaro, with whom I had a lot of fun during my stays in Grenoble. Gerrit, you put your precious dad's time on the line to help a nearly unknown PhD student navigate his life, this alone suffice to explain how grateful I am to have met a person like you. Alvaro, you are the master of perseverance, expertise, nuanced interesting suggestions (on top of being the best music, sci-fi/fantasy movie and novel dealer, obviously).

I met a lot of people along this journey and I cannot mention (someone would say remember) all of them. However, I would like to explicitly thank the people who helped me in the last year of my PhD, during my hard thinking about what to do with my career: Juan, Miguel, Enrique, Christophe, and Rosemary. It has been a tough choice and I really appreciated your spontaneous support.

In the end, I want to thank people who were there well before this journey and supported me during these years. Cristina, you taught me curiosity and wonder, which guided me along my research. These three years saw us pushing hard on the accelerator, and I've never been more fulfilled and happy. Giampaolo, we learned together how to discuss and build a joint line of thoughts, exploring the depths of our minds. This has been a crucial skill during these years. At the very origin of this, stands my family. Thank you, mamma and papà, Serena and Silvia for putting up with me and supporting me over these 29 years. Many of the choices that have brought me here are also due to you, and I could not be more grateful to you for that. Last I want to thank the people I share a lot of passions with and who helped me to enjoy life even in the hardest moments: VenerD&D (and particularly Berto, with whom I first discussed this strange idea of doing a PhD).

Thank you all. I am happy and satisfied, ready to explore new shores.

"It is hard to cast the skin," said Kaa as Mowgli sobbed and sobbed, with his head on the blind bear's side and his arms round his neck, while Baloo tried feebly to lick his feet.

"The stars are thin," said Gray Brother, snuffing at the dawn wind. *"Where shall we lair today? for, from now, we follow new trails."*

The Jungle Book, Rudyard Kipling